TOUGH NATURAL-FIBRE COMPOSITES

A thesis submitted for the degree of Doctor of Philosophy of Imperial College London
and Diploma of Imperial College

January 2015

By Mana Techapaitoon

Department of Mechanical Engineering

Imperial College London

ABSTRACT

Natural fibre composites (NFCs) possess relatively good specific strength and stiffness properties. However, natural fibres (NFs) often show relatively poor interfacial adhesion with respect to polymeric matrices, may contain relatively high levels of moisture and have variable mechanical properties due to the route by which they have been harvested and manufactured. These aspects may result in inconsistent mechanical properties of such composites, especially evident in a poor interlaminar fracture toughness. Thus, the present work investigates the mode I interlaminar fracture toughness, of NFCs based upon an anhydride-cured diglycidyl ether of bisphenol-A (DGEBA) epoxy matrix. Further, this matrix was used as a 'control' or modified with silica nanoparticles and/or rubbery microparticles. Two types of natural fibres were employed: unidirectional flax fibre (FF) and plain-woven regenerated cellulose fibre (CeF). Two very different routes were explored for the production of the NFCs based upon these materials. One route was via a resin infusion under flexible tooling (RIFT) process and a second route employed a resin transfer moulding (RTM) process. A very low value of the interlaminar fracture energy of about 20 J/m^2 was measured for the flax fibre-reinforced plastics (FFRPs), using the 'control epoxy matrix, produced by the RIFT manufacturing process which was initially employed. However, such composite manufactured via the RTM process possessed fracture energy of about 963 J/m^2. Further, this value was found to increase to 1264 J/m^2 when the epoxy matrix was modified using a combination of silica nanoparticles and rubbery microparticles. Hence, optimization studies using the RIFT manufacturing process were undertaken which led to a simple modification of this manufacturing route whereby the natural fibres were first oven-dried. This resulted in the final RIFT process giving values of the fracture toughness of the same order as those obtained from the RTM process. Also of note was the observation that the FFRPs manufactured via the RTM or the final RIFT process had similar values of toughness as those measured for glass fibre-reinforced plastics (GFRPs) made using the equivalent type of epoxy matrix. Similar observations were recorded in the case of the cellulose fibre-reinforced plastics (CeFFRPs). The present study has also considered the underlying mechanisms for the above observations and used analytical models to predict the toughening mechanisms and a good agreement between the predictions and the experimental data for the NFCs was obtained.

Declaration of Originality

This PhD Thesis work is my own and that all else is appropriately referenced.

Copyright Declaration

ACKNOWLEDGEMENT

I would like to express my sincere gratitude and appreciation to my supervisor, Prof. Anthony Kinloch[1], and my co-supervisors, Dr. Ambrose Taylor[1] and Dr. Wern Sze Teo[2] for their invaluable guidance, suggestions, assistance, patience and encouragement throughout the present research work. I would also like to thank Prof. John Watts[3] and Dr. Steven Hinder[3] for their support, guidance and suggestions; as well as Dr. Stephan Sprenger[4] for the supply of materials.

I would like to thank the Department of Mechanical Engineering for the excellent facilities and the staff, Dr. Ruth Brooker[1] and Dr. Judith Thei[1], for their support with respect to the equipment and testing procedures. Also, I would wish to thank Mr. Paul Woodward[1] for help with the specimen preparation, Mr. Suresh Viswanathan Chettiar[1] for help with the mechanical testing and my colleague, Mr. Huang Ming Chong[1] for assistance with various tests. I would also like to thank Dr. Mahmoud Ardakani[1] for his guidance and assistance on the SEM equipment, Mrs. Patricia Carry[1] for her help with the DSC, TGA and pycnometer equipment and Mr. Gary Senior[1] for his help with the RIFT manufacturing process.

For the one year that I spent in Singapore for an industrial attachment at SIMTech, I would like to thank my colleague, Mrs. Ma Cho Cho[2] for her help with the DSC, TGA and rheology equipment, Mr. Joel Lau Chun Hee[2] for help with the RTM manufacturing and Ms. Deng Xinying[2] for assistance with the SEM equipment; and other SIMTech staffs for their co-operation and help with both work and life.

Last, but not least, I would like to thank my family for their support and encouragement throughout the entire PhD. I would not have accomplished the present PhD Thesis without them.

[1] Imperial College London, UK
[2] Singapore Institute of Manufacturing Technology (SIMTech), Singapore
[3] University of Surrey, UK
[4] Evonik Hanse GmbH, Germany

TABLE OF CONTENTS

LIST OF FIGURES

LIST OF TABLES

NOMENCLATURE

List of English Alphabets

a	Crack length, mm
a_0	Initial crack length, mm
a_i	Width of a simplified cross-section of a warp or weft yarn (i = 1-2), mm
A_i	Cross-sectional area of a warp or weft yarn, mm^2
A_{CT}	Cross-sectional area of circular parallel compression plates (diameter of 150 mm)
A_{RTM}	Cross-sectional area of the pre-laid fibre in the RTM mould (305 mm x 215 mm)
b	Specimen width, mm
b_i	Height of a simplified cross-section of a warp or weft yarn (i = 1-2), mm
$b_{\min}$	Minimum specimen width required for plain strain conditions, mm
C	Specimen compliance (Mode I interlaminar fracture test)
D	Mid-span deflection under 3-point bend test, mm
E	Young's modulus, GPa
$E_t \,/\, \rho$	Specific tensile Young's modulus, 10^6 m^{2}s^{-2}
E_1	Longitudinal Young's Modulus, GPa
E_{1flex}	Flexural modulus obtained from mode I DCB interlaminar fracture test, GPa
E_2	Transverse Young's Modulus, GPa
E_B	Calibrated modulus from multi-span 3-point bend test, GPa
E'_B	Modulus from each span from multi-span 3-point bend test, GPa
E_f	Modulus of the reinforcing fibres, GPa
E_{flex}	Flexural modulus, GPa
E_m	Young's modulus of matrix, GPa
E_t	Tensile modulus, GPa
E_{tt}	Tensile modulus of 2D orthogonal plain-woven fabric, GPa
F	Large displacement correction factor for mode I DCB interlaminar fracture test
$F_{f,CT}$	Force required to maintain the fibre thickness from the fibre compression test, kN
$F_{f,RTM}$	RTM mould clamping force required to maintain the fibre thickness, kN
$F_{m,RTM}$	RTM mould clamping force required to counteract the resin hydrostatic pressure, kN
F_{RTM}	Total RTM mould clamping force, kN
g_i	Warp or weft interyarn gap (i = 1-2), mm
G_{12}	In-plane shear modulus, GPa
G_C	Critical strain release energy or mode I interlaminar fracture energy, J/m^2
G_{IC}	Mode I critical strain release energy or mode I interlaminar fracture energy, J/m^2
$G_{IC,\text{in}}$	Initiation value of mode I interlaminar fracture energy, J/m^2
$G_{IC,\text{pro}}$	Propagation value of mode I interlaminar fracture energy, J/m^2
G_{ICU}	Mode I interlaminar fracture energy of unmodified epoxy polymer, J/m^2
h	Specimen thickness, mm (Other tests) or Specimen thickness ($2h$), mm (Mode I DCB interlaminar fracture test only)
h_{tab}	Tab thickness, mm
I_i	Moment of inertia of a warp or weft yarn (i = 1-2), mm^4
J	Transformation variable
J_i	Transformation variable (i = 1-10)
k	Constant in the multi-span 3-point bend test calculation
k_{sys}	Machine compliance
K	Stress intensity factor

K_{IC}	Critical stress intensity factor, MPa·m$^{1/2}$
K_f^{vp}	Maximum stress concentration factor around voids due to fibre-reinforcements
K_p^{sb}	Maximum stress concentration factor around particles due to particles
K_p^{vp}	Maximum stress concentration factor around voids due to particles
l_1	Distance of the load point above the beam axis, mm
l_2	Distance of the load point along the beam axis, mm
l_f^b	Length of the reinforcing fibres at breakage, mm
l_f^p	Peeling length of the reinforcing fibres, mm
L	Specimen length, mm
L_i	Undulated length of a warp or weft curved beam, mm
L_{tab}	Tab length, mm
m	Slope of the tangent to the initial straight-line portion of the load-deflection curve
n_f^b	Number of fibres that break per unit area
n_f^p	Number of the peeling fibres per unit area
n_t^m	Total number of pixel counted in the resin-rich region
n_t^M	Total number of pixel counted
n_v^m	Number of pixels counted for micro-voids
n_v^M	Number of pixels counted for macro-voids
N	Loading block correction factor for mode I DCB interlaminar fracture test
N_1	Normal force acting on the warp yarn, N
p	Local hydrostatic stress/local mean stress, MPa
P	Applied load, N
P_c	Critical load at the onset of the crack propagation, N
$P_{\max}$	Maximum load, N
Q	Volumetric flow rate, cc/min
r_f	Radius of the fibres, mm
r_i	Internal radius of the pipeline for injection, mm
r_p	Radius of the particles, mm
r_y	Radius of plastic zone under plane stress condition/plane strain condition, mm
r_y^{sb}	Radius of plastic zone induced by shear band yielding, mm
r_y^{vp}	Radius of plastic zone induced by plastic void growth, mm
r_{yu}	Irwin prediction of plane strain plastic zone radius for the unmodified matrix at fracture, mm
R_{nfgf}	Ratio between fibre volume fraction of NFs and fibre volume fraction of GFs
R_S	Testing speed, mm/min
S	Specimen support span or specimen gauge length, mm
sf	Safety factor for the RTM process
t_c^T	Total thickness of the composite panels, mm
t_{gf}	Thickness of the GFRP region, mm
t_{mould}	RTM mould cavity thickness, mm
t_{nf}	Thickness of the NFRP region, mm
T_g	Glass transition temperature, °C
$T_{g,i}$	Glass transition temperature of constituent i (i = 1-2), °C
U_{si}^{sb}	Energy contributed from shear band yielding due to silica-nanoparticles, J
U_{si}^{vp}	Energy contributed from plastic void growth due to silica-nanoparticles, J
v_f	Volume fraction of the reinforcing fibres
v_{f1}	Volume fraction of the reinforcing fibres in longitudinal direction
v_{f2}	Volume fraction of the reinforcing fibres in transverse direction
v_{fv}	Volume fraction of the fibres that show plastic void growth

v_{gf}^{entire}	Volume fraction of the glass fibres in entire region
v_{gf}^{local}	Volume fraction of the glass fibres in its region
v_m	Volume fraction of the matrix
v_m^{entire}	Volume fraction of the matrix in entire region
v_{nf}^{entire}	Volume fraction of the natural fibres in entire region
v_{nf}^{local}	Volume fraction of the natural fibres in its region
v_p	Volume fraction of the particles
v_{pv}	Volume fraction of the particles that show plastic void growth
v_v	Volume fraction of the voids or void content, vol%
v_v^m	Volume fraction of the micro-voids
v_v^M	Volume fraction of the macro-voids
v_{vv}	Volume fraction of the enlarged voids due to the plastic void growth
v_w	Volume fraction of moisture/water or moisture content, vol%
V_{v0}	Initial volume of the voids, mm^3
V_{v1}	End volume of the voids, mm^3
x	Distance from the reference coordinate along the X-axis, mm
X_c	Longitudinal ultimate compressive strength, MPa
X_t	Longitudinal ultimate tensile strength, MPa
y	Distance from the reference coordinate along the Y-axis, mm
Y	Specimen and crack geometry dependent dimensionless parameter
Y_c	Transverse ultimate compressive strength, MPa
Y_t	Transverse ultimate tensile strength, MPa
w_i	Weight fraction of constituent *i* (*i* = 1-2)
W_{epoxy}	Weight of the epoxy in the mixture, g
W_{gf}	Weight of the glass fibres, g
W_{hardener}	Weight of the hardener in the mixture, g
W_{modifier}	Weight of the modifier in the mixture, g
W_{nf}	Weight of the natural fibres, g
z_i	Path of the curved beam as sinusoidal shape function (*i* = 1-2)

List of Greek Alphabets

α	Confidence interval value for t-test
β	Function of geometrical features in the stress intensity factor calculation
δ	Displacement, mm
Δ	Effective delamination extension to correct for rotation at the delamination front
Δ_t	Tension deformation of plain-woven fabric in the direction of tensile load
$\Delta\varepsilon$	Difference between the two strain points on stress-strain curve within the elastic region, %
$\Delta\sigma$	Difference in applied tensile stress between the two strain points on stress-strain curve within the elastic region, MPa
ΔG_f^{db}	Fracture energy contributed from debonding due to reinforcing fibre, J/m^2
ΔG_f^{fb}	Fracture energy contributed from fibre bridging due to reinforcing fibre, J/m^2
ΔG_f^{fd}	Fracture energy contributed from fibre defibrillation due to reinforcing fibre, J/m^2
ΔG_f^{vp}	Fracture energy contributed from plastic void growth due to reinforcing fibre, J/m^2
ΔG_r^{db}	Fracture energy contributed from debonding due to rubber-microparticles, J/m^2
ΔG_r^{rb}	Fracture energy contributed from rubber bridging due to rubber-microparticles, J/m^2
ΔG_r^{sb}	Fracture energy contributed from shear band yielding due to rubber-microparticles, J/m^2
ΔG_r^{vp}	Fracture energy contributed from plastic void growth due to rubber-microparticles, J/m^2
ΔG_{si}^{db}	Fracture energy contributed from debonding due to silica-nanoparticles, J/m^2
ΔG_{si}^{sb}	Fracture energy contributed from shear band yielding due to silica-nanoparticles, J/m^2
ΔG_{si}^{vp}	Fracture energy contributed from plastic void growth due to silica-nanoparticles, J/m^2
ε	Strain, %
ε'	Strain rate, s^{-1}
ε_{ff}	Failure strain of the fibres, %
ε_t	Tensile failure strain, %
ε_{xt}	Longitudinal tensile failure strain, %
$\dot{\gamma}$	Shear rate, s^{-1}
γ_{fu}	Shear strain at fracture of the unmodified matrix, %
ρ	Density, g/cm^3
ρ_c	Density of the composites, g/cm^3
ρ_f	Density of the reinforcing fibres, g/cm^3
ρ_{gf}	Density of the glass fibres, g/cm^3
ρ_{gfrp}	Density of the GFRP region, g/cm^3
ρ_m	Density of the matrix, g/cm^3
ρ_{nf}	Density of the natural fibres, g/cm^3
ρ_{nfrp}	Density of the NFRP region, g/cm^3
σ	Applied stress/strength, MPa
σ_c	Compressive strength, MPa
σ_{cri}	Critical applied stress, MPa
$\sigma_{m,RTM}$	Resin hydrostatic pressure in RTM process, MPa
σ_t	Tensile strength, MPa
σ_{tf}	Tensile strength of the fibres, MPa
σ_{UT}	Ultimate tensile strength, MPa
σ_y	Yield tensile stress/strength, MPa
σ_{yc}	Plane-strain compressive yield strength of the unmodified matrix, MPa
σ_{yt}	Uniaxial tensile yield strength of the unmodified matrix, MPa
υ	Poisson's ratio

υ_m	Poisson's ratio of the matrix
$\varnothing$	Diameter, mm
ψ_f	Increase in fracture energy caused by the toughening mechanisms contributed from fibre reinforcement.
ψ_r	Increase in fracture energy caused by the toughening mechanisms contributed from CTBN rubber-microparticles.
ψ_{si}	Increase in fracture energy caused by the toughening mechanisms contributed from silica-nanoparticles.
θ_i	Constant in the correction calculation for mode I interlaminar fracture energy (i = 1-5)
μ_m	Material constant allowing for the pressure-dependency of the yield stress
λ_r	Rubber extension ratio
Γ_r^t	Tearing energy of the CTBN rubber-microparticles as a function of temperature, J/m^2
$\Sigma\rho_f^A$	Total density per unit area of the fibre/fabric stack, g/cm^2

List of Abbreviations

100C-2h/150C-10h	100°C for 2 hours followed by 150°C for 10 hours curing schedule
100C-2h/150C-15h	100°C for 2 hours followed by 150°C for 15 hours curing schedule
100C-2h/150C-20h	100°C for 2 hours followed by 150°C for 20 hours curing schedule
100C-2h/150C-5h	100°C for 2 hours followed by 150°C for 5 hours curing schedule
120C-2h/160C-2h	120°C for 2 hours followed by 160°C for 2 hours curing schedule
5%	Point at 5% compliance offset on the load vs opening displacement curve under mode I DCB interlaminar fracture test
AEW	Amine equivalent weight (g/eq)
AFM	Atomic force microscopy
as-received	Fibre condition: As-received condition
ASTM	American Society for Testing and Materials
CBT	Corrected beam theory for mode I interlaminar test
CeF/CeFs	Cellulose fibre(s)
CeFRP/CeFRPs	Cellulose fibre-reinforced plastic(s)
CeFRP-PW/CeFRPs-PW	Plain-woven cellulose fibre-reinforced plastic(s)
CF/CFs	Carbon fibre(s)
CF-PW	Plain-woven carbon fibre
CF-UD	Unidirectional carbon fibre
CFRP/CFRPs	Carbon fibre-reinforced plastic(s)
CLT	Classical laminate theory
CSM	Chopped strand mat
CTBN	Carboxyl-terminated butadiene-acrylonitrile rubber
DCB	Double cantilever beam mode I interlaminar fracture test method
DGEBA	Diglycidyl ethers of bisphenol A epoxy polymer/resin
DSC	Differential scanning calorimetry thermoanalytical technique
DTG	Derivative thermogravimetric curve obtained from TGA
ECT	Edge crack torsion mode III interlaminar fracture energy test method
EEW	Epoxide equivalent weight (g/eq)
ELS	End-loaded split mode II interlaminar fracture test method
ENF	End-notched flexure mode II interlaminar fracture energy test method
EPFM	Elasto-plastic fracture mechanics
ESIS	European Standard Integrity Society
FEA	Finite element analysis
FEG-SEM	Field emission gun scanning electron microscopy
FF/FFs	Flax fibre(s)
FFRP/FFRPs	Flax fibre-reinforced plastic(s)
FFRP-UD/FFRPs-UD	Unidirectional flax fibre-reinforced plastic(s)
FRC/FRCs	Fibre-reinforced composite(s)
FRP/FRPs	Fibre-reinforced plastic(s)
GF/GFs	Glass fibre(s)
GF-PW	Plain-woven glass fibre
GF-PW+T	Plain-woven and twill 2x2 glass fibre
GF-QI-NCF	Quasi-isotropic non-crimp glass fibre
GF-UD	Unidirectional glass fibre
GFC/GFCs	Glass fibre composite(s)
GFRP/GFRPs	Glass fibre-reinforced plastic(s)
GFRP-PW+T/GFRPs-PW+T	Plain-woven glass fibre-reinforced plastic(s) with twill 2x2 glass backing
GFRP-UD/GFRPs-UD	Unidirectional glass fibre-reinforced plastic(s)
GSM	Planar density (g/m^2)
HBP	Hyperbranched polyester of third generation
LEFM	Linear-elastic fracture mechanics
MAX	Maximum point on the load vs opening displacement curve under Mode I DCB interlaminar fracture test
NCF	Non-crimp weaving architecture (Non-crimp fabric)
NF/NFs	Natural fibre(s)
NFC/NFCs	Natural fibre composite(s)
NFRP/NFRPs	Natural fibre-reinforced plastic(s)

NL	Point at which the load vs opening displacement curve become non-linear under mode I DCB interlaminar fracture test
O_2 plasma	Low pressure O_2 plasma treatment (at 50% power for 5 minutes in the present study)
OD/OD-modification	Drying in a fan-oven for 12 hours at 75°C
OD-50C	Fan-oven dry at 50°C
OD-50C/4hr	Fan-oven dry at 50°C for 4 hours
OD-75C	Fan-oven dry at 75°C
OD-75C/12hr	Fan-oven dry at 75°C for 12 hours
OM	Optical microscopy
OP/OP-modification	Treating with low pressure O_2 plasma treatment at 50% power for 5 minutes
P-value	Significance value for t-test
PAN	Polyacrylonitrile
PLLA	Poly(L-lactic acid)
Pre-preg	Pre-impregnated fibre/fabric for composite manufacturing
PTFE	Polytetrafluoroethylene
PW	Plain-woven weaving architecture (Plain-woven fabric)
PW+T	Plain-woven fabric with twill 2x2 fabric backing
QI	Quasi-isotropic
R	Rubber-microparticles
RIFT	Resin infusion under flexible tooling manufacturing process
RTM	Resin transfer moulding manufacturing process
s (subscript)	Symmetric stacking sequence
SCRIMP	Seeman composites resin infusion manufacturing process
SEM	Scanning electron microscopy
Si	Silica-nanoparticles
Si0R0	Unmodified/control DGEBA epoxy polymer
Si0R9	9 wt% rubber-microparticle modified DGEBA epoxy polymer
Si10R0	10 wt% silica-nanoparticle modified DGEBA epoxy polymer
Si12R0	12 wt% silica-nanoparticle modified DGEBA epoxy polymer
Si10R9	Hybrid 10 wt% silica-nanoparticle and 9 wt% rubber-microparticle modified DGEBA epoxy polymer
Si5R0	5 wt% silica-nanoparticle modified DGEBA epoxy polymer
T	Twill 2x2 weaving architecture (Twill 2x2 fabric)
TEM	Transmission electron microscopy
TG	Thermogravimetric curve obtained from Thermal gravimetric analysis (TGA)
TGA	Thermal gravimetric analysis technique
Twill 2x2	Twill 2x2 weaving architecture (Twill 2x2 fabric)
UD	Unidirectional weaving architecture (Unidirectional fabric)
VARTM	Vacuum assisted resin transfer moulding manufacturing process
VD/VD-modification	Drying under vacuum in the RIFT vacuum bagging for 6 hours at 50°C
VD-50C	Vacuum dry at 50°C in RIFT vacuum bagging
VD-50C/6hr	Vacuum dry at 50°C for 6 hours in RIFT vacuum bagging
VARI	Vacuum assisted resin infusion manufacturing process
VIS	Point at which delamination is observed visually on specimen under mode I DCB interlaminar fracture test
wt%	Weight-by-weight percentage
vol%	Volume-by-volume percentage

CHAPTER 1 INTRODUCTION AND AIMS

1.1 Introduction

1.2 Fibre-Reinforced Composites (FRCs)

A fibre-reinforced composite (FRC) is a mixture of two or more distinct constituents on a microscopic scale with different properties, i.e. the fibre/fabric reinforcement and the matrix [1]. The reinforcement can be in either in a continuous or discontinuous form. A composite can be classified based on the reinforcement, see Figure 1.1.

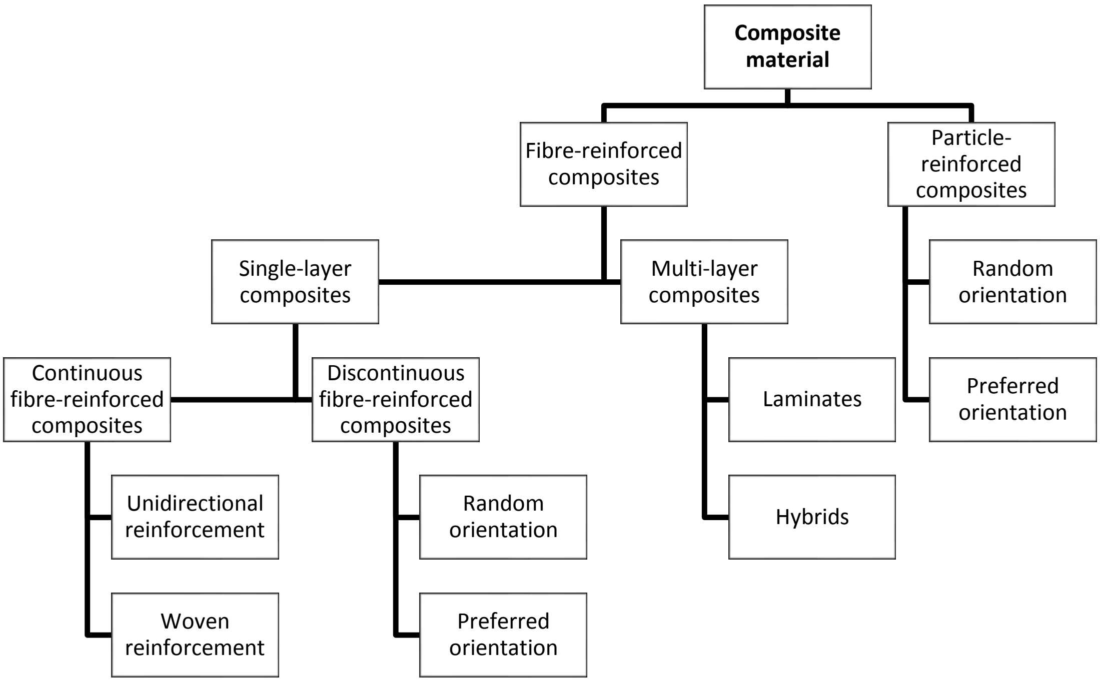

Figure 1.1: Classification of composite materials [1]

The orientation of the reinforcement can be designed to give the correct level of mechanical properties where needed. The matrix can be either ceramic, metal or polymer. Polymers are the most common matrix for composite materials [1]. The mechanical properties of these three classes of matrix material are considerably different, as shown in Table 1.1.

Table 1.1: Mechanical properties of ceramics, metals and polymers [1]

	Density, ρ (g/cm^3)	Young's modulus, E (GPa)	Strength, σ (MPa)	Failure strain, ε_t (%)
Ceramics				
Alumina Al_2O_3	3.87	382	332	0
Magnesia MgO	3.60	207	230	0
Zirconia ZrO_2	5.92	170	900	0
Metals				
Aluminium	2.70	69	77	47
Steel mild	7.86	210	460	35
Titanium-2.5% Sn	4.56	112	792	20
Polymers				
Epoxy	1.12	4	50	4
Nylon 6.6	1.50	9	70	-
Polystyrene	1.05	3	50	2

1.3 Fibre-Reinforced Plastic (FRP) Composites

A fibre-reinforced plastic or a fibre-reinforced polymer (FRP) composite is a material made of a combination of polymer matrix and fibre reinforcement. The fibres are usually glass, carbon, basalt or aramid. However, other fibres such as paper, wood, asbestos, plant fibres or even regenerated cellulose fibres have also been used. The polymer matrix used to make the composite can be a thermoplastic or thermosetting plastic depending on the application. Due to the anisotropic properties and the complex micro-structures of FRPs, failure by the propagation of a crack is usually more complex than in homogeneous materials. In FRPs, crack growth involves a combination of several mechanisms including breaking of the load-bearing fibres and the relatively weak matrix, and with the crack deviating along any weak interface [2]. Table 1.2 shows typical properties of FRPs where the fibres are either unidirectional (UD) or plain-woven (PW).

Table 1.2: Typical properties of FRPs [3]

Type of composites	**Carbon-fibre/epoxy**			**Glass-fibre/epoxy**		
Fibre volume fraction, v_f /fibre weaving architecture	0.60/UD	0.50/PW		0.60/UD	0.50/PW	
Fibre orientation	0°	0°/90°	±45°	0°	0°/90°	±45°
Density, ρ (g/cm^3)	1.60	1.60	1.60	1.90	1.90	1.90
Longitudinal Young's modulus, E_1 (GPa)	135	70	19.1	40	25	12.2
Transverse Young's modulus, E_2 (GPa)	10	70	19.1	8	25	12.2
Longitudinal ultimate tensile strength, X_t (MPa)	1500	600	120	1000	440	120
Longitudinal ultimate compressive strength, X_c (MPa)	1200	570	120	600	425	120
Transverse ultimate tensile strength, Y_t (MPa)	50	600	120	30	440	120
Transverse ultimate compressive strength, Y_c (MPa)	250	570	120	110	425	120
Longitudinal tensile failure strain, ε_{xt} (%)	1.05	0.85	-	2.50	1.75	-

1.4 Natural Fibre-Reinforced Plastic (NFRP) Composites

Natural fibre composites (NFCs) are emerging as a feasible alternative to glass fibre composites (GFCs) in several applications, e.g. automotive, boats, leisure, construction, etc [1]. This is due to an increasing environmental concern that sustainable materials should be found to replace petroleum-based ones. Hence, there has been much research in recent years on eco-composites that contain NFs and/or natural polymers as the matrix. Since suitable natural polymers still appear to be relatively expensive for commercial products, using NFs as the reinforcement in composites that employ synthetic polymers as the matrix is an attractive concept [4].

NFs can be grouped according to their origins of plant parts [5]. Typical NFs are composed of cellulose, hemicellulose, lignin, pectin, wax, water and other compositions depending on the type of NF, climate, aging conditions, soil features, etc. These fibres are sometimes called lignocellulosic fibre. Apart from the low energy consumption for their production and their relatively low unit cost, compared to synthetic fibres [6], they also have good acoustic, thermal insulation and good specific strength and stiffness properties due to their low density and cellular structure. However, NFs often exhibit a relatively poor fibre-matrix interfacial adhesion (possibly arising from a relatively high moisture content in the NFs), a low degradation temperature (up to about 200°C), poor resistance to moisture and variable mechanical properties which are dependent on the growing and harvesting conditions [4][7]. The main advantages and disadvantages of NFs are presented in Table 1.3.

Table 1.3: Summary of main advantages and disadvantages of NFs [6]

Advantages	Disadvantages
- Low cost - Renewability/recyclability/biodegradability - Low density - Non-abrasive - Low energy consumption - High specific properties - High strength and elasticity modulus - No skin irritations - No residues incinerated - Fast absorption/desorption of water - Good thermal conductivity	- High moisture absorption/degradation - Poor fracture resistance - Poor microbial resistance - Low thermal resistance - Local and seasonal quality - Demand and supply cycles

The problems associated with NFCs given above may result in inconsistent mechanical properties of such composites, especially evident in a poor interlaminar fracture toughness [6][8]. Thus, the present work investigates the mode I interlaminar fracture toughness, of NFCs. Two types of natural fibres were employed: unidirectional flax fibre (FF) and plain-woven regenerated cellulose fibre (CeF). The NFCs are based upon an anhydride-cured diglycidyl ether of bisphenol-A (DGEBA) epoxy matrix. Further, this matrix was used as an unmodified or modified with silica nanoparticles and/or rubbery microparticles. Two very different routes were explored for the production of the NFCs based upon these natural-fibre reinforced-plastic (NFRP) materials. One route was via a resin infusion under flexible tooling (RIFT) process and a second route employed a resin transfer moulding (RTM) process.

1.5 Aims

Thus, the main aim of the present study was to investigate and improve the mechanical properties, especially the mode I interlaminar fracture energy, of natural fibre-reinforced epoxy polymer composites under quasi-static loading conditions. The current work to improve the fracture toughness of the NFRPs may be categorized into four different stages.

- An initial study of the resin infusion under flexible tooling (RIFT) process: In this stage, the fracture energies of the NFRPs are studied and compared with those of the GFRPs. The addition of silica-nanoparticles and rubber-microparticles to the epoxy matrix to improve the toughness of the NFCs is also studied.
- A study of the resin transfer moulding (RTM) process: As the mechanical properties of the NFRPs manufacture using the initial RIFT manufacturing process were found to be relatively very poor, in this stage of the work the RTM method is employed to improve the fracture energies of the NFCs. The fracture energies of the GFRPs are also measured to give a direct comparison to the use of synthetic fibres, so allowing the toughness values of the NFRPs and the GFRPs to be directly compared.

- An optimization study of the RIFT process: In this stage, attempts to improve the fracture energies of the RIFT-processed NFRPs are investigated via several methods which involve various fibre modifications.
- A final study of the RIFT process: In this stage, the best option from the above optimization study of the RIFT process is studied in detail. The addition of silica nanoparticles and/or rubber microparticles into the epoxy matrix is also studied. A comparison of the toughnesses of the NFRPs with the fracture energies of the GFRPs is then undertaken.

The timeline of the present research study is illustrated in Figure 1.2.

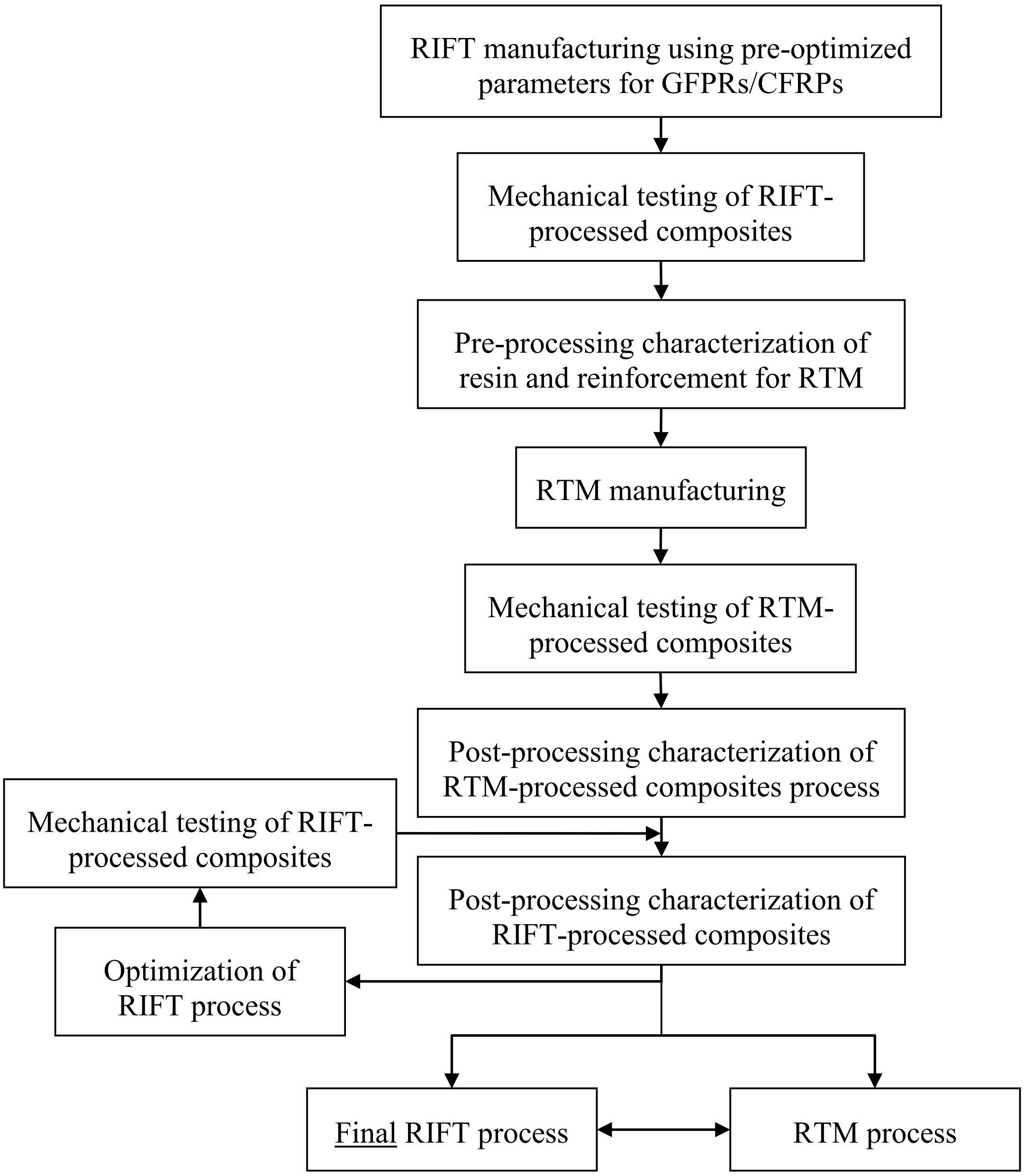

Figure 1.2: Timeline of the study

1.6 Outline of Thesis

The present thesis is divided according to the manufacturing process used and the mechanical properties determined. The Chapters that follow in the present thesis can be summarised as follow:

Chapter 2 presents a literature survey related to the present study, including synthetic FRPs, NFRPs, the basis of fracture mechanics tests, modification of the epoxy matrix via the addition of various types of particles and the manufacturing processing routes employed for FRPs.

Chapter 3 provides a detailed description of the materials used in the present study.

Chapter 4 describes the experimental methods used in the present study. These include the various characterization techniques employed, the fibre surface treatments used, the mechanical testing and the imaging studies which have been undertaken.

Chapter 5 gives a detailed description of the RIFT manufacturing method, which includes the three stages of the RIFT process optimization and the general physical properties of the composites so manufactured.

Chapter 6 gives a detailed description of the RTM manufacturing method, which includes the pre-processing properties of the fibre and epoxy matrices used, and a comparison of the composite properties with those obtained via the RIFT process.

Chapter 7 presents the flexural and tensile mechanical properties of the NFRPs and GFRPs from the different stages of the two different manufacturing methods discussed in ‘Chapter 5’ and ‘Chapter 6’. An analytical model to predict the tensile modulus of the FRPs is discussed and the predictions are compared with the experimental data.

Chapter 8 presents the results of the mode I interlaminar fracture energy tests of the NFRPs and GFRPs from the different stages of the two different manufacturing processes, i.e. the RIFT and RTM processes. An analytical model to predict the fracture energies of the particle modified FRPs is discussed and the predictions are compared with the experimental data.

Finally, Chapter 9 summarizes the main conclusions and presents recommendations for future work in this area.

CHAPTER 2 LITERATURE REVIEW

2.1 Introduction

The work discussed in the present thesis focuses on the properties of natural fibre (NF) reinforced epoxy polymers modified with nanoparticles and microparticles. The natural fibres (NFs) used include flax and regenerated cellulose fibres, and the modifiers used include silica-nanoparticles and rubber-microparticles. The present chapter provides a review of the published literature related to the main areas of the present study.

2.2 Epoxy Polymers

2.2.1 Introduction

Epoxy polymers have been extensively used in engineering applications such as paints/coatings, adhesives, composites, laminates, etc. and this chemical group includes two types of polymers: thermosets (that irreversibly harden or cure through chemical reaction) and thermoplastics (that reversibly harden upon cooling) [9]. A diglycidyl ether of bisphenol A (DGEBA) epoxy resin, which results in a thermosetting polymer, is used in the present study and is discussed below.

2.2.2 Chemistry

Epoxy polymers are polyether resins containing more than one epoxide group that chemically react either by the epoxide molecules reacting with each other or through their reaction with other reactive molecules. In both cases there is a conversion into an irreversible thermoset 3D cross-linking polymer upon curing, which occurs with or without the help of a catalyst [10].

A DGEBA epoxy resin formed from reacting epichlorohydrin with bisphenol A to form diglycidyl ethers of bisphenol A and an anhydride hardener, which gives a lower exotherm on curing in comparison with the epoxy polymer cured by an amine curing agent [11], were used in the present study. The chemical structure of a DGEBA epoxy resin is illustrated in Figure 2.1.

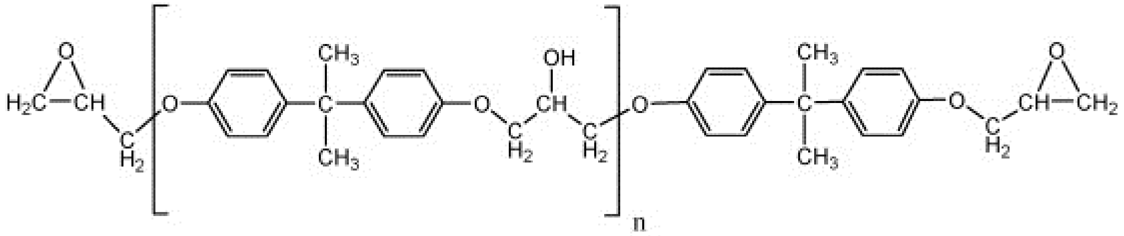

Figure 2.1: Chemical structure of Bisphenol-A epoxy resin ('n' typically has a value of 0-5) [10]

2.2.3 General Mechanical Properties of Thermosetting Polymers

As thermosetting resins readily cross-link during curing through a chemical reaction and are irreversible upon increasing temperature, they generally degrade or burn on reheating. This is because they do not soften sufficiently for reshaping due to their cross-linked structures that restrict the movement of polymer chains and increase the glass transition temperature. As a result, they are brittle and have a low fracture toughness, K_{IC}, of typically 0.5-1.0 MPa·m$^{1/2}$ [1]. Properties of common thermosetting polymers are listed in Table 2.1.

Table 2.1: Typical properties of thermosetting polymers

Type of polymer		Epoxy	Polyester	Phenolic	Polyimide
Density, ρ (g/cm^3)		1.10-1.40[1][12]	1.10-1.50[1]	1.22-1.30[1][12]	1.11-1.90[1][12]
Young's modulus, E (GPa)		2.1-6.0[1][12]	1.3-5.0[1][12][13][15]	3.4-4.4[1][12]	3.0-3.1[1][12]
Tensile strength, σ_t (MPa)		35-90[1][12]	45-85[1][12][13][16]	50-60[1][12]	75-190[1][12]
Compressive strength, σ_c (MPa)		130[12]	150[12]	130[12]	90-100[12]
Poisson's ratio, υ		0.37-0.40[12]	0.36[12]	0.35[12]	0.42-0.44[12]
Failure strain, ε_t (%)		5.0[12]	3.0[12]	1.0[12]	7.0[12]
Fracture toughness*	K_{IC} (MPa·m$^{1/2}$)	0.6-1.0[1][13]	0.50-0.72[1][13][13][15]	0.8[17]	0.5-3.0[13][18][19]
	G_{IC} (J/m^2)	20-133[1][14]	23-130[13][15][16]	180[17]	920-4780[18][20]

*See '2.5 Fracture Mechanics' for detailed discussion on K_{IC} and G_{IC}

2.3 Fibre-Reinforced Plastic (FRP) Composites

2.3.1 Introduction

A fibre-reinforced plastic (FRP) composite is a material made of a combination of polymer matrix and fibre reinforcement. The fibres are usually glass, carbon, basalt or aramid. However, other fibres such as paper, wood, asbestos, plant fibres or even regenerated cellulose fibres have also been used. The polymer matrix used to make the composite can be a thermoplastic or thermosetting plastic depending on the application.

2.3.2 General Mechanical Properties of FRPs

Due to the anisotropic properties and the complex micro-structures of FRPs, failure by the propagation of a crack is usually more complex than in homogeneous materials. In FRPs, crack growth involves a combination of several mechanisms including breaking of the load-bearing fibres and the relatively weak matrix, and with the crack deviating along any weak interface [2]. Table 2.2 shows typical properties of FRPs where the fibres are either unidirectional (UD) or plain-woven (PW). The latter type of fibre architecture consists of aligned warp and weft where each warp fibre passes alternately under and over each weft fibre [21], see 'Appendix I'.

Table 2.2: Typical properties of FRPs [3]

Type of composites	Carbon-fibre/epoxy			Glass-fibre/epoxy		
Fibre volume fraction, v_f /fibre weaving architecture	0.60/UD	0.50/PW		0.60/UD	0.50/PW	
Fibre orientation	0°	0°/90°	±45°	0°	0°/90°	±45°
Density, ρ (g/cm^3)	1.60	1.60	1.60	1.90	1.90	1.90
Longitudinal Young's modulus, E_1 (GPa)	135	70	19.1	40	25	12.2
Transverse Young's modulus, E_2 (GPa)	10	70	19.1	8	25	12.2
Longitudinal ultimate tensile strength, X_t (MPa)	1500	600	120	1000	440	120
Longitudinal ultimate compressive strength, X_c (MPa)	1200	570	120	600	425	120
Transverse ultimate tensile strength, Y_t (MPa)	50	600	120	30	440	120
Transverse ultimate compressive strength, Y_c (MPa)	250	570	120	110	425	120
Longitudinal tensile failure strain, ε_{xt} (%)	1.05	0.85	-	2.50	1.75	-

2.3.3 Fracture Toughness of FRPs

Normally, FRPs are made of high strength fibres in a relatively weak matrix and they are highly anisotropic materials. For example, an in-plane tensile strength of 700-1,200 MPa can be measured for a typical quasi-isotropic carbon fibre-reinforced epoxy, while only 50 MPa is measured through-the-thickness. FRPs are therefore susceptible to through-thickness failure, which is controlled by either the through-thickness strength or the interlaminar fracture toughness [22]. The propagation of a delamination in FRPs is controlled by the interlaminar fracture toughness, which can be represented by the critical energy release rate or fracture energy, G_C. This represents the energy consumed by the material as the delamination front advances through a unit area [22]. There are several modes of interlaminar fracture corresponding to the types of loads applied: mode I (opening), mode II (shear) and mode III (tearing), see Figure 2.2. In isotropic materials the mode I fracture toughness is normally the lowest in value, and hence the crack grows normal to the maximum applied tensile stress. However, anisotropic materials such as laminate composites are susceptible to through-thickness damage and transverse damage and, as a consequence it is possible to have delamination growth in all three modes.

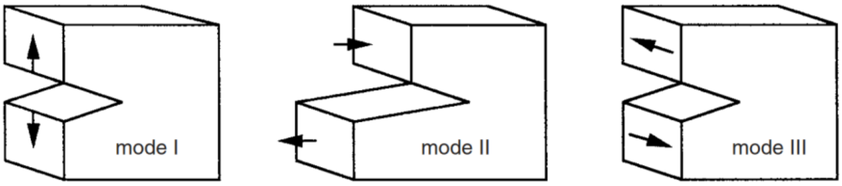

Figure 2.2: Schematic diagrams of the basic modes of cracking loading: mode I (opening), mode II (shear) and mode III (tearing) [22]

There are several test methods for measuring the interlaminar fracture energy of materials. For mode I, the double cantilever beam (DCB) test is the commonest amongst all the test methods. For mode II, there are two common methods: end-notched flexure (ENF) and end-loaded split (ELS). For mode III, the edge crack torsion (ECT) test is a common test method. The DCB test method was mainly employed in the present research study and it will be discussed in detail in sections '2.5.3' and '4.4.1'. Typical values of the mode I interlaminar fracture energy of different materials are presented in section '2.4.4' below.

2.4 Natural Fibre-Reinforced Plastic (NFRP) Composites

2.4.1 Introduction

Due to an increasing environmental concern that sustainable materials should be found to replace petroleum-based ones, there has been much research in recent years on eco-composites that contain NFs and/or natural polymers as the matrix. Since suitable natural polymers still appear to be relatively expensive for commercial products, using NFs as the reinforcement in composites that employ synthetic polymers as the matrix is an attractive concept [4].

2.4.2 Natural Fibres (NFs)

NFs can be grouped according to their origins of plant parts, see Table 2.3, and can be isolated from the plant by three general methods: mechanical (decertification: squeezing the plant through slotted rollers with cutting edges that spread the plant apart and separate the fibres from the other plant tissues), biological (retting/degumming: removing fibres using enzymes from micro-organisms) and chemical (chemical retting or pulping using dilute alkali or acids) [5].

Typical NFs are composed of cellulose, hemicellulose, lignin, pectin, wax, water and other compositions depending on the type of NF, climate, aging conditions, soil features, etc. These fibres are sometimes called lignocellulosic fibre. Table 2.4 shows the physical properties and composition details of some commonly used NFs.

Table 2.3: Six general types of natural fibres grouped according to their origins [5]

Bast[1]	Leaf[2]	Seed[3]					Core[4]	Grass/reeds[5]	Other[6]
		Fibres	Pod	Husk	Fruit	Hulls			
Hemp	Pineapple	Cotton	Kapok	Coir	Oil palm	Rice	Kenaf	Wheat	Wood
Ramie	Sisal		Loofah			Oat	Jute	Oat	Roots
Flax	Agava		Milk weed			Wheat	Hemp	Barley	Galmpi
Kenaf	Henequen					Rye	Flax	Bamboo	
Jute	Curaua							Bagasse	
Mesta	Banana							Corn	
Urena	Abaca							Rape	
Roselle	Palm							Esparto	
	Cabuja							Wheat	
	Albardine							Rye	
	Raphia							Sabai	
								Canary grass	

1 = fibres from inner bark or phloem of plants; 2 = fibres from leaf of plants;
3 = fibres from seed of plants; 4 = fibres from inside of the bast fibres in the centre of plants;
5 = fibres from grass or reed plants; 6 = fibres from other parts of plants.

Table 2.4: Physical properties and chemical composition of natural fibres

Fibre	Cell diameter (μm)	Average cell length (mm)	Spiral angle (Deg)	Cellulose (wt%)	Hemi-cellulose (wt%)	Pectin (wt%)	Lignin (wt%)	Waxes (wt%)	Moisture (wt%)
Bast/Core									
Flax[4][5][23][24]	5-76	4-77	10.0	43-75	18-22	2	2-23	2	7-10
Kenaf[4][5]	12-36	2-61	-	44-57	15-19	-	6-19	-	17
Jute[4][5][24][25]	5-25	2-120	8.0	45-71	13-20	<1	12-26	<1	12-13
Hemp[4][5][24][25]	10-51	5-55	6.2	57-77	18-22	1	4-13	<1	9-11
Ramie[5][24][25]	18-80	154-1200	7.5	68-91	13	2	<1	<1	8-9
Leaf									
Sisal[4][5][8][24][25][26]	7-200	2-3	10.0-25.0	67-78	10-14	10	8-11	2	3-11
Pineapple[4][5][8]	8-80	3-8	6.0-14.0	-	-	-	-	-	13
Banana[4][5]		2-4	11.0-12.0	-	-	-	-	-	15
Abaca[4][5][27]	17-122	4-5	-	-	-	-	-	-	9-14
Seed									
Coir[5][8][24][25]	10-460	1-150	45.0	43	<1	4	45	-	8-10
Cotton[4][5][25]	10-45	10-60	-	82-95	6	-	0-2	<1	8
Grass/Reed									
Bamboo[5][24][25][27]	25-40	1-4	-	26-65	30	-	5-31	-	9-10
Others									
Wood[5][27][29]	30-1200	-	-	38-49	19-32	-	22-34	-	12
Regenerated cellulose*	9-12	-	-	89-96	-	-	-	-	4-11

*Properties measured in the present study

Cellulose has a strong crystalline structure and is resistant to hydrolysis; however, it is easily hydrolysed by acid. Four different crystalline structures of cellulose are present including cellulose I, II, III and IV where the most studied forms of cellulose are cellulose I and II. Natural cellulose is cellulose I, which is the most widespread crystalline form, and which consists of an assembly succession of crystallites and disordered amorphous regions [30]. It is also metastable. Cellulose II is a regenerated/mercerized cellulose and is a more stable irreversible cellulose crystal [31][32][33]. Cellulose III is a liquid NH_3 or diamine treated cellulose I or cellulose II and is a reversible cellulose crystal [30]. Cellulose IV is a heat treated cellulose III in glycerol at 260°C and is seen as a distorted form of cellulose I [30].

Hemicellulose has a random, amorphous and hydrophilic structure that forms a support matrix for the cellulose. It has little strength and is soluble in alkali and hydrolysable in acid [7]. Lignin is an amorphous hydrophobic complex copolymer (considered as a thermoplastic) that gives rigidity to plants and is not hydrolysable in acid, which is however soluble in hot alkali, while pectin is a structural heteropolysaccharide that gives flexibility to plants [7]. Figure 2.3 illustrates the chemical structures of cellulose, hemicellulose, pectin and lignin. Their mechanical properties depend on the type of cellulose and geometry of the elementary cell. The cellulosic chains are arranged parallel to one another, forming bundles that each contains cellulosic macromolecules linked by hydrogen bonds and, through links with amorphous hemicelluloses and lignin, the cellulosic chains confer stiffness to fibres called microfibrils [4]. The natural fibre microfibril microstructure is illustrated in Figure 2.4.

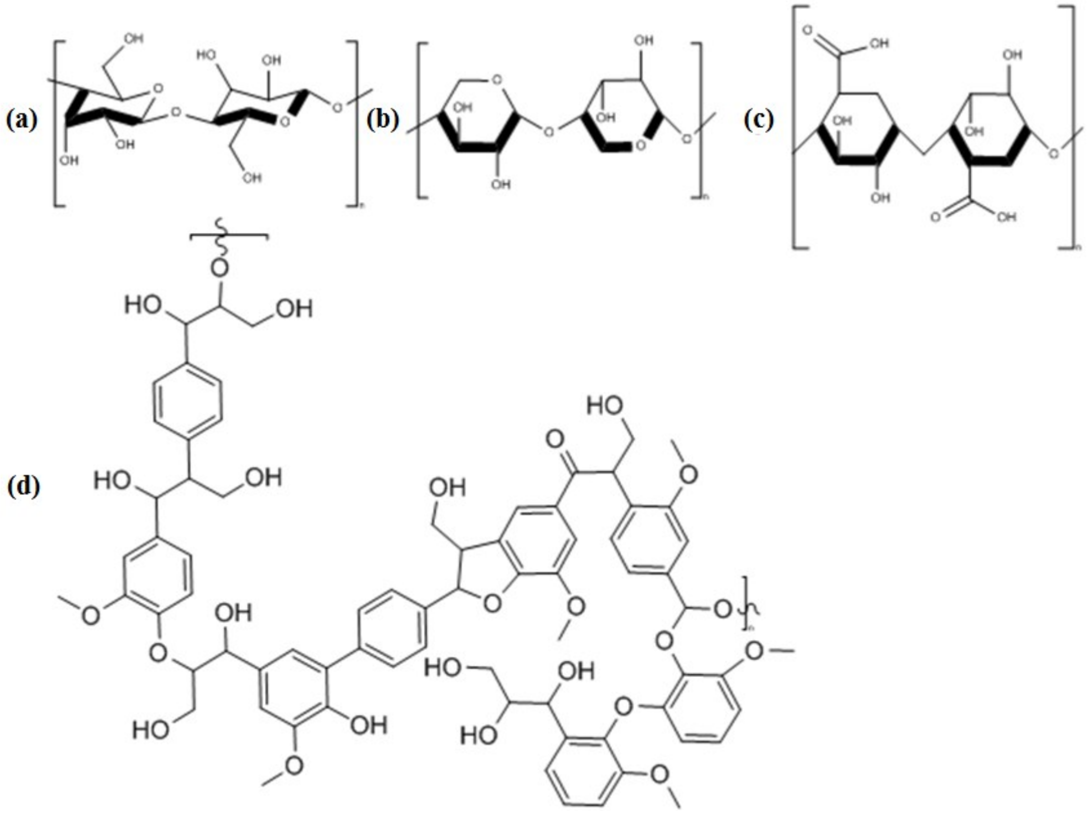

Figure 2.3: Chemical structures of (a) cellulose, (b) hemicellulose, (c) pectin and (d) lignin [34]

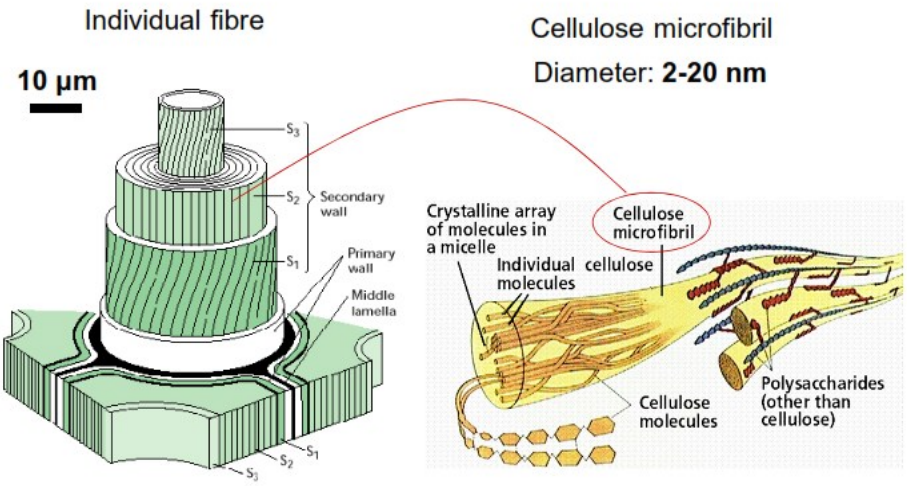

Figure 2.4: Micro-structure of a natural fibre microfibril [35]

NFs need to possess a relatively low energy for their production and to have a unit cost that is also relatively low, compared to synthetic fibres. They also often have good acoustic, thermal insulation and good specific strength and stiffness properties due to their low density and cellular structure. However, NFs have relatively poor interfacial adhesion, a low degradation temperature (up to about 200°C), poor resistance to moisture and variable mechanical properties which are dependent on the growing and harvesting conditions [4][7]. In contrast, synthetic fibres such as carbon, aramid and glass require a relatively large amount of energy in their production. However, some NF weaves and yarns require higher amounts of energy than that for glass fibres (GFs) when made into more complex architectural forms [4]. The main advantages and disadvantages of NFs are presented in Table 2.5.

Table 2.5: Summary of main advantages and disadvantages of NFs [6]

Advantages	Disadvantages
- Low cost - Renewability/recyclability/biodegradability - Low density - Non-abrasive - Low energy consumption - High specific properties - High strength and elasticity modulus - No skin irritations - No residues incinerated - Fast absorption/desorption of water - Good thermal conductivity	- High moisture absorption/degradation - Poor fracture resistance - Poor microbial resistance - Low thermal resistance - Local and seasonal quality - Demand and supply cycles

2.4.2.1 *Natural Fibres used in the Present Study*

Two types of NFs were used, namely flax fibre and regenerated cellulose fibre.

2.4.2.1.1 Flax fibre

Flax fibre (FF) is a cellulose polymer extracted from a stem of flax bast plant that contains numerous crystalline cellulose microfibrils and amorphous hemicellulose oriented at 10° to the fibre axis, see Figure 2.5 for the structure of flax [23]. A bundle of 10-40 non-uniform geometrical elementary fibres (diameter of 5-76 µm and length of 4-77 mm) are linked together mainly by pectin [23][36][37], as shown in Figure 2.6.

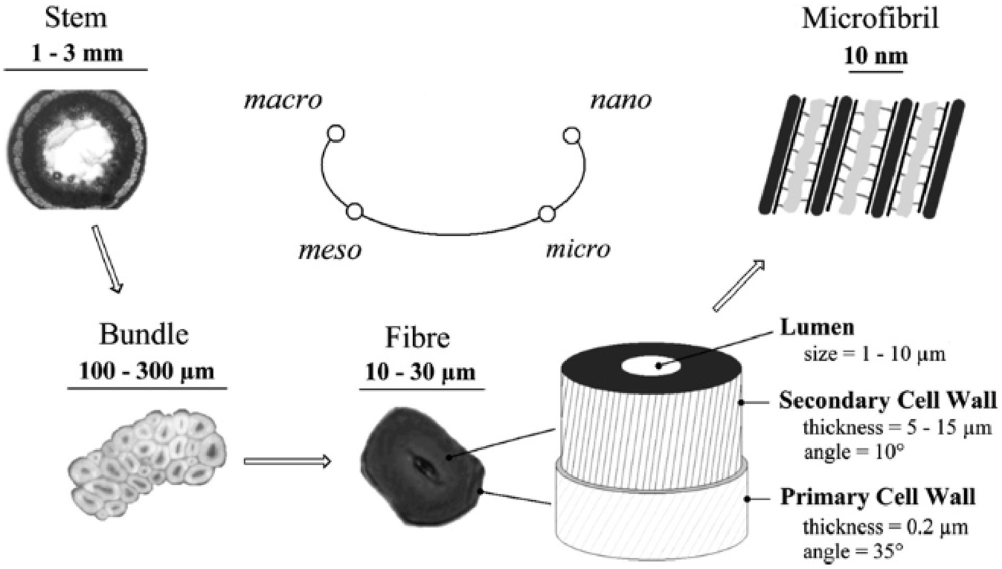

Figure 2.5: Muti-scale flax structure [36]

Figure 2.6: Structure of flax fibre bundle [23]

The properties and composition of flax fibre are summarized in Table 2.6.

Table 2.6: Properties and composition of flax fibre

Fibre diameter (µm)	Cell length (mm)	Spiral angle (Deg)	Cellulose (wt%)	Hemi-cellulose (wt%)	Pectin (wt%)	Lignin (wt%)	Waxes (wt%)	Water (wt%)
5-76[23]	4-77[23]	10.0[24]	71.0[24]	18.6[24]	2.3[24]	2.2[24]	1.7[24]	10.0[24]

2.4.2.1.2 Regenerated cellulose fibre

The regenerated cellulose fibre (CeF) used in the present study was continuous and non-twisted pure cellulose fibre [38]. The main difference between regenerated cellulose fibre and naturally occurring cellulosic-based fibres, such as flax and hemp fibres, is that cellulose I, which is an assembly of crystallites and disordered amorphous, is found in naturally occurring cellulosic-based fibres, while cellulose II, which is a more stable cellulose crystal found in regenerated cellulose, has the crystalline structure of a regenerated cellulose fibre [31][32][33].

2.4.3 **General Mechanical Properties of NFs and NFRPs**

NFs are being increasingly used as reinforcements in FRPs as they offer a relatively high specific strength and stiffness, comparable to GFs, but at a lower cost. Some of the mechanical properties of NFs and NFRPs are summarized in Table 2.7 and Table 2.8 respectively.

Table 2.7: Typical properties of NFs

Fibre	Density, ρ (g/cm^3)	Tensile strength, σ_t (MPa)	Young's modulus, E (GPa)	Specific modulus, E/ρ (10^6 m^{2}s^{-2})	Failure strain, ε_t (%)
Bast/Core					
Flax[4]	1.38-1.50	500-900	50-70	31-44	1.3-3.3
Kenaf[4][5][25]	1.20-1.40	195-1191	22-66	15-49	1.3-6.9
Jute[4][5][8][25]	1.23-1.52	187-860	13-60	14-39	1.5-8.0
Hemp[4][5][8][25]	1.35-1.50	310-1110	30-70	20-43	1.4-4.5
Ramie[4][5][8][25]	1.44-1.55	400-938	23-128	15	1.2-3.8
Leaf					
Sisal[4][5][8][25][26]	1.20-1.50	80-840	9-25	6-15	2.0-14.0
Pineapple[4][5][8]	1.44-1.56	170-1627	4-82	38-57	1.3-1.6
Banana[4]	1.30-1.35	529-914	27-32	20-25	1.0-3.0
Abaca[4][27]	0.83	12-452	12.9-41	15.6	3.4
Seed					
Coir[4][5][8][25]	1.15-1.25	106-240	4-6	4-5	15.0-40.0
Cotton[4][5][8][25]	1.21.1.60	287-800	5-13	3-10	2.0-12.0
Grass/Reed					
Bamboo[4][25][27]	0.60-1.50	140-800	11-36	18	1.4-3.7
Others					
Wood[39]	0.36-0.88	34-139	5-16	6-43	-
Regenerated cellulose[38]	1.50	675	35	23	6.2
E-glass[8][40]	2.50-2.58	3445	72.3	28	4.8
S-glass[40]	2.46	4890	90	36	5.7
Carbon (PAN)[8][40]	1.70-1.80	4000-4900	230-240	130	1.4-1.8

Table 2.8: Typical properties of NFRPs

Type of NFRPs	Flax fibre/ polyester[41][42]		Flax fibre/ epoxy[43]	Flax fibre/ polypropylene[43]	Cellulose fibre/ epoxy[38]		Glass fibre/ epoxy[3]	
Fibre orientation	0°	0°/90°	0°	0°	0°	0°/90°	0°	0°/90°
Fibre volume fraction, v_f	0.30	0.30	0.50	0.43	0.45	0.45	0.60	0.50
Density, ρ (g/cm^3)	1.30	1.30	1.31	1.13	1.30	1.30	1.90	1.90
Longitudinal Young's modulus, E_1 (GPa)	18.8	8.7	35	33	21	13	40	25
Longitudinal ultimate tensile strength, X_t (MPa)	174	85	365	275	320	160	1000	440
Longitudinal tensile failure strain, ε_{xt} (%)	1.5	1.7	1.35	1.22	4	3	2.50	1.75

2.4.4 Fracture Toughness of NFRPs

NFs have relatively poor interfacial adhesion with polymers and have variable mechanical properties [4][7], which can result in poor fracture toughness and inconsistent properties of the composites. Many attempts have been made towards improving mechanical properties, with efforts directed at improving the interface [44].

The fracture of composites can be classified into interlaminar and intralaminar fractures, as shown in Figure 2.7 [45]. In mode I, there has been extensive research on the intralaminar fracture toughness of NFRPs; this involves loading a notched specimen that has been precracked in either tension test (compact tension) or in 3-point bending test, where the crack runs parallel to the fibres through the thickness [45][46][47]. Different interlaminar fracture toughness test methods have been also developed and in mode I the double-cantilever beam test is the commonest test method [22][45]. This involves crack running between layers across the width (delamination) [48].

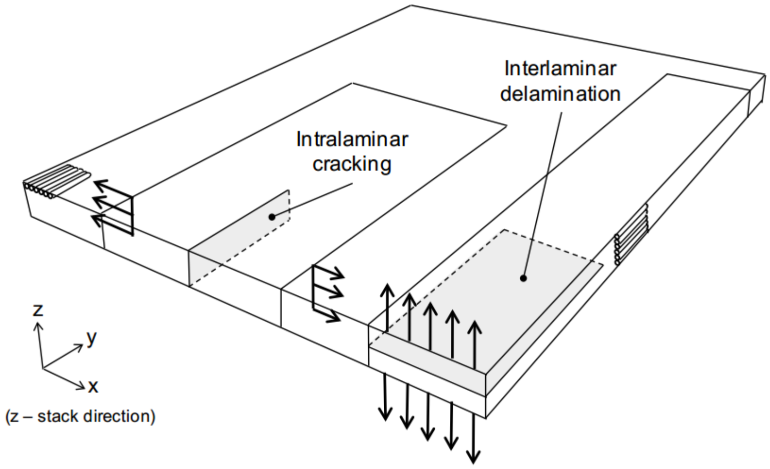

Figure 2.7: Intralaminar fracture vs interlaminar delamination (redrawn by [48] from [49])

There have been extensive research attempts to improve the fracture toughness of FRPs; these involve either or combination of a through-the-thickness reinforcement, e.g. 3D weaving or z-axis reinforcement [50][51][52], fibre surface treatment [52][53][54][55] and/or matrix modification via the addition of modifiers [14][56][57][58].

Pinto et al. [52] studied the improvement of the interlaminar fracture toughness of unidirectional and plain-woven jute fibre-epoxy composites with the attempt to use the idea of z-axis reinforcement and silane surface treatment of the fibres. It was found that the surface treatment increased the fracture toughness due to improved interfacial adhesion. The difference in fibre architecture had an effect on the fracture toughness where plain-woven preforms were found to have higher fracture toughness than the unidirectional preforms due to increased inter-ply interaction. The addition of z-axis reinforcement was also found to significantly improve the fracture toughness but reduce the tensile strength and modulus, probably due to the waviness and crimp of the longitudinal reinforcement and the accompanying reduction of the fibre volume content [50][52].

Zulkifli et al. [55] studied the effect of silane surface treatment on the interlaminar fracture toughness of silk-epoxy composites and only found marginal improvement in fracture toughness. On the other hand, Li et al. [53] studied the improvement of intralaminar fracture toughness of sisal fibre-reinforced vinylester via silane and permanganate surface treatments and found improvements in the fracture toughness due to enhanced interfacial bonding between the fibre and matrix. A study by Silva et al. [59] showed that an alkali surface treatment decreased the intralaminar fracture toughness of sisal-castor oil polyurethane composites by improving interfacial adhesion which compromised the main energy absorption mechanisms, while the same treatment increased the intralaminar fracture toughness coir-castor oil polyurethane composites by creating additional fracture mechanisms. These studies suggest that the selection of a surface treatment must be carried out with great care in order to improve the desired properties.

Hsieh et al. [56] investigated the effect of adding silica-nanoparticles and rubber-microparticles to the epoxy polymer in glass fibre-reinforced plastics (GFRPs) and carbon fibre-reinforced plastics (CFRPs). It was found that plastic shear-yielding, debonding of the matrix from the silica nanoparticles and plastic void-growth of the epoxy were present in the silica-nanoparticle modified FRPs. In the rubber particle modified epoxy polymers, rubber particle cavitation, plastic deformation and plastic void growth were present in FRPs. These toughening mechanisms were in addition to the fibre bridging and plastic deformation observed in the unmodified FRPs. The presence of the additional toughening mechanisms resulted in enhanced fracture toughness. Zeng et al. [58] reached the same conclusion upon incorporating rubber and/or silica-nanoparticles to the epoxy polymer in the CFRPs. However, no attempt has been made to investigate the effect of adding nanoparticles and/or microparticles to the matrix in NFRPs. Typical values of mode I intralaminar and interlaminar fracture toughness of different polymeric matrices and FRPs are summarized in Table 2.9 and Table 2.10 respectively.

Table 2.9: Typical values of mode I intralaminar fracture toughness of various polymeric matrices and FRPs

Reinforcement/treatment	**Matrix**	**Propagation fracture toughness, K_{IC} (MPa·m$^{1/2}$)**	**Propagation fracture energy, G_{IC} (J/m^2)**
N/A[60]	Polyester	0.62	100
GF-CSM[60]	Polyester	9.01	10210
Jute-nonwoven[60]	Polyester	2.56	970
Hemp-nonwoven[60]	Polyester	3.51	1840
Bamboo-nonwoven[61]	Polyester	1.7	-
Flax-PW[62]	Epoxy	7.1	-
Sisal-PW[53]	Vinylester	4.2	1159
Sisal-PW/Silane[53]	Vinylester	5.5	1488
Sisal-PW/Permanganate[53]	Vinylester	6.0	1682
Sisal-nonwoven[59]	Castor oil polyurethane	7.1	-
Sisal-nonwoven/NaOH[59]	Castor oil polyurethane	6.3	-
Coir-nonwoven[59]	Castor oil polyurethane	5.6	-
Coir-nonwoven/NaOH[59]	Castor oil polyurethane	7.7	-
Sisal-PW[59]	Castor oil polyurethane	11.5	-
Sisal-PW/NaOH[59]	Castor oil polyurethane	8.4	-

Table 2.10: Typical values of mode I interlaminar fracture toughness of various plastics and FRPs

Reinforcement/treatment	Matrix	Interface Reinforcement orientation	Propagation fracture energy, G_{IC} (J/m^2)
N/A[14]	DGEBA epoxy	N/A	131
N/A[14]	DGEBA epoxy + Si10R0	N/A	191
N/A[14]	DGEBA epoxy + Si0R9	N/A	697
N/A[14]	DGEBA epoxy + Si10R9	N/A	1059
GF-UD[56]	DGEBA epoxy	0°/0°	330±150
GF-UD[56]	DGEBA epoxy + Si10R0	0°/0°	1015±195
GF-UD[56]	DGEBA epoxy + Si0R9	0°/0°	885±60
GF-UD[56]	DGEBA epoxy + Si10R9	0°/0°	860±90
GF-QI-NCF[56]	DGEBA epoxy	0°/0°	718±96
GF-QI-NCF[56]	DGEBA epoxy + Si10R0	0°/0°	626±146
GF-QI-NCF[56]	DGEBA epoxy + Si0R9	0°/0°	1035±61
GF-QI-NCF[56]	DGEBA epoxy + Si10R9	0°/0°	1263±275
GF-PW/Epoxy silane 0.2 wt%[54]	Epoxy	0°/90° woven	645
GF-PW/Methacrylsilane 0.02 wt%[54]	Epoxy	0°/90° woven	728
GF-PW/Methacrylsilane 0.2 wt%[54]	Epoxy	0°/90° woven	288
GF-PW/Methacrylsilane 1.0 wt%[54]	Epoxy	0°/90° woven	216
GF-UD[63]	M10 Epoxy	0°/0°	118±3
T300 CF-UD[22]	914 Epoxy	0°/0°	140
T800 CF-UD[22]	914 Epoxy	0°/0°	250
XAS CF-UD[22]	9113 Epoxy	0°/0°	280
CF-PW[56]	DGEBA epoxy	0°/90° woven	439±91
CF-PW[56]	DGEBA epoxy + Si12R0	0°/90° woven	489±71
CF-PW[56]	DGEBA epoxy + Si0R9	0°/90° woven	1044±87
CF-PW[56]	DGEBA epoxy + Si10R9	0°/90° woven	1316±132
FF-nonwoven[64]	PLLA	Randomly oriented	323±43
FF-nonwoven[65]	PLLA	Randomly oriented	38.9±8.4
FF-nonwoven[65]	PLLA + 10 vol% HBP	Randomly oriented	73.2±7.9
FF-nonwoven[65]	PLLA + 30 vol% HBP	Randomly oriented	83.8±5.5
FF-nonwoven[65]	PLLA + 50 vol% HBP	Randomly oriented	115.4±6.9
Jute-UD[52]	Amine-cured Epoxy	0°/0°	600±40
Jute-UD/Silane 1.0 wt%[52]	Amine-cured Epoxy	0°/0°	650±40
Jute-PW[52]	Amine-cured Epoxy	0°/90° woven	700±20
Jute-PW/Silane 1.0 wt%[52]	Amine-cured Epoxy	0°/90° woven	800±50
Jute-PW[66]	Polyester	0°/90° woven	1200
Silk-PW[55]	Bisphenol-A Epoxy	0°/90° woven	747-1775
Silk-PW/Silane [55]	Bisphenol-A Epoxy	0°/90° woven	788-1883

2.4.5 Issues Relating to Utilization of Natural Fibres in Composites

2.4.5.1 *Mechanical Properties*

Unlike synthetic fibres, such as carbon, glass, aramid, etc. that have no limitation in terms of fibre length, the inherent properties of NFs restrict their length. Mat fabric and discontinuous NFs are typically found as reinforcements, but long continuous yarn spun from short interlocked fibres can be also made [4]. This last type of fibre architecture results in increased surface roughness which gives better interfacial mechanical locking and improved transverse properties [4]. However, the mechanical properties of the NFs are still inferior to those of synthetic fibres.

Furthermore, as cellulose in NFs contains large amounts of strongly polarized hydroxyl groups, with hydrophilic properties and acetal and ether linkages, it is therefore incompatible with nonpolar-hydrophobic matrices such as some thermoplastics [6][8][67], although they are more compatible with polar, acidic or basic groups (e.g. epoxy and phenolic resins) compared to non-polar polymers [6][68]. In addition, poor wetting and weak interfacial adhesion due to incompatibility restricts their application due to deficiencies in stress transfer that result in poor mechanical properties, e.g. in the value of fracture toughness [6][8]. As a result, NFRPs typically possess approximately five times lower fracture toughness compared with GFRPs, although NFs have been shown to provide a good specific stiffness compared with GFs.

2.4.5.2 *Moisture Absorption/Degradation*

The cellulose in NFs has a polar group which attracts water molecules through hydrogen bonding. Hence, moisture build-up within the cell walls, due to attachment of water molecules to the cellulose molecules, leads to swelling, dimensional changes and loss of fibre composition via leaching of lignin and water soluble products [69][70][71]. A study by Messeteau et al. [72] observed that dry NFs can quickly absorb moisture in laboratory atmosphere (2.0% in 90 sec).

As water penetrates into the interface through the micro-cracks caused by fibre swelling, it creates swelling stresses that may lead to composite matrix cracks where a capillarity mechanism becomes active (e.g. water molecules flow along the fibre–matrix interfaces and diffuse through the bulk matrix). As a result, debonding of the fibre and the matrix occurs due to water damage of the interface [73].

The moisture absorbed by NFRPs has several adverse effects on the properties and the long-term performance of the composites [74][75][76][77], such as reduced flexural stiffness and strength [78], reduced tensile stiffness and strength [79] and reduced impact strength [73].

Moisture absorption increases with increasing fibre volume fraction [80] and the process can be severely influenced by an increased temperature where the effect is irreversible. It may be reduced by fibre surface treatment or by a coupling agent [78][81]. As NFRPs are very poor in moisture resistance, they are susceptible to moisture absorption and vulnerable to moisture degradation [67].

2.4.5.3 *Thermal Degradation*

NFs typically have low degradation temperatures that are not suitable for some high temperature processing methods for example, for thermoplastic processing, or for any high temperature application, where processing temperatures are higher than 200°C [69][82]. Higher lignin content results in lower degradation temperatures and more char formation, which is an important process of self-protecting as it protects the core of the material and its structural integrity, while higher cellulose content results in higher flammability [83][84][85].

The presence of silica or ash in fibres as well as higher crystallinity and lower polymerization of fibre microstructure may also contribute to better fire resistance performance [83].

Most NFs start to decompose at a temperature of about 215±10°C and lose approximately 60% of their weight within a temperature range of 215-310±10°C [86]. The degradation process of NFs starts with dehydration and emission of volatile components and is followed by rapid weight loss due to oxidative decomposition and the formation of char at high temperatures [87].

2.4.5.4 *Fibre Surface Treatment*

Chemical, heat and/or mechanical surface treatments of fibres such as alkali, acetylation, peroxide, graft copolymerization, coupling agents, permanganate, physical plasma, etc. are usually required in order to enhance their properties, including their moisture resistance, wettability, mechanical properties, etc., by removing several non-cellulose components such as proteins, inorganic salts and colouring matters found in fibre lumen, as well as other waxy and additive substances [6]. The fibre surface treatment involved in the present study is a vacuum plasma surface treatment.

Plasma is an ionized gas in the form of charged ions, electrons and neutral particles where large amounts of energy are released upon collisions of the particles. This occurs when the molecules gain enough energy to make the electrons in the gas leave the nucleus of the atom [88][89]. The plasma state can be achieved by heating (pulsed), applying a voltage, or injecting electromagnetic waves [89]. In textile and natural fibre applications, only low temperature plasma is applicable.

Plasma treatment is a treatment method that induces changes on the fibre surface (cleaning, ablation, polymerization, and crosslinking) where an ionized region is formed creating superficial free radicals on the surface. The composition of this region depends on the gas feed, e.g. oxygen, nitrogen, argon, hydrogen, air, etc., which always includes high energy photons, electrons, ions, radicals and excited species and different compounds are created upon reactions between components in the plasma environment and the fibre's surface regions [5][90].

It was also found that the plasma surface treatment resulted in increased wettability and reduced water absorption of the cellulosic fibres, due to the decrease in phenolic and secondary alcoholic groups or oxidation of basic structural component, lignin and hemicelluloses [91][92][93]. This led to an increased modulus and strength of the NFRPs although the degradation of the fibre caused by the treatment decreased the strength of the treated fibre [92][93][94].

2.5 Fracture Mechanics

2.5.1 Introduction

This section introduces the basic fracture mechanics concept used in the present research under quasi-static loading, mode I double cantilever beam (DCB) interlaminar fracture test method and the toughening mechanisms involved in FRPs are discussed.

2.5.2 Quasi-static Fracture

Fracture mechanics studies crack propagation in materials and quantifies the resistance of materials to fracture [14]. Linear-elastic fracture mechanics (LEFM) is a methodology that allows the study of the fracture toughness of homogeneous, isotropic materials [95]. Although composites are not homogeneous, they generally exhibit linear-elastic behaviour and the yielding is constrained to a small zone at crack tip. Hence, LEFM can be applied to composite materials using the energy criterion to calculate the amount of energy required to initiate and propagate a crack [95].

The fracture of a component is a result of the extension of small crack-like defects embedded in the component, see Figure 2.8, under three different basic modes of crack loading: mode I (opening), mode II (shear) and mode III (tearing), see Figure 2.2.

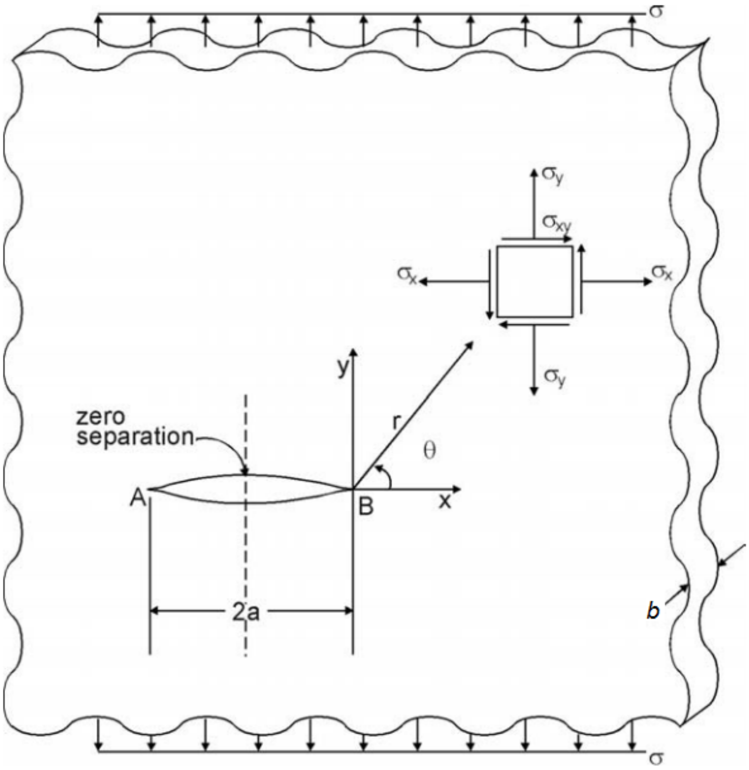

Figure 2.8: Schematic of an infinite plane with a crack-like defect [96]

The intensity or magnitude of the stresses in the crack tip region is linearly proportional to the remotely applied stress and proportional to the square root of the half crack length. It is defined by stress intensity factor as [96]:

$$K = \sigma\beta\sqrt{\pi a} \tag{2.1}$$

where σ is the applied stress and β is the function of geometrical features and crack length, a. In isotropic materials, the fracture toughness is usually defined in terms of the stress intensity factor, K_{IC}, and usually occurs under mode I loading. It is expressed as [22][97]:

$$K_{IC} = Y\sigma_{cri}\sqrt{a} \tag{2.2}$$

where Y is the specimen and crack geometry dependent dimensionless parameter and σ_{cri} is the critical applied stress.

As the material contains a crack, the stress at sharp crack tip should be theoretically infinite. However, the material will yield and a plastic zone will form in front of the crack tip. The size of the plastic zone ahead of the crack depends on whether the specimen is subject to a plane strain or a plane stress case. LEFM is used when the plastic zone is small as in the plane strain condition, while elasto-plastic fracture mechanics (EPFM) is used under the plane stress condition [98].

The radius of plastic zone as a function of critical stress intensity factor, K_{IC}, and yield stress, σ_y, shown in Figure 2.9, can be derived as [14]:

Plane stress condition

$$r_y = \frac{1}{2\pi}\left(\frac{K_{IC}}{\sigma_y}\right)^2 \tag{2.3}$$

Plane strain condition

$$r_y = \frac{1}{6\pi}\left(\frac{K_{IC}}{\sigma_y}\right)^2 \tag{2.4}$$

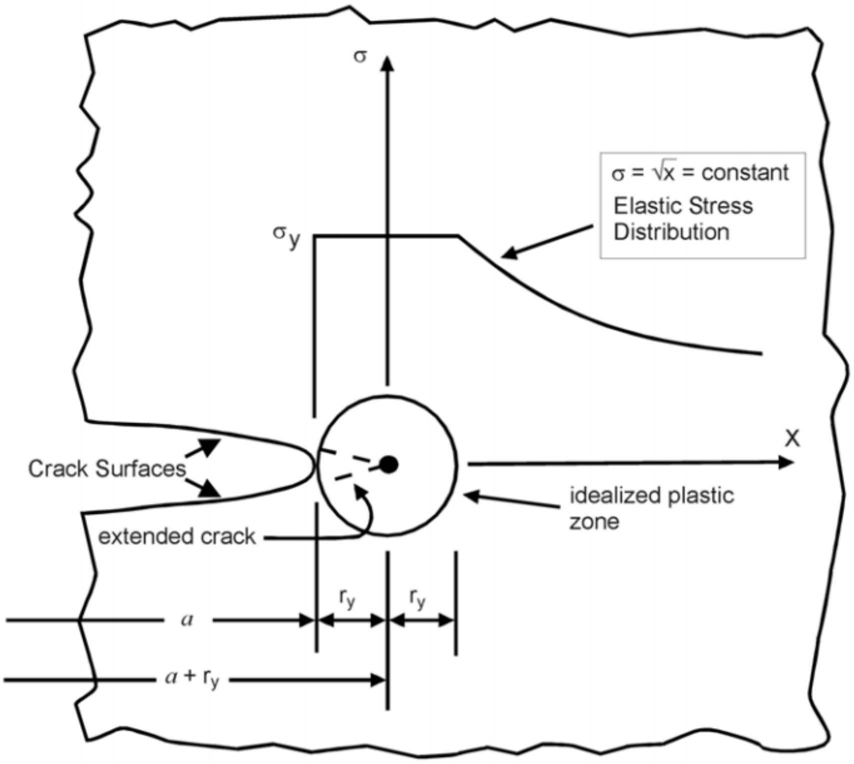

Figure 2.9: Schematic of a model showing plastic zone with crack tip plastic deformation [96]

The specimen width, *b*, is the determinant of the stress intensity factor for mode I where a large width contributes to plane strain fracture, while a small width contributes to plane stress fracture, see Figure 2.10. The minimum width required for plane strain conditions (i.e. the fracture test is performed under plane strain conditions) is defined as [99]:

$$b_{\min} \geq 2.5\left(\frac{K_{IC}}{\sigma}\right)^2 \tag{2.5}$$

Note: It should be noted that for bulk specimens the term, *b*, is referred to as the specimen thickness. However, for composites and the DCB test, *b* is referred to as the specimen width. Thus, *b* is taken as the specimen width throughout the present study.

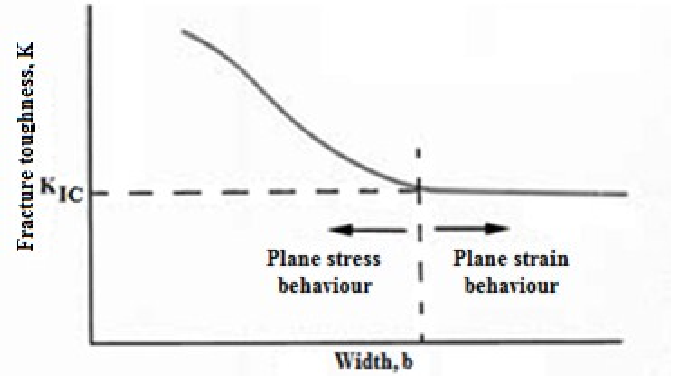

Figure 2.10: Schematic of the effect of plate width on fracture toughness [99]

In laminated composites, fracture can occur in either, or in combination of, the three basic loading modes of fracture and is normally expressed as fracture energy or fracture toughness, G_C [22]. The mode I fracture toughness, G_{IC}, is the energy consumed by the material as the delamination front advances through a unit area in opening mode which is defined as [22][100]:

$$G_{IC} = \frac{P_c}{2b} \cdot \frac{\partial C}{\partial a} \tag{2.6}$$

where P_c is the critical load at the onset of the crack propagation, b is defined as the width of the specimen and C is the specimen compliance measured with respect to the crack length, a (the ratio between the displacement and load).

For linear-elastic isotropic materials under plane strain conditions, K_{IC} and G_{IC} are related by the following expression [22]:

$$G_{IC} = \frac{\left(1-\upsilon^2\right)K_{IC}^2}{E} \tag{2.7}$$

where E is the Young's modulus and υ is the Poisson's ratio of the material.

2.5.3 The Double Cantilever Beam (DCB) Test

For mode I, the DCB is the commonest amongst all the test methods. Figure 2.11 shows schematic diagrams of the DCB test method. The test measures the fracture energy, G_{IC} [22].

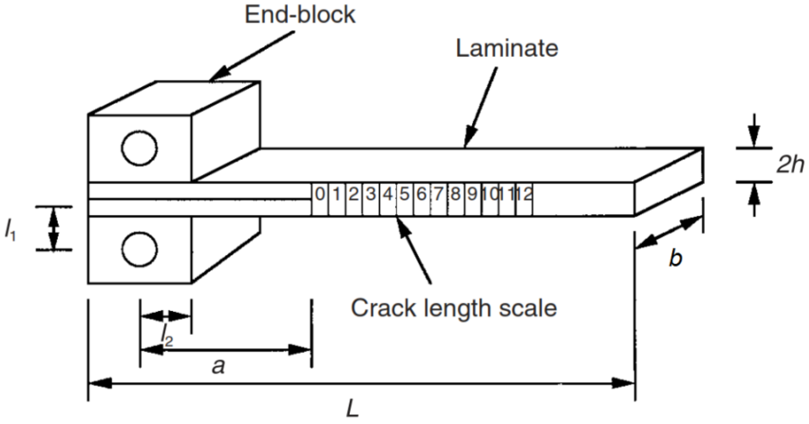

Figure 2.11: Mode I double cantilever beam (DCB) interlaminar fracture toughness test method [22]

Figure 2.12 shows the nominal load-displacement curves for a DCB test. The calculation of mode I interlaminar fracture energy test using the DCB method will be explained in section '4.4.1'.

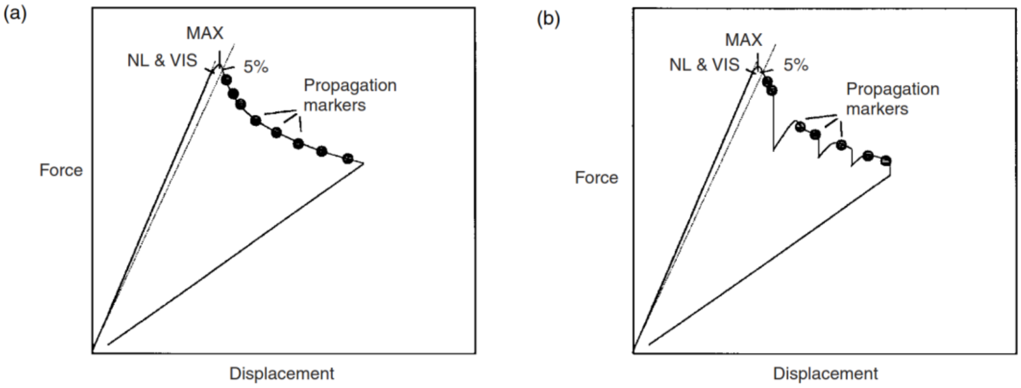

Figure 2.12: Load–displacement curves for DCB tests: (a) brittle matrix and (b) unstable crack growth (edited from [22])

2.5.4 **Toughening Mechanisms in FRPs**

The failure mechanisms in FRPs may include matrix cracking, fibre breakage, fibre pull-out (debonding), transverse-ply cracking, and delamination. These mechanisms may occur independently or interactively.

2.5.4.1 ***Matrix Cracking***

Matrix cracking is usually the first damage mechanism to occur in FRPs. A crack is formed in the matrix when the work done by the applied stress is greater than the increase in elastic strain energy of the FRPs plus the fracture surface work of the matrix per unit area of cross-section [2]. After the matrix has cracked, the bridging fibres are then assumed to carry the entire load formerly shared with the matrix. The load then transfers all responsibility for load bearing to the reinforcing fibres in which other failure mechanisms are introduced [2].

2.5.4.2 ***Fibre Bridging, Debonding and Pull-out***

In FRPs that have a relatively low toughness matrix compared to the fibres, and a weak interface, a transverse matrix crack of the composites leaves uncracked fibres behind providing fibre bridging across the crack which results in fibre breakage leading to fibre debonding and fibre pull-out, see Figure 2.13 [101]. Fibre debonding at the interface at the crack front (fibre pull-out) is determined by the frictional resistance between the matrix and fibre; low frictional resistance promotes pull-out which contributes to toughening [101].

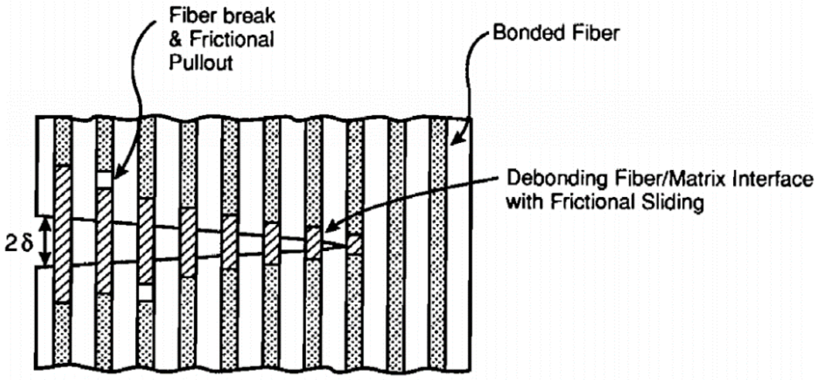

Figure 2.13: Schematic of fibre debonding, fibre pull-out, fibre breakage and matrix crack [101]

2.5.4.3 ***Fibre Breakage***

This mechanism is closely related to the fibre pull-out. Fibre breakage can occur either in composites with brittle fibres and a ductile matrix where the fibre breaks prior to the matrix cracking, or in composites with a brittle matrix and with high interfacial strength between fibre and matrix where matrix cracking leads to fibre bridging followed by fibre fracture reducing the potential pull-out contribution to toughening [101].

2.5.4.4 ***Delamination***

In laminated continuous-fibre-reinforced composites, weak fibre-matrix interface regions between the laminations are susceptible to delaminations (separation of the individual plies) due to cyclic loading, low velocity impact, moisture/temperature induced stress, eccentricities in the structural load path as in opening mode, discontinuities in the structures that may induce a large out-of-plane stress or residual stress, or to interlaminar shear stresses from shear/tension coupling that cause out-of-plane distortion [2]. A minor delamination may have no effect on the tensile properties of the composites but usually has a significant effect on their compression performance, and may lead to premature buckling of the laminate, excessive vibration, intrusion of moisture, stiffness degradation and loss of fatigue life, which all promote the rapid growth of the delamination [2]. Figure 2.14 shows a schematic illustration of the delamination buckling failure mechanism.

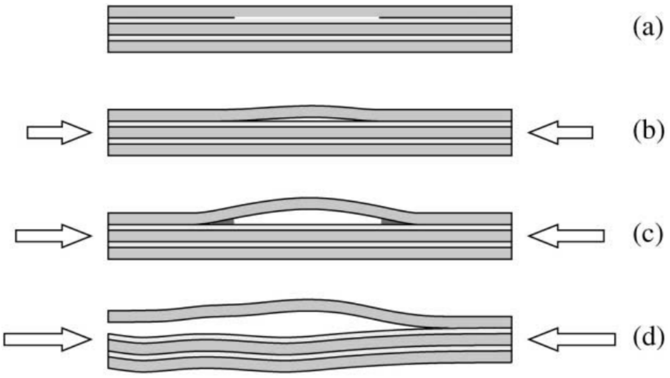

Figure 2.14: Schematic of delamination buckling failure mechanism: (a) initial delamination, (b) local buckling, (c) delamination growth and (d) failure [102]

2.5.4.5 ***Transverse Ply Crack***

A transverse ply crack parallel to the fibre direction in cross-ply laminate composites is usually the first damage mechanism to occur under uniaxial loading due to fibre-matrix debonding and/or matrix cracking, see Figure 2.15. It usually leads to interlaminar delamination, fibre fracture, and degradation of the load-carrying capability of the whole laminate [103].

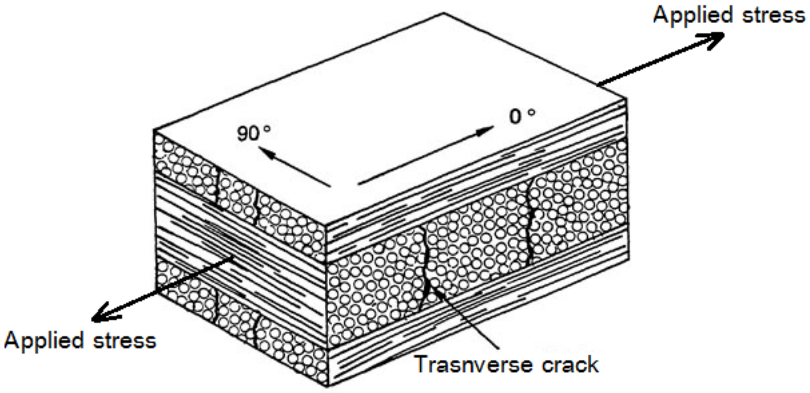

Figure 2.15: Schematic of a transverse crack under uniaxial loading [104]

2.6 Particle Modified Plastics and FRPs

2.6.1 Introduction

Due to the high cross-linking structure of epoxy polymers, they exhibit a relatively brittle manner and have a poor resistance to fracture. The addition of particulate phases can improve the toughness of the materials and these particulate phases can be pre-formed particles or may form a particulate phase via phase separation from a homogenous solution upon curing [56][105]. The pre-formed particles can be ceramic particles (e.g. glass, alumina or silica), metal particles (e.g. aluminium), polymer particles (e.g. polyetheretherketone or polytetrafluoroethylene), core–shell rubber particles (e.g. polysiloxane) and thermoplastics (e.g. poly (ether sulfone), poly (ether imide) or polystyrene) [56]. The particles that are formed via an in-situ phase separation are typically based upon a carboxyl-terminated butadiene-acrylonitrile (CTBN) rubber.

The two types of particulate phases used in the present study are silica-nanoparticles and CTBN rubber-microparticles. A summary of the particulate phases and toughening mechanisms involved with the toughened epoxy polymers and FRPs follows.

2.6.2 Silica-Nanoparticle Modified Plastics and FRPs

The main function of the silica-nanoparticles is to increase the toughness of the matrix of the FRPs [106]. The crack growth mechanisms involved are crack deflection caused by the nanoparticles or void formation between the particle and resin leading to an increased fracture energy [107]. This toughening effect appears to increase with decreasing particle size [108]. Additionally, it was found that the addition of silica-nanoparticles also improves the strength, stiffness and fatigue behaviour of thermosetting resins and FRPs [109].

A study by Hsieh and his colleagues showed a slight improvement of the mode I interlaminar fracture energy of an epoxy reinforced with glass and carbon fibres with the addition of silica-nanoparticles [56]. Manjunatha and his colleagues [110] studied the tensile fatigue behaviour of GFRPs employing a silica-nanoparticle modified epoxy polymer and found that the fatigue life was increased by about three to four times compared with the unmodified GFRPs. It was found that there was suppressed matrix cracking and a reduced crack propagation rate in the nanoparticle-modified matrix composite. Further details of the silica-nanoparticle modified epoxy polymer used in the present study can be found in section ‘3.2.3’.

2.6.3 Rubber-Microparticle Modified Plastics and FRPs

The addition of rubber particles is a well-known approach to improve the fracture energy of plastics and FRPs [111][112]. The increase in fracture energy is controlled by many factors such as particle size, particle concentration, particle mechanical properties and the properties of the epoxy itself [56][113]. However, a decrease in stiffness of the material is a side effect [111]. It is important that the failure mechanisms and toughening processes involved are fully understood. It was found that fracture resistance was increased by the rubber particle modification of epoxy polymers where different types of rubber particles could have different toughening mechanisms involved; soft particles tend to cavitate which introduces shear banding, while hard particles tend to deflect and bifurcate the crack [112]. Further details of the rubber-microparticle modified epoxy polymer used in the present study can be found in section '3.2.3'.

2.6.4 Hybrid Modified Plastics and FRPs

The aforementioned two phases used to modify the epoxy polymers in the present study, i.e. silica-nanoparticles and rubber-microparticles were combined to produce a hybrid modified epoxy polymer for composite fabrication. A significant increase in the fracture energy was found in the hybrid modified epoxy polymer as a result of hybrid toughening; however, a slight decrease in stiffness of the material was seen due to the rubber softening effect [56]. It was realized that the dispersion of the rubber-microparticles was not affected by the addition of silica-nanoparticles; however the silica-nanoparticle phase tended to agglomerate [14][56]. Further details of the hybrid modified epoxy polymer used in the present study can be found in section '3.2.3'.

2.6.5 Mechanical and Thermal Properties of Particle Modified Plastics and FRPs

Hsieh et al. studied the effects of particle toughening on the mechanical and thermal properties of epoxy polymers and found that the addition of silica-nanoparticles resulted in an increase in stiffness and glass transition temperature, while CTBN rubber-microparticles gave the opposite effect [56], see Table 2.11.

Table 2.11: Summary of mechanical and thermal properties of silica-nanoparticle and CTBN rubber-microparticle modified epoxy polymers [56]

Formulation*	E (GPa)	T_g (°C)
Si0R0	2.90±0.09	147.8±0.9
Si10R0	3.28±0.08	148.3±1.4
Si0R9	2.31±0.04	140.1±2.3
Si10R9	2.74±0.05	140.3±2.1

*Si0R0 = unmodified DGEBA epoxy polymer; Si10R0 = 10 wt% silica-nanoparticle modified DGEBA epoxy polymer; Si0R9 = 9 wt% CTBN-microparticle modified DGEBA epoxy polymer; and Si10R9 = 10 wt% silica-nanoparticle + 9 wt% CTBN-microparticle modified DGEBA epoxy polymer.

2.6.6 Toughening Mechanisms in Particle Modified Plastics and FRPs

Hsieh et al. also studied the toughening mechanisms involved in silica-nanoparticle and CTBN rubber-microparticle modified epoxy polymers [56]. The toughening mechanisms are summarized in Table 2.12 and illustrated in Figure 2.16 [14][56]. The toughening mechanisms are reviewed in detail below (note that some toughening mechanisms are only effective for micron-sized particles).

Table 2.12: Summary of toughening mechanisms in silica-nanoparticle and CTBN rubber-microparticle modified epoxy polymers [56]

Formulation	K_{IC} (MPa·m$^{1/2}$)	G_{IC} (J/m^2)	Silica-nanoparticle	Rubber-microparticle
Si0R0	0.69	133	N/A	N/A
Si10R0	0.81	191	- Debonding - Plastic void growth (14%, Ø 34 nm)	N/A
Si0R9	1.41	697	N/A	- Rubber cavitation - Plastic void growth (Ø 1.18 μm)
Si10R9	2.28	1059	- Debonding - Plastic void growth (13%, Ø 35 nm)	- Rubber cavitation - Plastic void growth (Ø 1.45 μm)

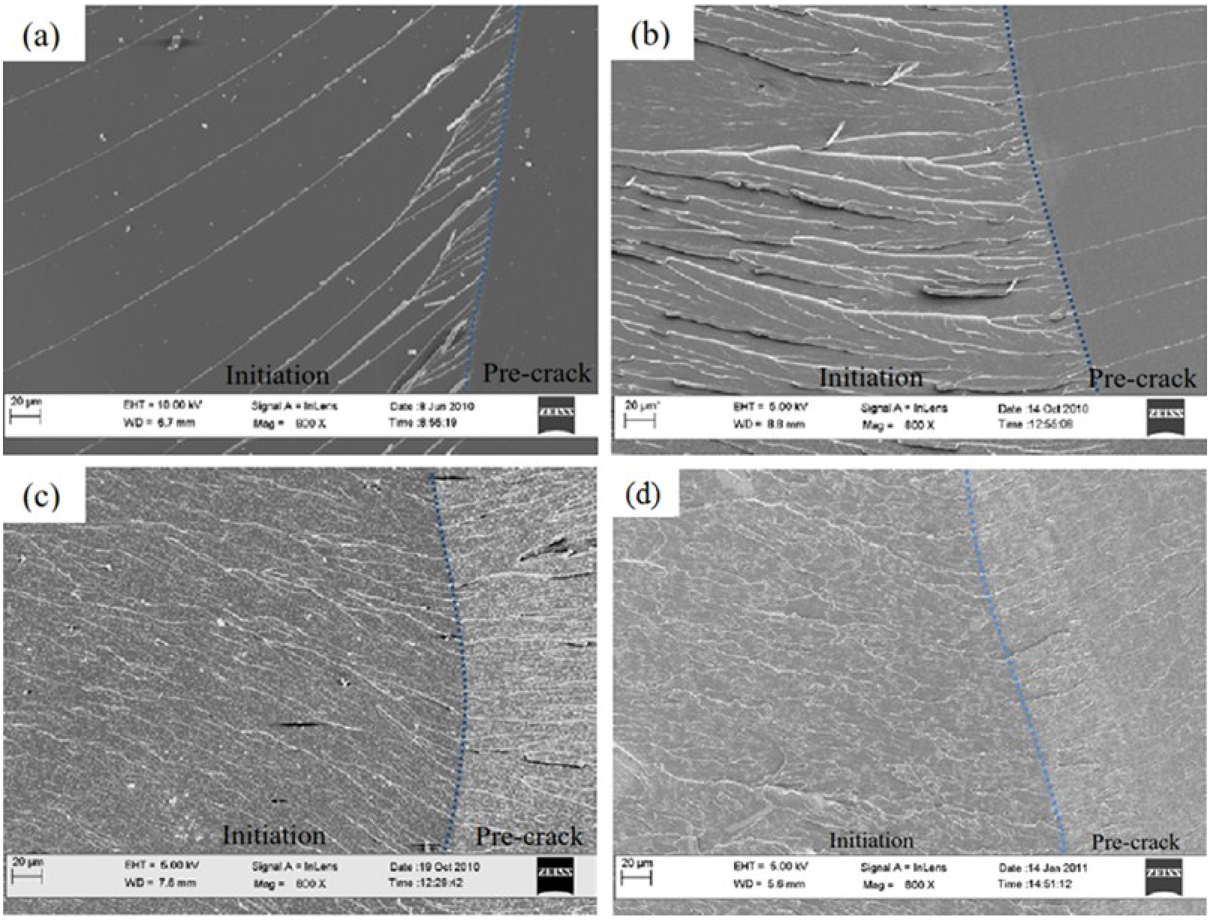

Figure 2.16: FEG-SEM images of fracture surfaces of (a) unmodified (Si0R0) epoxy polymer, (b) 10 wt% silica-nanoparticle modified (Si10R0) epoxy polymer, (c) 9 wt% rubber-microparticle modified (Si0R9) epoxy polymer and (d) hybrid modified (Si10R9) epoxy polymer (10 wt% silica-nanoparticle + 9 wt% rubber-microparticle) [56]

2.6.6.1 *Rigid Particle Toughening Mechanisms*

2.6.6.1.1 Crack Pinning

The crack pinning mechanism involves bowing of the crack front once it gets pinned by the rigid particles forming secondary cracks. The formation of a new fracture surface and the increase in length of the elliptical crack front lead to an increase in the measured fracture energy, see Figure 2.17 and Figure 2.18 [95][114].

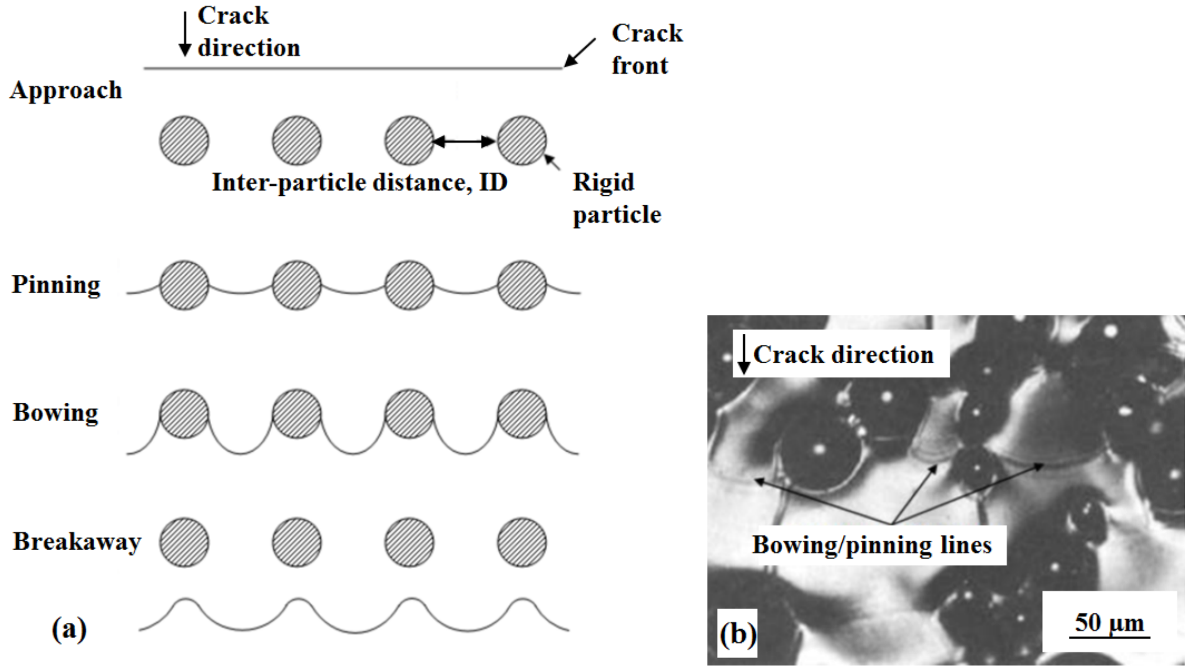

Figure 2.17: (a) A schematic model of the crack pinning mechanism and (b) an optical image of a glass-particle modified polymer showing the crack pinning mechanism [95][114]

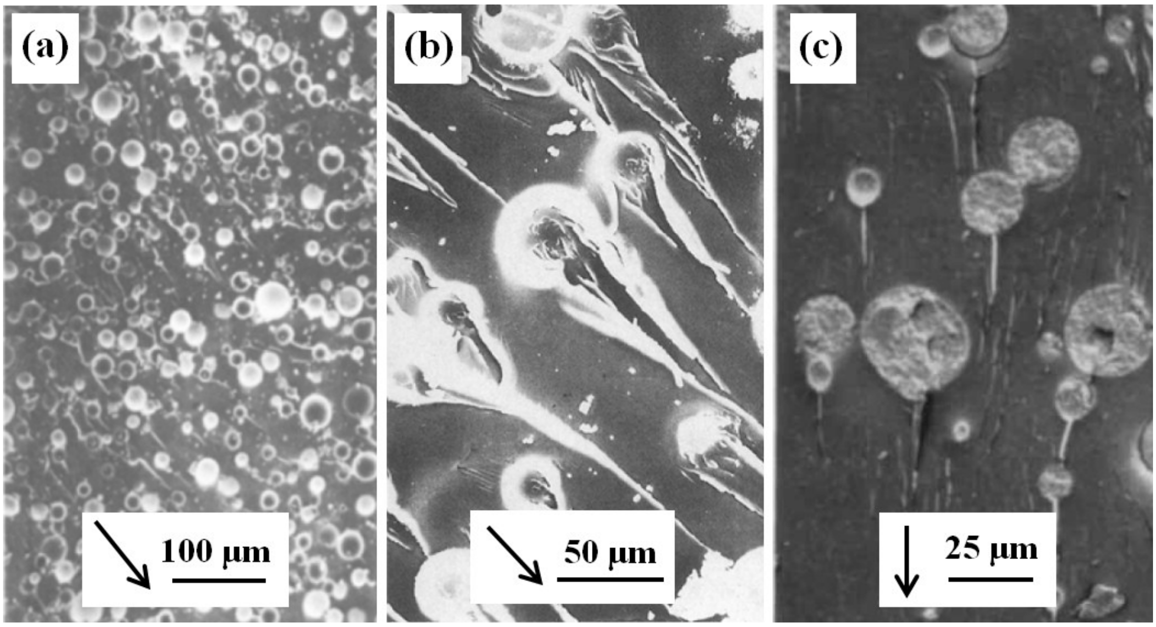

Figure 2.18: SEM images of (a) and (b) glass particle modified polymer and (c) DGEBA epoxy resin/diaminodiphenylsulfone showing the crack pinning mechanism (arrows show crack directions) [112][114][116]

2.6.6.1.2 Plastic Void Growth

The plastic void growth of the matrix is initiated by debonding of the rigid particle, or cavitation of the rubbery particle (see below) as a result of the stress concentration around the particles, which leads to the relief of triaxial stress in the adjacent region, see Figure 2.19 and Figure 2.20 [113].

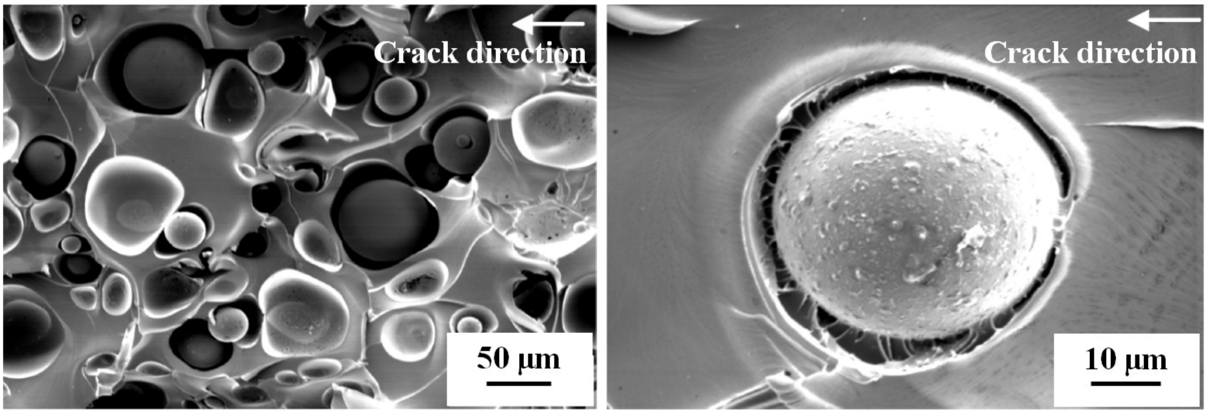

Figure 2.19: SEM images of fracture surfaces of microparticle modified epoxy polymers showing particle debonding and plastic void growth [117]

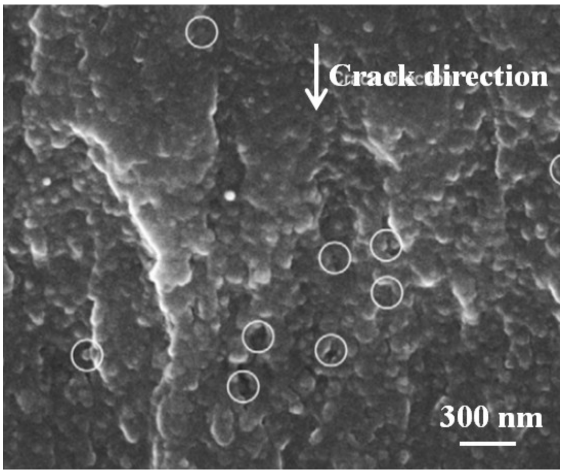

Figure 2.20: A high-resolution FEG-SEM image of the fracture surface of $0.133v_p$ silica-nanoparticle modified epoxy showing void growth mechanism [113]

2.6.6.1.3 Crack Deflection, Crack Bifurcation and Crack Bridging

The crack deflection mechanism involves the stress concentration caused by the stress fields around the particles where the crack tends to propagate. The crack will propagate along the lowest resistance to crack propagation path, see Figure 2.21 [112]. Crack bifurcation is a similar mechanism where a crack bifurcates along the lowest resistance paths. In crack bridging, the crack propagates through the particles as the lowest resistance path, see Figure 2.22 [112]. The tilted crack introduces an increase in the area of fracture surface and introduces some mode II or mode III loading, which results in a higher fracture energy [95].

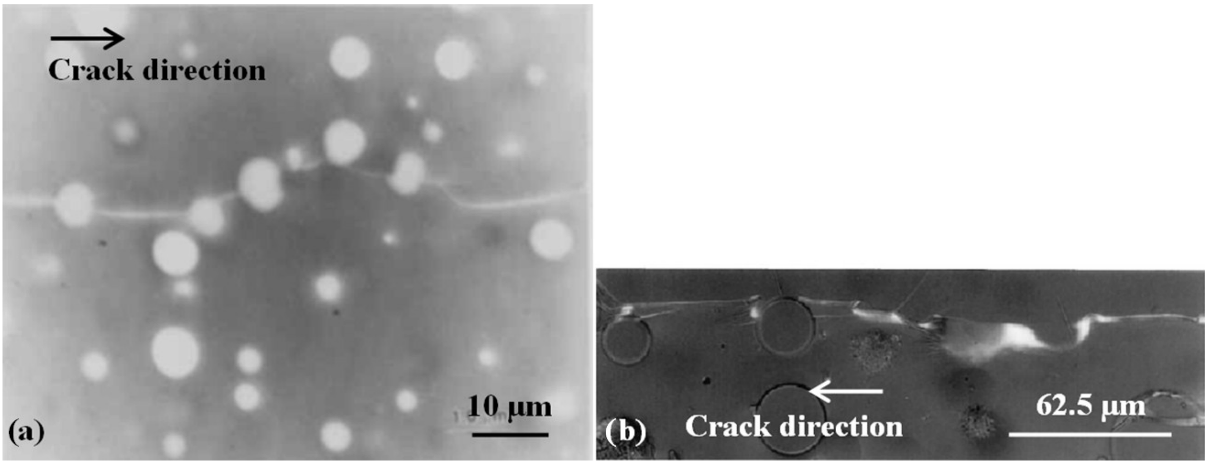

Figure 2.21: (a) A TEM image of the damaged dispersed acrylic rubber modified DGEBA epoxy resin/diaminodiphenylsulfone and (b) an optical image of a glass bead modified polymer showing the crack deflection mechanism [112]

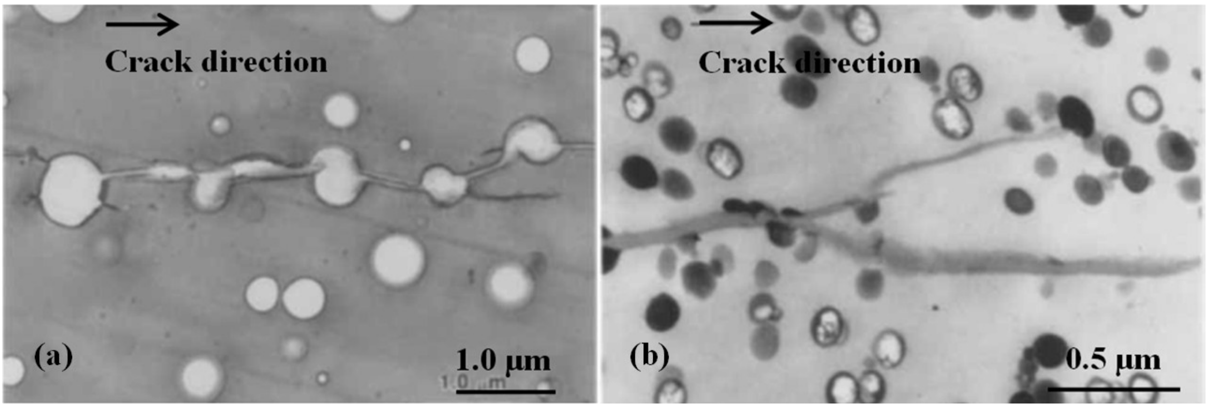

Figure 2.22: A TEM image of (a) a region behind the crack tip of dispersed acrylic rubber modified DGEBA epoxy resin/diaminodiphenylsulfone and (b) damaged crack wake of the grafted-rubber concentrate modified epoxy showing crack bifurcation and crack bridging mechanism [112]

2.6.6.2 *Rubber Particle Toughening Mechanisms*

2.6.6.2.1 Rubber Cavitation

Rubber cavitation is another toughening mechanism in rubber modified plastics and FRPs where soft rubbers cavitate due to the high strength of the interface between matrix and rubbers [95]. This cavitation of the rubber particles and the triaxial stress create plastic void growth of the epoxy polymeric matrix, see Figure 2.23 [112][118].

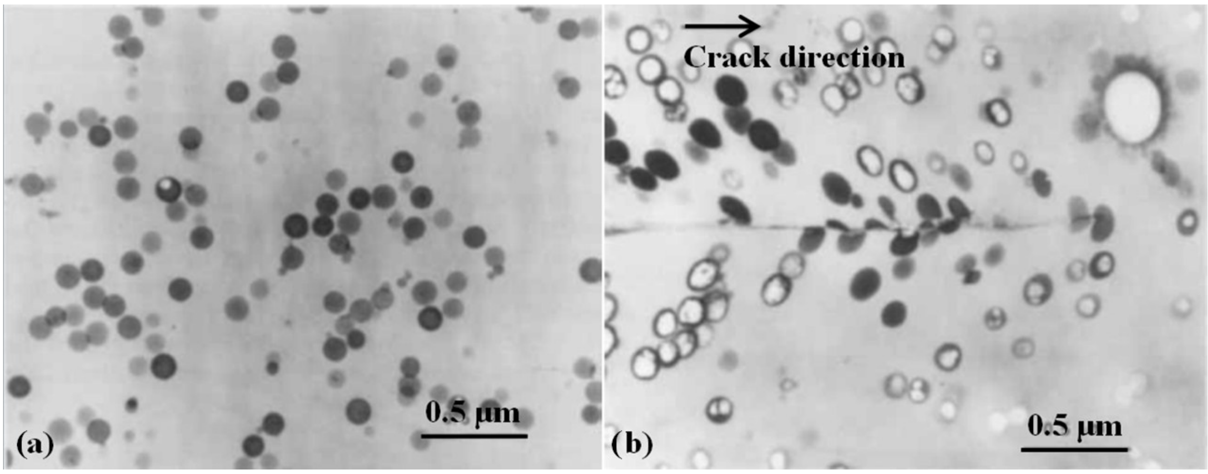

Figure 2.23: TEM images of (a) undamaged grafted-rubber concentrate modified epoxy and (b) damaged grafted-rubber concentrate modified epoxy at the crack tip showing rubber cavitation under a double-notch four-point bend test [112].

2.6.6.2.2 Rubber Bridging

Rubber bridging is a toughening mechanism that involves the rubber particles in the crack path being stretched by the two opposing crack surfaces, see Figure 2.24 [119]. This mechanism was found to only marginally increase the fracture energy of the composites [57].

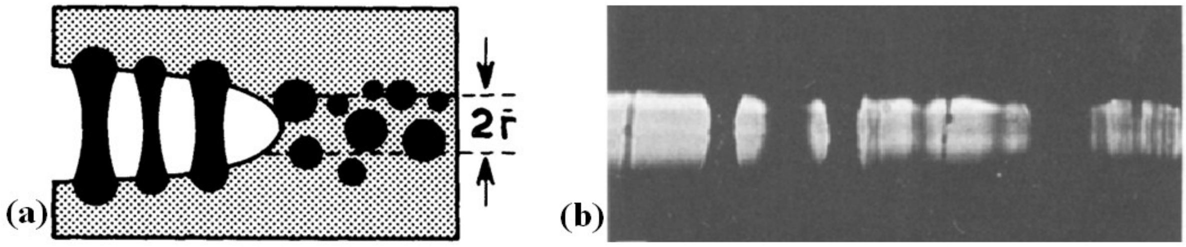

Figure 2.24: (a) A schematic diagram of the region near the crack tip and (b) an optical image of the epoxy-rubber composite showing a rubber bridging mechanism [119]

2.6.6.2.3 Shear Banding and Plastic Deformation

In particle modified plastics, shear band and plastic deformation are facilitated by other mechanisms such as particle cavitation and debonding. This occurs by the creation of stress concentrations and shear localization where shear yielding can take place or through creating stress concentrations around the particles where plastic deformation is formed, which absorbs energy and so enhances the toughness of the materials, see Figure 2.25 [112][120].

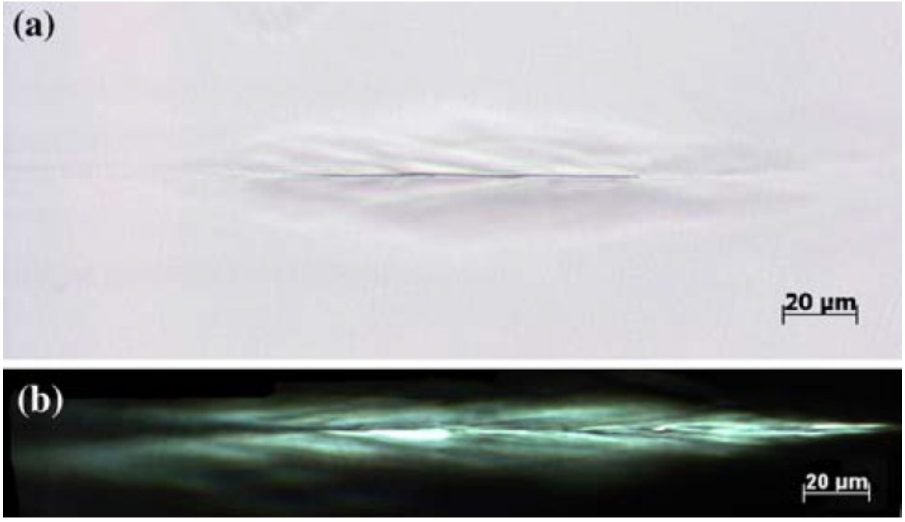

Figure 2.25: A TEM image of an epoxy polymer with 11 wt% silica nanoparticles showing the plastic-deformed region taken using (a) normal light and (b) between crossed polarisers; crack propagation is from left to right [56]

2.7 Processing of FRPs

2.7.1 Introduction

There are many different manufacturing processes that possess their own limitations and benefits which are suitable for different combinations of materials, e.g. resins, fibres, core structures, etc. This section describes some commonly used composite manufacturing processes and their benefits, limitations and applications as well as their advantages and disadvantages.

2.7.2 Comparison of Composite Manufacturing Processes

2.7.2.1 *Introduction*

The properties of FRPs can be designed by the appropriate selection of the resins, reinforcements and/or cores. However, different processing routes can also result in significantly different properties of the composites, see Table 2.13 [121]. The present section compares different FRP processing methods.

Table 2.13: Cost comparison and process efficiency of different FRPs processing methods [122]

Process	Typical Cycle time	Equipment Capital (£1000)	Mould capital (£)	Product value per cycle (£)	Product value per hour (£)	Process efficiency*
Spray lay-up	3 hrs	5	100-500	5-25	2-8	400-1600
Hand lay-up	5 hrs	0	100-500	5-25	1.5	10000
Vacuum bagging	1 hr	5	100-500	1-4	1-4	200-800
Filament winding	4 hrs	20-100	1000	10-100	2.5-25	119-250
Pultrusion	0.5-3 m/min	50-100	2000-10000	3/m	90-540	2884-5400
Injection (VARI)	10-60 mins	5-10	300-1000	1-10	6-10	1200-10000
Compression	3 mins	50	5000-20000	1-5	20-100	365-1428
Autoclave (pre-preg)	8 hrs	150	1000	10-100	1.25-12	8.3-79

*Process efficiency = Product value per hour x 10^6/total capital

2.7.2.2 *Spray Lay-up*

Spray lay-up is an open-moulding composite manufacturing process where resin (primarily polyester) and reinforcement (primarily chopped glass roving) are sprayed separately or simultaneously onto the reusable mould or as a secondary layer over the core materials, see Figure 2.26 [121]. This process is typically used to fabricate simple enclosures and lightly loaded structural panels, e.g. caravan bodies, truck fairings, bathtubs, shower trays, small dinghies, etc.

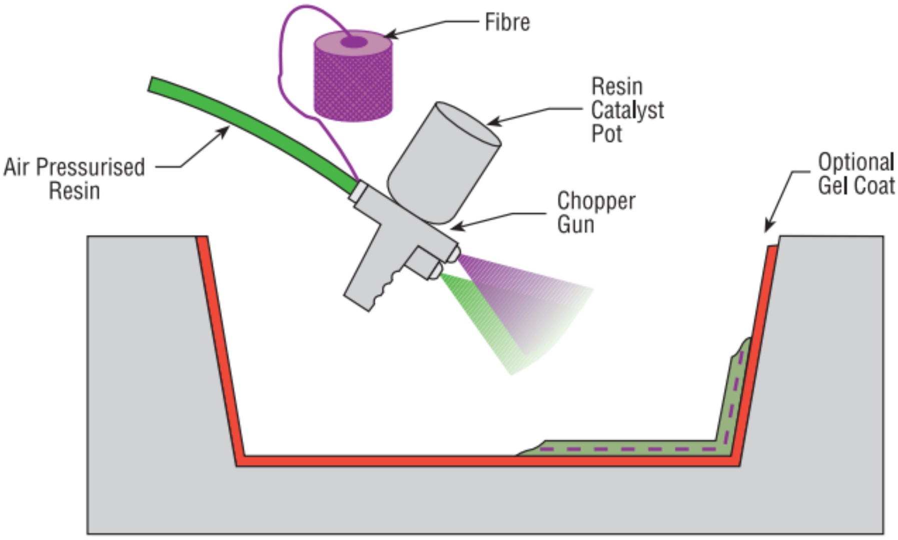

Figure 2.26: Schematic of spray lay-up process [121]

2.7.2.3 *Hand Lay-up (Wet Lay-up)*

Hand lay-up is a process that impregnates the resin into fibres/fabrics by rolling/brushing resin onto fibres/fabrics; laminates are often cured under standard atmospheric conditions, see Figure 2.27 [121]. Any type of fibres and core structures can be used and the resins used are generally epoxy, polyester, vinylester and phenolic. This process is generally employed to manufacture wind turbine blades and boats.

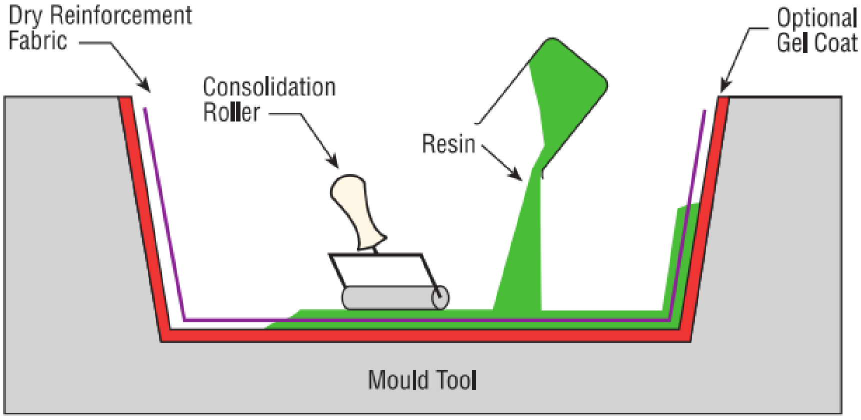

Figure 2.27: Schematic of hand lay-up process [121]

2.7.2.4 *Vacuum Bagging*

This process is similar to the wet lay-up process described above, with additional vacuum bagging to improve the degree of consolidation, see Figure 2.28 [121]. Any type of fibres and core structures can be used and the resins are generally epoxy and phenolic. This process is used to manufacture race car components and large cruising boats.

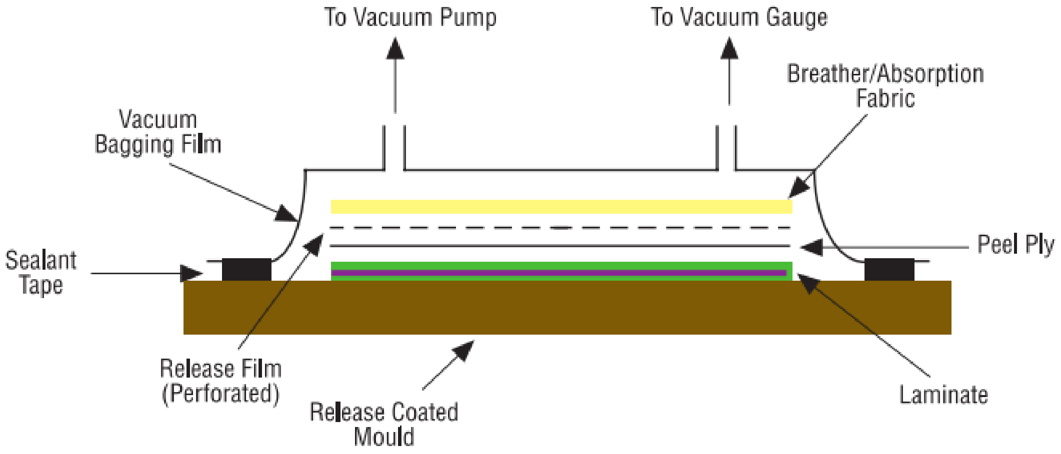

Figure 2.28: Schematic of vacuum bagging process [121]

2.7.2.5 *Filament Winding*

In the filament winding process, fibre tows are wound onto a mandrel after passing through a resin bath. The process can control the fibre orientation by varying the feeding mechanism and rotational rate. This process is primarily used to manufacture symmetrical circular hollow components, see Figure 2.29 [121]. Any type of fibres can be used without a core structure and the resins are generally epoxy, polyester, vinylester and phenolic. This process is used to manufacture storage tanks, pipelines and gas cylinders.

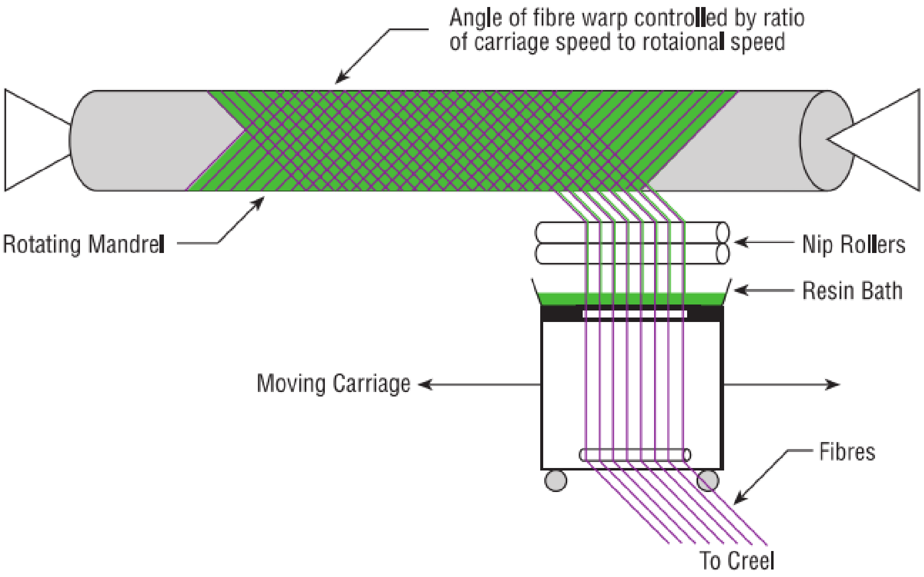

Figure 2.29: Schematic of filament winding process [121]

2.7.2.6 *Pultrusion*

In pultrusion, fibres are pulled from the ‘creel’ through a resin bath and heated die. The process completes the impregnation, controls the resin content and cures the materials into its final shape, see Figure 2.30 [121]. Fabrics may be introduced into the die to incorporate fibres in other orientations. Additionally, the process can incorporate moulding to make a non-constant cross-sectional profile [121]. Any type of fibres without a core structure can be used and resins are generally epoxy, polyester, vinylester or phenolic. This process is used to manufacture roof structures, bridges, ladders and frameworks.

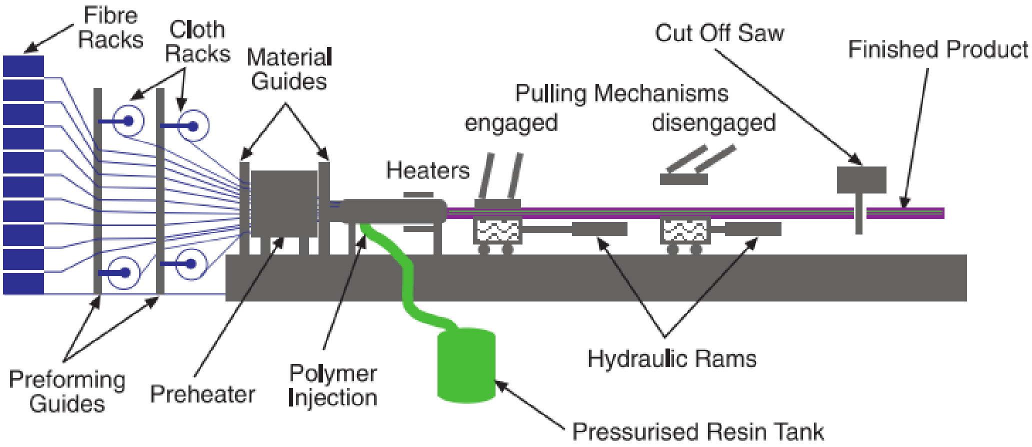

Figure 2.30: Schematic of pultrusion process [121]

2.7.2.7 *Resin Transfer Moulding (RTM)*

In the RTM process, dry fabrics or pre-formed fabrics are laid-up onto a mould and then clamped by the second-part mould. Resin is injected under pressure, with or without vacuum assist, until all the fibres are fully wetted. The inlet is then closed, see Figure 2.31 [121]. Injection and cure can take place at ambient or elevated temperature. Any type of fibres/fabrics can be used for this process with a wide range of resins including epoxy, polyester, vinylester and phenolic. This process is not suitable for cored-composite parts, where cores would be filled in with resin during the process [121]. Small complex aircraft, automotive components and seats are generally manufactured using this process.

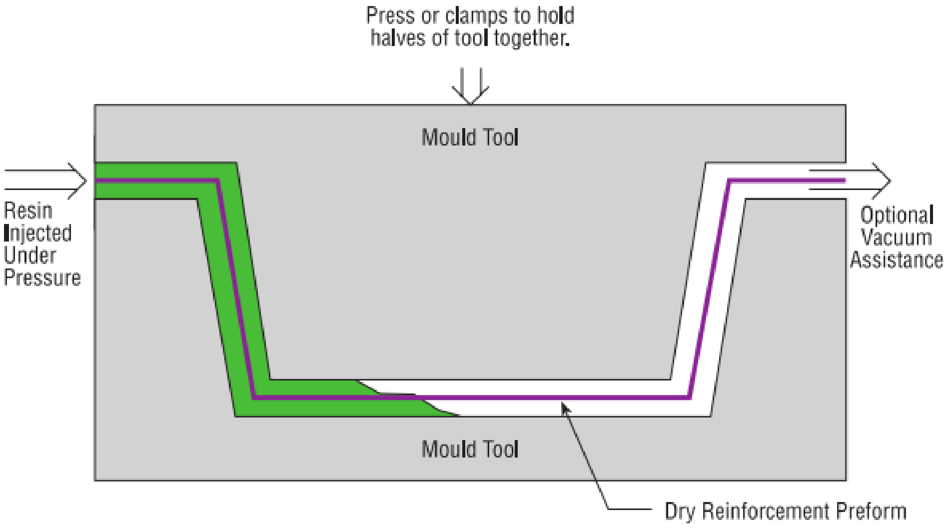

Figure 2.31: Schematic of RTM process [121]

2.7.2.8 *Other Infusion Processes*

Infusion processes might include the Seeman composites resin infusion manufacturing process (SCRIMP), resin infusion under flexible tooling (RIFT), vacuum assisted resin transfer moulding (VARTM), etc. In the infusion process, dry fabrics are laid-up either 1) onto the mould and then covered with peel ply, flow medium and vacuum bag or 2) between peel plies, flow media and vacuum bags. The resin is then infused into the fabrics under vacuum, see

Figure 2.32 [121]. Epoxy, polyester and vinylester resins are normally used in these processes with any type of fabrics and cores. This process is generally used to manufacture small yachts, train and truck body panels and wind turbine blades.

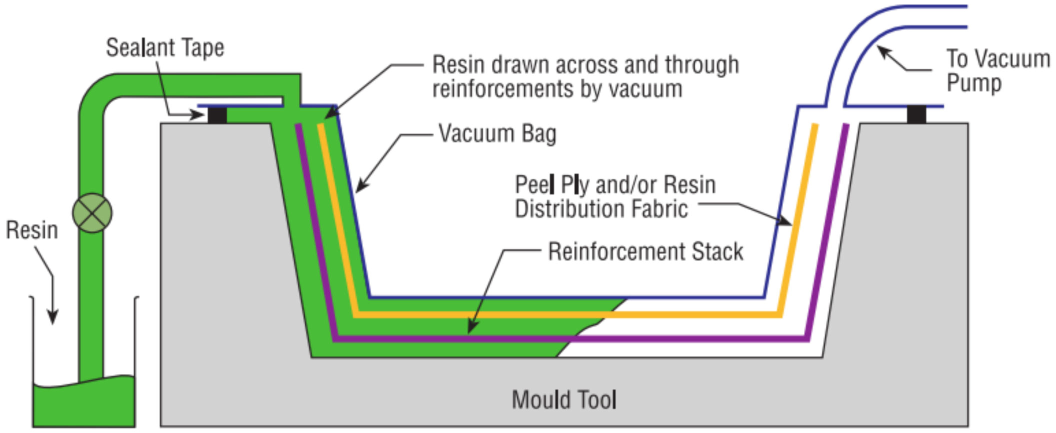

Figure 2.32: Schematic of resin infusion process [121]

2.7.2.9 *Autoclave (Pre-preg)*

In this process, fibres/fabrics are first pre-impregnated with resin under pressure and heat prior to manufacturing. The pre-preg is normally stored frozen to freeze the catalytic process and is then defrosted before being laid-up onto a mould by hand or automatically. The pre-preg is vacuumed and normally pressurized and heated up to 120-180°**C** in an autoclave to allow the resin to reflow and cure, see Figure 2.33 [121]. Resins that are generally used in this process are epoxy, polyester, phenolic and high temperature resins such as polyimides, cyanate esters and bismaleimides that incorporate any type of fibres and high pressure and temperature cores [121]. This process is generally used to manufacture aircraft and high performance car structural components.

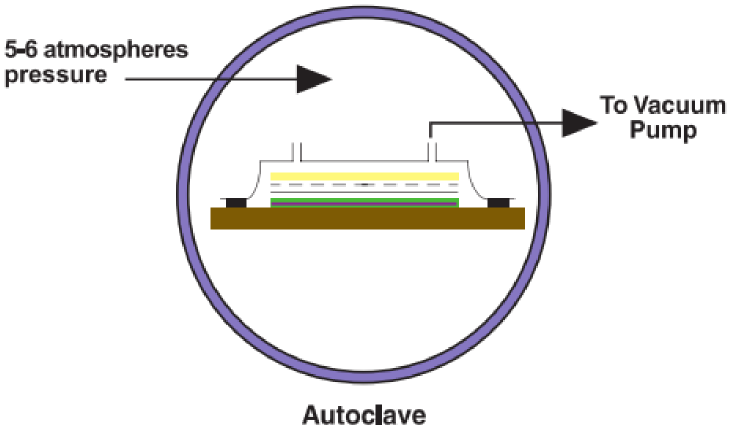

Figure 2.33: Schematic of pre-preg autoclave process [121]

The advantages and disadvantages of different composite manufacturing processes are summarized in Table 2.14.

Table 2.14: Summary of advantages and disadvantages of different manufacturing processes [121][123][124]

Process	Advantages	Disadvantages
Spray lay-up	- Long history of success and widespread use - Low cost tooling and material systems - Very economical for making small to large parts in small to medium volume	- Generally poor mechanical and thermal properties (requirement for low viscosity of resin, short fibre instead of long or continuous fibres, not suitable for primary structural parts) - Difficult to control the mixing ratio, volume fraction, thickness, dimension accuracy, repeatability, etc. (human dependent) - One-sided smooth surface - Chemical emission/airborne (health concern)
Hand lay-up	- Long history of success, widespread use and simple process - Low cost tooling (room temp curing) - Longer fibres than spray lay-up - Wide range of materials	- Generally poor mechanical properties (volume fraction, void) (human dependent) - Difficult to control the mixing ratio, volume fraction, void, thickness, dimension accuracy, repeatability, etc. (human dependent) - Chemical emission/airborne (health concern)
Vacuum bagging	- Higher fibre content and lower void content than hand lay-up - Better fibre wetting (pressure and flow of resin) - Low chemical emission/airborne than spray lay-up and hand lay-up (health concern)	- Added cost (labour and consumable materials) - Higher skills required - Difficult to control the mixing ratio - Higher chemical emission/airborne than infusion and pre-preg processes (health concern)
Filament winding	- Fast, automatic, economical processes giving consistent products - Full control of resin and fibre content (good mechanical properties) - High fibre content and continuous fibre (good mechanical properties) - Low cost of fibre (use of fibre instead of fabric) - Low material wastage	- Non-smooth external surface - Lower mechanical and thermal properties (requirement for low viscosity of resin) - High cost tooling (mandrel) - Geodesic requirement limits fibre directions (fibre cannot be laid along the length of a component) - Plane of weakness sometimes occurs between winding layers with high void content - Only for relatively simple geometries and convex shaped components
Pultrusion	- Fast, automatic, economical processes giving consistent products - Full control of resin and fibre content (good mechanical properties) - High fibre content, long/continuous fibre along profile (good mechanical properties) - Low cost of fibre (use of fibre instead of fabric) - Low chemical emission/airborne than spray lay-up and hand lay-up (health concern)	- High cost tooling (heated die) - Constant/near constant cross-section of component limitation - Fibres along the profile only

Table 2.14 (continued)

Process	Advantages	Disadvantages
Resin transfer moulding (RTM)	- High fibre volume and low void - Low chemical emission/airborne than spray lay-up and hand lay-up (health concern) - Two-sided smooth surfaces - Low labour cost	- High cost tooling (matched tooling, large tooling to withstand pressure) - Limit to smaller components - Good resin flow design is required to reduce unwetted areas - Slow process - High energy consumption (large tooling)
Other infusion processes, e.g. SCRIMP, RIFT, VARTM, etc.	- Low cost tooling (one-sided vacuum bagging, and less strength of tooling required) - No limitation to small parts - Standard hand lay-up tool can be used sometimes - Core structures can be incorporated	- One-sided smooth surface - Complex processes require skills - Lower mechanical and thermal properties (requirement for low viscosity of resin) - Good resin flow design is required to reduce unwetted areas - Slow process
Autoclave (pre-preg)	- Resin and fibre contents are fully controlled - High fibre volume content (good mechanical properties) - Automation process (repeatability and labour cost saving) - Good mechanical and thermal properties (high viscosity resin can be used)	- High cost materials - Slow process and high energy consumption (autoclave) - Limitation of component size (autoclave) - High cost tooling (high temperature and pressure) - Complex process (thicker laminates need to be vacuumed/debulked to remove air entrapped)

2.7.3 Concerns with RTM and RIFT Processes

The two manufacturing processes were used in the present study and so concerns with these processes are discussed [125][126].

- In the RTM process, the high pressure used to inject resin into the mould with pre-positioned, preformed reinforcement might shift/deform the reinforcement resulting in resin rich/dry spots. In the RIFT process, vacuum pressure is used to draw the resin to infuse into the layers of reinforcement where a difference in local pressure gradient might vary the thickness of the component resulting in variation of fibre volume fraction as well as resin rich/dry spots.
- Good design of injection ports is necessary. For example, software simulation to minimize the average resin path by properly and adequately positioning inlets and outlets in the mould to prevent air entrapment between flow fronts and fast tracks that might create resin rich/dry spots.
- Due to differences in fibre structures, weaving architectures and lay-up, the speed of injection might affect the impregnation of the reinforcement. Fast injection might create voids inside the fibre bundles due to difference in speed of resin flow between bundles and within bundles, while, on the flip side, capillary flow within the bundles may fast track the resin flow and entrap air bubbles between the fibre bundles with slow injection, see Figure 2.34.
- Due to the exothermic chemical reaction that takes place during curing, shrinkage in thick parts may result in cracking/warpage and so heat must be controlled properly.

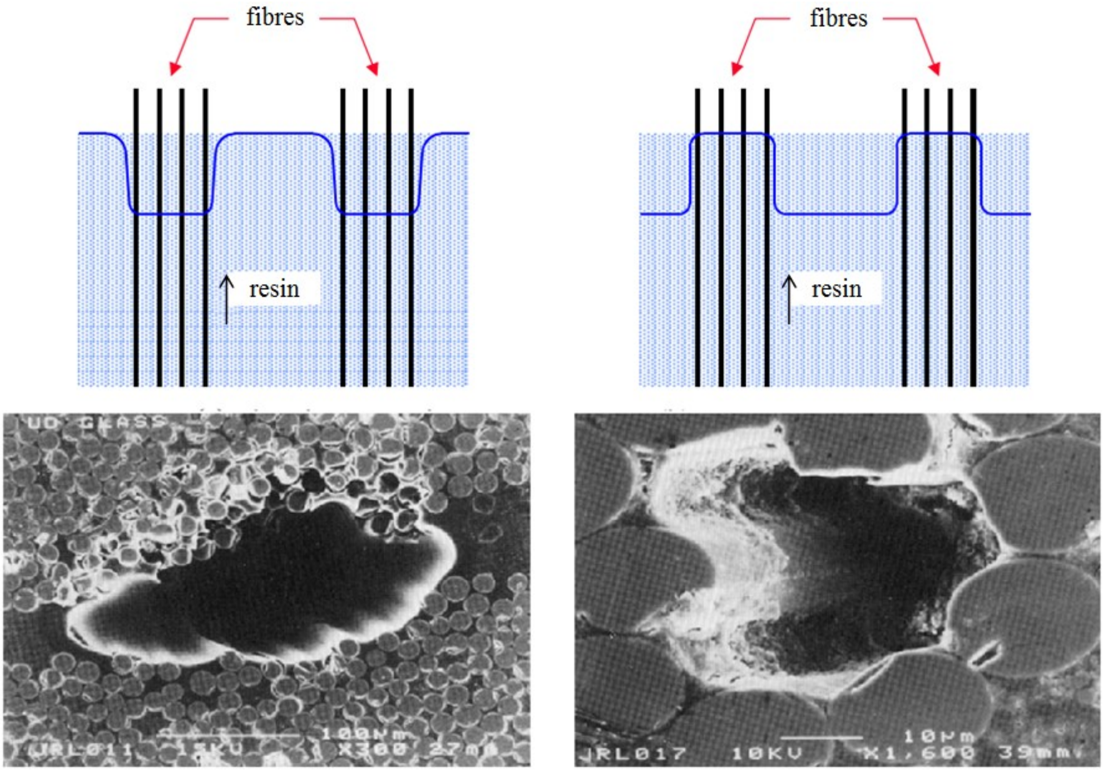

(a) fast impregnation (b) slow impregnation

Figure 2.34: Two cases of resin impregnation which may result in void formation: (a) low resin velocity (Inter-bundle void) and (b) fast resin velocity (Intra-bundle void) [125]

2.8 Concluding Remarks

The present chapter has reviewed epoxy polymers, FRPs and NFRPs together with a discussion of their basic mechanical properties. The basic principles of fracture mechanics and toughening mechanisms of particle modified epoxy polymers and FRPs have also been summarised. The different composite manufacturing processes have been described. The materials and experimental methods used in the present study will be discussed in 'Chapter 3' and 'Chapter 4' respectively.

CHAPTER 3 MATERIALS

3.1 Introduction

The present chapter describes the materials used in the present study, including the epoxy polymer formulations and the reinforcements of flax fibre, regenerated cellulose fibre and glass fibre.

3.2 Epoxy Polymers

3.2.1 Introduction

This section describes in detail the formulations of epoxy polymers that include unmodified, silica-nanoparticle modified, rubber-microparticle modified and hybrid modified epoxy polymers, as well as their morphology and general mechanical properties.

3.2.2 Epoxy Polymers

The epoxy resin in the present study was a standard diglycidyl ether of bisphenol A (DGEBA) with an epoxide equivalent weight (EEW) of 185 g/eq, 'LY556' supplied by Huntsman, UK. The curing agent was an accelerated methylhexahydrophthalic acid anhydride with an amine equivalent weight (AEW) of 170 g/eq, 'Albidur HE600', supplied by Nanoresins, Germany.

3.2.3 Modified Epoxy Polymers

The epoxy, hardener, silica-nanoparticles and rubber-microparticles were mixed at predefined ratios, see Table 3.1. Formulations at different modifier concentrations, namely unmodified, silica-nanoparticle modified, rubber-microparticle modified and hybrid modified epoxy resins, were used in the present study. The concentration of the modifier in the epoxy polymer was calculated as the percentage weight (wt%) of the total mixture:

$$wt\% = \frac{W_{\text{modifier}}}{W_{\text{modifier}} + W_{\text{epoxy}} + W_{\text{hardener}}} \times 100\% \tag{3.1}$$

where W_{modifier} is the weight of the modifier in the mixture (i.e. silica-nanoparticles and/or rubber-microparticles), W_{epoxy} is the weight of the epoxy in the mixture and W_{hardener} is the weight of the hardener in the mixture.

Table 3.1 shows the different formulations used in the present study and the terminology used.

Table 3.1: Percentage weight of silica-nanoparticles and rubber-microparticles in different epoxy formulations

Formulation name	Silica-nanoparticle	CTBN rubber-microparticle
	wt%	wt%
Si0R0	0	0
Si10R0	10	0
Si0R9	0	9
Si10R9	10	9

3.2.3.1 *Silica-nanoparticle Modification*

The surface modified silica-nanoparticles were in the form of a dispersion of silica-nanoparticles with a silica-nanoparticle concentration of 40 wt% in a DGEBA epoxy resin

(EEW = 295 g/eq), 'Nanopox F400', supplied by Nanoresins, Germany. The silica-nanoparticles have a very narrow particle-size distribution with a defined size of 20 nm [127], see Figure 3.1. Due to the small size and agglomerate-free properties of the silica-nanoparticle, the very low viscosity of the mixture (even at a concentration of 40 wt%), the modified resin can easily penetrate the fibre structure of the FRPs. This results in a well-dispersed and uniform particle distribution in the resin matrix and the FRPs [127], see Figure 3.2.

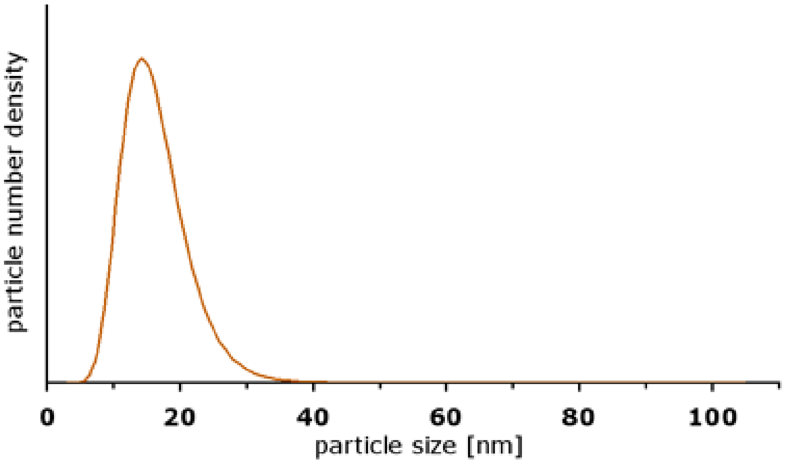

Figure 3.1: The particle number density vs the particle size for the silica-nanoparticles [127]

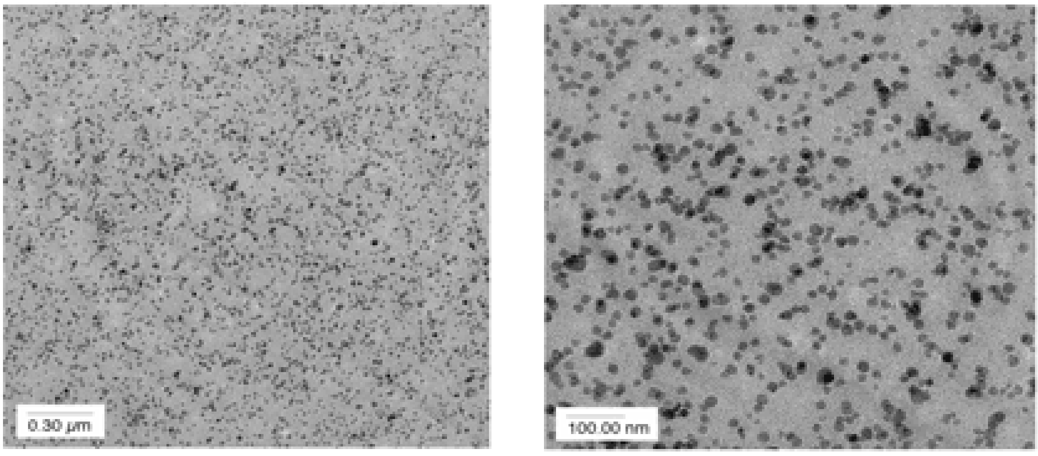

Figure 3.2: TEM images of a cured Nanopox® sample with 5 wt% Silica-nanoparticles (Si5R0) [127]

3.2.3.2 *Rubber-microparticle Modification*

The reactive liquid rubber was based on a carboxyl-terminated butadiene-acrylonitrile (CTBN) rubber and was obtained as a CTBN-epoxy adduct with a rubber concentration of 40 wt% in a DGEBA epoxy resin (EEW = 330 g/eq), 'Albipox 1000', supplied by Nanoresins, Germany. The CTBN rubber was 'Hycar 1300 x 8' from 'Emerald Performance Materials', USA and was initially dissolved and pre-reacted in the epoxy resin as an adduct. During the curing process, the rubber-microparticle modified epoxy adduct underwent phase-separation of the CTBN via a nucleation and growth process to form spherical CTBN rubber-microparticles [105].

Figure 3.3 shows the particulate phase of the CTBN rubber particles that formed during the curing schedule where nucleation was visible at 50 mins into the curing cycle and maximum phase separation occurred at vitrification (i.e. the transformation of a viscous liquid into the glass state) after 70 minutes (at 150^{0}C) [105].

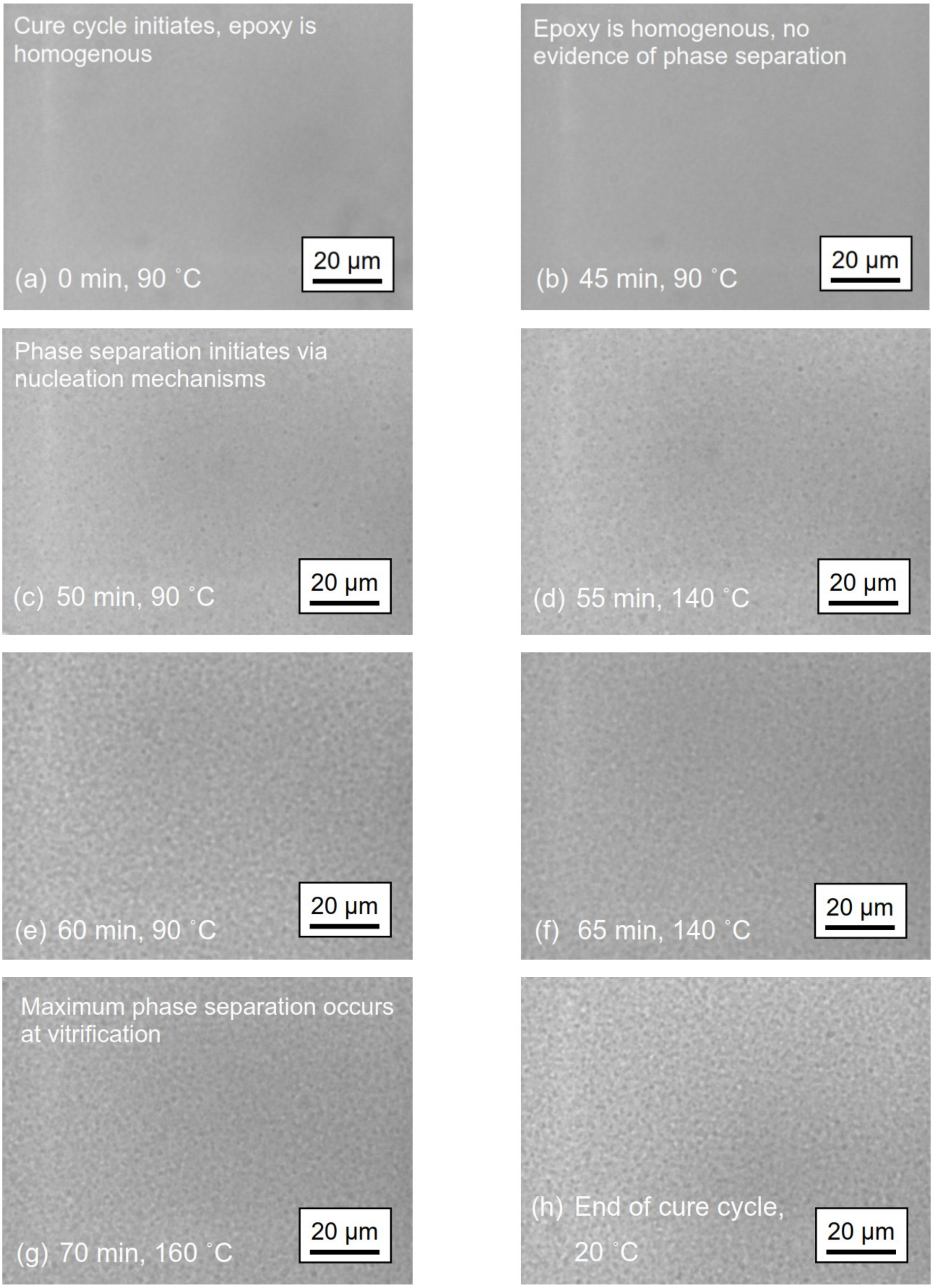

Figure 3.3: Optical images of a sample of 9 wt% CTBN rubber modified (Si0R9) DGEBA polymer during curing showing how the morphology of the rubber modified epoxy varies with respect to temperature and time [105]

3.2.3.3 *Morphology of Modified Epoxy Polymers*

The morphology of the different modified epoxy resins after curing at 100°C for 2 hours followed by a 150°C post-cure for 10 hours was studied using atomic force microscopy (AFM). This was done to check the dispersion of the silica-nanoparticles and CTBN rubber-microparticles as well as the homogeneous nature of the polymer by recording the oscillating signal of the cantilever when in contact with the sample surfaces. Height and phase images were then obtained.

Figure 3.4 to Figure 3.7 show AFM height and phase images of the cured unmodified (Si0R0) epoxy polymer, 10 wt% silica-nanoparticle modified (Si10R0) epoxy polymer, 9 wt% CTBN rubber-microparticle modified (Si0R9) epoxy polymer and hybrid modified (Si10R9) epoxy polymer (10 wt% silica-nanoparticle + 9 wt% CTBN rubber-microparticle) respectively. Well-dispersed silica-nanoparticle and rubber-microparticle phases were obtained in the Si10R0 epoxy polymer and Si0R9 epoxy polymer, see Figure 3.5 and Figure 3.6. However, agglomeration of the silica-nanoparticles was found to occur in the Si10R9 epoxy polymer with a well-dispersed rubber-microparticle phase, see Figure 3.7 [14]. In fact, the reasons for agglomeration of the silica-nanoparticles are not known when rubber-microparticle phase is present [14].

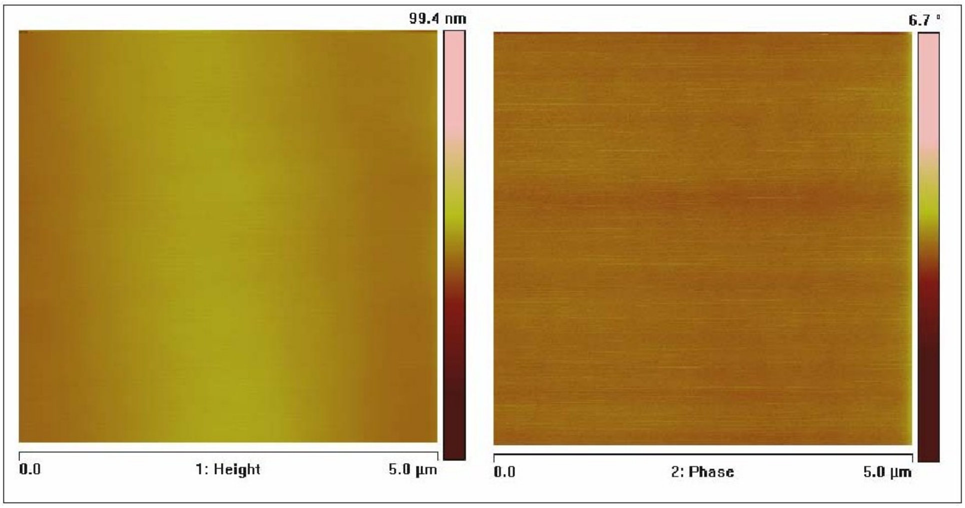

Figure 3.4: AFM images of the cured unmodified (Si0R0) epoxy polymer [14]

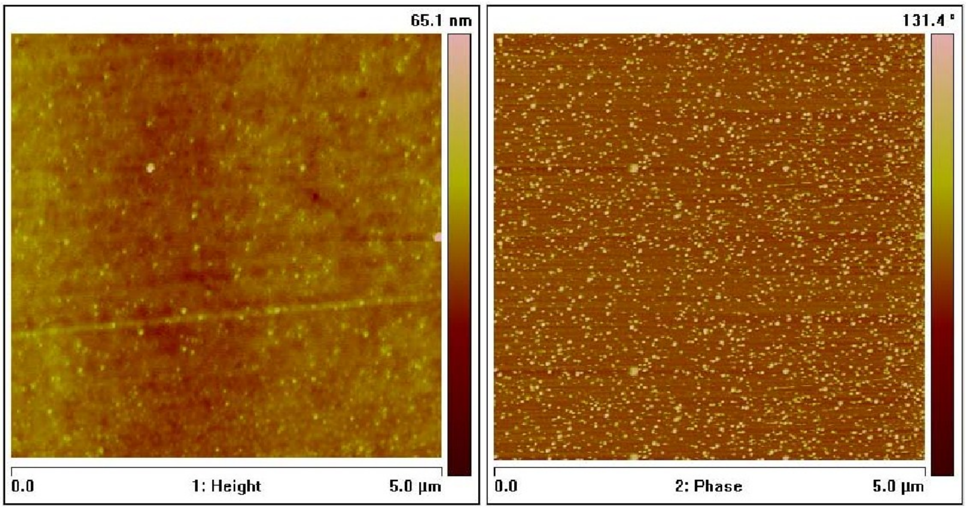

Figure 3.5: AFM images of the 10 wt% silica-nanoparticle modified (Si10R0) epoxy polymer [14]

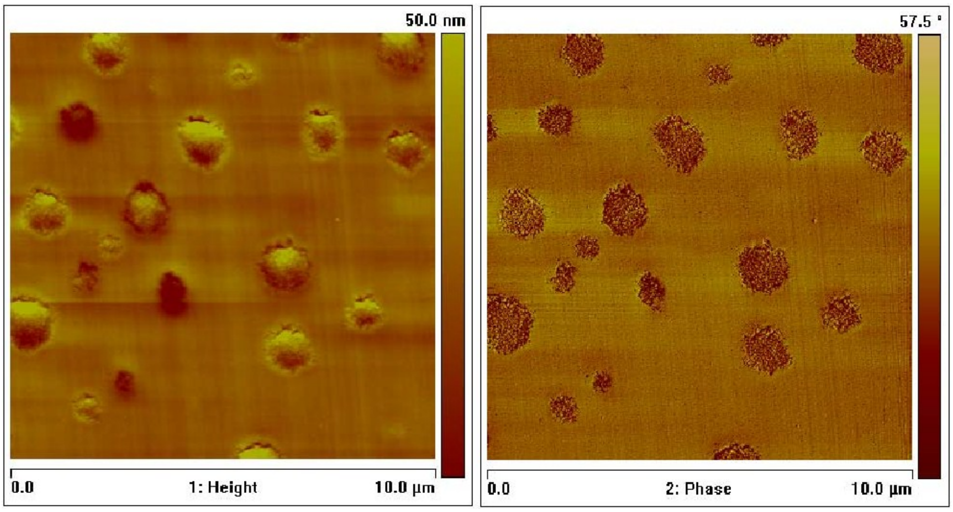

Figure 3.6: AFM images of the 9 wt% CTBN rubber-microparticle modified (Si0R9) epoxy polymer [14]

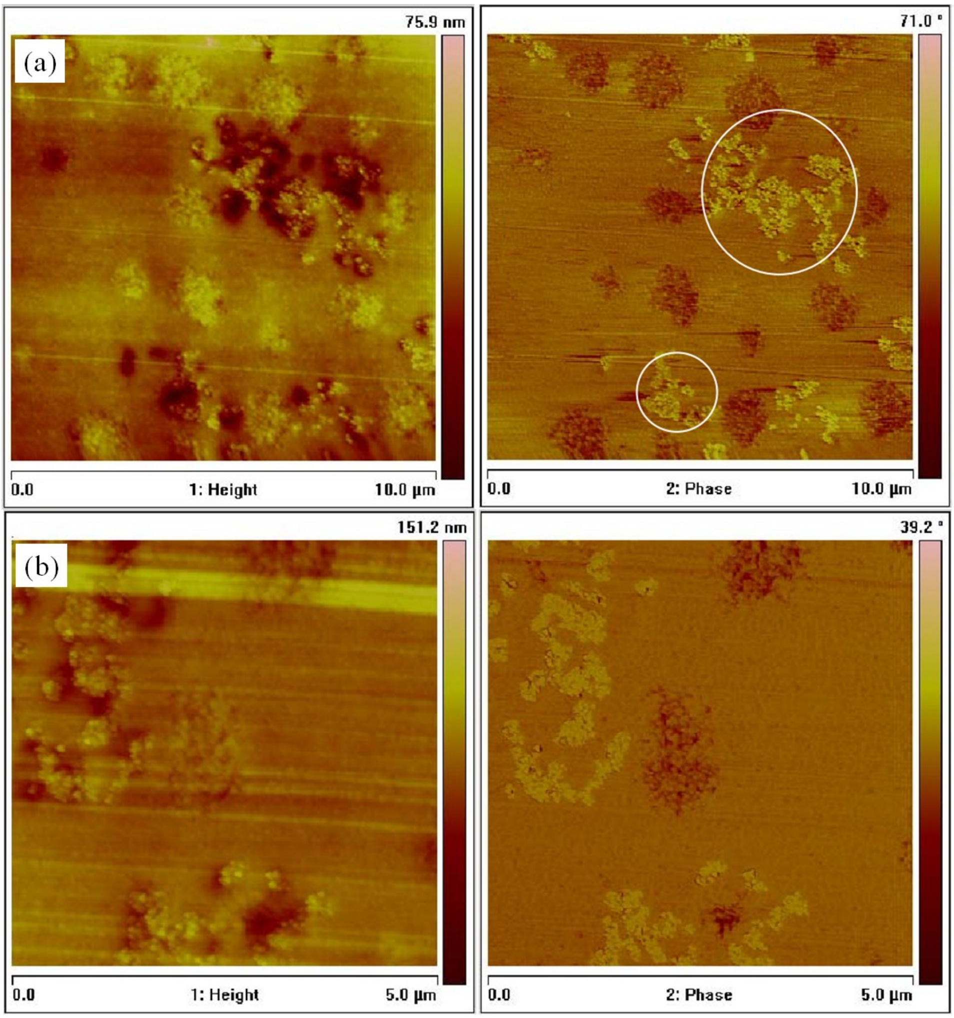

Figure 3.7: AFM images of the hybrid modified (Si10R9) epoxy polymer (10 wt% silica-nanoparticle + 9 wt% CTBN rubber-microparticle) in different scanning size: (a) 10 µm square and (b) 5 µm square showing silica-nanoparticle agglomerates as circled [14]

3.2.4 Properties of Epoxy Polymers

The general mechanical properties of the different formulations of the unmodified and modified epoxy polymers used in the present study are summarized in Table 3.2.

Table 3.2: Mechanical properties of unmodified/modified epoxy polymers [14]

Formulation	E (GPa)	K_{IC} (MPa·m$^{1/2}$)	G_{IC} (J/m^2)
Si0R0	2.90±0.09	0.69±0.03	133±8
Si10R0	3.28±0.08	0.81±0.09	191±21
Si0R9	2.31±0.04	1.41±0.04	697±28
Si10R9	2.74±0.05	2.28±0.05	1059±34

It was found that modifying the epoxy polymer with silica-nanoparticles alone slightly improved the Young's modulus and fracture energy. Addition of rubber-microparticles to the epoxy polymer slightly reduced the Young's modulus, while significantly improving the fracture energy. The hybrid modified epoxy polymer showed an improvement of the fracture energy as a contribution from silica-nanoparticles and rubber-microparticles with a slight decrease in the Young's modulus. With the hybrid system, there is a much higher concentration of modifiers which may contribute to the improvement of the fracture energy, see Table 3.2.

3.3 Fibre Reinforcements

3.3.1 Introduction

This section describes in detail the different reinforcements used in the present study which included flax fibre, regenerated cellulose fibre and glass fibre. Their general properties are also discussed.

3.3.2 Reinforcements

Different types and architectures of reinforcements used in the present study are summarized in Table 3.3.

Table 3.3: Different types and architectures of reinforcements used in the present study

Fibre type*	Fibre architecture*	Planar density (GSM)	Supplier
Flax fibre[41]	Unidirectional	275	Composites Evolution, UK
Cellulose fibre[38]	Plain-woven	210	Porcher Industries, France
Glass fibre[128]	Unidirectional	500	SP Systems, UK
Glass fibre[129]	Plain-woven	86	SP Systems, UK
Glass fibre[130]	Twill 2x2	165	SP Systems, UK

*Detailed descriptions of different fibre types and architectures can be found in 'Appendix I'

3.3.2.1 *Flax Fibre*

The flax fibre used in the present study was in the form of continuous spun yarns from short interlocked fibres woven into fabrics [4]. The weaving architecture of flax fibre used in the present study was unidirectional, see Figure 3.8.

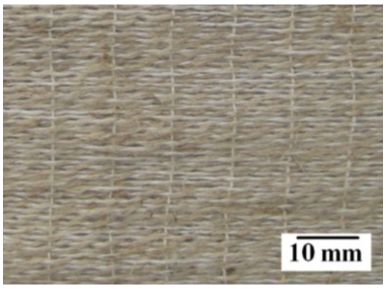

Figure 3.8: Unidirectional flax fibre used in the present study [41]

3.3.2.2 *Cellulose Fibre*

The regenerated cellulose fibre used in the present study was a continuous and non-twisted pure cellulose fibre in a plain-woven architecture [38], Figure 3.9.

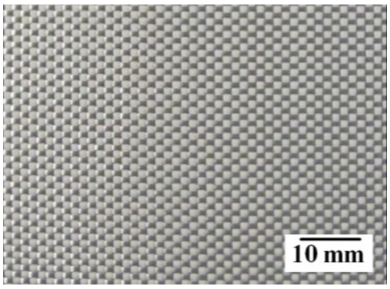

Figure 3.9: Plain-woven cellulose fibre used in the present study [38]

3.3.2.3 *Glass Fibre*

Three different weaving architectures of glass fibre, namely unidirectional, plain-woven and twill 2x2 fabrics, were used in the present study in order to fabricate the composite samples/specimens that would match the weaving architectures of the NFRPs, see 'Appendix I'.

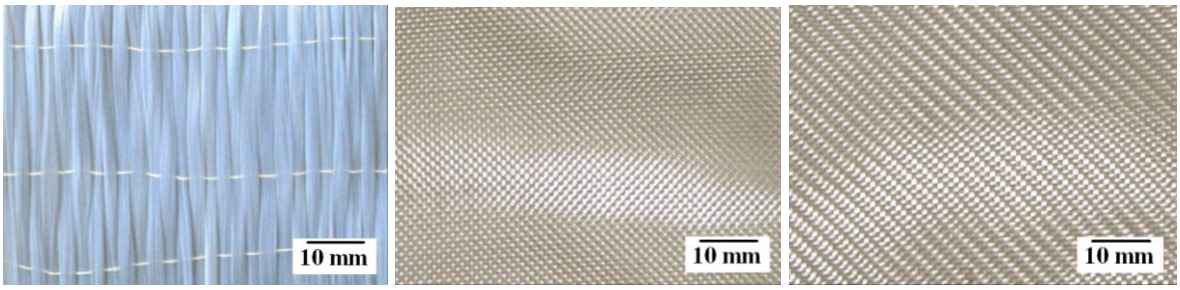

Figure 3.10: Glass fibre used in the present study: unidirectional fabric (left) [128], plain-woven fabric (middle) [129] and twill 2x2 fabric (right) [130]

3.3.3 **Properties of Reinforcements**

Table 3.4 shows the mechanical properties of reinforcements used in the present study.

Table 3.4: Typical properties of reinforcements used in the present study

Reinforcement	**Density, ρ (g/cm^3)***	**Moisture Content, v_w (wt%)***	**Tensile Strength, σ_{tf} (MPa)**	**Young's Modulus, E (GPa)**	**Specific modulus (10^6 m^{2}s^{-2})**	**Failure Strain, ε_t (%)**
Flax fibre (as-received)[41]	1.586	8.6±1.6	500	50	33	2.0
Flax fibre (VD-50C/6hr)[41] ^	1.592	7.7±1.0				
Flax fibre (OD-50C/4hr)[41] †	1.622	3.3±1.6				
Flax fibre (OD-75C/12hr)[41] **	1.638	<1.0				
Cellulose fibre (as-received)[38]	1.604	10.0±3.2	675	35	21-23	6.2
Cellulose fibre (OD-50C/4hr)[38] †	1.652	3.0±1.3				
Cellulose fibre (OD-75C/12hr)[38] **	1.673	<1.0				
E-glass[40]	2.627	nil	3445	72.3	28	4.8

*Values measured in the present study
^VD-50C/6hr = vacuum dry at 50°C for 6 hours in RIFT vacuum bagging.
†OD-50C/4hr = fan-oven dry at 50°C for 4 hours.
**OD-75C/12hr = fan-oven dry at 75°C for 12 hours.

It was found that the NFs had high moisture contents, while a negligible moisture content was found in GFs. NFs have lower tensile strength and Young's modulus than those of GFs but due to a significantly lower density of the NFs, the specific modulus values of NFs are comparable to that of GFs. As may be seen from Table 3.4, moisture has little effect on the general mechanical properties. However, whether the moisture content in the NFs significantly affects the toughness, G_{IC}, of the NFRPs will be a major consideration of the present research.

Figure 3.11 shows the relationship of the moisture content reduction and the drying condition for the FFs used in the present study.

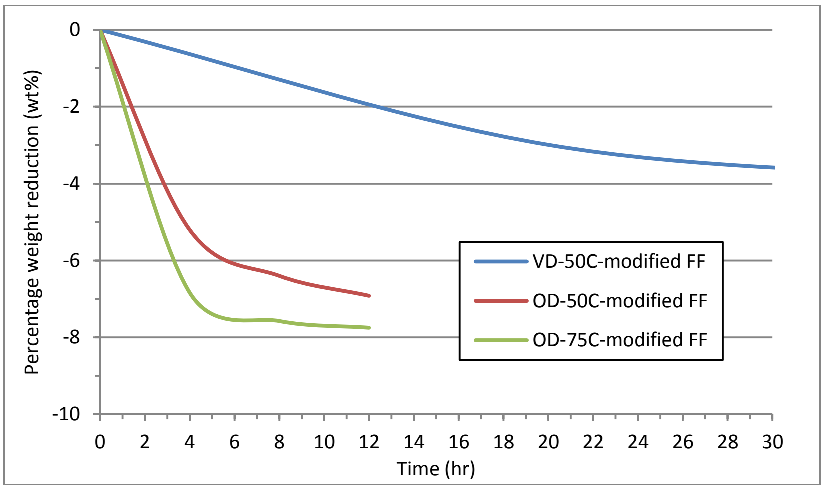

Figure 3.11: Typical moisture reduction vs drying condition of FFs used in the present study

From Figure 3.11, it was found that drying the FFs under the vacuum did not result in a significant reduction of the moisture content, while drying the FFs in the fan-oven yielded a more significant reduction of the moisture content. Increasing the temperature from 50°C to 75°C improved the moisture removal rate. At 75°C, the moisture content in the NFs reduced upon drying in the fan-oven and started to level off at a moisture content of below 1 wt% after 12 hours. The same outcome was obtained for the CeFs.

3.4 Concluding Remarks

The present chapter has presented the details of the materials used in the present study including the different formulations of epoxy polymers, modifiers and fibre reinforcements. This has included the general properties and mechanical properties of the materials.

In the next chapter, the experimental aspects will be discussed. These include the pre- and post-processing characterisation techniques, the mechanical test techniques and the imaging techniques.

CHAPTER 4 EXPERIMENTAL METHODS

4.1 Introduction

The present chapter describes the experimental methods used to investigate the pre-processing and post-processing material characteristics and properties.

4.2 Characterisation Techniques

4.2.1 Fibre Compaction Tests

4.2.1.1 *Background*

As the resin transfer moulding (RTM) process utilized the 2-part closed mould process, where the cavity thickness was fixed, it was necessary to determine 1) the minimum number of layers of reinforcement to be pre-laid within the mould cavity to avoid preform movement during resin injection, and 2) the clamp load required to contain the system to obtain the required fibre volume fraction. The different types of reinforcements were tested using a fibre compaction test to determine the number of layers required, and the necessary holding pressure to achieve the required thickness of the FRP sample and the required fibre volume fraction.

4.2.1.2 *Test Procedures*

A parallel plate compression test was conducted on an increasing number of layers of reinforcement, using a loading rate of 0.5 mm/min and an Instron 4505 universal testing machine with an Instron 100 kN load cell, see Figure 4.1, to obtain the load-displacement curve. The tests were undertaken from a thickness of approximately 1 mm up to 6 mm under a load of up to 25 kN.

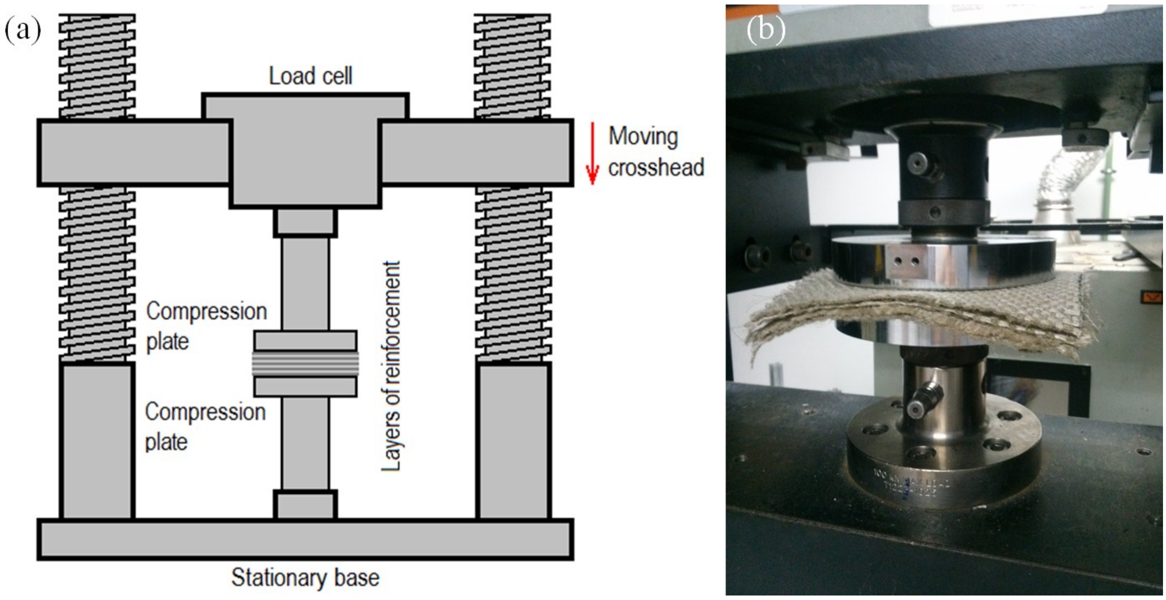

Figure 4.1: (a) Fibre compaction diagram (redrawn from [131]) and (b) test set-up

4.2.1.3 *Data Processing*

The value of the load at a particular thickness from the load-displacement curves (load-thickness curves) was used to calculate the mould clamp load. The mould clamp load was equivalent to the combined value of the resin hydrostatic pressure and the load needed to maintain the required thickness. For further details, see ‘Appendix V’.

4.2.1.4 *Calculations*

The total RTM mould clamp load, F_{RTM}, equals the safety factor, sf, multiplied by the combination of the RTM mould clamp load required to maintain the fibre thickness, $F_{f,RTM}$, and the RTM mould clamp load required to counteract the resin hydrostatic pressure, $F_{m,RTM}$, is given by:

$$F_{RTM} = \left(F_{f,RTM} + F_{m,RTM}\right) \times \mathrm{sf} \tag{4.1}$$

where:

$$F_{f,RTM} = F_{f,CT} \frac{A_{RTM}}{A_{CT}} \tag{4.2}$$

and:

$$F_{m,RTM} = A_{RTM} \sigma_{m,RTM} \tag{4.3}$$

where $F_{f,CT}$ is the load required to maintain the fibre thickness from the compaction test, A_{RTM} is the cross-sectional area of the fibre pre-laid in the RTM mould (with a size of 305 mm x 215 mm), A_{CT} is the cross-sectional area of the circular parallel compression plates (with a diameter of 150 mm) and $\sigma_{m.RTM}$ is the resin hydrostatic pressure in the RTM process (i.e. 0.4 MPa).

4.2.2 **Rheological Tests**

4.2.2.1 *Background*

It was important to measure the deformation of the matrix under the influence of the imposed stress by analysing the rheological behaviour of the matrix materials, since the flow characteristics of the epoxy matrices greatly influence the processing characteristics of the FRPs [132].

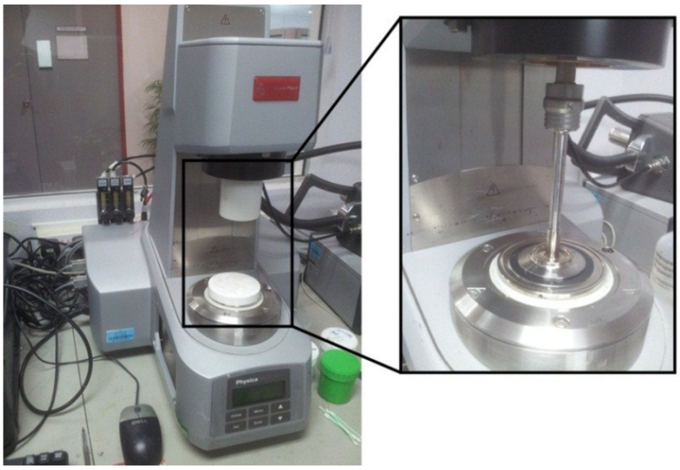

Figure 4.2: Rheometry test equipment

4.2.2.2 *Test Procedures*

Rheological tests were conducted prior to the manufacturing of the FRPs to study the viscosity of the different epoxy resins employed in the present study as a function of shear rate, time and temperature in order to optimize the injection/infusion parameters. The following standards were employed: ASTM D4440-08 [133] and ASTM D4473-08 [134]. A 'MCR-301' rheometer from Anton Paar, Austria was used together with a measuring tool with a diameter of 50 mm, a concentricity = ±10 µm, a parallelity = ±4 µm, an angle = 0.995° and a truncation of 55 µm, see Figure 4.2. The temperature was controlled using a built-in heater and a 'Lauda Ecoline Star Edition RE 204' external water cooling system from LAUDA-Brinkmann, USA. The tests were conducted at a gap of 0.5 mm using the rotational mode.

4.2.2.3 *Data Processing*

The relationship between viscosity, shear rate, shear stress, time and temperature was analysed in order to ensure the processability of all the different types of epoxy matrices under all the processing conditions.

4.2.3 **Differential Scanning Calorimetry**

4.2.3.1 *Background*

Differential scanning calorimetry (DSC) is a thermoanalytical technique in which the difference in the amount of heat required to equally increase the temperature of a test sample and a reference sample, as a function of increasing test temperature, is measured. The reference sample has a well-defined heat capacity over the range of temperatures to be scanned. At the glass transition temperature of the test sample, a change in the heat required to increase the temperature of the test sample can be identified.

4.2.3.2 *Test Procedures*

The DSC tests were conducted using 'DSC Q200' equipment from TA Instruments, USA, see Figure 4.3, in accordance with ASTM E1356-08 [135]. The tests were carried out on materials that had been dried at 75°C for 12 hours (to remove the moisture, as the properties of the materials may be affected by the moisture content) then cut and weighed. The samples were loaded into an aluminium container with an initial sample weight of 2.5-5 mg and the tests were conducted at a heating rate of 20°C/min from 30°C to 250°C with a nitrogen flow rate of 50 ml/min for two cycles. The first cycle was to erase the temperature history of the materials and the second cycle was to measure accurately the glass transition temperature. Samples from different locations on the composite panels were chosen and tested in order to assess the quality and manufacturing consistency of the composites, see Figure 4.4.

Figure 4.3: Differential scanning calorimeter apparatus

4.2.3.3 *Data Processing*

The DSC curves were analysed using the 'Universal Analysis 2000' software in order to determine the glass transition temperature. Two or three runs from each location were performed to determine the reproducibility of the glass transition temperature measurement. The typical standard deviation of the glass transition temperature was found to be below 3°C for all materials.

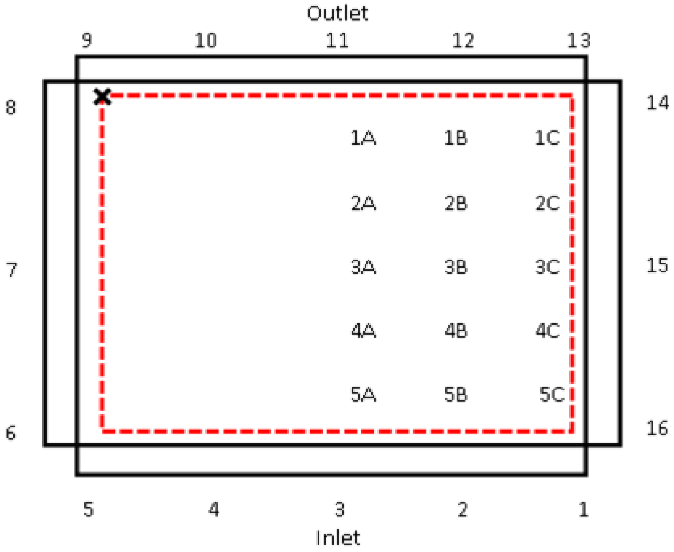

Figure 4.4: Sampling locations throughout the composite panels for DSC and TGA tests (location 1-16 are fibre-free regions and location 1A-5C are composite regions)

4.2.4 Thermogravimetric Analysis

4.2.4.1 *Background*

Thermogravimetric analysis (TGA) is a thermal analysis method where changes in the physical/chemical properties are measured as a function of increasing temperature and time [136]. It is commonly used to determine the characteristics of materials that exhibit mass loss or gain due to decomposition, oxidation, or loss of volatiles as well as to determine the moisture content within the materials. It may also be used to ascertain the residual content after burn-off of the glass fibre reinforcement or the silica-nanoparticles.

4.2.4.2 *Test Procedures*

The TGA tests were conducted using 'TGA Q500' equipment from TA Instruments, USA, see Figure 4.5, in accordance with ASTM E2550-11 [137]. The tests were carried out on materials that had been dried at 75°C for 12 hours (to remove the moisture as the properties of the materials may be affected by the moisture content) then cut and weighed. The samples were loaded in a standard open sample pan of 11 mm in diameter and 1.5 mm deep with an initial sample weight of 15-20 mg. The tests were conducted in a pure air stream at a flow rate of 60 ml/min at a heating rate of 10°C/min from 30°C up to 800°C.

Figure 4.5: Thermogravimetric analysis apparatus

4.2.4.3 *Data Processing*

The thermogravimetric (TG) weight loss curve and the time-derivative thermogravimetric (DTG) weight loss curve obtained were analysed using the 'Universal Analysis 2000' software that assessed the degradation temperature, degradation mechanism and patterns that occurred during thermal decomposition of constitutive materials of the sample with increase in temperature. To assess the quality and manufacturing consistency of the composites, e.g. uniformity of the distribution and concentration of silica-nanoparticles, the composite was sampled from various locations for testing, see Figure 4.4. Two to three specimens from each location were tested to determine the consistency. The distribution of silica-nanoparticles was found to be uniform throughout the composite panels with the typical standard deviation of the silica weight content lying within 0.5 wt% for all composite systems.

4.2.5 **Pycnometer Tests**

4.2.5.1 *Background*

A gas pycnometer is an equipment used to determine the density of solids [138][139]. A gas pycnometer can be used with ceramics, catalysts, cements, nuclear fuels, petrochemicals, soils, fertilizers, carbon blacks, charcoals, fibres, minerals, pharmaceuticals and powdered cosmetics [139]. The apparatus consists of a pair of tanks with the same volume that supply gas to the measuring and reference containers. The difference in pressure between the measuring and reference containers is calculated, which provides the variation of the volume of the gas between the two containers. The volume of the sample can then be determined [138].

4.2.5.2 *Test Procedures*

The determination of the density was conducted in accordance with ASTM D2320-98 (2012) [140] using an 'AccuPyc II 1340' gas pycnometer from Micromeritics, USA, see Figure 4.6. The materials were dried at 75°C for 12 hours (to remove the moisture, as the properties of the materials may be affected by the moisture content) then cut and weighed. The samples were placed in the container to approximately fill 40-60% of the cylindrical container, which had a cell volume of 11.1410 cm^3 and an expansion volume of 9.2406 cm^3. The tests were conducted using pure Helium at a temperature of 25°C and at a rate of 0.0050 psig/min.

Figure 4.6: Pycnometer apparatus

4.2.5.3 *Data Processing*

The apparatus measures the volume of the sample and then converts the volume into density, using the input weight, to a resolution of 10^{-4} g/cm^3. Ten cycles of volume measurement were carried out to obtain accurate results. The standard deviation was calculated. The typical standard deviation of the density was found to be below 1% for all composite systems.

4.2.5.4 *Calculations*

The fibre volume fraction could be then calculated from the measured densities of the composite, reinforcement and cured matrix. The typical standard deviation of the fibre volume fraction was between 1-4% for all the composite systems. The fibre volume fraction is given by:

$$v_f = \left(\rho_c - \rho_m\right) / \left(\rho_f - \rho_m\right) \tag{4.4}$$

where v_f is the fibre volume fraction (neglecting the effect of any voids), ρ_c is the density of the composite, ρ_m is the density of the matrix and ρ_f is the density of the reinforcement.

4.3 Fibre Surface Treatment

4.3.1 Plasma Treatment

4.3.1.1 *Background*

There are several different types of low temperature plasma methods available based on their working pressure, see Table 4.1. During plasma treatment, the surface of the fibres is bombarded with ions, electrons, radicals, neutrals and UV radiation from the plasma [141]. As a result, a large variety of outcomes can be achieved. Different gases can also be used to introduce different types of surface chemistry.

Table 4.1: Different types of low temperature plasmas and their operating pressures [88]

Plasma type	**Operating pressure**			
	kPa	Torr (mmHg)	Atmospheric (atm)	Bar
Vacuum (low pressure)	0-0.29	0-2.175	0-0.003	0-0.0029
Vacuum (medium pressure)	0.3-7	2.25-52.5	0.003-0.069	0.003-0.07
Atmospheric pressure	101.3	760	1	1.103

4.3.1.2 *Procedures*

The plasma treatment used in the present study was conducted using a ‘Pico Version D’ low pressure plasma treatment apparatus from Diener, Germany, see Figure 4.7. The NF fabric was placed on a grid inside the treatment chamber to allow the treatment of both sides of the fabric. The NF fabric was treated with oxygen plasma at 50% power for 5 mins [142]. The treated NF fabric was then immediately processed using the RIFT manufacturing method, in order to avoid contamination of the treated surface.

Figure 4.7: Plasma treatment apparatus

4.4 Mechanical Properties

4.4.1 The Mode I Interlaminar Fracture Toughness Test

4.4.1.1 *Test Procedures*

The fracture toughness tests were conducted using double cantilever beam (DCB) specimens in accordance with ASTM D5528-13 [143] and the corrected beam theory (CBT) analysis was employed to calculate the mode I fracture energy, G_{IC}, of the composites. The tests were undertaken at a testing speed of 1 mm/min using an Instron 5584 universal testing machine with an Instron 5 kN load cell. The test set-up is shown in Figure 4.8.

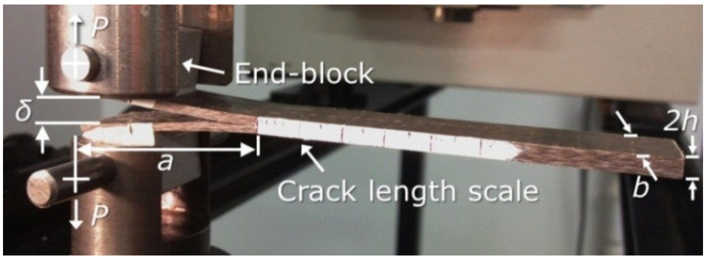

Figure 4.8: DCB interlaminar fracture toughness test set-up

The 150 mm x 20 mm DCB specimens were cut from the fabricated composite panels. Along the first 50 mm length of the specimens, a polytetrafluoroethylene (PTFE) film had been inserted between the middle plies of the fibre stack prior to resin injection/infusion, to serve as a pre-crack. The pre-cracked ends of the specimens were adhesively-bonded to aluminium end blocks and painted with a thin layer of typewriter erasing liquid on one side of the specimen, see Figure 4.8. A crack length scale was drawn at 2 mm intervals on the white surface to allow the visual measurement of crack growth during the test, aided by a low power travelling optical microscope, see Figure 4.9. The actual specimen geometry is given in Table 4.2.

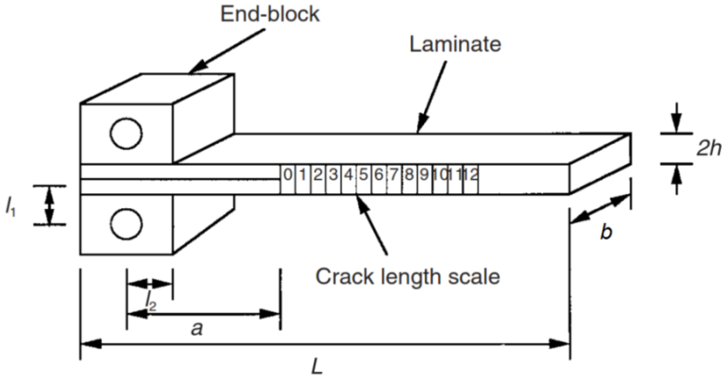

Figure 4.9: DCB interlaminar fracture toughness test method [22]

Table 4.2: DCB specimen geometry

Parameter	Dimension
Specimen length, L	150 mm
Specimen width, b	20 mm
Specimen thickness, $2h$	2.6-5.6 mm*
Distance of the load point above the beam axis, l_1	9.6-10.6 mm
Distance of the load point along the beam axis, l_2	10 mm
Initial crack length, a_0	40 mm

*Thickness varies accordingly to the materials and processing methods used.

The composite specimens were stored in sealed plastic bags with desiccant at room temperature then, prior to testing, the specimens were conditioned by heating at 75°C for 12 hours. The specimens were then allowed to cool to room temperature for up to about 4 hours before they were tested, as the properties of the materials may have been affected by the moisture content. For each test, the specimen was loaded until a sharp natural crack was formed beyond the inserted PTFE film. This was done in order to be able to determine the true crack initiation value of the fracture energy. The specimen was unloaded and reloaded. The specimen was then continuously loaded and values of the crack length and the associated load-displacement data were collected. After up to 50 mm of crack growth, the specimen was unloaded and the displacement offset at zero-load upon unloading was also recorded, as required by the ASTM standard. The typical number of replicate tests was five.

4.4.1.2 *Calculations*

From the ASTM standard [143], the following equations are given to determine the various parameters.

Mode I interlaminar fracture energy

$$G_{IC} = (\frac{F}{N})\frac{3P\delta}{2b(a+|\Delta|)} \tag{4.5}$$

where P is the applied load, δ is the displacement, b is the width of the specimen, a is the crack length, Δ is the effective delamination extension to correct for rotation at the delamination front, F is the large displacement correction factor and N is the loading block correction factor.

Flexural elastic modulus

$$E_{1flex} = \frac{64(a+|\Delta|)^3 P}{\delta b h^3} \tag{4.6}$$

where h is the half-thickness of the specimen.

Large displacement correction factor

$$F = 1-\theta_1\left(\frac{\delta}{L}\right)^2 - \theta_2\left(\frac{\delta l_1}{L}\right)^2 \tag{4.7}$$

where L is the length of the specimen, l_1 is the distance of the load point above the beam axis, which is defined in Figure 4.9, and:

$$\theta_1 = \frac{3}{10} and \quad \theta_2 = \frac{3}{2} \tag{4.8}$$

Loading block correction factor

$$N = 1-\theta_3\left(\frac{l_2}{L}\right)^3 - \theta_4\left(\frac{\delta l_1}{L^2}\right) - \theta_5\left(\frac{\delta}{L}\right)^2 \tag{4.9}$$

where l_2 is half the width of the loading block, which is shown in Figure 4.9, and:

$$\theta_3 = 1, \quad \theta_4 = \frac{9}{8}\left(1-\left(\frac{l_2}{a}\right)^2\right) \text{ and } \theta_5 = \frac{9}{35} \tag{4.10}$$

4.4.2 The Flexural Test

4.4.2.1 *Test Procedures*

Three-point flexural tests were conducted in accordance with ASTM D790-10 [144] to determine the flexural modulus, E_{flex}, of the composites, incorporating the European Standard Integrity Society (ESIS) proposal for a multi-span 3-point flexural test method with a multi-span calibration [142] in order to eliminate the shear effect, see 'Appendix II'. The tests were conducted using an Instron 5584 universal testing machine with an Instron 5 kN load cell on the 200 mm x 15 mm specimens that had been cut from the fabricated composite panels. The testing speed, R_s, was calculated to give a strain rate of 1% per min. The test set-up is shown in Figure 4.10. The composite specimens were stored in sealed plastic bags with desiccant at room temperature then, prior to testing, the specimens were conditioned by heating at 75°C for

12 hours. The specimens were then allowed to cool to room temperature for up to about 4 hours before they were tested. The typical number of replicate tests was four.

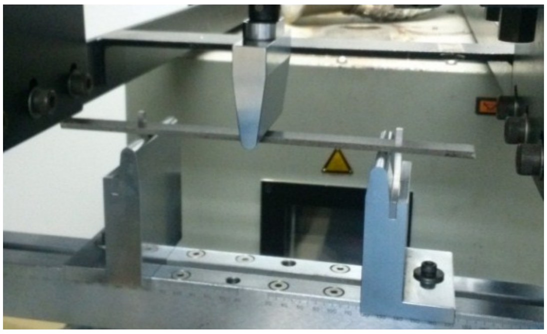

Figure 4.10: Three-point flexural test set-up

4.4.2.2 *Calculations*

Testing speed

$$R_s = \frac{\varepsilon' S^2}{6h} \tag{4.11}$$

where ε' is the strain rate (1% per min), S is the support span and h is the specimen thickness

Normal stress under 3-point flexural test

$$\sigma = \frac{3PS}{2bh^2} \tag{4.12}$$

where σ is the normal stress on the outer surfaces of the specimen, P is the applied load and b is the specimen width where the material properties are assumed to be uniform throughout the thickness [22].

The flexural modulus from the 3-point test is specified as follows [22]:

Flexural modulus

$$E_{flex} = \frac{S^3 m}{4bh^3} \tag{4.13}$$

where m is the slope of the tangent to the initial straight-line portion of the load-deflection curve. However, due to large deflections of the beam, ASTM gives a correction to the stress equation. The following equation shows this correction to the stress equation.

Corrected normal stress under 3-point flexural test

$$\sigma = \frac{3PS}{2bh^2}\left(1 + \frac{6D^2}{S^2} - \frac{4hD}{S^2}\right) \tag{4.14}$$

where D is the mid-point deflection of the beam.

4.4.3 **The Tensile Test**

4.4.3.1 *Test Procedures*

The tests were conducted in accordance with ASTM D3039/D3039M-08 [145], see Figure 4.11 for the test diagram and test set-up. The composite specimens were stored in sealed plastic bags with desiccant at room temperature then, prior to testing, the specimens were conditioned by heating at 75°C for 12 hours. The specimens were then allowed to cool to room temperature for up to about 4 hours before they were tested. The tests were undertaken at a rate of 1 mm/min using an Instron 5585H universal testing machine with an Instron 250 kN load cell. The force and displacement were recorded.

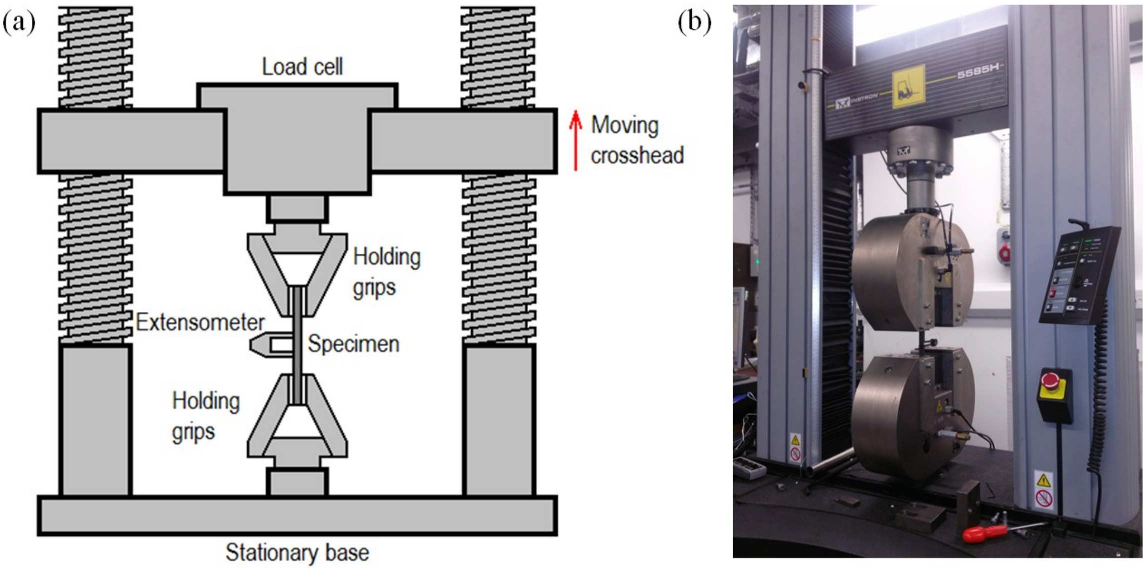

Figure 4.11: (a) Tensile test diagram (redrawn from [131]) and (b) tensile test set-up

The specimens were cut from the fabricated composite panels into the recommended configurations, see Figure 4.12. The specimens were attached with an extensometer for recording the displacement. The specimens had GFRP end-tabs bonded onto both ends to give uniform load distribution and to promote failure in the loading-direction. The typical number of replicate tests was four. The actual specimen geometry is given in Table 4.3.

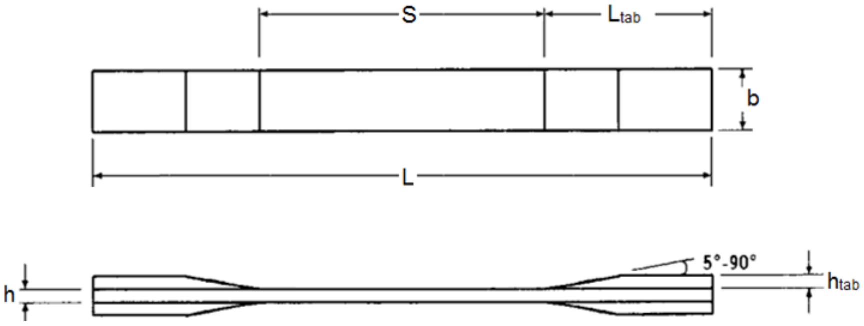

Figure 4.12: Tensile test specimen [145]

Table 4.3: Tensile specimen geometry

Parameter	Dimension
Specimen length, L	200 mm
Specimen width, b	15 mm
Specimen thickness, h	2.6-5.6 mm*
Gauge length, S	100 mm
Tab length, L_{tab}	50 mm
Tab thickness, h_{tab}	4 mm
Tab bevel angle	90°

*Thickness varies accordingly to the materials and processing methods used.

4.4.3.2 ***Calculations***

Ultimate tensile strength

$$\sigma_{UT} = P_{\max} / bh \tag{4.15}$$

where $P_{\max}$ is the maximum load before failure, b is the specimen width and h is the specimen thickness.

Tensile modulus

$$E_t = \Delta\sigma / \Delta\varepsilon \tag{4.16}$$

where E_t is the tensile modulus of elasticity, $\Delta\sigma$ is the difference in applied tensile stress between the two strain points and $\Delta\varepsilon$ is the difference between the two strain points within the elastic region.

4.5 Imaging Studies

4.5.1 **Optical Microscopy**

A cured transparent epoxy polymer block made using 'Araldite 2020' from Huntsman, UK, with the samples for study embedded into it was prepared by polishing with a 'LaboPol-21' grinding machine from Struers, Denmark using progressively finer grades of emery paper at intervals of 240, 800, 1200, 2500 and 4000 grit. This resulted in a grinding smoothness equivalent to 3 μm at the final stage, see Figure 4.13a. For the samples to be examined at high magnification, additional polishing was performed using 1 μm diamond polishing solutions on a 'Multicloth M' polishing cloth from Metprep, UK. An 'AXIO Scope' optical microscope (OM) from Carl Zeiss, Germany, see Figure 4.13b, was used to obtain the bright field reflected light microscopy images which could be used to assess the quality of the composite, e.g. void content determination. The method for determining the void content is discussed in 'Appendix III'.

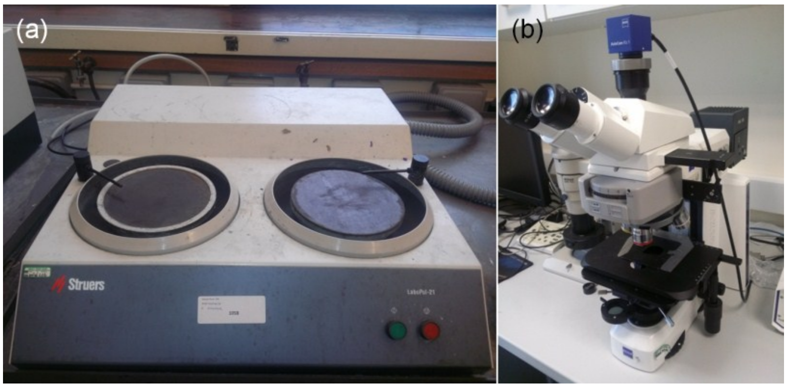

Figure 4.13: (a) Grinding machine and (b) optical microscope

4.5.2 **Scanning Electron Microscopy**

The fracture surfaces of the mode I interlaminar fracture samples were inspected using either a Hitachi S-3400N scanning electron microscope (SEM) or a high resolution 'LEO Gemini 1525' field emission gun scanning electron microscope (FEG-SEM) from Carl Zeiss, Germany, see Figure 4.14b. Specimens were cut from the tested specimens using a diamond cutting machine and were mounted onto a SEM sample stub using carbon conductive adhesive tabs. They were then coated with chromium (a chromium target was set at 120 mA for 60 sec to give an approximately 20 nm thick chromium coating) using a 'Quorum Q150T S' turbo-pumped chromium sputter coating machine from Quorum Technologies, UK to obtain a conductive sample, see Figure 4.14a. Conductive silver paint was also used to make a conductivity link from the surface of the sample to the sample stub. These precautions made the samples being examined in the FEG-SEM less likely to charge during imaging.

Figure 4.14: (a) Chromium sputter coating machine and (b) FEG-SEM

4.5.3 Atomic Force Microscopy

An atomic force microscope (AFM) was used to inspect the morphology of the particle modified FRPs. Sample preparation involved microtoming the surfaces of the samples using a 'PowerTome XL' ultramicrotome from RMC Products, USA to give very smooth surfaces, see Figure 4.15a. A tapping mode scan of the surfaces of the samples was conducted using a 'Multi-Mode 8' scanning probe microscope from Veeco, USA with a silicon probe that had a 5 nm-diameter tip, see Figure 4.15b. The height and phase images were captured at a 512 × 512 pixel resolution at a scanning rate of 1 Hz, and the image analysis was conducted using the 'NanoScope IV' software.

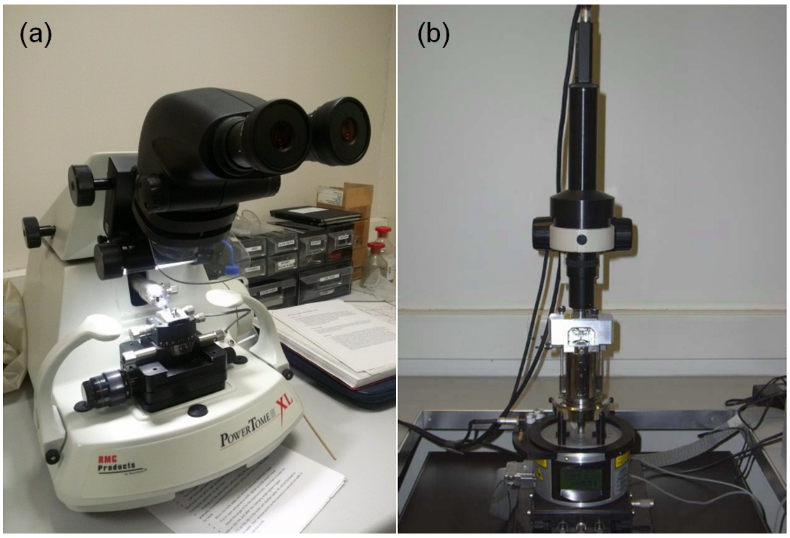

Figure 4.15: (a) Ultramicrotome and (b) atomic force microscope

4.6 Concluding Remarks

The present chapter has discussed the details of the experimental methods used to characterize the different fibre-reinforced composites examined in the present study.

The next part of the present thesis will discuss the manufacturing methods studied, which include the resin infusion under flexible tooling (RIFT) and the resin transfer moulding (RTM) methods. The results from the pre-processing characterisation of the fibres and the epoxy matrix polymers, and those from post-processing characterisation of the composites, using the experimental methods described in the present chapter will also be discussed.

RESULTS AND DISCUSSIONS - PART I: MANUFACTURING ASPECTS

Two manufacturing techniques were involved in the present study: 1) a resin infusion under flexible tooling (RIFT) process, see ‘Chapter 5’, and 2) a resin transfer moulding (RTM) process, see ‘Chapter 6’. These two techniques share similar principles whereby resin is drawn by an applied vacuum or injected by an applied pressure, respectively, into pre-laid reinforcement within the vacuum bagging or mould cavity. Once the epoxy matrix is cured and post-cured, the composite part is then removed. These two manufacturing processes may, however, yield significantly different composite properties.

The present study mainly aimed to optimize the two processes and improve the fracture toughness of the composites, as well as compare the flexural modulus, tensile properties and related properties of the NFRPs manufactured by these two processes.

The study began by conducting an initial examination of the RIFT process to determine the feasibility by employing different FRPs and to better understand the effect of changes in the RIFT manufacturing process on their properties and characteristics. The RIFT-processed NFRPs were initially found to have a relatively poor fracture toughness caused by poor interfacial adhesion between the epoxy polymer and the NFs. The RTM process was then employed and found to significantly improve the fracture toughness of the NFRPs. Optimization of the RIFT process was then carried out to eliminate the compatibility issues and to enhance the fracture toughness of the NFRPs. The present part discusses the two processes, namely the RIFT and the RTM processes, in detail.

The key manufacturing differences of these two processes are presented in Table P.1.

Table P.1: Summary of key manufacturing differences between RIFT and RTM processes

	RIFT process	RTM process
Injection/Infusion	- Vacuum-aided infusion (-0.1 MPa)*	- Injection under high pressure (0.4 MPa)
Tooling	- 1-sided open mould with flexible vacuum bagging on the other side	- 2-piece closed fixed-cavity mould
Component produced	- Thickness varies (due to history of local pressure and flow front) - One-sided smooth surface	- Consistent thickness (due to fixed cavity mould) - Two-sided smooth surfaces

*Relative pressure to atmospheric pressure

CHAPTER 5 THE RIFT METHOD

5.1 Introduction

The present chapter describes the method of resin infusion under flexible tooling (RIFT) that was employed, including the different stages of optimization and the post-processing characteristics and properties of the RIFT-processed FRPs.

5.2 The RIFT Process

A stack of fibre/fabric was pre-laid in between the top and bottom pre-laid-up consumable stacks, see Figure 5.1. The fibre/fabric stack contained a 50 mm wide polytetrafluoroethylene (PTFE) film with a thickness of 10 μm inserted along one side in between the middle layers of the fibre/fabric stack to act as a pre-crack in the DCB specimens for the mode I fracture toughness test. The bagged complete stack was vacuum sealed using high temperature sticky tape with the outlet connected to the vacuum pump and with the inlet connected to the resin container through a valve. Once the bagged stack was fully vacuumed (i.e. a pressure of approximately -0.1 MPa relative to atmospheric pressure), the valve was opened to allow the resin to infuse into the reinforcement stack of fibre/fabric until the resin fully wetted the reinforcement. The inlet was then closed to stop further infusion. The temperature was automatically controlled for curing under the vacuum to promote compaction and consolidation. The fabricated FRPs were then cut into specimens using either a wet diamond-saw machine (for the GFRPs) or a laser cutting machine to avoid contact with moisture (for the NFRPs). Finally, the specimens were dried at 75°C for 12 hours before testing.

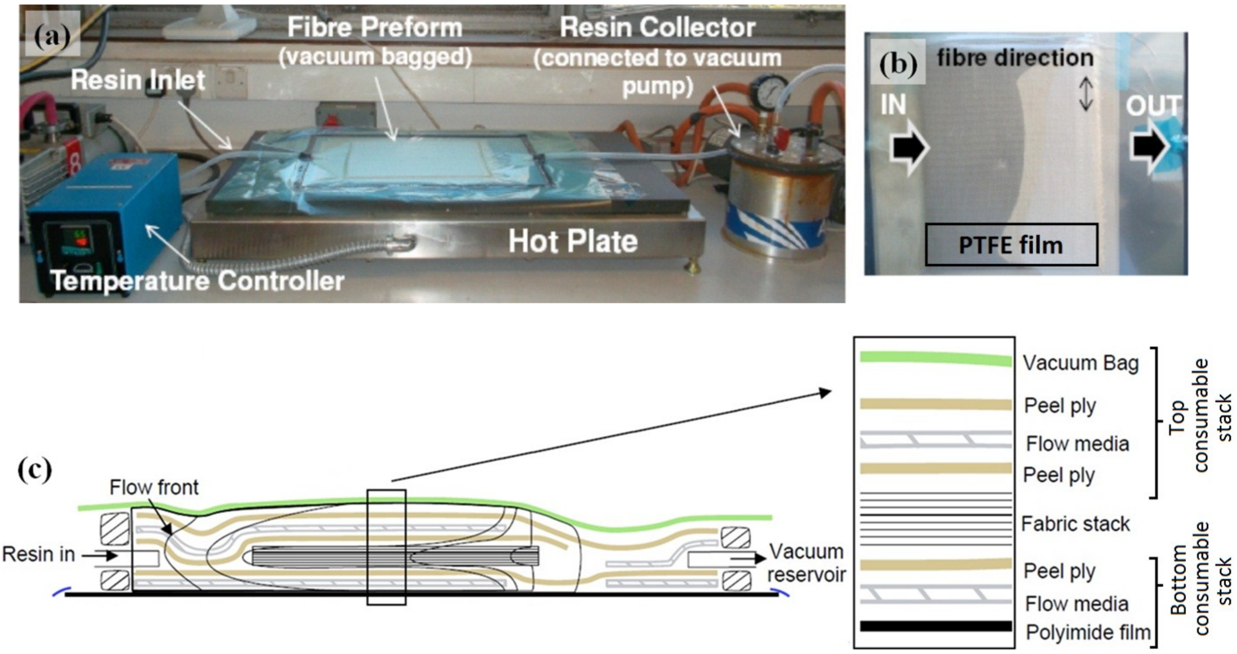

Figure 5.1: RIFT process: (a) set-up, (b) top view and (c) schematic [105] of side-view, through thickness of mid-plane and flow front of the resin

5.3 Optimization of RIFT Process

5.3.1 Introduction

As the mechanical properties of the NFRPs were found to be greatly affected by the manufacturing routes, three stages of RIFT process optimization, namely an initial study, an optimization study and a final study, were investigated.

5.3.2 RIFT Process – Initial Study

The initial study of the RIFT process was aimed at studying the feasibility of the RIFT process settings which had been used by Hsieh [14] for manufacturing the hybrid modified (Si10R9) epoxy polymers with carbon and glass fibre as the reinforcements. These initial settings were employed to manufacture the silica-nanoparticle and CTBN rubber-microparticle modified FRPs with NFs (e.g. FFs and CeFs) and GF as the reinforcements.

This initial process involved infusing the resin at 50°C then curing at 100°C for 2 hours, followed by a post-cure at 150°C for 10 hours. Finally, the cured panel was cooled down to room temperature, see Table 5.1.

Table 5.1: Summary of RIFT process settings in the initial study

Resin & fibre preparation	
- Mixing	50°C for 15 mins stir*
- Degassing	50°C for 20 mins under vacuum*
- Fibre conditioning	50°C for 30 mins under vacuum
Resin injection	
- Resin & mould temperature	50°C
- Flow rate	5-15 cc/min^
- Packing pressure	Vacuum (-0.1 MPa)†
Cure	
- Heating rate	5°C/min
- Cure conditions	100°C for 2 hrs under vacuum
Post-cure	
- Heating rate	1°C/min
- Post cure conditions	150°C for 10 hrs under atmospheric pressure

*Due to the limitation of equipment, mixing and degassing must be carried out separately.
^Flow rate is largely dependent on the resin viscosity, fibre architecture, stacking sequence and orientation, fibre packing, local pressure, etc.
†Relative pressure to atmospheric pressure.

The number of layers of the fibre/fabric reinforcements was calculated under the assumption that all the reinforcements would pack equivalently within the vacuum bagging and give an equivalent fibre volume fraction (a value of v_f of 0.35 was aimed for). Hence, all the composite panels manufactured would have a similar thickness of approximately 4 mm. The estimated total thickness of the composite panels can be calculated from:

$$t_c^T = \frac{\sum \rho_f^A}{\rho_f v_f} \tag{5.1}$$

where $\sum \rho_f^A$ is the total density per unit area of the fibre/fabric stack, ρ_f is the density of the fibre (density of as-received fibre was used) and v_f is the fibre volume fraction (note that the actual thickness of composite plates with different reinforcements varied as the fibre volume fraction varied). Table 5.2 shows the properties of the different composite systems manufactured in this initial study of the RIFT process.

Table 5.2: Summary of properties of the different composite panels manufactured in the initial RIFT process

Matrix formulation*	Fibre type and architecture^	Stacking sequence	Total thickness, t_c^T (mm)	Target fibre volume fraction, v_f
Si0R0 Si10R0 Si0R9 Si10R9	Unidirectional Flax (FF-UD)	$(0)_8$	3.96	0.35
	Plain-woven Cellulose (CeF-PW)	$(0)_{10}$	3.74	0.35
	Unidirectional Glass (GF-UD)	$(0)_8$	4.35	0.35
	Plain-woven and Twill 2x2 Glass (GF-PW+T)†	$[(0_T)_{10}(0_{PW})_2]_s$	3.96	0.35

*For each fibre type and architecture, all four matrix formulations were used.

^For further details, see 'Appendix I'.

†As the only balanced plain-woven glass fibre (balanced ratio of warp to weft yarns) was available in a very low density per unit area (GSM), in order to match the balanced plain-woven cellulose fibre, the balanced twill 2x2 glass fibre backing was added to the stacking sequence of plain-woven glass fibre. This minimally affected the mechanical properties of the GFRPs while having fewer numbers of layers for ease of manufacturing. Hence, the direct comparison between the CeFRPs-PW and GFRPs-PW+T could be made.

As can be seen from Table 5.2, the number of layers in the stacks of the different initial RIFT-processed FRPs can be calculated (note that the actual fibre volume fraction and the thickness of the different initial RIFT-processed FRPs, which varied, are shown later in Table 5.6 in section '5.4').

5.3.3 **RIFT Process – Optimization Study**

Due to the compatibility issues between the NFs and epoxy polymers, which resulted in poor interfacial adhesion between the fibres and the matrix, air voids were introduced in the above initial study of the RIFT manufacturing process. As a result, the RIFT-processed NFRPs possessed poor fracture toughness, as will be shown later in Table 8.1 in section '8.2.1'. However, the RTM-processed NFRPs did not have a problem with the interfacial adhesion between the fibres and the matrix while possessing significantly higher fracture toughness, as will be shown later in section '8.2.4'. Thus, an optimization study of the RIFT process was undertaken, which was aimed at enhancing the compatibility between the NFs and the matrix, using unidirectional flax fibre (FF-UD) with a $(0)_8$ stacking sequence and an unmodified (Si0R0) epoxy polymer matrix.

The optimization process again involved infusing the resin at 50°C then curing at 100°C for 2 hours, followed by a post-cure at 150°C for 10 hours. Finally, the composite panel was cooled down to room temperature. However, three different manufacturing options were attempted: 1) drying the fibres in a fan-oven at 75°C for 12 hours (OD); 2) O_2 plasma treatment of the fibres at 50% power for 5 minutes (OP); and 3) drying the fibres under vacuum in the RIFT-vacuum bagging at 50°C for 6 hours (VD), see Table 5.3. The properties of RIFT-processed NFRPs from the optimization study are presented later in Table 5.7 in section '5.4'.

Table 5.3: Summary of RIFT process settings in the optimization study

Resin & fibre preparation	
- Mixing	50°C for 15 mins stir*
- Degassing	50°C for 20 mins under vacuum*
- Fibre pre-processing	1) 75°C for 12 hrs fan-oven dry (OD) 2) 50% power for 5 mins O_2 plasma treatment (OP)
- Fibre conditioning	3) 50°C for 6 hrs vacuum dry (VD)
Resin injection	
- Resin & mould temperature	50°C
- Flow rate	5-15 cc/min^
- Packing pressure	Vacuum (-0.1 MPa)†
Cure	
- Heating rate	5°C/min
- Cure conditions	100°C for 2 hrs under vacuum
Post-cure	
- Heating rate	1°C/min
- Post cure conditions	150°C for 10 hrs under atmospheric pressure

*Due to the limitation of equipment, mixing and degassing must be carried out separately.

^Flow rate is largely dependent on the resin viscosity, fibre architecture, stacking sequence and orientation, fibre packing, local pressure, etc.

†Relative pressure to atmospheric pressure.

5.3.4 RIFT Process – Final Study

From the section ‘5.3.3’ above, the best method to improve the fracture toughness, see Table 8.2 in section ’8.2.2’, was found to be drying the NFs in a fan-oven at 75°C for 12 hours (OD). Thus, this optimization was selected as the final RIFT process. This final study of the RIFT process involved the manufacture of FFRPs and CeFRPs with unmodified (Si0R0), silica-nanoparticle modified (Si10R0), rubber-microparticle modified (Si0R9) and hybrid modified (Si10R9) epoxy polymers and it involved infusing the resin at 50°C then again curing at 100°C for 2 hours, followed by a post-cure at 150°C for 10 hours. Finally, the composite panel was cooled down to room temperature, see Table 5.4.

Table 5.4: Summary of RIFT process settings in the final study

Resin & fibre preparation	
- Mixing	50°C for 15 mins stir*
- Degassing	50°C for 20 mins under vacuum*
- Fibre pre-processing	75°C for 12 hrs fan-oven dry (OD)
- Fibre conditioning	50°C for 30 mins under vacuum
Resin injection	
- Resin & mould temperature	50°C
- Flow rate	5-15 cc/min^
- Packing pressure	Vacuum (-0.1 MPa)†
Cure	
- Heating rate	5°C/min
- Cure conditions	100°C for 2 hrs under vacuum
Post-cure	
- Heating rate	1°C/min
- Post cure conditions	150°C for 10 hrs under atmospheric pressure

*Due to the limitation of equipment, mixing and degassing must be carried out separately

^Flow rate is largely dependent on the resin viscosity, fibre architecture, stacking sequence and orientation, fibre packing, local pressure, etc.

†Relative pressure to atmospheric pressure.

The summary of estimated properties the different composite panels manufactured in the final RIFT process is shown in Table 5.5.

Table 5.5: Summary of estimated properties of the different composite panels manufactured in the final RIFT process

Matrix formulation*	Fibre type and architecture^	Stacking sequence	Total thickness, t_c^T (mm)†	Target fibre volume fraction, v_f**
Si0R0 Si10R0 Si0R9 Si10R9	Unidirectional flax fibre (FF-UD)	$[(0)_{4GF}(0)_{2FF}]_s$^^	3.95	0.38
	Plain-woven cellulose fibre (CeF-PW)	$[(0)_{4GF}(0)_{4CeF}]_s$^^	4.03	0.54

*For each fibre type and architecture, all four matrix formulations were used.

^For further details, see 'Appendix I'.

†Thickness obtained from the fibre compaction test results at 2 kN load over the area equivalent to the parallel compression plates used in the fibre compaction test: 0.1 MPa from the vacuum pressure plus 10% extra from the RIFT equipment loads (the absolute vacuum had been assumed achievable by the RIFT process resulting in a relative pressure of 0.1 MPa over the area of 18,000 mm^2 or the load of 1.8 kN (cross-sectional area of the parallel compression plates), see section '4.2.1'.

**The estimated volume fraction of the NF in the NFRP regions in the glass-fibre backed NFRPs was calculated based on the fibre density after being fan-oven dried at 75°C for 12 hours using the total volume per unit area of certain stacking sequences (fibre volume fraction = total density per unit area/fibre density/thickness), see 'Appendix VI'.

^^Glass fibre backing was required in order to eliminate the plastic deformation and promote linear-elastic behaviour for LEFM assumption.

The properties of the RIFT-processed NFRPs from the final study are presented later in Table 5.8 in section '5.4'.

5.3.5 **Conclusions**

Details of the RIFT optimization processes have been discussed above. The post-processing characteristics and properties of the RIFT-processed FRPs are discussed as follow.

5.4 Post-Processing Properties and Characteristics of RIFT-processed FRPs

5.4.1 Introduction

Mechanical testing showed that the properties of the RIFT-processed GFRPs were comparable to those obtained from the RTM process but the mechanical properties of the RIFT-processed NFRPs from the initial study were far inferior to those manufactured using the RTM process. For example, the latter composites possessed up to three times lower flexural modulus and sixty times lower fracture energy. However, the fracture properties of the final RIFT-processed NFRPs were found to exceed those of the GFRPs, and even those of the RTM processed NFRPs, see ‘Chapter 7’ and ‘Chapter 8’.

The post-processing characterization was undertaken to evaluate the characteristics and properties of the composites, such as the density, fibre volume fraction, void content, glass transition temperature and silica-nanoparticle distribution. These properties were determined in order to assess the quality and manufacturing consistency of the composites, obtained from the different stages of the RIFT process optimization. This information assisted in interpreting the factors affecting the general mechanical and fracture properties.

5.4.2 Glass Transition Temperature, T_g

Each composite panel was tested to determine the glass transition temperature of the epoxy matrix. The glass transition temperature was measured as described in section ‘4.2.3’. The test was undertaken to ensure that the curing schedule used in the present study fully cured the epoxy resin. This test was also employed to ensure that each composite panel was cured sufficiently and uniformly and this was done by sampling from different locations from each composite panel.

5.4.3 Density, Fibre Volume Fraction and Void Content

The density, fibre volume fraction and void content of each composite panel were determined and calculated using the methods and calculations described in section ‘4.2.5’, ‘Appendix III’ and ‘Appendix VI’.

5.4.4 Silica-nanoparticle Content

The silica-nanoparticle content was determined by measuring the mass of the remaining substances after a burn-off technique described in section ‘4.2.4’. This test was employed to ensure a uniform distribution of silica-nanoparticles had been obtained from each composite panel.

5.4.5 RIFT Results

The properties of the RIFT-processed FRPs, including glass transition temperature, density, fibre volume fraction, void content and silica-nanoparticle content from the different stages of optimization are shown in Table 5.6 to Table 5.8.

Table 5.6: Summary of properties of the different composite panels manufactured in the initial RIFT process

Fibre type and architecture	Matrix formulation	Measured glass transition temperature, T_g (°C)	Estimated glass transition temperature, T_g (°C)*	Density, ρ (g/cm^3)	Fibre volume fraction, v_f	Void content, v_v (vol%)
Unidirectional Flax (FF-UD)	Si0R0	90	79	1.311	0.31	15
	Si10R0	94	66	1.321	0.23	13
	Si0R9	80	65	1.326	0.38	17
	Si10R9	83	59	1.328	0.33	16
Plain-woven Cellulose (CeF-PW)	Si0R0	79	71	-^	-^	14
	Si10R0	80	58	-^	-^	16
Unidirectional Glass (GF-UD)	Si0R0	146	141	2.068	0.61	2
	Si10R0	125	121	2.004	0.55	2
	Si0R9	123	120	2.118	0.65	2
	Si10R9	103	111	2.133	0.65	2
Plain-woven and Twill 2x2 Glass (GF-PW+T)	Si0R0	150	141	1.785	0.41	2
	Si10R0	127	121	1.774	0.38	2
	Si0R9	121	120	1.783	0.42	2
	Si10R9	107	111	1.839	0.44	2
Atmospheric-pressure cured (dry) bulk epoxy polymer†	Si0R0	141	-	-	-	-
	Si10R0	121	-	-	-	-
	Si0R9	120	-	-	-	-
	Si10R9	111	-	-	-	-

*Total dissolution of moisture from the fibres (i.e. 8.6 wt% for FFs, 10.0 wt% for CeFs and 0.0 wt% for GFs) into the atmospheric-pressure cured particle modified bulk epoxy polymer was assumed, see Table 3.4 for moisture content properties of the NFs. The glass transition temperature was estimated using the Fox equation described in 'Appendix IV'.

^Values could not be obtained due to the poor quality of the composites and the Si0R9 and Si10R9 CeFRPs could not be successfully manufactured.

†Glass transition temperatures for the different formulations of atmospheric-pressure cured (dry) bulk epoxy polymers cured under 100C-2h/150C-10h curing schedule (100°C for 2 hours followed by 150°C for 10 hours). See Table 6.1 for further details.

As may be seen from Table 5.6, the glass transition temperature was found to generally decrease when either silica-nanoparticles or rubber-microparticles were added. Addition of both types of particles further reduced the glass transition temperature. It was also found that the RIFT-processed NFRPs from the initial study possessed a relatively low glass transition temperature, low fibre volume fraction and high void content compared to those of the GFRPs.

According to Fox [147], the presence of a low molecular-weight diluent lowers the glass transition temperature of a polymer. Water dissolved in the epoxy polymer will have a similar effect. Hence, the decrease in glass transition temperature in the FFRPs and CeFRPs can be partially attributed to the dissolution of moisture from the NFs in the epoxy polymer. The estimated glass transition temperature of the bulk epoxy polymer with the complete dissolution of all moisture present in the fibres (i.e. 8.6 wt% for FFs and 10.0 wt% for CeFs) was found to be somewhat lower than the measured glass transition temperature of the NFRPs. This suggests that only a partial amount of moisture present in the NFs have entered the polymer matrix. The rest could have remained within the NFs or removed by vacuum during processing. Nevertheless, the decrease in the glass transition temperature of the matrices, as predicted using the Fox equation, confirms that the presence of the water molecules (adsorbed and absorbed by the NFs) dissolving during manufacture into the epoxy matrix may explain the observed decrease in the glass transition temperature values.

Furthermore, the combination of both the strongly polarized and hydrophilic NFs and the water trapped within the NFs may also result in poor fibre-matrix interfacial adhesion, and hence led to a large amount of voids in the NFRPs and a low fibre volume fraction of the NFRPs. This effect was also probably enhanced by the transformation of the water into steam at the high temperatures reached during curing. The relatively low glass transition temperature of the epoxy polymer matrix and the poor fibre-matrix interfacial adhesion, as a result of water dissolution from the NFs, will adversely affect both the general mechanical and fracture properties, see ‘Chapter 7’ and ‘Chapter 8’.

In the GFRPs, a relatively high fibre volume fraction and low void content were found. The glass transition temperature of the GFRPs was found to be consistent with the estimated values (no moisture dissolution in the matrix was assumed). This suggests that the dissolution of moisture in the epoxy polymers in the GFRPs was negligible.

The distribution of the silica-nanoparticles was found to be uniform throughout all the RIFT-processed composite panels with the typical standard deviation of the silica content being below 0.5 wt% for all the composite systems. However, the fibre volume fraction was found to vary considerably among the RIFT-processed FRPs with different formulations. This was probably due to the processing variability (dependent on resin flow front (viscosity dependency) and local pressure gradient) and the fibre orientation affecting the nesting conditions for different fibre types.

Attempts to enhance the compatibility between the NFs and the epoxy polymers in order to improve the mechanical properties, using different methods, were then carried out in the optimization study. A summary of the properties of the RIFT-processed FRPs from this optimization study is shown in Table 5.7.

Table 5.7: Summary of properties of the different composite panels manufactured in the optimization study of the RIFT process

Fibre type and architecture and matrix formulation	**Modification**	**Measured glass transition temperature, T_g (°C)**	**Estimated glass transition temperature, T_g (°C)***	**Density, ρ (g/cm^3)**	**Fibre volume fraction, v_f**	**Void content, v_v (vol%)**
Unidirectional flax fibre (FF-UD) - Si0R0	Initial study	90	79	1.311	0.31	15
	VD	99	85	1.318	0.32	13
	OP	87	71	1.325	0.34	12
	OD	126	133	1.364	0.44	1
Atmospheric-pressure cured (dry) bulk epoxy polymer^	-	141	-	-	-	nil

*Total dissolution of moisture from the NFs (i.e. 7.7 wt% for VD, 8.6 wt% for OP and 1 wt% for OD) into the atmospheric-pressure cured particle modified bulk epoxy polymer was assumed, see Table 3.4 for moisture content properties of the NFs. The glass transition temperature was estimated using the Fox equation described in ‘Appendix IV’.

^Glass transition temperatures for the atmospheric-pressure cured (dry) bulk Si0R0 epoxy polymer cured under 100C-2h/150C-10h curing schedule (100°C for 2 hours followed by 150°C for 10 hours). See Table 6.1 for details.

As may be seen from Table 5.7, the VD- and OP-modifications (drying under vacuum and treating with O_2 plasma treatment) did not yield significant effect on glass transition temperature, fibre volume fraction and void content. Although significantly improved values of the glass transition temperature, fibre volume fraction and void content were obtained by fan-oven drying the NFs (OD-modification), the glass transition temperature of the OD-modified FFRPs was found to be lower than the estimated value. This must have been due to the rapid moisture absorption of the FFs during their transportation from the oven to the RIFT equipment, which increased the moisture content in the FFs and as a result, more dissolution of water into the epoxy matrix.

Drying the NFs in a fan-oven at 75°C for 12 hours (OD-modification) was found to be the best method to improve the properties, as discussed in detail in 'Chapter 7' and 'Chapter 8'. Thus, this method of fibre preparation was selected for the final RIFT process. A summary of the general properties of the RIFT-processed FRPs from this final study is shown in Table 5.8.

Note: The moisture content in the NFs reduced upon drying in the fan-oven and started to level off at a moisture content of below 1 wt% after 12 hours at 75°C, see Figure 3.11.

Table 5.8: Summary of properties of the different composite panels manufactured in the final RIFT process

Fibre type and architecture	Matrix formulation	Measured glass transition temperature, T_g (°C)	Estimated glass transition temperature, T_g (°C)*	Density, ρ (g/cm^3)	Fibre volume fraction, v_f	Void content, v_v (vol%)
Unidirectional flax fibre (FF-UD)	Si0R0	126	133	1.364	0.44	1
	Si10R0	119	114	1.380	0.40	1
	Si0R9	107	113	1.317	0.36	1
	Si10R9	106	104	1.378	0.44	1
Plain-woven cellulose fibre (CeF-PW)	Si0R0	110	133	1.454	0.64	1
	Si10R0	99	114	1.486	0.67	1
	Si0R9	98	113	1.450	0.65	1
	Si10R9	94	104	1.477	0.67	1
Atmospheric-pressure cured (dry) bulk epoxy polymer^	Si0R0	141	-	-	-	nil
	Si10R0	121	-	-	-	nil
	Si0R9	120	-	-	-	nil
	Si10R9	111	-	-	-	nil

*Total dissolution of moisture from the NFs (i.e. 1 wt% for FFs and CeFs) into the atmospheric-pressure cured particle modified bulk epoxy polymer was assumed, see Table 3.4 for moisture content properties of the NFs. The glass transition temperature was estimated using the Fox equation described in 'Appendix IV'.

^Glass transition temperatures for the different formulations of atmospheric-pressure cured (dry) bulk epoxy polymers cured under 100C-2h/150C-10h curing schedule (100°C for 2 hours followed by 150°C for 10 hours). See Table 6.1 for further details.

Table 5.8 shows that the values of the glass transition temperature, density and fibre volume fraction were consistently higher for the final RIFT-processed NFRPs, compared to those from the initial study, see Table 5.6. Also, as therefore expected, Table 5.8 shows that the void content of the final RIFT-processed NFRPs was relatively low compared to those from the initial study, again see Table 5.6. This was probably due to the reduction of the moisture content (e.g. approximately 8-10 wt% moisture content of the NFs in the initial RIFT process vs approximately below 1 wt% moisture content of the NFs in the final RIFT process). A lower moisture content resulted in a lower void content and higher glass transition temperature, and vice versa. This was confirmed by the higher glass transition temperature of 126°C observed for the final RIFT-processed Si0R0 FFRP, which was a result of the reduction of water dissolution in the epoxy matrix [147], compared to the glass transition temperatures of 90°C observed for the initial RIFT-processed Si0R0 FFRP. However, as discussed above, it was noted from Table 5.8 that the values of the measured glass transition temperatures for the final RIFT-processed NFRPs were generally somewhat lower than the estimated values from the Fox equation [147]. It is suggested that this might arise from moisture absorption by the NFs during their transportation from the drying oven to the RIFT manufacturing equipment, which will lead to the measured values of the glass transition temperatures of the epoxy matrices indeed being somewhat lower than the estimated values. However, the glass transition temperature was still found to generally decrease when either silica-nanoparticles or rubber-microparticles were added. Addition of both types of particles further reduced the glass transition temperature.

Again, the distribution of the silica-nanoparticles was found to be uniform throughout all the RIFT-processed composite panels with the typical standard deviation of the silica content being below 0.5 wt% for all the composite systems. However, the fibre volume fraction was found to vary considerably among the RIFT-processed FRPs with different formulations. This was probably due to the processing variability (dependent on resin flow front (viscosity dependency) and local pressure gradient).

5.4.6 Morphology of Silica-nanoparticle and Rubber-microparticle Modified Fibre-reinforced Epoxy Polymers

The morphology of the RIFT-processed silica-nanoparticle and rubber-microparticle modified FRPs was studied using atomic force microscopy (AFM) to investigate the dispersion of these particles in the composite panels with different reinforcements, see section ‘4.5.3’.

The AFM images revealed that the morphology of the silica-nanoparticles and rubber-microparticles in the RIFT-processed FRPs with different types of reinforcements of the same matrix formulations were identical, regardless of the type of reinforcement used. For example, the Si10R9 FFRP showed identical morphology of particles to those of the Si10R9 CeFRPs and GFRP. Hence, only AFM images of the FRPs with different matrix formulations are shown in Figure 5.2.

Matrix formulation	Height image	Phase image
Si0R0	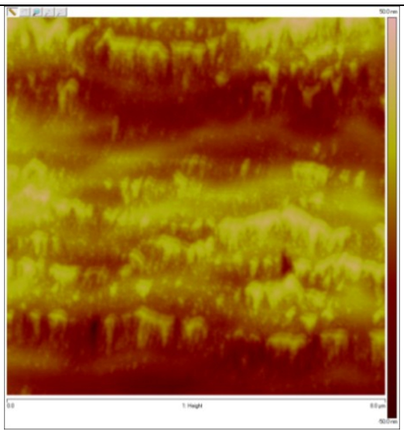	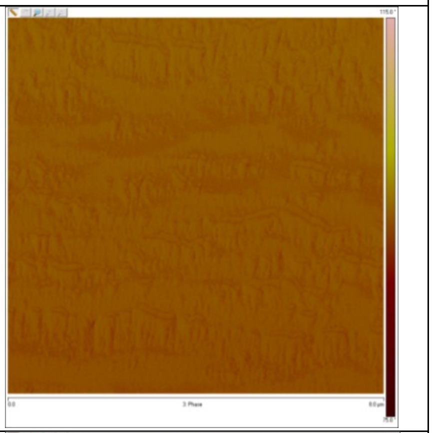
Si10R0	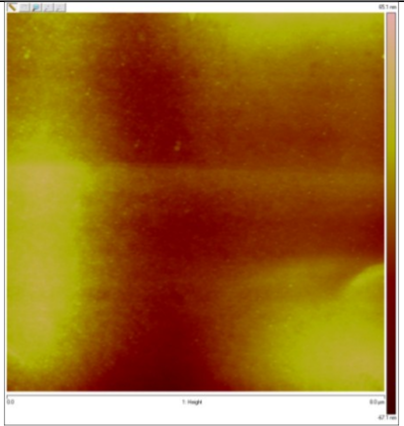	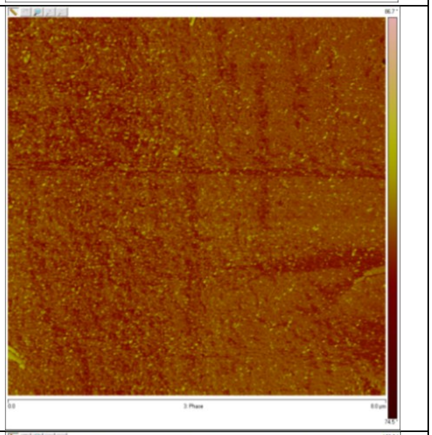
Si0R9	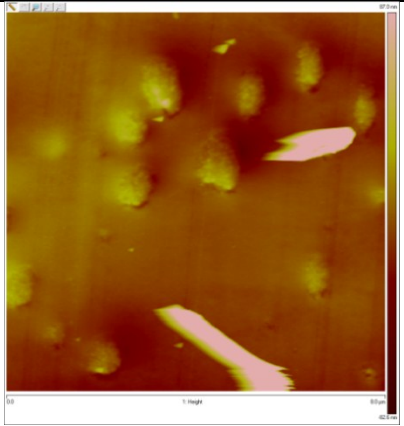	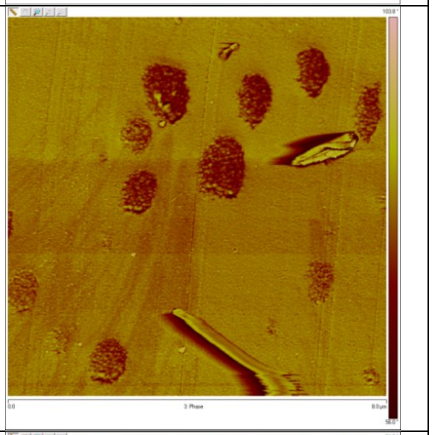
Si10R9	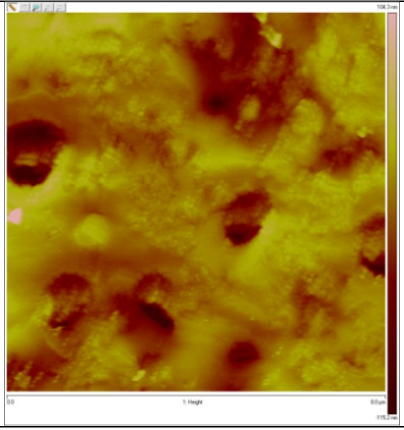	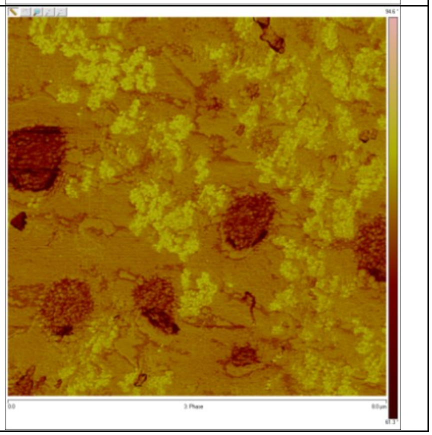

Figure 5.2: AFM images of different matrix formulations from the RIFT-processed FRPs (images are 10 μm wide)

The AFM phase image of the unmodified (Si0R0) FRPs revealed a relatively featureless microstructure that indicated a homogeneous microstructure. A uniform dispersion of silica-nanoparticles was observed in the silica-nanoparticle modified (Si10R0) FRPs, which indicated that the silica-nanoparticles could penetrate well in between the fibre reinforcements. The phase separable CTBN added to the rubber-microparticle modified (Si0R9) FRPs was also found to be well-dispersed. However, for the hybrid modified (Si10R9) FRPs, the rubber-microparticles were well dispersed but there was some degree of agglomeration of the silica-nanoparticles, as may be seen from Figure 5.2. This effect is similar to the finding from Hsieh et al. [56].

5.5 Concluding Remarks

The present chapter has described the resin infusion under flexible tooling (RIFT) processing method in detail. The main issues in the initial RIFT process that was employed were found to be: 1) the compatibility issue between the epoxy polymers and the water-attracting NFs, which resulted in poor interfacial adhesion between the matrix and the fibres, and introduced air voids; 2) the cure of the NFRPs under the applied vacuum which enlarged the voids of trapped air, and created a very large volume of air voids; and 3) the moisture from the NFs dissolving into the epoxy matrix and so reducing the glass transition temperature.

It was found that plasma surface treatment of the NFs did not significantly improve the fibre-matrix interfacial adhesion or the mechanical properties of the RIFT-processed NFRPs. Indeed, the key solution to improving the fibre-matrix interfacial adhesion, minimizing the moisture entrapped in the NFs and air voids and improving the mechanical properties of the RIFT-processed NFRPs was to pre-dry the NFs prior to using the RIFT manufacturing method.

The RTM process was also employed to manufacture the composite panels and this will be discussed in the next chapter.

CHAPTER 6 THE RTM METHOD

6.1 Introduction

The present chapter describes the resin transfer moulding (RTM) processing in detail, including the pre-processing characteristics and properties of the epoxy resins and the fibres, the RTM process and the post-processing characteristics and properties of the RTM-processed FRPs.

6.2 Pre-processing Characteristics – RTM Process

6.2.1 **Introduction**

Prior to manufacturing the composites using the RTM method, pre-processing characterization of the epoxy resins and fibres was necessary in order to evaluate the processability of the epoxy resins and the fibres. Also, it was necessary to assess their behaviour under various manufacturing conditions and study how these factors affected the properties of the composites.

6.2.2 **Pre-processing Properties and Characteristics of the Epoxy Resins – RTM Process**

6.2.2.1 ***Viscosity***

The different formulations of epoxy matrices were tested to determine their rheological properties, e.g. flow viscosity and gelation/curing characteristics, at different shear rates and temperatures. This was done in order to study the factors influencing the resin flow behaviour and the shear stress, and determine how the resins would flow, gel and cure during RTM manufacturing, see section ‘4.2.2’.

6.2.2.1.1 Shear Rate and Temperature Dependency

The effects of shear rate and temperature on the viscosity and shear stress were determined under shear rates that increased from 0.05 s^{-1} up to 5000 s^{-1} at three different temperatures: 25°C, 50°C and 75°C. This was done to ensure that the resins were injected under desirable conditions, i.e. where the viscosity was sufficiently low for injection. Figure 6.1 to Figure 6.4 show the effect of the shear rate and temperature on the measured viscosity and shear stress of the different epoxy resins.

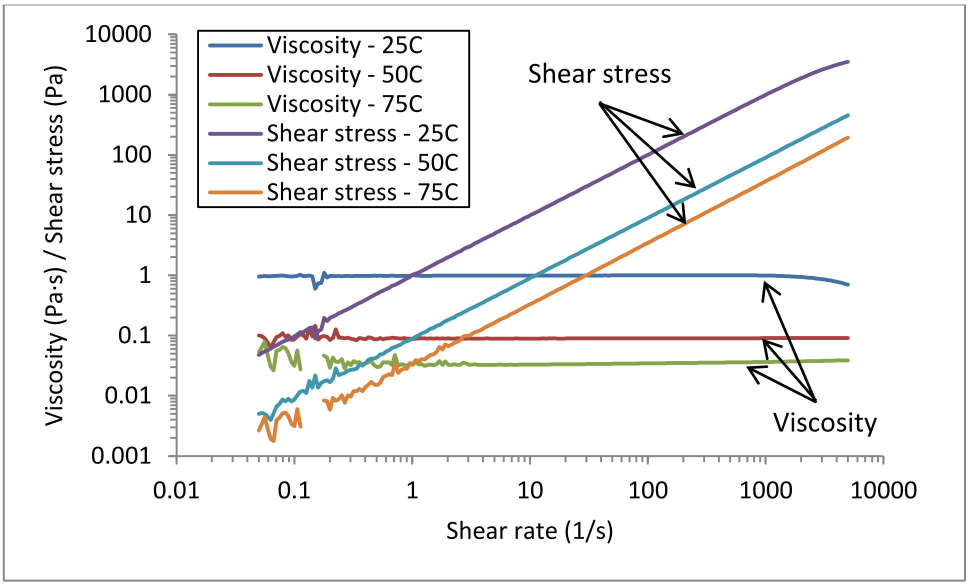

Figure 6.1: Viscosity and shear stress vs shear rate of unmodified (Si0R0) epoxy resin at different temperatures

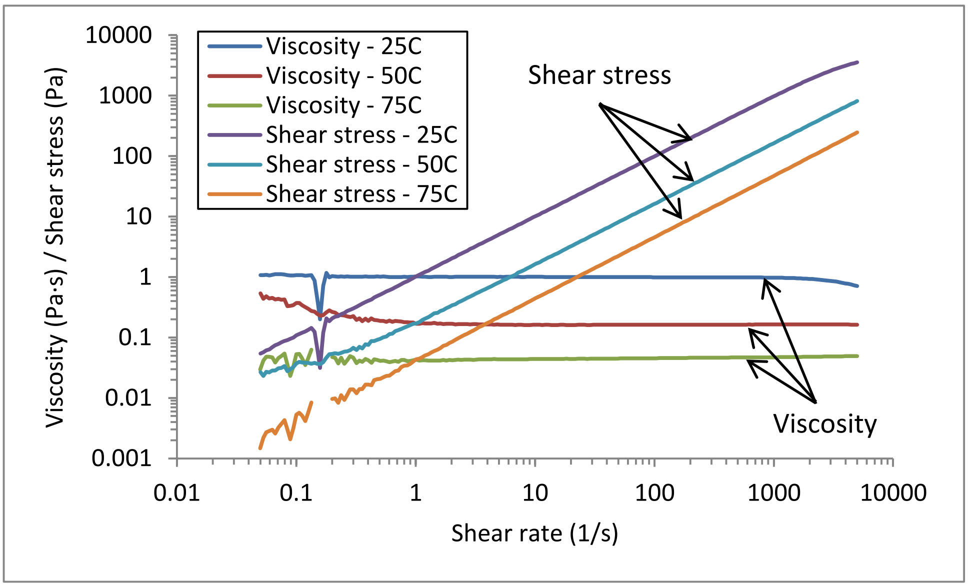

Figure 6.2: Viscosity and shear stress vs shear rate of silica-nanoparticle modified (Si10R0) epoxy resin at different temperatures

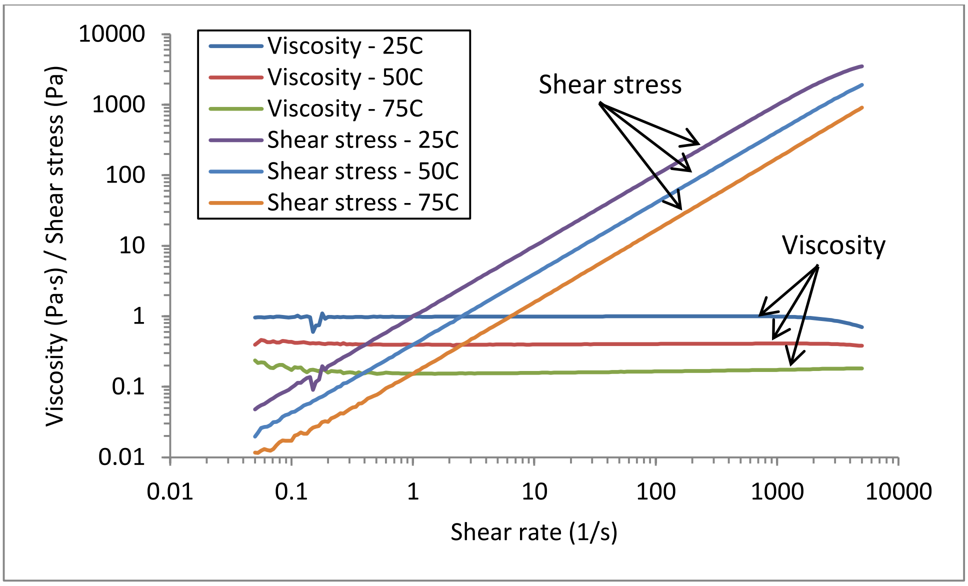

Figure 6.3: Viscosity and shear stress vs shear rate of rubber-microparticle modified (Si0R9) epoxy resin at different temperatures

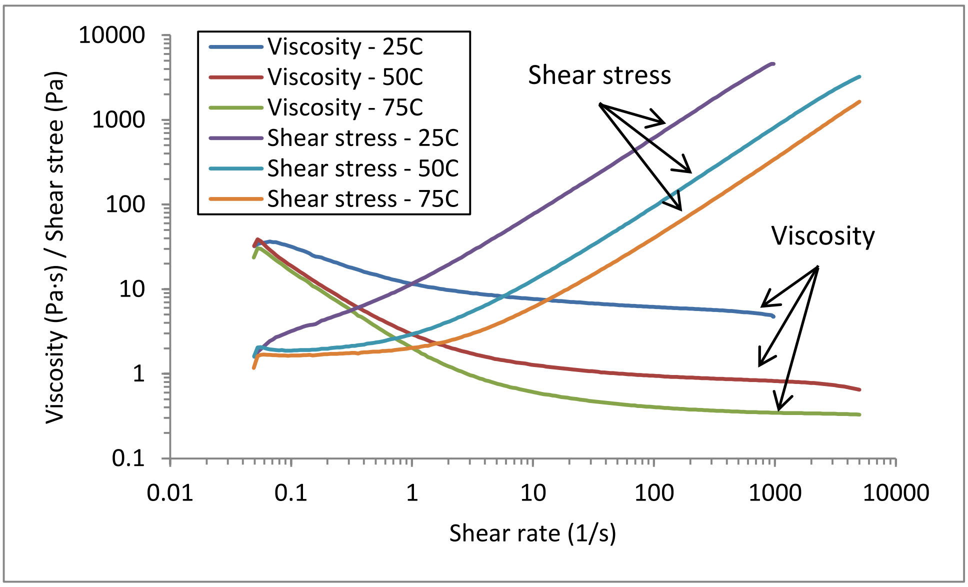

Figure 6.4: Viscosity and shear stress vs shear rate of hybrid modified (Si10R9) epoxy resin at different temperatures

As can be seen from Figure 6.1 to Figure 6.3, the viscosity of the unmodified (Si0R0), silica-nanoparticle (Si10R0) and rubber-microparticle (Si0R9) modified epoxy resins was independent of the shear rate. In other words, the viscosity remained constant upon increasing the shear rate. However, the viscosity of the hybrid modified (Si10R9) epoxy resin was affected by shear rate, see Figure 6.4. For the Si10R9 epoxy resin, the viscosity decreased as the shear rate increased. Further, it can be seen that the viscosity of all the epoxy resins decreased as the temperature was increased. Adding either silica-nanoparticles or rubber-microparticles resulted in a higher viscosity and a higher shear stress; and the rubber-microparticles had a more significant impact on the viscosity than the silica-nanoparticles. The combination of both silica-nanoparticles and rubber-microparticles further increased the viscosity. However, at either an increased temperature or an increased shear rate, the viscosity of the Si10R9 epoxy resin decreased noticeably.

Now, the RTM equipment can only work with resins having a maximum viscosity of approximately 1 Pa·s [148]. At a temperature of 25°C, the flow viscosity was found to be excessively high for injection, while at a temperature of 75°C, the epoxy resin was found to gel and cure prematurely, as indicated by the steeper increase in viscosity with time in Figure 6.5 below. At a temperature of 50°C, the flow viscosity started to decrease below 1 Pa·s when the shear rate was increased to 20 s^{-1}, again see Figure 6.4. The resin injection condition was therefore designed based on these results to ensure proper flow behaviour (i.e. excessively slow flow introduces excessive viscosity, while excessively fast flow creates excessive shear stress). The volumetric flow rate, Q, can be calculated from the shear rate, $\dot{\gamma}$, and the internal radius, r_i, of the pipe of approximately 3 mm from:

$$Q = \frac{\dot{\gamma}}{4} \qquad (6.1)$$

Hence, a volumetric flow rate of approximately 25 cc/min (i.e. for a shear rates of 20 s^{-1}) at a temperature of 50°C was used for the RTM process.

6.2.2.1.2 Simulated Process Conditions

The different formulations of epoxy resins were tested to assess their viscosity behaviour under conditions equivalent to that which the resins would undergo during the RTM process. This was done in order to ensure that the resins would behave appropriately during the manufacturing conditions and, for example, they would not prematurely gel or cure in the resin injector or in the mould.

This study consisted of two sub-tests where the test conditions were equivalent to the conditions: 1) within the resin injector; and 2) within the mould respectively.

Within the resin injector

The test was carried out with the aim of maintaining the resins at the shear rate of 20 s^{-1} at three different temperatures: 25°C, 50°C and 75°C for 150 mins. For ease of testing, only the Si10R9 epoxy resin was employed (i.e. the highest viscosity formulation). This test simulated the condition of the residual epoxy resins when inside the injector from the time the epoxy resins were mixed inside the injector until the time the resins in the mould had gelled and cured, see Figure 6.5. The test was also undertaken to ensure that the viscosity of the residual resins was sufficiently low for ease of cleaning (i.e. typically below 3 Pa·s [148]).

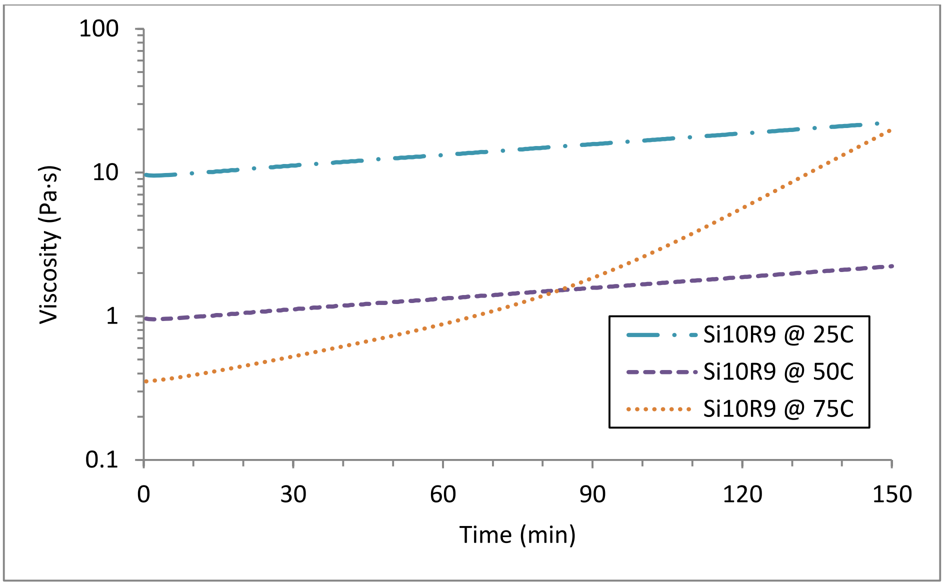

Figure 6.5: Viscosity vs time of hybrid modified (Si10R9) epoxy resin at a shear rate of 20 s^{-1} and different temperatures

As may be seen from Figure 6.5, at a temperature of 25°C, the viscosity of the resin was excessively high for injection, while at a temperature of 75°C, the viscosity of the resin increased rapidly as it gelled at this temperature. At a temperature of 50°C, the viscosity of the resin was sufficiently low for injection and essentially remained unchanged over 150 mins. Thus, a temperature of 50°C was selected for the injection cylinder for the RTM process.

Within the mould

This test simulated the conditions from the time the epoxy resins were mixed and degassed in the resin injector and injected into the mould until the time the resins had gelled and cured, see Figure 6.6. The test was carried out with the aim of initially maintaining the resin at a shear rate of 20 s^{-1} at 50°C for 60 mins, then the temperature was ramped to a temperature of 100°C at a rate of 5°C/min where the temperature was held until the resins had gelled and cured. These were the conditions that would be experienced by the epoxy resin during the RTM manufacturing whilst in the mould. It was confirmed that all the epoxy resins started to gel and cure after completion of the resin injection stage (i.e. after 60 mins) but before the residual epoxy resins in the resin injector had cured and gelled (i.e. before 150 mins), see Figure 6.5. Therefore, it was decided that the temperature-time cycle shown in Figure 6.6 should be selected for the RTM manufacturing method.

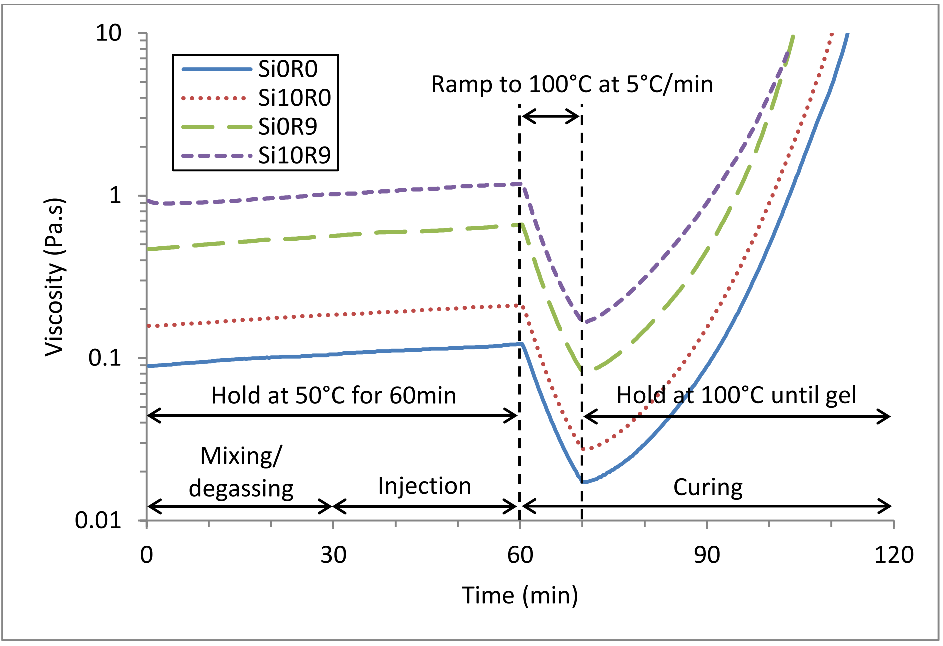

Figure 6.6: Viscosity vs time of Si0R0, Si10R0, Si0R9 and Si10R9 modified epoxy resins as they went through the curing cycle.

6.2.2.2 *Glass Transition Temperature, T_g*

The different formulations of the epoxy polymers were tested to determine their glass transition temperatures. The glass transition temperature was measured using the DSC equipment, see section '4.2.3'. The tests were undertaken to ensure that the curing schedules used in the present RTM manufacturing method fully cured the epoxy resins. Table 6.1 and Figure 6.7 show the glass transition temperatures of the different formulations of the epoxy polymers from different curing schedules.

Table 6.1: Summary of glass transition temperature of different formulations of cured unmodified/modified epoxy resins under different curing conditions

Curing schedule*	Glass transition temperature, T_g (°C)			
	Si0R0	Si10R0	Si0R9	Si10R9
100C-2h/150C-5h	127	113	115	103
100C-2h/150C-10h	141	121	120	111
100C-2h/150C-15h	141	124	122	112
100C-2h/150C-20h	145	127	120	113
120C-2h/160C-2h	139	105	112	107

*100C-2h/150C-5h = 100°C for 2 hours followed by 150°C for 5 hours curing schedule; 100C-2h/150C-10h = 100°C for 2 hours followed by 150°C for 10 hours curing schedule; 100C-2h/150C-15h = 100°C for 2 hours followed by 150°C for 15 hours curing schedule; 100C-2h/150C-20h = 100°C for 2 hours followed by 150°C for 20 hours curing schedule; and 120C-2h/160C-2h = 120°C for 2 hours followed by 160°C for 2 hours curing schedule.

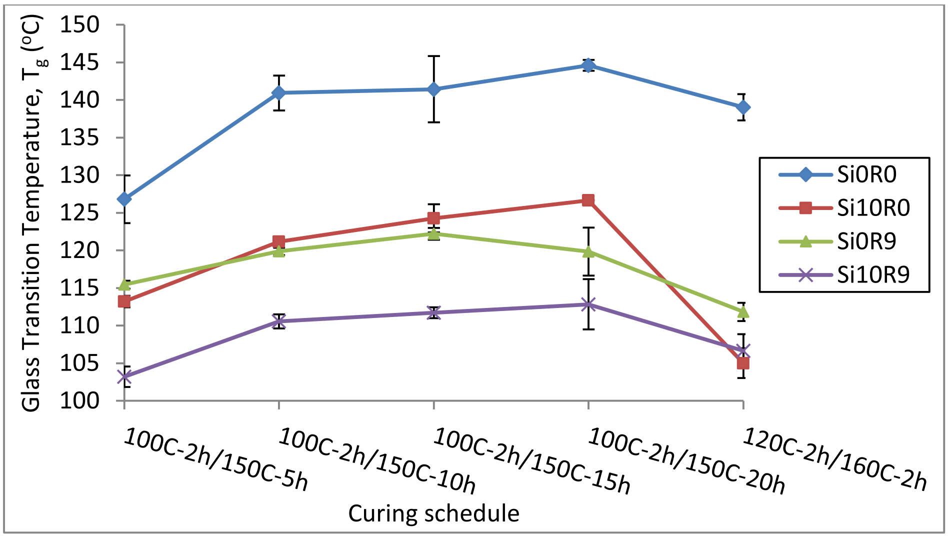

Figure 6.7: Summary of glass transition temperature of different formulations of cured unmodified/modified epoxy resins under different curing conditions

As may be seen from Table 6.1 and Figure 6.7, the 100C-2h/150C-5h and 120C-2h/160C-2h curing schedules did not fully cure the epoxy resins and resulted in a relatively low glass transition temperature. However, the 100C-2h/150C-10h, 100C-2h/150C-15h and 100C-2h/150C-20h curing schedules resulted in higher glass transition temperatures, with an increasing glass transition temperature for the extended periods of post-cure.

Due to limited access to the equipment, the 100C-2h/150C-10h curing schedule that was used to manufacture RIFT-processed FRPs was not applicable to the RTM process. Instead, the 100C-2h/150C-15h curing schedule was used. This procedure allowed the operators to start the cure at the end of the day and end it the next day. These two curing schedules did not result in a significantly different glass transition temperature for the epoxy polymers, as the typical standard deviation of the glass transition temperature was found to be below 3°C for all the cured epoxy materials. The lower value of glass transition temperature for the Si10R0 material compared to the Si0R0 material was probably due to the silica-nanoparticles inhibiting the cure of the epoxy polymer.

6.2.2.3 *Degradation Temperature*

The degradation temperatures of the different formulations of the epoxy polymers were measured using the TGA equipment, see section '4.2.4', to ensure that the curing schedule used in the present study did not degrade the epoxy polymers. Figure 6.8 shows the percentage weight loss of the different epoxy polymers upon increasing the temperature. Table 6.2 summarizes the degradation temperatures of the different formulations of the various epoxy polymeric matrices.

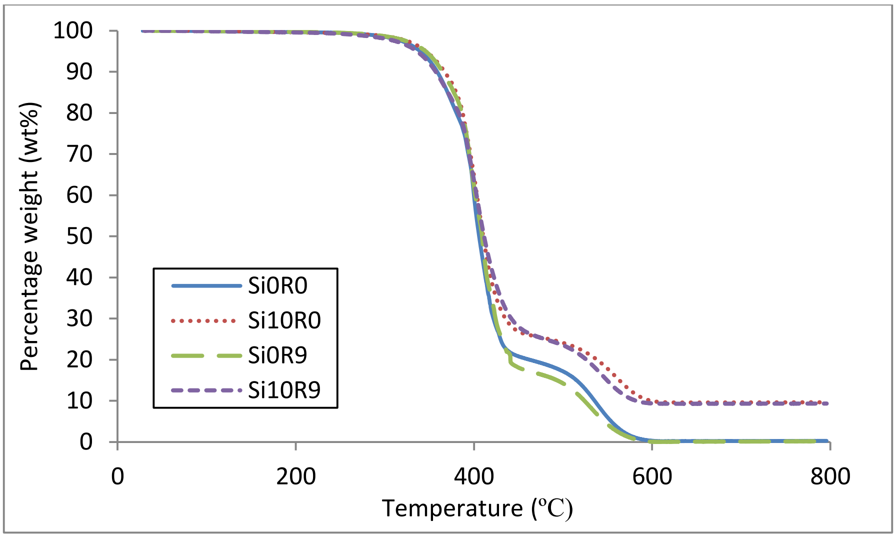

Figure 6.8: Percentage weight vs temperature of the different formulations of epoxy polymeric matrices

Table 6.2: Degradation temperature of the different formulations of epoxy polymeric matrices

Material	Onset degradation temperature (°C)	Peak degradation temperature (°C)	Residual percentage weight at 800°C, wt% (Si content)
Si0R0	331	403	<0.5
Si10R0	328	405	9.6±0.5
Si0R9	331	411	<0.5
Si10R9	326	405	9.4±0.8

It was found that the epoxy polymers used in the present study had a degradation temperature of approximately 330°C, which far exceeded both the maximum processing temperature of 150°C and the degradation temperature of the NFs of over 290°C. Thus, the epoxy polymers used would not degrade under the RTM manufacturing conditions. These tests also confirmed that only the silica-nanoparticles survived as a residue at a temperature higher than 800°C, and hence a burn-off method could be used to examine the silica-nanoparticle content and distribution. The measured residue was approximately 9.5 wt%, which agreed well with the theoretical value of 10 wt% of silica-nanoparticles.

6.2.3 **Pre-processing Properties and Characteristics of the Fibre – RTM Process**

6.2.3.1 ***Fibre Compaction Test***

The number of layers of fibre/fabric reinforcements required to be pre-laid within the mould cavity to obtain the required fibre volume fraction was determined using the method discussed in section '4.2.1'. The determination of the number of layers of fibre/fabric reinforcements, the mould clamp load and the fibre volume fraction are shown in detail in 'Appendix V'. Table 6.3 summarizes the number of layers of fibre/fabric reinforcements and the corresponding stacking sequences.

Table 6.3: Summary of fibre compaction test of the reinforcements used in RTM process

Fibre type and architecture*	Stacking Sequence^	Total thickness, t_c^T (mm)	Fibre volume fraction, v_f †
Unidirectional Flax (FF-UD)	$[(0_{GF})_4(0_{FF})_2]_s$^^	4	0.37††
Plain-woven Cellulose (CeF-PW)	$[(0_{GF})_4(0_{CeF})_4]_s$^^	4	0.55††
Unidirectional Glass (GF-UD)	$(0)_{14}$	4	0.67
Plain-woven and Twill 2x2 Glass (GF-PW+T)**	$[(0_T)_{14}(0_{PW})_2]_s$	4	0.47

*For further details, see ‘Appendix I’.

^For further details, see ‘Appendix V’.

†The estimated fibre volume fraction was calculated based on the fibre density after being fan-oven dried at 50°C for 4 hours using the total volume per unit area of certain stacking sequences (fibre volume fraction = total density per unit area/fibre density/thickness). The details of the calculation of the fibre volume fraction of the NFRP regions in the glass-fibre backed NFRPs are shown in ‘Appendix VI’.

**As the only balanced plain-woven glass fibre (balanced ratio of warp to weft yarns) was available in a very low density per unit area (GSM), in order to match the balanced plain-woven cellulose fibre, the balanced twill 2x2 glass fibre backing was added to the stacking sequence of plain-woven glass fibre. This minimally affected the mechanical properties of the GFRPs while having fewer numbers of layers for ease of manufacturing. Hence, the direct comparison between the CeFRPs-PW and GFRPs-PW+T could be made.

^^Glass fibre backing was required in order to eliminate the plastic deformation and promote linear-elastic behaviour for LEFM assumption, see ‘Chapter 8 Fracture Properties’.

††The estimated volume fraction of the NF in the NFRP regions in the glass-fibre backed NFRPs, , see ‘Appendix VI’.

An estimate of the resulting fibre volume fraction of the RTM-processed FRPs is also shown in Table 6.3. The estimated fibre volume fractions of different FRPs were found to vary considerably. This was due to the differences in the fibre types, architectures and their microstructures. (However, the actual fibre volume fraction of the RTM-processed FRPs varied somewhat and this aspect will be discussed later in Table 6.7 in section ‘6.4’.)

6.2.3.2 *Moisture Content*

The moisture content of the fibres was evaluated under three different fibre conditions: 1) as-received fibres; 2) fibres after drying at 50°C for 4 hours; and 3) fibres after drying at 75°C for 12 hours. A weighing-scale with a resolution of $1\text{x}10^{-4}$ grams was used to weigh the samples. Tests were carried out on fibres that had been pre-conditioned with an initial sample weight of approximately 10 grams. Table 6.4 shows the moisture content of the fibres used in the present study.

Table 6.4: Summary of moisture content of the fibres

Reinforcement	Conditions	Moisture content, v_w (wt%)
Flax fibre (FF)	As-received	8.6±1.6
	Oven-drying at 50°C for 4 hours*	3.3±1.6
	Oven-drying at 75°C for 12 hours^	<1.0
Cellulose fibre (CeF)	As-received	10.0±3.2
	Oven-drying at 50°C for 4 hours*	3.0±1.3
	Oven-drying at 75°C for 12 hours^	<1.0
Glass fibre (GF)	As-received	nil

*Equivalent to the NFs in the RTM mould prior to the resin injection.

^Equivalent to the NFs in the RIFT vacuum bagging prior to the resin infusion (final RIFT process).

High moisture contents were measured in the as-received NFs, while negligible moisture content was observed in the GFs. Drying the NFs significantly reduced moisture content.

6.2.3.3 *Degradation Temperature*

The degradation temperature of the different NFs was measured using the TGA equipment, see section '4.2.4', to ensure that the curing schedule used in the present study did not degrade the NFs. Figure 6.9 shows the loss of weight of the as-received NFs with increasing temperature. Table 6.5 summarizes the degradation temperature of the as-received NFs.

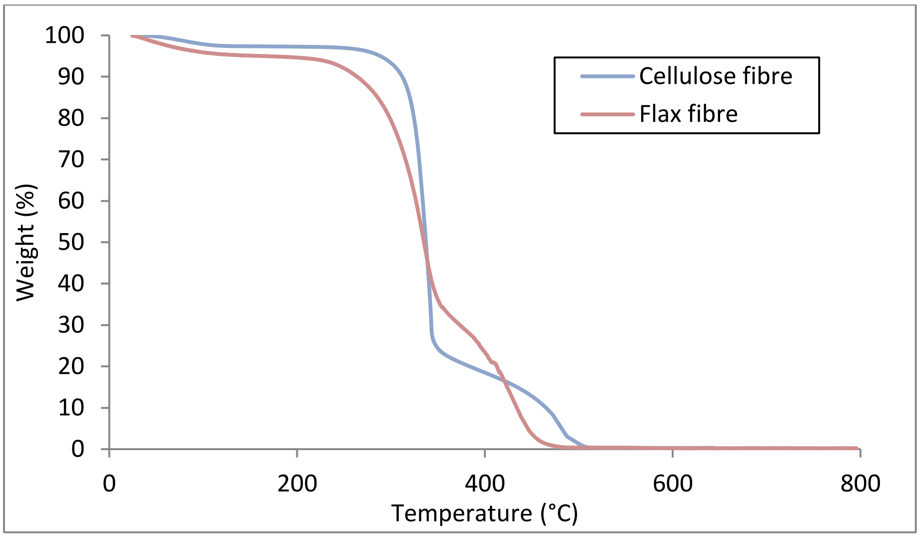

Figure 6.9: Percentage weight vs temperature of natural fibres

Table 6.5: Degradation temperature of the fibres

Material	Onset degradation temperature (°C)	Peak degradation temperature (°C)	Residual percentage weight at 800°C, wt%
Flax fibre (FF)	290	335	<0.5
Cellulose fibre (CeF)	320	339	<0.5
Glass fibre (GF)	Over 800*	Over 800*	100

*The test was carried out up to a temperature of 800°C

It was found that the NFs used in the present study had a degradation temperature of over 290°C, while the GF possessed a degradation temperature of over 800°C. These degradation temperatures far exceeded the RTM maximum processing temperature of 150°C. Thus, the fibres used would not degrade under the manufacturing conditions. It is noted that the initial weight loss of the NFs seen in Figure 6.9 was due to the loss of moisture content in the NFs with increasing temperature. Although the weight loss at 100°C measured using the TGA equipment was different from the moisture content measured in section '6.2.3.2', they were reasonably comparable (they were measured using different measurement methods).

6.2.4 **Conclusions**

The pre-processing characteristics of the epoxy resins and the fibres have been discussed, which defined the processing conditions of the epoxy resins and the fibres using the RTM method. The details of the set-up for the RTM process are discussed below.

6.3 The RTM Process

6.3.1 **Introduction**

The manufacturing of FRPs using the RTM process was carried out after the <u>initial</u> study of the RIFT process to determine whether the RTM process would improve the mode I interlaminar fracture toughness of the NFRPs.

The present section describes in detail the RTM manufacturing process. It involved manufacturing FRPs with different matrix formulations and different types of fibre/fabric reinforcements. The details are discussed below.

6.3.2 The RTM Manufacturing Process

Prior to manufacturing using the RTM method, the mould was cleaned with acetone and 'Zyvax Waterclean' mould release agent cleaner, then sealed with 'Zyvax sealer SF' water-based mould sealer and coated with 'Zyvax Water Shield' water-based release coating from Zyvax, USA. A stack of fibre/fabric was pre-laid in the mould cavity (using a fixed-thickness of 4 mm). The stack contained a 50 mm wide polytetrafluoroethylene (PTFE) film with a thickness of 10 µm inserted along one side in between the middle layers of the fibre/fabric stack which acted as a pre-crack in the DCB specimens for the mode I fracture toughness test. The mould was vacuum sealed using a rubber band sealing. The outlet was connected to a vacuum pump and the inlet was connected, through a valve, to a 'Radius 5000cc' RTM resin injector from Radius Engineering, USA. Once the mould was subjected to the applied vacuum of a pressure of approximately -0.1 MPa (i.e. relative pressure to atmospheric pressure), the resin was injected under pressure until the resin came out of the outlet. The outlet valve was then shut off to allow the pressure to increase to force the resin within the mould, see Figure 6.10. The fabricated FRPs were then cut into test specimens using a water jet cutting machine, and then dried at 75°C for 12 hours.

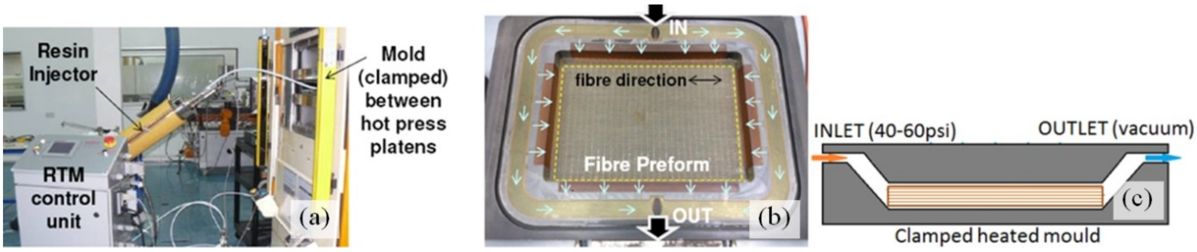

Figure 6.10: RTM process: (a) set-up, (b) in-mould top view and (c) side view

Due to limited access to the equipment, the 100C-2h/150C-10h curing schedule that was used to manufacture RIFT-processed FRPs was not applicable to the RTM process. Instead, the 100C-2h/150C-15h curing schedule was used. This procedure allowed the operators to start the cure at the end of the day and end it the next day. The resin was injected at 50°C then it was cured at 100°C for 2 hours, followed by a post-cure at 150°C for 15 hours and, finally, the composite panel was cooled down to room temperature. Table 6.6 summarizes the final settings employed in the RTM manufacturing method to produce the FRPs.

Table 6.6: Summary of RTM process settings

Resin & fibre preparation	
- Mixing	50°C for 20 mins stir under vacuum
- Degassing	
- Fibre conditioning	50°C for 4 hrs under vacuum
Resin Injection	
- Resin temperature	50°C
- Mould temperature	50°C
- Flow rate	25 cc/min
- Packing pressure	High pressure (0.4 MPa)
Cure	
- Heating rate	2°C/min
- Cure conditions	100°C for 2 hrs under vacuum
Post-Cure	
- Heating rate	1°C/min
- Post cure conditions	150°C for 15 hrs under atmospheric pressure

6.3.3 Conclusions

Details of the RTM manufacturing process have been discussed above. The post-processing characteristics of RTM-processed FRPs are discussed below.

6.4 Post-processing Properties and Characteristics of RTM-processed FRPs

6.4.1 Introduction

As for the post-processing characterization of the RIFT-processed composites, the characteristics and properties of the composites, such as density, fibre volume fraction, void content, glass transition temperature and silica-nanoparticle content and distribution were evaluated. These studies were aimed at assessing the quality and manufacturing consistency of the composite panels that were processed by the RTM method. This information assisted in interpreting the factors affecting the general mechanical and fracture properties, see 'Chapter 7' and 'Chapter 8'.

6.4.2 Glass Transition Temperature, T_g

Each composite panel was tested to determine the glass transition temperature of the epoxy matrix. The glass transition temperature was measured as described in section '4.2.3'. These tests were undertaken to ensure that the curing schedule used in the present study fully cured the epoxy resins. These tests were also employed to ensure that each composite panel was fully and uniformly cured. These aspects were studied by determining the glass transition temperature of samples taken from different locations from each composite panel.

6.4.3 Density, Fibre Volume Fraction and Void Content

The density, fibre volume fraction and void content of each composite panel were determined and calculated using the methods and calculations described in section '4.2.5', 'Appendix III' and 'Appendix VI'.

6.4.4 Silica-nanoparticle Content

The silica-nanoparticle content was determined by measuring the mass of the remaining substances after a burn-off technique, as described in section '4.2.4'. This test was employed to ensure a uniform distribution of silica-nanoparticles had been obtained from each composite panel.

6.4.5 RTM Results

The properties of the RTM-processed FRPs, including glass transition temperature, density, fibre volume fraction and void content are shown in Table 6.7.

Table 6.7: Summary of properties of RTM-processed FRPs

Fibre type and architecture	Matrix formulation	Measured glass transition temperature, T_g (°C)	Estimated glass transition temperature, T_g (°C)*	Density, ρ (g/cm^3)	Fibre volume fraction, v_f	Void content, v_v (vol%)
Unidirectional Flax (FF-UD)^	Si0R0	138	115	1.366	0.42	2
	Si10R0	124	101	1.395	0.41	2
	Si0R9	120	99	1.358	0.42	5
	Si10R9	108	97	1.388	0.42	6
Plain-woven Cellulose (CeF-PW)^	Si0R0	143	117	1.452	0.57	2
	Si10R0	123	103	1.484	0.60	1
	Si0R9	119	101	1.447	0.60	2
	Si10R9	100	99	1.466	0.59	3
Unidirectional Glass (GF-UD)	Si0R0	141	141	2.099	0.63	1
	Si10R0	125	124	2.112	0.62	1
	Si0R9	-†	122	-†	-†	-†
	Si10R9	-†	112	-†	-†	-†
Plain-woven and Twill 2x2 Glass (GF-PW+T)	Si0R0	143	141	1.839	0.45	1
	Si10R0	123	124	1.859	0.44	1
	Si0R9	119	122	1.809	0.44	1
	Si10R9	100	112	1.854	0.45	1
Atmospheric-pressure cured (dry) bulk epoxy polymer**	Si0R0	141	-	-	-	nil
	Si10R0	124	-	-	-	nil
	Si0R9	122	-	-	-	nil
	Si10R9	112	-	-	-	nil

*Total dissolution of moisture from the fibres (i.e. 3.3 wt% for FFs, 3.0 wt% for CeFs and 0.0 wt% for GFs) into the atmospheric-pressure cured particle modified bulk epoxy polymer was assumed, see Table 3.4 for moisture content properties of the NFs. The glass transition temperature was estimated using the Fox equation described in 'Appendix IV'.

^The details of the calculation of the density and fibre volume fraction of the NFRP regions in the glass-fibre backed NFRPs are shown in 'Appendix VI'.

†Values could not be obtained as the composites were not manufactured and unnecessary for the study.

**Glass transition temperatures for the different formulations of atmospheric-pressure cured (dry) bulk epoxy polymers cured under 100C-2h/150C-15h curing schedule (100°C for 2 hours followed by 150°C for 15 hour).

As may be seen from Table 6.7, the glass transition temperature was found to generally decrease when either silica-nanoparticles or rubber-microparticles were added. Addition of both types of particles further reduced the glass transition temperature.

Comparing the values given in Table 6.7 to those previously given in Table 5.6 for the initial RIFT manufacturing method, a higher density, a higher fibre volume fraction and a lower void content for the NFRPs were achieved from the RTM method compared to those obtained from the initial RIFT process. The measured glass transition temperatures of the RTM-processed NFRPs were found to be higher than the estimated glass transition temperatures of the epoxy polymer matrix (i.e. assuming that it contained the level of moisture that was in the fibres at the pre-manufacturing level). In fact, it was found that the glass transition temperatures of all the RTM-processed NFRPs were consistent with the measured glass transition temperatures of the corresponding dry (atmospheric-pressure cured) bulk epoxy polymers. This was due to the fact that the fixed cavity of the RTM mould allowed moisture to evaporate and escape from the fibres through spaces between the mould and the fibres, and hence reduced the moisture in the NFs. A lower moisture content resulted in a lower void content and higher glass transition temperature, and vice versa (e.g. approximately 8-10 wt% moisture content of the NFs in the initial RIFT process vs approximately 3 wt% moisture content of the NFs in the RTM process), see Table 3.4 in section '3.3.3'. These observations led to a higher density and higher fibre volume fraction for the RTM-processed NFRPs compared to the initial RIFT-processed NFRPs.

Further, the measured glass transition temperatures of the RTM-processed NFRPs were found to be equivalent to the measured glass transition temperatures of the corresponding dry (atmospheric-pressure cured) bulk epoxy polymers. In contrast, the measured glass transition temperatures of the final RIFT-processed NFRPs, see Table 5.8, were found to be slightly lower than the values of the measured glass transition temperatures of the corresponding dry (atmospheric-pressure cured) bulk epoxy polymers. This suggests that the moisture in the NFs had indeed entirely evaporated and escaped through spaces between the RTM mould and the fibres.

The density and fibre volume fraction of the RTM-processed NFRPs were found to be consistent with those from the final RIFT process, except for the relatively higher fibre volume fraction of the RIFT-processed CeFRPs compared to those from the RTM process. This was because the fixed-mould cavity was used in the RTM process, while the flexible vacuum bagging was used in the RIFT process, again see Table 5.8. It was also noted that a higher void content was observed for the higher viscosity matrix formulations in the RTM method, while this phenomenon did not occur in the final RIFT method. This suggests that a somewhat higher amount of air was trapped in the higher viscosity matrix formulations during the RTM manufacturing conditions.

In the GFRPs, there was no significant difference observed when comparing the properties of GFRPs from the two manufacturing methods. Also, the glass transition temperatures of the RTM-processed GFRPs were found to be consistent with those from the RIFT process and the the measured glass transition temperatures of the corresponding dry (atmospheric-pressure cured) bulk epoxy polymers. This suggests that the dissolution of the moisture from the GFs into the epoxy polymers in the GFRPs from the two processes was negligible, as would indeed be expected.

The distribution of the silica-nanoparticles was found to be uniform throughout all the RTM-processed composite panels with the typical standard deviation of the silica content being below 0.5 wt% for all the composite systems. Also, the fibre volume fraction was found to be consistent among the RTM-processed FRPs with different formulations. On the other hand, this property varied in the RIFT-processed FRPs considerably. Again, this was due to the geometry of the moulds used in the two different processes.

6.4.6 Morphology of Silica-nanoparticle and Rubber-microparticle Modified Fibre-reinforced Epoxy Polymers

The morphology of the RTM-processed silica-nanoparticle and rubber-microparticle modified FRPs was studied using atomic force microscopy (AFM) to investigate the dispersion of these particles in the composite panels with the different reinforcements, see section '4.5.3'.

As for the RIFT-processed FRPs, the AFM images revealed that the morphology of the silica-nanoparticles and rubber-microparticles in the RTM-processed FRPs with different types of reinforcements of the same matrix formulations were identical, regardless of the types of reinforcements. For example, the Si10R9 FFRP showed identical morphology of particles to those of the Si10R9 CeFRPs and GFRP. Hence, only AFM images of the FRPs with the different matrix formulations are shown in Figure 6.11.

Again, as for the RIFT-processed FRPs, a relatively featureless microstructure was observed in the unmodified (Si0R0) FRPs which showed a homogeneous microstructure. A uniform dispersion of silica-nanoparticles and rubber-microparticles was observed in the silica-nanoparticle modified (Si10R0) FRPs and the rubber-microparticle modified (Si0R9) FRPs, respectively. However, the hybrid modified (Si10R9) FRPs were found to have some degree of silica-nanoparticle agglomeration, whilst having a good dispersion of the rubber-microparticles.

Matrix formulation	**Height image**	**Phase image**
Si0R0	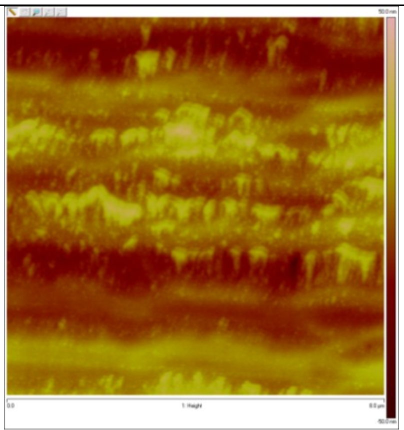	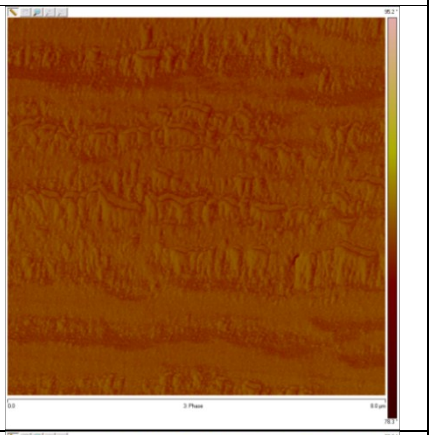
Si10R0	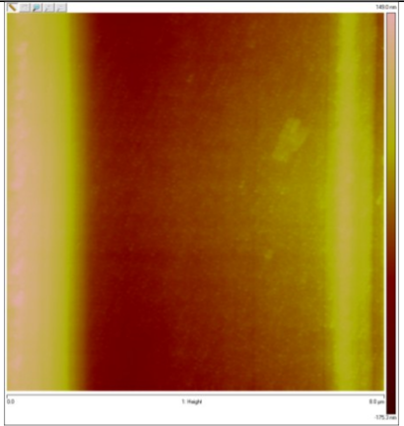	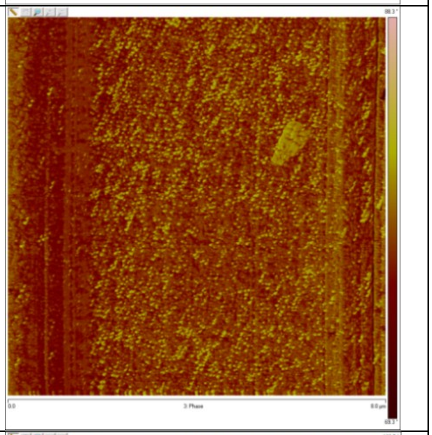
Si0R9	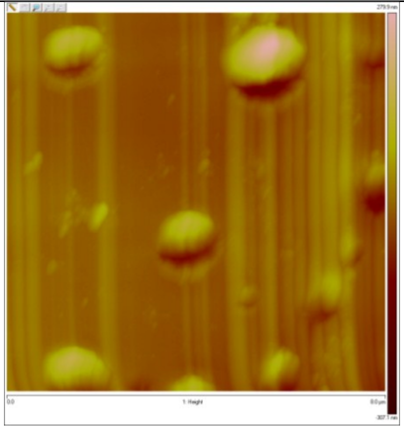	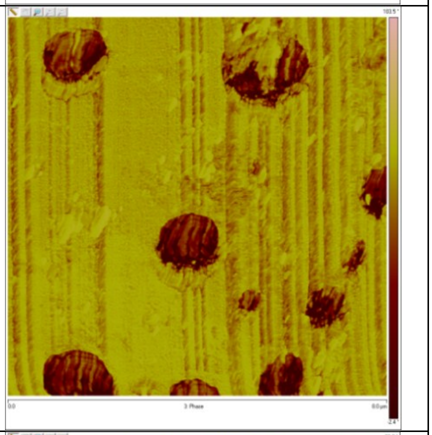
Si10R9	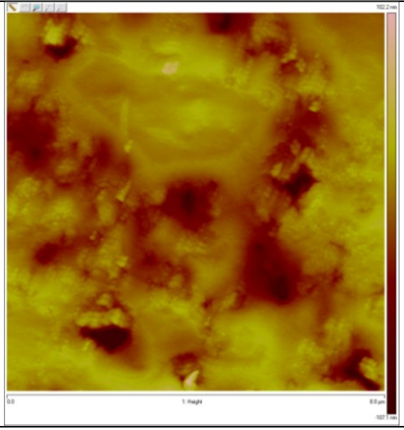	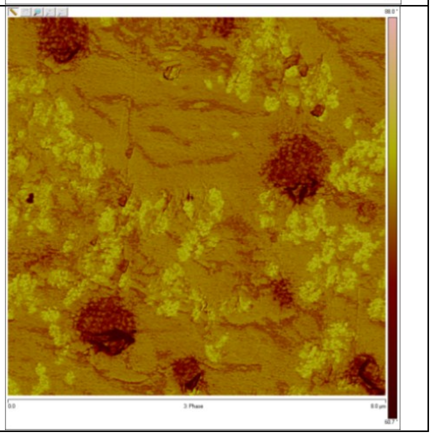

Figure 6.11: AFM images of different matrix formulations from the RTM-processed FRPs (images are 10 µm wide)

6.5 Comparison of Final RIFT and RTM Manufacturing Methods

The two manufacturing methods employed in the present study, namely the RIFT and RTM methods, share similar principles. They may, however, yield significantly different mechanical properties, as will be discussed in ‘Chapter 7’ and ‘Chapter 8’. Table 6.8 summarizes the key differences in the two manufacturing methods, while Table 6.9 summarizes the properties of the FRPs from the two manufacturing methods.

Table 6.8: Summary of key difference of final parameters in final RIFT and RTM processes

Final parameters	Final RIFT	RTM
Resin & fibre preparation		
- Mixing	50°C for 15 mins stir	50°C for 20 mins stir under vacuum
- Degassing	50°C for 20 mins under vacuum	
- Fibre pre-processing	75°C for 12 hrs fan-oven dry (OD)	-
- Fibre conditioning	50°C for 30 mins under vacuum	50°C for 4 hrs under vacuum
Resin Injection		
- Resin temperature	50°C	50°C
- Mould temperature	50°C	50°C
- Flow rate	5-15 cc/min	25cc/min
- Injection duration	30-100 mins	25 mins
- Packing pressure	Vacuum (-0.1 MPa)*	Under high pressure (0.4 MPa)
- Injection duration	Approx. 30-100 mins	Approx. 25 mins
Cure		
- Heating rate	5°C/min	2°C/min
- Cure conditions	100°C for 2 hours under vacuum	100°C for 2 hrs under vacuum
Post-Cure		
- Heating rate	1°C/min	1°C/min
- Post cure conditions	150°C for 10 hrs under atmospheric pressure	150°C for 15 hrs under atmospheric pressure

*Relative pressure to atmospheric pressure

As may be seen from Table 6.9, the glass transition temperature was found to generally decrease when either silica-nanoparticles or rubber-microparticles were added. Addition of both types of particles further reduced the glass transition temperature. It was found that the glass transition temperatures of all the RTM-processed NFRPs were relatively consistent with the measured glass transition temperatures of the corresponding dry (atmospheric-pressure cured) bulk epoxy polymers. They were, however, consistently higher than those obtained from the final RIFT process, regardless of the void content of the resulting NFRPs. This suggests that the moisture in the NFs most probably had entirely evaporated and escaped during the RTM manufacturing method. However, as discussed in ‘Chapter 5’, the entrapped moisture and any additional moisture absorbed during the transportation of the reinforcements to the RIFT manufacturing equipment had dissolved in the epoxy matrices during the final RIFT manufacturing method. This was due to the flexible RIFT vacuum bagging changing the contour according to the profile of the pre-laid fibre/fabric reinforcement. This trapped the moisture inside, whereas the fixed cavity of the RTM mould allowed the moisture to evaporate and escape from the fibres through spaces between the mould and the fibres. Hence, the estimated glass transition temperature of the dry bulk epoxy matrix, assuming complete dissolution of all the moisture present in the fibres (i.e. less than 1 wt% at pre-manufacturing for the final RIFT process), was found to be somewhat higher than the measured glass transition temperature of the final RIFT-processed NFRPs.

The fibre volume fractions of the FFRPs from the two manufacturing methods were found to be equivalent, except that the fibre volume fractions of the final RIFT-processed CeFRPs were somewhat higher than those from the RTM process. Again, due to the contour changing RIFT vacuum bagging, the CeF reinforcement was better packed. Also, the fibre volume fraction was found to be consistent among the RTM-processed FRPs with different formulations. On the other hand, this property varied in the RIFT-processed FRPs considerably.

In the final RIFT process, the flow speed of the epoxy resins during the infusion was mainly controlled by the permeability of the epoxy resins through the fibres, which was governed by the packing, alignment and weave pattern of the reinforcement and the viscosity of the resins, see section ‘6.2.2.1’. High viscosity matrix formulations tended to flow at slow speed, and hence the entrapped air could escape. Instead, in the RTM process, the flow speed of the epoxy resins was fully controlled by the pre-programmed injection speed. This suggests that the pre-programmed constant flow speed in the RTM method might have created a higher level of voids, especially in the higher viscosity matrix formulations, as the entrapped air required a longer duration to escape. The approximate duration for injection in the RTM process was 25 mins, compared to 30-100 mins in the RIFT process depending on the formulations used.

Again, due to the contour changing behaviour of the flexible RIFT vacuum bagging, a poor quality surface with fabric-like pattern was obtained on the top side, while the bottom side surface was in a not quite good quality. In contrast, the RTM-processed composite panels have a smooth surface on both sides.

Table 6.9: Summary of properties of final RIFT- and RTM-processed NFRPs vs epoxy polymers

Manufac-turing method	**Matrix formulation**	**Measured glass transition temperature, T_g (°C)**		**Estimated glass transition temperature, T_g (°C)***		**Fibre volume fraction, v_f**		**Void content, v_v (vol%)**	**Surface quality**
		FFs^	CeFs^	FFs^	CeFs^	FFs^	CeFs^		
Final RIFT-processed NFRPs	Si0R0	126	110	133	133	0.44	0.64	1	Poor
	Si10R0	119	99	114	114	0.40	0.67	1	
	Si0R9	107	98	113	113	0.36	0.65	1	
	Si10R9	106	94	104	104	0.44	0.67	1	
RTM-Processed NFRPs	Si0R0	138	143	115	117	0.41	0.54	2	Good
	Si10R0	124	123	101	103	0.40	0.57	1-2	
	Si0R9	120	119	99	101	0.41	0.58	2-5	
	Si10R9	108	100	97	99	0.40	0.56	3-6	
		100C-2h/ 150C-10h^	100C-2h/ 150C-15h^						
Atmospheric-pressure cured (dry) bulk epoxy polymer	Si0R0	141	141		-	-	-	nil	-
	Si10R0	121	124		-	-	-	nil	-
	Si0R9	120	122		-	-	-	nil	-
	Si10R9	111	112		-	-	-	nil	-

*Estimated for the ‘matrix + absorbed water from the fibres’. Total dissolution of moisture from the fibres (i.e. about 1 to 3 wt%, as indicated) into the atmospheric-pressure cured particle modified(dry) bulk epoxy polymer was assumed. The glass transition temperature was estimated using the Fox equation described in ‘Appendix IV’.

^FFs = values for the NFRPs with FF reinforcement; CeFs = values for the NFRPs with CeF reinforcement.

†100C-2h/150C-10h = curing schedule used for the RIFT process (100°C for 2 hours followed by 150°C for 10 hours); 100C-2h/150C-15h = curing schedule used for the RTM process (100°C for 2 hours followed by 150°C for 15 hour).

The main advantages and disadvantages of the two manufacturing methods are summarized in Table 6.10.

Table 6.10: Summary of main advantages and disadvantages between final RIFT and RTM processes

Final RIFT process	RTM process
Advantages - Low-cost tooling [121][123] - Real-time monitoring of the flow (transparent flexible vacuum bagging) [121][123] - The flow speed adapts according to the matrix viscosity **Disadvantages** - High amount of micro- and macro-voids (processed under vacuum and entrapped moisture by flexible vacuum bagging) [121][123] - Relatively low fibre volume fraction for NFs (low packing pressure) [121][123] - Inconsistency of properties, e.g. fibre volume fraction and void content (due to local pressure and flow behaviour) [125][126] - Low glass transition temperature (shorter post-curing duration) - One-sided smooth surface [121][123]	**Advantages** - In-process paint/coating [121][123] - One-sided smooth surface [121][123] - Low amount of micro- and macro-voids (high consolidation under high pressure and escapable moisture through mould cavity) [121][123][146] - High fibre volume fraction (high processing pressure) [121][123] **Disadvantages** - Flow cannot be monitored (closed mould) [121][123] - Expensive tooling [121][123]

6.6 Concluding Remarks

The present chapter has described the resin transfer moulding (RTM) processing method in detail, including the pre-processing characteristics and properties of the epoxy resins and the fibres used in the RTM process, the RTM manufacturing process, and post-processing characteristics and properties of the RTM-processed FRPs.

The RTM process involved a procedure where the mould was subjected to an applied vacuum. During this time the amount of air and moisture entrapped in the fibre was greatly reduced. This had little influence on the GFRPs as the GFs intrinsically possess negligible amounts of moisture. However, the moisture content in the NFs was greatly reduced under these RTM manufacturing conditions. As a result, the NFRPs manufactured using the RTM method contained a relatively low amount of water and a relatively low degree of voids.

The next part of the PhD thesis will discuss and summarize the mechanical properties of the FRPs from the two different manufacturing processes employed in the present study.

RESULTS AND DISCUSSIONS - PART II: MECHANICAL PROPERTIES

Two manufacturing techniques were involved in the present study: 1) a resin infusion under flexible tooling (RIFT) process, and 2) a resin transfer moulding (RTM) process. These two techniques share similar principles, however, they initially yielded significantly different physical properties of the FRPs produced, see ‘Chapter 5’ and ‘Chapter 6’. Thus, they may also yield significantly different mechanical properties.

The present part of the PhD thesis discusses the results from the mechanical property studies in two separate chapters: 1) the general mechanical properties, including flexural and tensile properties, are discussed in ‘Chapter 7’; and 2) the mode I interlaminar fracture properties are discussed in ‘Chapter 8’.

CHAPTER 7 GENERAL MECHANICAL PROPERTIES

7.1 Introduction

The present chapter summarizes the flexural and tensile Young's modulus, tensile strength and tensile failure strain results of the FRPs manufactured by the two manufacturing methods. An analytical model for calculating the tensile modulus is also discussed.

7.2 General Mechanical Properties

7.2.1 Flexural Moduli of RIFT-processed NFRPs vs GFRPs – Initial Study

For simplicity, only the flexural moduli were measured for the composites manufactured using the initial RIFT process. Table 7.1 summarizes the values of the flexural moduli of the initial RIFT-processed FRPs.

Table 7.1: Summary of the flexural moduli of RIFT-processed NFRPs vs GFRPs – Initial study

Fibre type and architecture	Modification	Fibre volume fraction, v_f	Void content, v_v (vol%)	Flexural modulus, E_{flex} (GPa)
Unidirectional Flax (FF-UD)	Si0R0	0.31	15	12.5±1.1
	Si10R0	0.23	13	12.9±0.6
	Si0R9	0.38	17	15.1±0.8
	Si10R9	0.33	16	13.2±0.3
Plain-woven Cellulose (CeF-PW)	Si0R0	-*	14	5.7±0.2
	Si10R0	-*	16	6.4±1.1
Unidirectional Glass (GF-UD)	Si0R0	0.61	2	51.5±3.4
	Si10R0	0.55	2	51.7±10.6
	Si0R9	0.65	2	54.1±8.7
	Si10R9	0.65	2	54.7±1.9
Plain-woven and Twill 2x2 Glass (GF-PW+T)^	Si0R0	0.41	2	20.0±1.0
	Si10R0	0.38	2	22.6±4.7
	Si0R9	0.42	2	21.9±0.2
	Si10R9	0.44	2	23.5±0.6

*Values could not be obtained due to the poor quality of the composites.

^As the only balanced plain-woven glass fibre (balanced ratio of warp to weft yarns) was available in a very low density per unit area (GSM), in order to match the balanced plain-woven cellulose fibre, the balanced twill 2x2 glass fibre backing was added to the stacking sequence of plain-woven glass fibre. This minimally affected the mechanical properties of the GFRPs while having fewer numbers of layers for ease of manufacturing. Hence, the direct comparison between the CeFRPs-PW and GFRPs-PW+T could be made.

As may be seen from Table 7.1, the flexural moduli of both the NFRPs were found to be about four times lower than was measured for the GFRPs with the same fibre/fabric reinforcement architecture. For example, a modulus of 12.5 GPa was measured for the Si0R0 FFRP-UD, compared to a value of 51.5 GPa for the Si0R0 GFRP-UD. The same trend was observed for the fibre/fabric reinforcement with the plain-woven architecture. Further, an increase of the modulus from 5.7 GPa for the Si0R0 CeFRP-PW to 20.0 GPa for the Si0R0 GFRP-PW+T was recorded. This was due to the lower fibre volume fraction achieved in the NFRPs as the cellular structure and porous nature of the NFs [4] restricted the compaction of the pre-laid-up NF reinforcement under vacuum pressure during the RIFT manufacturing process. For example, 75% lower flexural moduli were observed for the initial RIFT-processed FFRPs with only approximately 50% lower average fibre volume fraction compared to the RIFT-processed GFRPs-UD. Such a lower fibre volume fraction would be expected to decrease the flexural modulus by only 47% using the rule of mixtures [1][149][150].

The lower tensile moduli of the NFs, see Table 3.4, also contributed to the lower flexural moduli of the NFRPs [4][38][40]. A 24% reduction in the flexural moduli for the FFRPs-UD compared to the GFRPs-UD was estimated using the rule of mixtures [1][149][150] with about 34% lower tensile modulus being measured for the FFs, compared to the GFs [4][40].

Also, a relatively high void content was observed in the NFRPs. This could be due to the poor wettability and poor fibre-matrix interfacial adhesion as a result of the fibre-matrix incompatibility [4][7], and the transformation of the water trapped in the NFs into steam at the high temperatures reached during curing. There was also found to be the dissolution of water in the epoxy matrix. This was confirmed by the reduction of the glass transition temperature [147], see Table 5.6. For example, a glass transition temperature of 90°C was measured for the initial RIFT-processed Si0R0 FFRP, compared to a value of 141°C for the glass transition temperature of the atmospheric-pressure cured Si0R0 epoxy polymer. A glass transition temperature of 146°C was measured for the Si0R0 GFRP-UD with only a minimal void content of 2%. However, only about a 2% increase in the flexural moduli of the FFRPs was predicted using the rule of mixtures [1][149][150] when the void content was almost entirely reduced from the observed values of about 13-17% to 2%, because the flexural modulus was principally determined by the fibre modulus, which was unaltered.

The same poor quality of the composites manufactured using the initial RIFT process was observed for the CeFRPs. For example, approximately 75% lower flexural moduli were observed for the CeFRPs, compared to the GFRPs-PW+T. Additionally, due to their poor quality of the CeFRPs, the fibre volume fraction could not be measured, but up to 16% void content was observed.

A relatively wide variation of about 20% was observed for the fibre volume fraction of the FFRPs, with the different matrix modifications. Values of 6-7% were observed for the RIFT-processed GFRPs with the same fibre/fabric reinforcement architecture. This observation was generally due to the differences in the viscosity of the different matrix formulations that affected the flow behaviour and local pressure [126]. However, the wide variation of the packing density of the FFs was due to the irregular cross-sections of the NFs and the variation of the diameter and density of the NF yarns [151]. In addition to the poor wettability and poor fibre-matrix interfacial adhesion as a result of the fibre-matrix incompatibility [4][7]. Additionally, the flexural modulus of the FRPs was affected by the change of the fibre volume fraction. However, the modulus of the FRPs was only marginally affected by the addition of either silica-nanoparticles or rubber-microparticles, as the majority of the load was carried by the fibres. This observation is in a good agreement with the study conducted by Manjunatha and his colleagues [110]. As a result, the moduli of the FRPs varied considerably depending on their fibre volume fraction rather than the matrix modification.

7.2.2 Flexural Moduli of RIFT-processed NFRPs vs GFRPs – Optimization Study

Efforts to improve the mechanical properties of the NFRPs were attempted, see section '5.3.3'. For simplicity, only the unidirectional flax fibre (FF-UD) reinforced unmodified (Si0R0) epoxy polymer composite was employed in the optimization study to improve the flexural moduli of the NFRPs. Table 7.2 summarizes the values of the flexural moduli of the FFRPs from the optimization study of the RIFT process and compares them with those of the GFRPs manufactured via the same process.

Table 7.2: Summary of flexural moduli of RIFT-processed NFRPs vs GFRPs with Si0R0 matrix formulation – Optimization study

Fibre type and architecture	Modification	Fibre volume fraction, v_f	Void content, v_v (vol%)	Flexural modulus, E_{flex} (GPa)
Unidirectional Flax (FF-UD)	Initial study	0.31	15	12.5±1.1
	Vacuum dry (VD)*	0.32	13	17.7±2.6
	Plasma treatment (OP)*	0.34	12	16.8±0.8
	Fan-oven dry (OD)*	0.44	1	18.7±0.6
Unidirectional Glass (GF-UD)	Initial study	0.61	2	51.5±3.4

*VD = vacuum-dry under vacuum in the RIFT vacuum bagging for 6 hours at 50°C prior to processing; OP = plasma treatment with low pressure O_2 plasma at 50% power for 5 minutes; OD = fan-oven dry in the fan-oven for 12 hours at 75°C prior to processing. For further details, see section '5.3.3'.

Table 7.2 summarizes the three modifications involved in the optimization study of the RIFT process. These include 1) VD: the attempt to dry the fibres in the RIFT vacuum bagging under vacuum, 2) OP: the attempt to incorporate a plasma treatment on the FF surface to enhance fibre-matrix compatibility and 3) OD: the attempt to dry the fibres in the fan-oven. It was found that all three modifications significantly improved the flexural moduli of the RIFT-processed FFRPs.

However, a significantly improved fibre volume fraction was only observed for the OD-modified FFRP with a 42% increase in the fibre volume fraction to $v_f = 0.44$, while the fibre volume fractions observed from the VD- and OP-modified FFRPs remained unchanged. This confirmed an improved wettability and an improved fibre packing density for the OD-modified FFRP.

The OD-modification also gave a significant reduction in the void content (the void content was reduced from about 15% to about 1%), which confirmed the elimination of nearly all the water from the NFs, prior to the RIFT manufacturing process, see Table 7.2. As a result, the water evaporating into steam under the high temperature reached during curing was mostly reduced. Hence, a minimal amount of voids was present. For example, the moisture content in the FFs was reduced from approximately 8.6 wt% to below 1 wt% by drying in the fan-oven (OD), see Table 3.4. This was confirmed by the higher glass transition temperature of 126°C observed for the OD-modified FFRP, which was a result of the reduction of water dissolution in the epoxy matrix [147]. This may be compared to the glass transition temperatures of 87-99°C observed for the VD- and OP-modified FFRPs, see Table 5.7. On the other hand, the moisture content of the vacuum-dried (VD) FFs remained unchanged, which restricted the wetting of the fibre by the epoxy polymer and weakened the fibre-matrix interfacial adhesion. As a result, a relatively high void content of 13% were recorded. The plasma surface treatment (OP) also gave the same poor outcome.

However, the flexural modulus of the OD-modified FFRP of 18.7 GPa was found to be much inferior to the value of 51.5 GPa for the GFRP-UD, due to the lower fibre volume fraction achieved in the FFRP and the inferior tensile modulus of the FFs [4][40]. Nevertheless, the OD-modified FFRP was found to perform best among the three modifications, with an up to 11% higher flexural modulus. The OD-modification was selected for the final RIFT process. Whether the OD-modification could improve the fracture energy of the NFRPs will be discussed in 'Chapter 8 Fracture Properties'.

7.2.3 Flexural and Tensile Properties of RIFT-processed NFRPs vs GFRPs – Final Study

As the fan-oven drying of the FFs (i.e. OD-modification) revealed a significant improvement of the flexural moduli of the RIFT-processed FFRPs, the OD-modified NFRPs with different matrix modifications were further examined in this final RIFT study.

7.2.3.1 *Flexural and Tensile Properties of RIFT-processed FFRPs vs GFRPs – Final Study*

Table 7.3 summarizes the flexural and tensile properties of the RIFT-processed FFRPs from the initial and final RIFT processes, and compares them with the RIFT-processed GFRPs.

Table 7.3: Summary of flexural and tensile properties of RIFT-processed FFRPs vs GFRPs

Matrix formulation	Initial RIFT FF-UD		Final RIFT (OD-modification) FF-UD						RIFT GF-UD					
	v_f	E_{flex} (GPa)	v_f	E_{flex} (GPa)	E_t (GPa)	E_t/ρ (10^6 m^2s^{-2})	σ_t (MPa)	ε_t (%)	v_f	E_{flex} (GPa)	E_t (GPa)	E_t/ρ (10^6 m^2s^{-2})	σ_t (MPa)	ε_t (%)
Si0R0	0.31	12.5 ±1.1	0.44	18.7 ±0.6	20.1 ±0.1	14.7 ±0.1	163 ±2	1.2 ±0.1	0.61	51.5 ±3.4	46.5 ±1.5	22.5 ±0.7	1144 ±25	1.9 ±0.1
Si10R0	0.23	12.9 ±0.6	0.40	14.2 ±0.2	17.7 ±0.2	12.8 ±0.1	161 ±5	1.1 ±0.1	0.55	51.7 ±10.6	41.2 ±1.4	20.6 ±0.7	1018 ±52	2.0 ±0.1
Si0R9	0.38	15.1 ±0.8	0.36	14.1 ±0.6	15.5 ±0.4	11.8 ±0.3	153 ±5	1.4 ±0.1	0.65	54.1 ±8.7	44.7 ±0.5	21.1 ±0.2	1243 ±46	2.1 ±0.1
Si10R9	0.33	13.2 ±0.3	0.44	16.1 ±0.6	17.2 ±0.2	12.5 ±0.1	151 ±5	1.4 ±0.3	0.65	54.7 ±1.9	45.8 ±0.4	21.5 ±0.2	1263 ±37	2.1 ±0.2

As may be seen from Table 7.3, the final RIFT process generally improved the flexural moduli of the FFRPs compared to the values from the initial study. As discussed previously, this arises from the reduction of the moisture content in the FFs from about 8.6 wt% to below 1 wt%. This resulted in a significantly improved fibre volume fraction and a significant reduction in the void content. A 42% increase in the fibre volume fraction to $v_f = 0.44$ was also achieved. It is noteworthy that the final RIFT process reduced the void contents of the FFRPs from about 13-17% to about 1%, which was comparable to the void contents of about 2% for the GFRPs, see Table 7.1.

In the FRPs, the majority of the load is carried by the fibre/fabric reinforcement and the general mechanical properties, such as flexural modulus, tensile modulus and tensile strength, are primarily dictated by the mechanical properties of the fibre/fabric reinforcement and its fibre volume fraction. Manjunatha and his colleagues [110] found that modifying the glass fibre-reinforced epoxy polymer with either silica-nanoparticles or rubber-microparticles only slightly changed the tensile modulus and tensile strength. The same conclusion is valid for all the FRPs shown in Table 7.3.

It was observed from Table 7.3 that the flexural moduli, tensile moduli and tensile strengths of the final RIFT-processed FFRPs were generally inferior to those of the RIFT-processed GFRPs-UD. For example, up to three times lower flexural and tensile moduli were observed for the final RIFT-processed FFRPs. Additionally, the tensile strengths for the final RIFT-processed FFRPs were found to be up to eight times lower than those of the RIFT-processed GFRPs. Also, up to two times lower tensile failure strains were recorded for the final RIFT-processed FFRPs. This was due to the lower fibre volume fractions achieved in the FFRPs and the inferior mechanical properties of the FFs compared to those of the GFs [4][40]. However, such lower fibre volume fractions achieved in the FFRPs and inferior mechanical properties of the FFs would be expected to produce only about a half-fold decrease in the flexural and tensile moduli and up to a seven times decrease in tensile strength respectively using the rule of mixtures [1][149][150]. Due to the low density of the FFs [4], the specific tensile moduli, E_t/ρ, of the FFRPs were found to be up to only 30% lower than the values from the GFRPs, see Table 7.3.

The general mechanical properties obtained from the final RIFT-processed FFRPs were found to be significantly inferior to the previously reported results by Lineo [43]. For example from Table 2.8, it may be seen that values of 35 GPa and 365 MPa for the tensile modulus and the tensile strength of the Si0R0 FFRP-UD manufactured via the RTM process were achieved by Lineo [43], compared with the present values of 20.1 GPa and 163 MPa respectively (i.e. 74% and 124% lower values of tensile modulus and tensile strength, respectively). It is noted that the curing schedule used by Lineo [43] is not known and the FFs were harvested from different sources with different extracting processes. This may result in different mechanical properties of the FFs. It is also noteworthy that the present FFRPs-UD produced by the final RIFT process possessed an average fibre volume fraction some 18% lower than that reported by Lineo [43]. However, such a lower volume fraction would only be expected to produce a 15% decrease in the values of tensile modulus and tensile strength. Also, the Lineo FFRPs were made with pre-treated non-crimp flax tape, while the pre-dried unidirectional woven FFs used in the present study to produce the FFRPs-UD contained a degree of fibre waviness and crimping (crimping is a waviness or distortion of the in-plane interlacing warp and weft yarns in woven fabrics caused by stitching used in the weaving process [152]). The existence of fibre waviness/crimping may compromise the mechanical properties of the FFRPs.

For the GFRPs, it was found that the tensile moduli and tensile strengths obtained from the present study were both about 16% superior to those reported by Performance Composites [3] with an equivalent fibre volume fraction, see Table 2.8. Although both GFs used were E-glass, it is noted that the present study used a higher processing temperature to manufacture the GFRPs, and the GFs used in the two GFRPs were from the different suppliers. This might result in a variation of the mechanical properties of the GFRPs.

7.2.3.2 *Flexural and Tensile Properties of RIFT-processed CeFRPs vs GFRPs – Final Study*

Again, the final RIFT process significantly improved the flexural moduli of the CeFRPs compared to the values from the initial study, see Table 7.4. This was as a result of the significant void content reduction (i.e. from about 14-16% to about 1%). This was due to the reduction of the moisture content in the CeFs from about 10 wt% to below 1 wt% and also due to the improved fibre volume fraction, which had been observed in the FFRPs, see Table 7.3. Table 7.4 summarizes the flexural and tensile properties of the RIFT-processed CeFRPs from the initial and final RIFT processes and compares them with the RIFT-processed GFRPs.

Table 7.4: Summary of flexural and tensile properties of RIFT-processed CeFRPs vs GFRPs

Matrix formulation	Initial RIFT CeF-PW		Final RIFT (OD-modification) CeF-PW						RIFT GF-PW+T^					
	v_f	E_{flex} (GPa)	v_f	E_{flex} (GPa)	E_t (GPa)	E_t/ρ (10^6 m^2s^{-2})	σ_t (MPa)	ε_t (%)	v_f	E_{flex} (GPa)	E_t (GPa)	E_t/ρ (10^6 m^2s^{-2})	σ_t (MPa)	ε_t (%)
Si0R0	-*	5.7 ±0.2	0.64	12.1 ±0.8	13.4 ±0.1	9.2 ±0.1	122 ±1	1.0 ±0.1	0.41	21.3 ±0.3	21.1 ±0.1	12.2 ±0.1	442 ±2	1.8 ±0.1
Si10R0	-*	6.4 ±1.1	0.67	13.0 ±1.0	13.7 ±0.9	9.2 ±0.6	130 ±3	1.1 ±0.1	0.38	19.4 ±0.9	19.6 ±0.3	11.4 ±0.2	370 ±12	1.8 ±0.1
Si0R9	-*	-*	0.65	11.4 ±1.0	13.2 ±0.3	9.1 ±0.2	142 ±2	1.3 ±0.1	0.42	21.9 ±0.2	20.7 ±0.2	11.6 ±0.1	430 ±1	1.8 ±0.1
Si10R9	-*	-*	0.67	12.7 ±1.1	14.1 ±0.5	9.6 ±0.3	147 ±2	1.3 ±0.1	0.44	23.5 ±0.6	21.7 ±0.6	11.8 ±0.3	411 ±3	1.7 ±0.1

*Values could not be obtained due to the poor quality of the composites.

^As the only balanced plain-woven glass fibre (balanced ratio of warp to weft yarns) was available in a very low density per unit area (GSM), in order to match the balanced plain-woven cellulose fibre, the balanced twill 2x2 glass fibre backing was added to the stacking sequence of plain-woven glass fibre. This minimally affected the mechanical properties of the GFRPs while having fewer numbers of layers for ease of manufacturing. Hence, the direct comparison between the CeFRPs-PW and GFRPs-PW+T could be made.

As discussed earlier, the general mechanical properties are primarily dictated by the mechanical properties of the fibre and its volume fraction, and the matrix modification only slightly affects them. From Table 7.4, the general mechanical properties, e.g. flexural moduli, tensile moduli and tensile strengths of both the CeFRPs and GFRPs were comparable for the different matrix formulations.

As for the final RIFT-processed FFRPs, it was also observed that the general mechanical properties of the final RIFT-processed CeFRPs were generally inferior to those of the RIFT-processed GFRPs-PW+T even with a 59% higher average fibre volume fraction. Up to two times lower flexural and tensile moduli were observed for the final RIFT-processed CeFRPs, for example. Additionally, the tensile strengths for the final RIFT-processed CeFRPs were found to be up to four times lower than those of the RIFT-processed GFRPs. Also, up to two times lower tensile failure strains were recorded for the final RIFT-processed CeFRPs. This was entirely due to the inferior mechanical properties of the CeFs compared to those of the GFs [38][40]. With a 52% lower tensile modulus and a 80% lower tensile strength of the CeFs and a 59% higher average fibre volume fraction of the CeFRPs, only a 24% lower tensile modulus and a 49% lower tensile strength would be expected for the CeFRPs using the rule of mixtures [1][149][150].

However, due to the low density of the CeFs [4], the specific tensile moduli of the CeFRPs, E_t/ρ, were found to be only 21% lower than the values from the GFRPs, see Table 7.4.

The tensile modulus of 13.4 GPa for the final RIFT-processed Si0R0 CeFRP-PW was found to be in good agreement with the value of 13 GPa previously reported by Porcher Industries [38], with less than a 5% difference. However, due to the significantly lower tensile failure strain of the present CeFRP, the tensile strength for the present CeFRP was found to be 24% lower than the value of 160 MPa obtained from Porcher Industries [38]. It is also noteworthy that a 45% higher fibre volume fraction was achieved in the present study and the processing method used by Porcher Industries is not known. Hence, this comparison is not completely valid.

For the Si0R0 GFRPs, it was found that the general mechanical properties, e.g. tensile modulus and tensile strength obtained from the present study were up to 20% lower than those obtained from Performance Composites [3], see Table 2.8. Such lower mechanical properties could be explained by the 20% lower fibre volume fraction of the GFRPs used in the present study.

Again, it is noted that the present study used a higher curing temperature to manufacture the GFRPs, and the GFs used to manufacture the two GFRPs were from different suppliers. This may result in a variation of their mechanical properties.

7.2.4 Flexural and Tensile Properties of Final RIFT- and RTM-processed NFRPs vs GFRPs

A significant improvement of the general mechanical properties of the RIFT-processed NFRPs was established via the OD-modification (final RIFT process). Although the RIFT and RTM processes share similar principles, they may yield significantly different composite properties. A comparison between the final RIFT- and RTM-processed FRPs is described below.

7.2.4.1 *Flexural and Tensile Properties of Final RIFT- and RTM-processed FFRPs vs GFRPs*

Table 7.5 summarizes the flexural and tensile properties of the final RIFT-processed (OD-modified) FFRPs and the RTM-processed FFRPs and compares them with the RIFT- and RTM-processed GFRPs. The typical tensile stress-strain curves for these FRPs are shown in Figure 7.1.

Table 7.5: Summary of flexural and tensile properties of final RIFT- and RTM-processed FFRPs vs GFRPs

Matrix formu-lation	**Final RIFT (OD-modification) – FF-UD**						**RTM – FF-UD***					
	v_f	E_{flex} (GPa)	E_t (GPa)	E_t/ρ ($10^6 m^2 s^{-2}$)	σ_t (MPa)	ε_t (%)	v_f	E_{flex} (GPa)	E_t (GPa)	E_t/ρ ($10^6 m^2 s^{-2}$)	σ_t (MPa)	ε_t (%)
Si0R0	0.44	18.7 ±0.6	20.1 ±0.1	14.7±0.1	163 ±2	1.2 ±0.1	-	-	-	-	-	-
Si10R0	0.40	14.2 ±0.2	17.7 ±0.2	12.8±0.1	161 ±5	1.1 ±0.1	0.45	28.8 ±0.5	27.9 ±0.2	19.9±0.2	194 ±8	1.0 ±0.1
Si0R9	0.36	14.1 ±0.6	15.5 ±0.4	11.8±0.3	153 ±5	1.4 ±0.1	-	-	-	-	-	-
Si10R9	0.44	16.1 ±0.6	17.2 ±0.2	12.5±0.1	151 ±5	1.4 ±0.3	-	-	-	-	-	-
	RIFT – GF-UD						**RTM – GF-UD***					
Si0R0	0.61	51.5 ±3.4	46.5 ±1.5	22.5±0.7	1144 ±25	1.9 ±0.1	-	-	-	-	-	-
Si10R0	0.55	51.7 ±10.6	41.2 ±1.4	20.6±0.7	1018 ±52	2.0 ±0.1	0.62	53.4 ±0.3	51.9 ±0.1	24.6±0.1	1167 ±6	2.0 ±0.1
Si0R9	0.65	54.1 ±8.7	44.7 ±0.5	21.1±0.2	1243 ±46	2.1 ±0.1	-	-	-	-	-	-
Si10R9	0.65	54.7 ±1.9	45.8 ±0.4	21.5±0.2	1263 ±37	2.1 ±0.2	-	-	-	-	-	-

*Because the flexural and tensile properties were minimally affected by the matrix formulation, the tests were only conducted on Si10R0 modified FRPs from the RTM process.

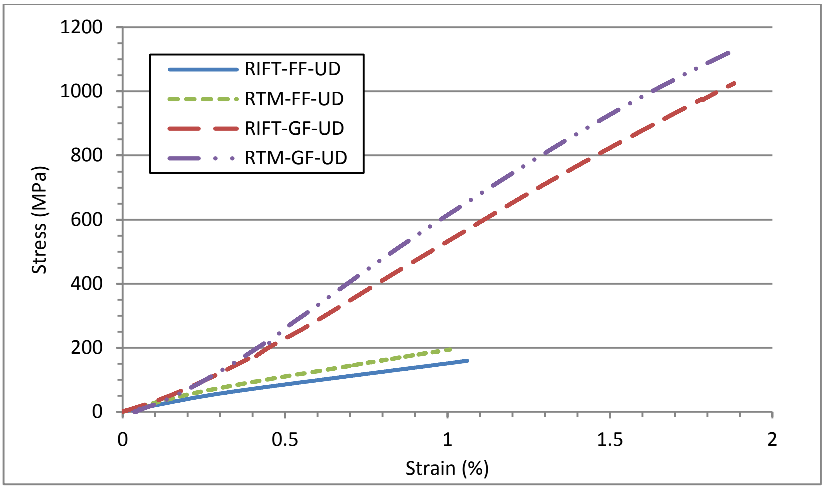

Figure 7.1: Tensile stress-strain for the RIFT- and RTM-processed FFRPs vs GFRPs

From Table 7.5 and Figure 7.1, the RTM process was found to generally result in better general mechanical properties of the FFRPs, e.g. higher flexural moduli, higher tensile moduli and higher tensile strengths, compared to the values obtained from the final RIFT process. A major reason for this was due to a somewhat higher fibre volume fraction of the RTM-processed FFRPs. The above proposals are supported by the slightly higher tensile moduli and tensile strengths for the RTM-processed GFRPs which were observed, compared to those from the RIFT process due to a slightly higher fibre volume fraction in the RTM-processed GFRPs. As discussed in section ‘6.5’, another cause for the better mechanical performance of the RTM-processed FFRP was due to the lower amount of moisture dissolved in the epoxy matrices during the RTM manufacturing method, compared to the RIFT process.

In the RTM-processed FRPs, up to two times lower flexural and tensile moduli were observed when comparing the FFRP and the GFRP due to a 27% lower fibre volume fraction achieved in the FFRP and about a 30% lower tensile modulus of the FFs [4][40], see Table 2.8. Additionally, a 27% lower fibre volume fraction and an 85% lower tensile strength of the FFs would be expected to result in up to six times lower tensile strength of the FFRP compared to the GFRP using the rule of mixtures [1][149][150]. These findings are in very good agreement with the observed results. However, the specific tensile modulus, E_t/ρ, of the RTM-processed FFRP was found to be only 24% lower than the RTM-processed GFRP. Again, this was due to the lower density of the FFs [4][40].

Despite the improved general mechanical properties of the RTM-processed FFRP compared to the RIFT-processed FFRPs, see Table 7.5, they were still significantly inferior to previously reported values of 35 GPa and 365 MPa by Lineo [43], with respect to the tensile modulus and tensile strength, see Table 2.8. Up to a 20% lower tensile modulus and a 47% lower tensile strength were recorded for the present RTM-processed FFRP. However, the 10% lower volume fraction measured would only be accepted to produce a 9% decrease in the values of tensile modulus and the tensile strength. Despite both of the two FFRPs being produced via the RTM manufacturing process, the curing schedule used by Lineo [43] is not known. As discussed earlier, the mechanical properties of the FFs may vary depending on the sources from which they were harvested and the detailed extracting processes. Also the existence of fibre waviness/crimping in the FFs used in the present study may lead to a decrease in the mechanical properties of the FFRPs.

The mechanical properties of the RTM-processed GFRP were generally superior to those obtained from Performance Composites [3] with a 30% higher tensile modulus and a 17% higher tensile strength respectively, see Table 2.8. As discussed earlier, the present study used a higher curing temperature and the GFs used to manufacture the two GFRPs were from different suppliers. This may result in a variation of their mechanical properties.

It is noted that the general mechanical properties of the RTM-processed Si10R0 FFRP and GFRP were used in the comparison with the unmodified (Si0R0) FFRP studied by Lineo [43] and the unmodified (Si0R0) GFRP studied by Performance Composites [3]. However, Manjunatha and his colleagues [110] suggested that modifying the FRPs with silica-nanoparticles slightly improved the tensile modulus and tensile strength only. Indeed, from Table 7.5, an increase in tensile modulus and tensile strength would be expected, if equal fibre volume fractions were obtained.

7.2.4.2 *Flexural and Tensile Properties of Final RIFT- and RTM-processed CeFRPs vs GFRPs*

Table 7.6 summarizes the flexural and tensile properties of the final RIFT-processed (OD-modified) CeFRPs and the RTM-processed CeFRPs and compares them with the RIFT- and RTM-processed GFRPs. The typical tensile stress-strain curves for these FRPs are shown in Figure 7.2.

Table 7.6: Summary of flexural and tensile properties of final RIFT- and RTM-processed CeFRPs vs GFRPs

Matrix formu-lation	Final RIFT (OD-modification) – CeF-PW						RTM – CeF-PW*					
	v_f	E_{flex} (GPa)	E_t (GPa)	E_t/ρ ($10^6 m^2 s^{-2}$)	σ_t (MPa)	ε_t (%)	v_f	E_{flex} (GPa)	E_t (GPa)	E_t/ρ ($10^6 m^2 s^{-2}$)	σ_t (MPa)	ε_t (%)
Si0R0	0.64	12.1 ±0.8	13.4 ±0.1	9.2±0.1	122 ±1	1.0 ±0.1	-	-	-	-	-	-
Si10R0	0.67	13.0 ±1.0	13.7 ±0.9	9.2±0.6	130 ±3	1.1 ±0.1	0.38^	15.1 ±0.4	14.1 ±1.1	10.1±0.8	111 ±2	1.0 ±0.3
Si0R9	0.65	11.4 ±1.0	13.2 0.3	9.1±0.2	142 ±2	1.3 ±0.1	-	-	-	-	-	-
Si10R9	0.67	12.7 ±1.1	14.1 0.5	9.6±0.3	147 ±2	1.3 ±0.1	-	-	-	-	-	-
	RIFT – GF-PW+T†						RTM – GF-PW+T*†					
Si0R0	0.41	21.3 ±0.3	21.1 ±0.1	12.2±0.1	442 ±2	1.8 ±0.1	-	-	-	-	-	-
Si10R0	0.38	19.4 ±0.9	19.6 ±0.3	11.4±0.2	370 ±12	1.8 ±0.1	0.44	25.9 ±0.4	24.5 ±0.2	13.2±0.1	461 ±42	1.7 ±0.2
Si0R9	0.42	21.9 ±0.2	20.7 ±0.2	11.6±0.1	430 ±1	1.8 ±0.1	-	-	-	-	-	-
Si10R9	0.44	23.5 ±0.6	21.7 ±0.6	11.8±0.3	411 ±3	1.7 ±0.1	-	-	-	-	-	-

*Because the flexural and tensile properties were minimally affected by the matrix formulation, the tests were only conducted on Si10R0 modified FRPs from the RTM process.

^Highest fibre volume fraction achieved in RTM process for pure CeFRPs.

†As the only balanced plain-woven glass fibre (balanced ratio of warp to weft yarns) was available in a very low density per unit area (GSM), in order to match the balanced plain-woven cellulose fibre, the balanced twill 2x2 glass fibre backing was added to the stacking sequence of plain-woven glass fibre. This minimally affected the mechanical properties of the GFRPs while having fewer numbers of layers for ease of manufacturing. Hence, the direct comparison between the CeFRPs-PW and GFRPs-PW+T could be made.

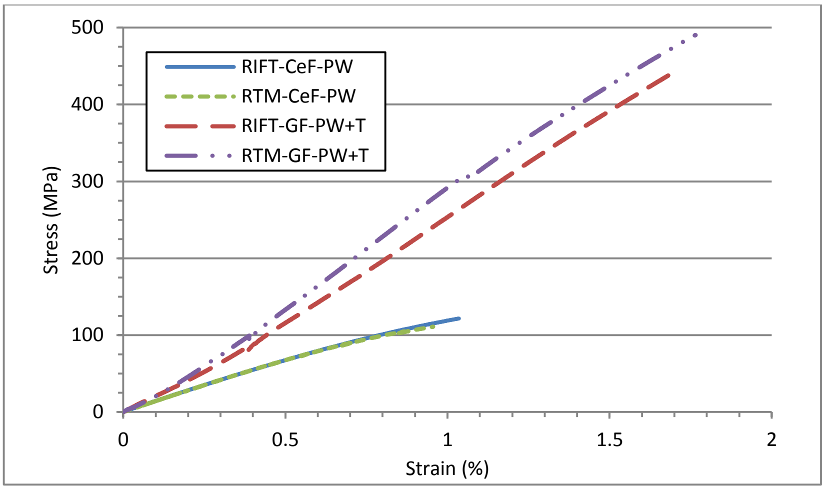

Figure 7.2: Tensile stress-strain for the RIFT- and RTM-processed CeFRPs vs GFRPs

As may be seen from Table 7.6 and Figure 7.2, considering a 76% lower fibre volume fraction was observed for the RTM-processed CeFRPs compared to the RIFT-processed CeFRPs, only a 17% lower tensile strength was observed for the RTM-processed CeFRPs. In contrast, a slightly higher flexural and tensile moduli were observed for the RTM-processed CeFRP, compared to those from the RIFT process. The tensile failure strain of the CeFRPs from the two manufacturing methods was found to be comparable because it was dictated by the tensile failure strain of the CeFs. Again, due to the lower content of water dissolved in the epoxy matrices during the RTM manufacturing process, a higher mechanical performance of the RTM-processed CeFRP was observed. Again, up to a 25% higher tensile modulus and tensile strength for the RTM-processed GFRP were observed, compared to those from the RIFT process. This could be due to a slightly higher fibre volume fraction in the RTM-processed GFRPs.

It was found that up to two times lower flexural modulus, tensile modulus and tensile failure strain and up to four times lower tensile strength were observed in the RTM-processed CeFRP, compared to the RTM-processed GFRP. However, the specific tensile modulus of the RTM-processed CeFRP was found to be only 31% lower than the RTM-processed GFRP. Again, this was due to the lower fibre volume fraction achieved in the CeFRP and the inferior mechanical properties of the CeFs [38][40], see Table 2.8. Such a lower fibre volume fraction of the CeFRP and inferior mechanical properties of the CeFs would be expected to contribute to an approximately 60% reduction in flexural modulus and tensile modulus and an 80% reduction in tensile strength using the rule of mixtures [1][149][150]. This is in good agreement with the observed values.

The tensile modulus of 14.1 GPa for the RTM-processed Si10R0 CeFRP was found to be 8% higher, compared to that previously reported results of 13 GPa by Porcher Industries [38], even with an 18% lower fibre volume fraction. In contrast, the tensile strength of the RTM-processed Si10R0 CeFRP was found to be about 44% lower. However, such a lower fibre volume fraction would only be expected to contribute to a 13% reduction in the tensile strength. This was probably due to the differences in the manufacturing settings, where the process used by Porcher Industries [38] is not known.

On the other hand, the general mechanical properties of the RTM-processed Si10R0 GFRP were found to in a good agreement with those obtained for the GFRP from Performance Composites [3] with less than a 5% difference in all the properties, see Table 2.8. A tensile modulus and tensile strength of 25.9 GPa and 461 MPa respectively, for the present GFRP were measured respectively, compared to values of 25 GPa and 440 MPa for the GFRP from Performance Composites [3].

Again, It is noted that the general mechanical properties of the RTM-processed Si10R0 CeFRP and GFRP were used in the comparison with the unmodified (Si0R0) CeFRP studied by Porcher Industries [38] and unmodified (Si0R0) GFRP studied by Performance Composites [3]. However, modifying the FRPs with silica-nanoparticles slightly affects the tensile modulus and tensile strength [110]. Hence, the comparison between the Si0R0 and Si10R0 was principally valid. This may be seen in Table 7.6 where the minimal variation of the results among the different matrix modifications was observed. Whether the final RIFT process would improve the fracture energy of the NFRPs will be discussed in ‘Chapter 8 Fracture Properties’.

7.3 Analytical Model of Tensile Young’s Modulus of Fibre-reinforced Modified Matrix Composites

7.3.1 Introduction

A fibre-reinforced composite (FRC) is a mixture of two or more distinct constituents on a microscopic scale with different properties, i.e. the fibre/fabric reinforcement and the polymer matrix [1]. The reinforcement can be in either continuous or discontinuous forms. The orientation of the reinforcement can be designed to give the mechanical properties where needed. Due to the complex mechanical behaviour of the FRCs, it is beneficial to be able to predict the mechanical properties of the FRPs based on the properties of the fibre/fabric reinforcement and the matrix [1].

7.3.2 Unidirectional Flax Fibre-Reinforced Plastics (FFRPs - UD)

The longitudinal Young’s modulus of the continuous unidirectional fibre-reinforced composites can be predicted using the rule of mixtures [1][149][150].

7.3.2.1 *The Rule of Mixtures*

The longitudinal Young’s modulus of the continuous unidirectional fibre-reinforced composites can be expressed by:

$$E_1 = E_m v_m + E_f v_f \tag{7.1}$$

where E_m and E_f are the Young’s modulus of the matrix and the reinforcement respectively, and v_m, v_f and v_v are the volume fraction of the matrix, reinforcement and voids respectively and:

$$1 = v_m + v_f + v_v \tag{7.2}$$

All the parameters used to predict the tensile modulus of the unidirectional FFRPs using the rule of mixtures are summarized in Table 7.7. The predictions of the tensile modulus of the FFRPs are then summarized in Table 7.8 and Figure 7.3.

Table 7.7: Parameters used in predicting the Young's modulus of unidirectional FFRPs

Parameter	Symbol	Unit	Value	Source
Young's modulus of flax fibre	E_f	GPa	50.0±9.5	[41]&present study
Young's modulus of epoxy polymer, Si0R0	E_m	GPa	2.90±0.09	[56]
Young's modulus of epoxy polymer, Si10R0	E_m	GPa	3.28±0.08	[56]
Young's modulus of epoxy polymer, Si0R9	E_m	GPa	2.31±0.04	[56]
Young's modulus of epoxy polymer, Si10R9	E_m	GPa	2.74±0.05	[56]
Volume fraction of flax fibre	v_f	-	0.41±0.03	Present study
Volume fraction of matrix	v_m	-	0.58±0.04	Present study
Volume fraction of voids	v_v	-	0.01	Present study

Table 7.8: Summary of the measured and predicted values of the Young's modulus of unidirectional FFRPs

Matrix formulation	Measured values*		Predicted values^		Percentage difference, %†	t-test P-value**
	v_f	E (GPa)	E (GPa)	Normalized E (GPa)		
Si0R0	0.44	20.1±0.1	24.0±6.8	25.3±7.1	23	0.54
Si10R0	0.40	17.7±0.2	24.4±6.9	23.9±6.7	30	0.45
Si0R9	0.36	15.5±0.4	23.4±6.8	21.1±6.2	31	0.46
Si10R9	0.44	17.2±0.2	23.8±6.8	25.1±7.1	38	0.38

*The measured values of E of the final RIFT-processed FFRPs

^The predicted values of E (predicted E at $v_f = 0.41$) were normalized to match the v_f of the measured values of E with the same matrix formulation.

†Percentage difference between measured E and normalized predicted E

**Comparison of measured E and normalized predicted E using two-tailed independent t-test with a confidence interval value, α, of 0.05 (unequal variances assumed).

P-value ≤ 0.05 = the two groups are significantly different and P-value > 0.05 = the two groups are insignificantly different.

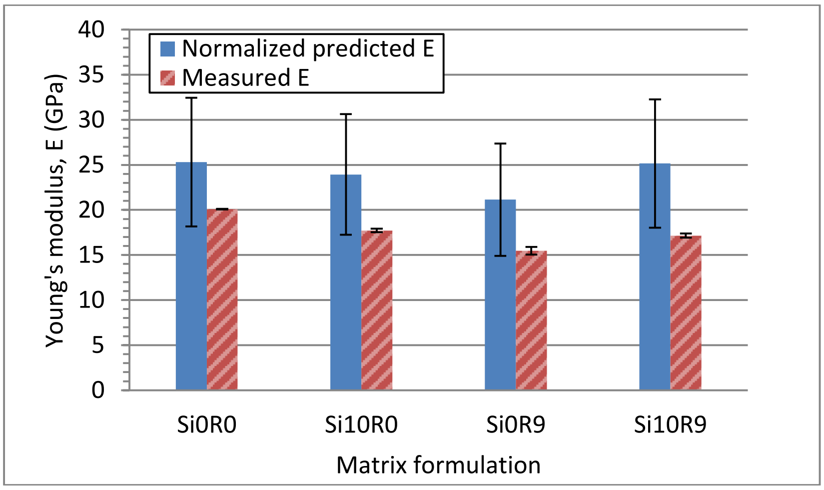

Figure 7.3: The measured and predicted normalized values of the Young's modulus of the unidirectional FFRPs

As may be seen from Table 7.8 and Figure 7.3, although the normalized predicted results were slightly higher than the measured values, the experimental data was still within the expected variations of the predicted results. This was because the model assumed that 1) the fibres were perfectly aligned with no fibre crimping or waviness, and 2) the fibre-matrix interfacial adhesion was perfect. Also, the Young's modulus of the FFs is largely dependent on the measured gauge length and diameter. The FFs are made of spun mechanical interlocked microfibrils [4] bonded together with pectin [36] and there are naturally occurring defects throughout the fibres, which are susceptible to fibre breakage, and manufacturing defects, e.g. fibre-matrix interfacial defects and voids. Hence, the fibres or microfibres may break at defects, where the measured Young's modulus of the composites may be compromised.

The wide variations of the predicted values of Young's modulus was noticed as the properties of the FFs have very large variations depending on the harvesting conditions, origins, extraction processes as well as naturally occurring intrinsic defects [4][7].

7.3.3 Plain-woven Cellulose Fibre-Reinforced Plastics (CeFRPs - PW)

Woven fibre-reinforced composites have gained interests in engineering applications due to their balanced properties, excellent impact resistance and ease of handling [153]. However, due to the interlacing architecture of the plain-woven fibre/fabric, the mechanical behaviour of the composites is not well understood [153], see Figure 7.4.

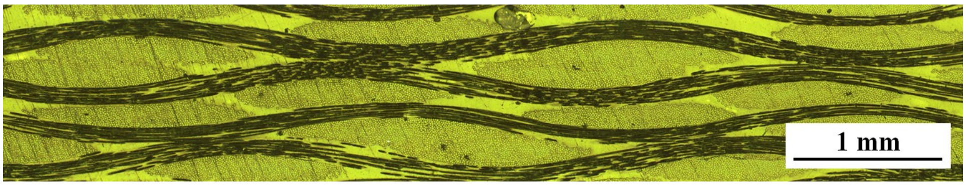

Figure 7.4: An optical microscopy image of a cross-section of CeFRPs in the present study

Efforts have been made to develop a number of analytical models to predict the elastic modulus of the woven fibre composites. Ishikawa and Chou [153] proposed three different analytical models to predict the modulus of composites based on the classical laminate theory (CLT), namely 1) a mosaic model (i.e. the fibre continuity and undulation are not taken into account), 2) a fibre undulation model (i.e. the continuity and undulation of fibres are considered and the model is suitable for plain-woven composites), and 3) a bridging model (i.e. where load transfer among the interlaced regions is simulated and the model is suitable for satin-woven composites). Naik and Shembekar [154] further developed the models of Ishikawa and Chou to evaluate different elastic properties of plain-woven fibre composites considering the fibre undulations in two orthogonal directions. More detailed trigonometric functions were also used. Redman and Douglas [155] developed a model to predict the stiffness of braided fibre composites based on the CLT and the rule of mixtures, where the stiffness of each offset fibre is analysed separately. Thus, the fibre undulation can be neglected. Carey et al. [156] developed rectilinear and sinusoidal crimp models for a 2D braided fibre composite to predict the elastic modulus using the CLT and the principle of equivalent strain energy. However, none of these models considered the interaction of orthogonal interlacing yarns.

Thus, a significant amount of research has been conducted [157] to analyse the elastic properties of woven composites and to determine detailed stress fields from the mechanical properties of the constituents using the finite element analysis (FEA). However, complexity is the main drawback. A new analytical solution for elastic modulus of plain-woven composites was established by Xiong et al. [157]. The model considers the interaction forces between the warp and weft yarns. The two orthogonal yarns in a micromechanical unit cell are idealized as curved beams using sinusoidal shape functions [157]. This modified curve beam model employs the strain energy of the representative unit cell. The advantage of this model is that it requires fewer geometric parameters of the warp and weft yarns than the other models mentioned above [157]. This model is considered in detail below.

7.3.3.1 *The Modified Curve Beam Model*

The idealized 2D orthogonal plain-woven fibre-reinforced composite unit cell is shown in Figure 7.5, where the two orthogonal yarns can be idealized as curved beams using sinusoidal shape functions [157]. The cross-section of a typical warp or weft yarn can be simplified in order to calculate easily the area of the cross-section, see Figure 7.6.

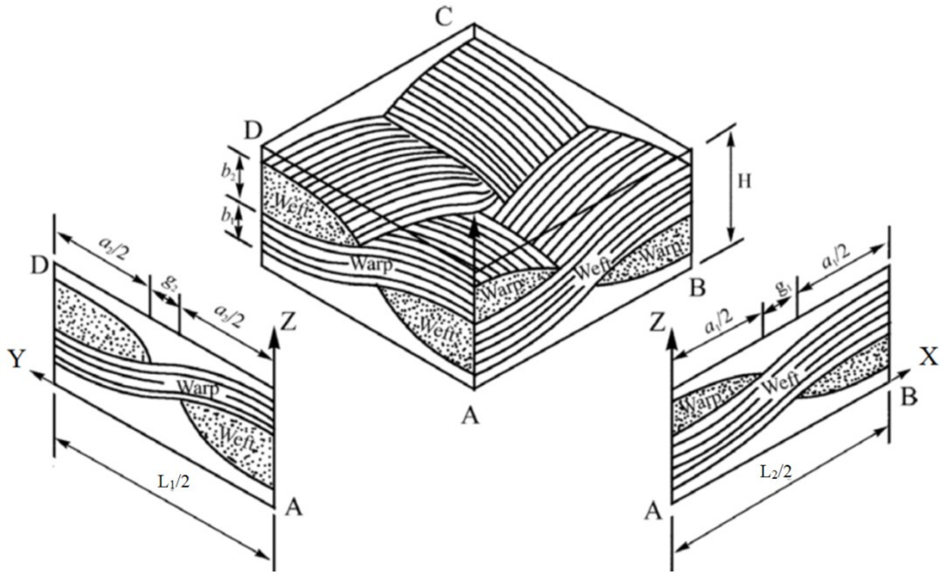

Figure 7.5: An idealized 2D orthogonal plain-woven lamina unit cell [158]

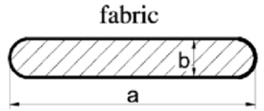

Figure 7.6: An approximate cross-section of a typical warp and weft yarn [157]

The cross-sectional area and the moment of inertia of a warp or weft yarn can be calculated by (see Figure 7.5 for definition of symbols):

$$A_i = \frac{1}{4}\pi b_i^2 + b_i\left(a_i - b_i\right) \tag{7.3}$$

and

$$I_i = \frac{1}{64}\pi b_i^4 + \frac{1}{12}b_i^3\left(a_i - b_i\right) \tag{7.4}$$

where a_i and b_i are the width and height of the simplified cross-section of a warp ($i = 1$) or weft yarn ($i = 2$), shown in Figure 7.6. The path of the curved beams can be expressed by sinusoidal shape functions as:

$$z_1 = \frac{b_2}{2}\sin\frac{2\pi x}{L_1} \qquad z_2 = \frac{b_1}{2}\sin\frac{2\pi y}{L_2} \tag{7.5}$$

where

$$L_1 = 2a_2 + 2g_2 \qquad L_2 = 2a_1 + 2g_1 \tag{7.6}$$

Based on the potential energy principle, the shift of the warp yarn along the direction of the external tensile load, Δ_t, can be calculated by:

$$\Delta_t = \frac{J}{E_f}N_1 = \frac{2J_2 + 2J_7 - \dfrac{J_4^2}{2J_1} + \dfrac{2J_4J_5J_6 - 2J_1J_6^2 - J_4^2J_5^2/\left(2J_1\right)}{4J_1J_3 + 4J_1J_{10} - J_5^2 - J_1J_9^2/J_8}}{E_f}N_1 \tag{7.7}$$

where E_f is the elastic modulus of the fibre, N_1 is the normal force acting on the warp yarn and:

$$J_1 = \frac{1}{I_1}\int_0^{L_1/2}\left[\sqrt{1+\frac{b_2^2\pi^2}{L_1^2}\sin^2\left(\frac{2\pi x}{L_1}\right)}\right]dx \tag{7.8}$$

$$J_2 = \frac{b_2^2}{4I_1}\int_0^{L_1/2}\left[1-\cos\left(\frac{2\pi x}{L_1}\right)\right]^2\left[\sqrt{1+\frac{b_2^2\pi^2}{L_1^2}\sin^2\left(\frac{2\pi x}{L_1}\right)}\right]dx \tag{7.9}$$

$$J_3 = \frac{1}{4I_1}\int_0^{L_1/2}x^2\left[\sqrt{1+\frac{b_2^2\pi^2}{L_1^2}\sin^2\left(\frac{2\pi x}{L_1}\right)}\right]dx \tag{7.10}$$

$$J_4 = \frac{b_2}{I_1}\int_0^{L_1/2}\left[1-\cos\left(\frac{2\pi x}{L_1}\right)\right]\left[\sqrt{1+\frac{b_2^2\pi^2}{L_1^2}\sin^2\left(\frac{2\pi x}{L_1}\right)}\right]dx \tag{7.11}$$

$$J_5 = \frac{1}{I_1}\int_0^{L_1/2}x\left[\sqrt{1+\frac{b_2^2\pi^2}{L_1^2}\sin^2\left(\frac{2\pi x}{L_1}\right)}\right]dx \tag{7.12}$$

$$J_6 = \frac{b_2}{2I_1}\int_0^{L_1/2}x\left[1-\cos\left(\frac{2\pi x}{L_1}\right)\right]\left[\sqrt{1+\frac{b_2^2\pi^2}{L_1^2}\sin^2\left(\frac{2\pi x}{L_1}\right)}\right]dx \tag{7.13}$$

$$J_7 = \frac{1}{A_1}\int_0^{L_1/2}\frac{1}{\sqrt{1+\frac{b_2^2\pi^2}{L_1^2}\sin^2\left(\frac{2\pi x}{L_1}\right)}}dx \tag{7.14}$$

$$J_8 = \frac{1}{I_2}\int_0^{L_2/2}\left[\sqrt{1+\frac{b_1^2\pi^2}{L_2^2}\sin^2\left(\frac{2\pi y}{L_2}\right)}\right]dy \tag{7.15}$$

$$J_9 = \frac{1}{I_2}\int_0^{L_2/2}y\left[\sqrt{1+\frac{b_1^2\pi^2}{L_2^2}\sin^2\left(\frac{2\pi y}{L_2}\right)}\right]dy \tag{7.16}$$

$$J_{10} = \frac{1}{I_2}\int_0^{L_2/2}y^2\left[\sqrt{1+\frac{b_1^2\pi^2}{L_2^2}\sin^2\left(\frac{2\pi y}{L_2}\right)}\right]dy \tag{7.17}$$

where L_i is the undulated length of the warp or weft curved beam and A_i is the cross-sectional area of the warp or weft yarn. The tensile modulus of 2D orthogonal plain-woven fabric, E_{tt}, can be obtained by:

$$E_{tt} = \frac{N_1 L_1}{A_1\Delta_t} = \frac{E_f L_1 / A_1}{2J_2 + 2J_7 - \frac{J_4^2}{2J_1} + \frac{2J_4J_5J_6 - 2J_1J_6^2 - J_4^2J_5^2/\left(2J_1\right)}{4J_1J_3 + 4J_1J_{10} - J_5^2 - J_1J_9^2/J_8}} \tag{7.18}$$

Using the rule of mixtures, the elastic modulus of the plain-woven fibre-reinforced composite can be expressed by:

$$E = E_{tt} v_{f2} + E_m \left(1 - v_{f2}\right) = E_f \frac{L_1 v_{f2}}{A_1 J} + E_m \left(1 - v_{f2}\right) \tag{7.19}$$

All parameters used to predict the tensile modulus of the plain-woven CeFRPs using the modified curve beam model are summarized in Table 7.9. The predictions of the tensile modulus of the CeFRPs are then summarized in Table 7.10 and Figure 7.7.

Table 7.9: Parameters used in predicting the Young's modulus of plain-woven CeFRPs

Parameter	Symbol	Unit	Value	Source
Young's modulus of cellulose fibre	E_f	GPa	35.0±3.6	[38]&present study
Young's modulus of epoxy polymer, Si0R0	E_m	GPa	2.90±0.09	[56]
Young's modulus of epoxy polymer, Si10R0	E_m	GPa	3.28±0.08	[56]
Young's modulus of epoxy polymer, Si0R9	E_m	GPa	2.31±0.04	[56]
Young's modulus of epoxy polymer, Si10R9	E_m	GPa	2.74±0.05	[56]
Cellulose fibre volume fraction	v_f	-	0.62±0.04	Present study
Volume fraction of cellulose fibre (longitudinal direction)	v_{f1}	-	0.31±0.02	Present study
Volume fraction of cellulose fibre (transverse direction)	v_{f2}	-	0.31±0.02	Present study
Volume fraction of matrix	v_m	-	0.37±0.04	Present study
Volume fraction of voids	v_v	-	0.01	Present study
Width of a simplified cross-section of a warp/weft yarn	a_1, a_2	mm	1.30	Present study
Height of a simplified cross-section of a warp/weft yarn	b_1, b_2	mm	0.18	Present study
Warp/weft interyarn gap	g_1, g_2	mm	0.10	Present study
Undulated length of a warp/weft curved beam	L_1, L_2	mm	2.80	Present study

Table 7.10: Summary of the measured and predicted values of the Young's modulus of plain-woven CeFRPs

Matrix formulation	Measured values*		Predicted values^		Percentage difference, %†	t-test P-value**
	v_f	*E* (GPa)	*E* (GPa)	Normalized *E* (GPa)		
Si0R0	0.64	13.4±0.1	12.0±2.4	12.3±2.5	1	0.96
Si10R0	0.67	13.7±0.9	12.2±2.4	12.9±2.5	2	0.92
Si0R9	0.65	13.2±0.3	11.8±2.5	12.3±2.6	1	0.97
Si10R9	0.67	14.1±0.5	12.0±2.5	12.7±2.6	3	0.88

*The measured values of *E* of the final RIFT-processed CeFRPs

^The predicted values of *E* (predicted *E* at $v_f = 0.62$) were normalized to match the v_f of the measured values of *E* with the same matrix formulation.

†Percentage difference between measured *E* and normalized predicted *E*

**Comparison of measured *E* and normalized predicted *E* using two-tailed independent t-test with a confidence interval value, α, of 0.05 (unequal variances assumed).

P-value ≤ 0.05 = the two groups are significantly different and P-value > 0.05 = the two groups are insignificantly different.

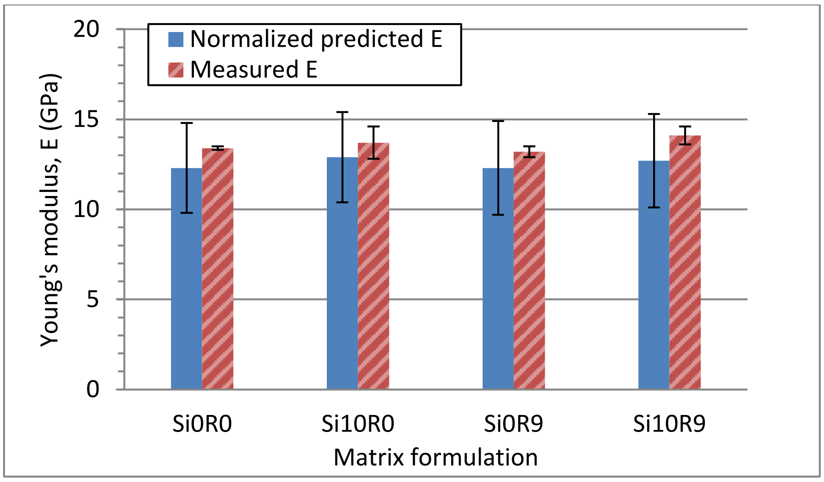

Figure 7.7: The measured and predicted values of the Young's modulus of the plain-woven CeFRPs

As may be seen from Table 7.10 and Figure 7.7, the comparison between the measured and the normalized predicted Young' moduli using a t-test shows a very good prediction. Although the interaction between the orthogonal interlacing warp and weft yarns has been considered, it was clear that the model has its drawbacks. The model simplified the complex cross-sectional area of both warp and weft yarns as a rounded rectangle which could result in an inaccurate prediction of the cross-sectional area and the moment of inertia of both warp and weft yarns. The model also depicted the paths of the warp and weft yarns using the sinusoidal shape functions, which could also result in an inaccurate prediction, see Figure 7.4 for the actual microstructure of a plain-woven FRP.

7.4 Concluding Remarks

The present chapter has summarized the finding of the general mechanical properties, which include the flexural modulus and tensile Young's modulus, tensile strength and tensile failure strain, of the FRPs manufactured by the two manufacturing methods used in the present study. A comparison of the values measured with the literature has also been discussed. Finally, a comparison of the experimental results with predictive analytical models of the tensile moduli for the unidirectional and plain-woven fibre-reinforced composites has been discussed.

It has been observed that the initial RIFT-processed NFRPs possessed very poor general mechanical properties due to the poor fibre-matrix interfacial adhesion, the low fibre volume fraction and the relatively high void content. Drying the NFs (termed the final RIFT process) significantly improved the fibre wettability and the fibre-matrix interfacial adhesion, and hence improved the fibre packing density and reduced the void content. As a result, the flexural and tensile properties were significantly enhanced. However, the flexural and tensile properties of the NFRPs manufactured by the RTM process were still slightly superior to those from the final RIFT process, due to a lower moisture content present in the NFs during the RTM manufacturing process. Hence, the water dissolution into the epoxy matrices was minimized and the fibre volume fraction of the RTM-processed NFRPs was improved. However, the general mechanical properties of either the final RIFT- or RTM-processed NFRPs were significantly inferior to those obtained from the GFRPs, due to the lower fibre volume fraction achieved in the NFRPs and/or the inferior mechanical properties of the NFs.

An analytical model for the unidirectional fibre-reinforced composites using the rule of mixtures slightly overpredicted the tensile modulus of the NFRPs because the model assumed that there was no fibre or manufacturing defect. Also the fibre misalignment and fibre waviness/crimping were not taken into account. However, the analytical model for the plain-woven fibre-reinforced composites took into account the fibre waviness/crimping and the interaction between the interlacing warp and weft yarns. As a result, this model accurately predicted the tensile modulus of the NFRPs.

However, whether the final RIFT process improved the fracture toughness, G_{IC}, of the NFRPs, will be discussed in the following chapter.

CHAPTER 8 FRACTURE PROPERTIES

8.1 Introduction

The present chapter first summarizes the studies on the interlaminar fracture energies, G_{IC}, of the RIFT-processed NFRPs, and their improvement using the different RIFT process optimization options. It then compares the values of G_{IC} with those from the NFRPs manufactured via the RTM process. A comparison of the fracture energies of the NFRPs with the GFRPs manufactured via the two processes is also made. The fracture and toughening mechanisms involved for the different materials are discussed. Finally, an analytical model for predicting the mode I interlaminar fracture energy is developed.

8.2 Fracture properties

8.2.1 **Mode I Interlaminar Fracture Properties of RIFT-processed NFRPs vs GFRPs – Initial Study**

The mode I interlaminar fracture energies of the NFRPs manufactured via the initial RIFT process are summarized in Table 8.1. The values for the RIFT-processed GFRPs are also given for comparison.

Table 8.1: Summary of mode I interlaminar fracture energies of RIFT-processed NFRPs vs GFRPs – Initial study

Fibre type and architecture	Matrix formulation	Fibre volume fraction, v_f	Void content, v_v (vol%)	Propagation fracture energy, G_{IC} (J/m^2)	Significance value of G_{IC} (GF-UD vs GF-PW+T), t-test P-value^
Unidirectional Flax (FF-UD)	Si0R0	0.31	15	19±5	-
	Si10R0	0.23	13	252±49	-
	Si0R9	0.38	17	139±29	-
	Si10R9	0.33	16	233±41	-
Plain-woven Cellulose (CeF-PW)	Si0R0	-*	14	20±1	-
	Si10R0	-*	16	23±2	-
Unidirectional Glass (GF-UD)	Si0R0	0.61	2	534±109	Si0R0: 0.901
	Si10R0	0.55	2	842±44	
	Si0R9	0.65	2	996±68	Si10R0: <0.001
	Si10R9	0.65	2	1257±56	
Plain-woven and Twill 2x2 Glass (GF-PW+T) †	Si0R0	0.41	2	541±36	Si0R9: 0.016
	Si10R0	0.38	2	621±59	
	Si0R9	0.42	2	1287±127	Si10R9: 0.096
	Si10R9	0.44	2	1372±73	

*Values could not be obtained due to the poor quality of the composites.

^Comparison of fracture energies of the GFRPs-UD and GFRPs-PW+T with the same matrix formulations using two-tailed independent t-test with a confidence interval value, α, of 0.05 (unequal variances assumed).

P-value ≤ 0.05 = the two groups are significantly different and P-value > 0.05 = the two groups are insignificantly different.

†These GFRP DCB specimens were backed with twill 2x2 GF fabric to increase the stiffness of the arms. The fracture plane was through the PW fabric layers.

It should be noted that in Table 8.1, and in all the Tables in the present Chapter, the values of the interlaminar fracture energy, G_{IC}, are the steady-state propagation values and the scatter is represented by ±one standard deviation.

Table 8.1 shows that the initial RIFT-processed NFRPs had significantly lower fracture energies than those of the GFRPs with the same fibre/fabric reinforcement architecture. For example, a fracture energy of 252 J/m^2 was measured for the silica-nanoparticle (Si10R0) modified FFRP, compared to a value of 842 J/m^2 for the Si10R0 GFRP-UD. This was due to the high moisture content in the NFs, which led to a poor physical properties of the NFRPs, see Table 5.6. Moisture contents of up to 10 wt% were measured for the NFRPs, compared to the negligible moisture content for the GFRPs, see Table 3.4. As a result, high void contents, low fibre volume fractions, poor fibre-matrix interfacial adhesion, and hence low fracture energies were observed for the NFRPs, see Table 8.1.

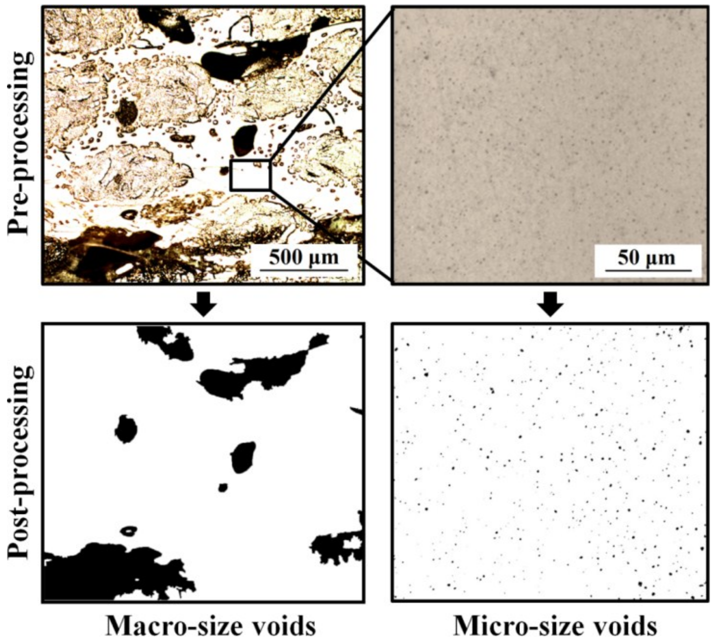

Figure 8.1 OM images of initial RIFT-processed Si0R0 FFRP showing macro-voids and micro-voids

The optical microscopy (OM) study of the composite cross-sections revealed a high number of macro-voids and micro-voids, see Figure 8.1, embedded within the initial RIFT-processed FFRPs. These were caused by the transformation of the water trapped in the NFs into steam at the high temperatures reached during curing of the epoxy matrix. This 1) restricted the contact between the fibres and polymer matrix and led to the high void contents of up to 17% in the NFRPs, and 2) promoted water dissolution in the epoxy matrices. As discussed earlier in 'Chapter 7 General Mechanical Properties', this was confirmed by the reduction of the glass transition temperature [147], see Table 5.6. For example, a glass transition temperature of 90°C was measured for the initial RIFT-processed unmodified (Si0R0) FFRP, compared to a value of 141°C for the glass transition temperature of the Si0R0 epoxy polymer. For comparison, a glass transition temperature of 146°C was measured for the Si0R0 GFRP-UD with only a minimal void content of 2%. The moisture absorption was also found to promote the inherent defects, e.g. voids and delamination, and reduce the degree of fibre-matrix adhesion, which resulted in a decrease in the measured interlaminar fracture energy [159]. High void contents and reduced glass transition temperatures were also observed in the initial RIFT-processed CeFRPs. As a result, poor fracture energies were also measured for the initial RIFT-processed CeFRPs. For example, a fracture energy of 20 J/m^2 was measured for the Si0R0 CeFRP-PW, compared to a value of 541 J/m^2 for the Si0R0 GFRP-PW+T.

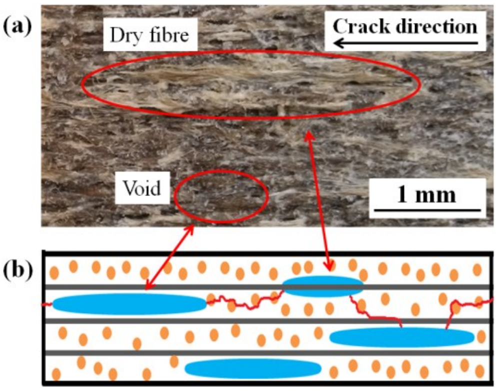

Figure 8.2: (a) Image of fracture surface of initial RIFT-processed FFRP and (b) graphical image of its cross-section with the presence of macro-voids and rubber-microparticles (red lines represent the crack path, blue eclipses represent macro-voids, orange circles represent rubber particles and grey lines represent fibre reinforcement)

Low fibre volume fractions were also observed in the initial RIFT-processed FFRPs due to the cellular structure and porous nature of the FFs [4], which restricted the compaction of the pre-laid-up FFs under vacuum pressure during the RIFT manufacturing method. Inspection of the fracture surfaces using SEM, as will be discussed in section '8.3.3.1.1', revealed that the debonded surface was relatively clean, indicating poor fibre-matrix interfacial adhesion. It can be seen that the fracture surface was covered with voids, which reduced the effective fracture-resisting area in the crack path of the composites, see Figure 8.2. These voids also initiated cracks by acting as pre-cracks and reduced the transverse load transfer between the fibres and the matrix which promoted brittle fracture behaviour (i.e. unstable crack (i.e. 'stick-slip') growth). Although the CeFs were uniform continuous fibres [38] with less intrinsic defects, compared to the FFs, similar fracture surfaces were also observed for the initial RIFT-processed CeFRPs.

For the GFs, the negligible moisture content gave no water evaporation into steam or water dissolution in the epoxy matrices, see Table 3.4. This was suggested by the relatively high glass transition temperatures, see Table 5.6, and the low void contents, see Table 8.1. The fracture surfaces of the RIFT-processed GFRPs revealed the fibre bridging and plastic deformation/shear yielding of epoxy matrices were operative toughening mechanisms, as will be discussed in section '8.3.3.2'. Also, the SEM images revealed that pieces of the epoxy matrix were attached to the surfaces of the GFs throughout the fracture surfaces, which arose from plastic deformation/shear yielding of the epoxy. This indicated a good degree of fibre-matrix interfacial adhesion in the GFRPs. A good fibre packing density was also achieved in the GFRPs. As a result, relatively high fibre volume fractions of 0.55 to 0.65 were achieved.

As discussed previously in section '5.4.6', the AFM images revealed that the morphology of the silica-nanoparticles and rubber-microparticles in the RIFT-processed FRPs with the same matrix formulations were identical, regardless of the type of reinforcement used. The AFM phase images of the Si0R0 FRPs revealed a relatively featureless microstructure that indicated a homogeneous microstructure. A good dispersion of silica-nanoparticles was observed in the Si10R0 FRPs, which indicated that the silica-nanoparticles could penetrate into the reinforcement. The phase-separable CTBN added to the Si0R9 FRPs was also found to be well-dispersed. However, for the Si10R9 FRPs, the rubber-microparticles were well dispersed but there was some degree of agglomeration of the silica-nanoparticles, see Figure 5.2

As will be discussed in section '8.3.2', for both NFRPs and GFRPs, the fracture surfaces of the Si0R0 FRPs were relatively smooth and glassy with some plastic deformation/shear yielding of the epoxy matrices evident, which is typical for a brittle thermosetting polymer [160]. The fracture surfaces of the Si10R0 FRPs exhibited a relatively brittle fracture with plastic void growth of the matrix initiated by debonding of the rigid silica-nanoparticles. Rubber particle cavitation was observed on the fracture surfaces of the rubber-microparticle (Si0R9) modified FRPs. Thus, void growth of the rubber particles and plastic deformation of the epoxy matrix had occurred. These observed toughening mechanisms were in a good agreement with the research by Hsieh et al. [56] and Kinloch & Taylor [160].

From Table 8.1, it can be seen that the addition of silica-nanoparticles had a greater impact on the fracture energy of the initial RIFT-processed FFRPs rather than the addition of rubber-microparticles. A fracture energy of 252 J/m^2 was measured for the Si10R0 FFRP, whilst only a value of 139 J/m^2 was recorded for the Si0R9 FFRP. The further addition of rubber-microparticles to the Si10R0 FFRP, to form a hybrid (Si10R9) modified FFRP, slightly decreased the fracture energy, with a value of 233 J/m^2. This was probably because the water molecules could disrupt the rubber–matrix interface and degrade the fracture behaviour of the rubber [159][161]. Also, the presence of macro-voids and the large size of the rubber-microparticles (i.e. larger than 1 μm, see Figure 5.2) resulted in the non-homogeneous properties of different matrix regions, where the crack tended to propagate along the path with the lowest resistance to propagation [112], e.g. voids, brittle matrices, softened rubber-microparticles, fibre-matrix interfaces and particle-matrix interfaces. Hence, a reduced fracture energy was obtained in the Si0R9 FFRP. In contrast, the silica-nanoparticles were not affected by the water molecules and, due to the small size of the silica-nanoparticles (i.e. approximately 20 nm), a good dispersion of the particles was achieved (giving homogeneous properties), see Figure 5.2. However, the CeFRPs did not show similar trend to the FFRPs. A fracture energy of 20 J/m^2 was measured for the Si0R0 CeFRPs, whilst the addition of silica-nanoparticles did not statistically increase the fracture energy. Finally, due to the poor quality of the initial RIFT-processed CeFRPs, the properties of the Si0R9 and Si10R9 modified CeFRPs could not be determined.

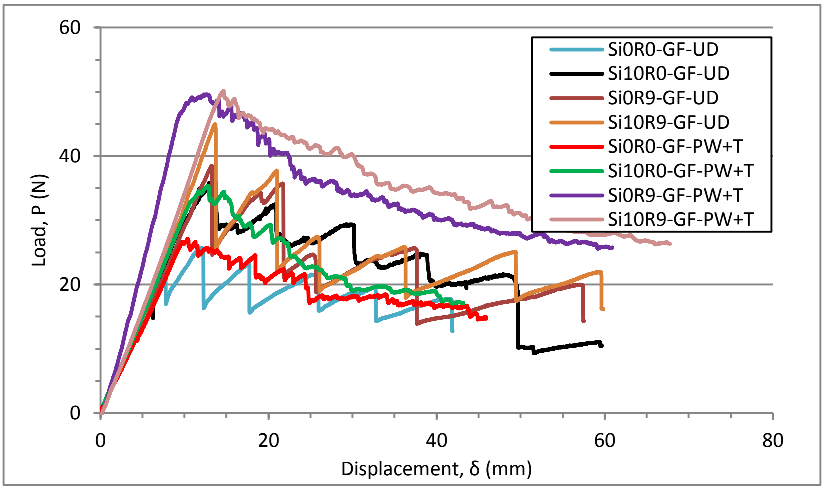

Figure 8.3: Load-displacement curves for RIFT-processed GFRPs

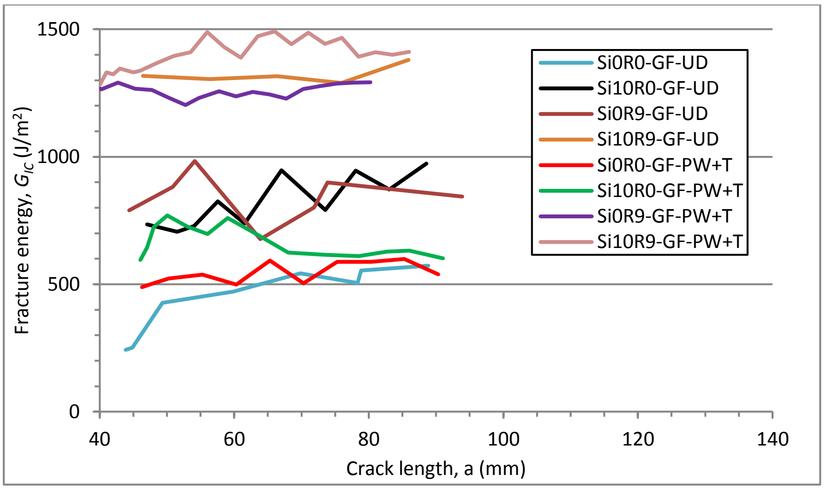

Figure 8.4: R-curves for RIFT-processed GFRPs

A comparison between the interlaminar fracture energies of the GFRPs-UD and GFRPs-PW+T was not conclusive. The fracture energies of both the GFRPs with the Si0R0 and Si10R9 matrix formulations were found to be comparable (P-value > 0.05), while the values of both the GFRPs with the Si10R0 and Si0R9 matrix formulations were different (P-value < 0.05), see Table 8.1. This was probably due to the different toughening mechanisms induced by the particles in the composites with different fibre reinforcement architectures. As can be seen from Figure 8.3, the unstable crack (i.e. 'slip-stick') growth induced by the stitches (i.e. the stitches in the weft direction) was found to be less catastrophic for the Si10R0 GFRP-UD, compared to the Si0R0 GFRP-UD. More significant toughening mechanisms were also observed in the Si10R0 GFRP-UD. This resulted in a significant increase in the measured fracture energy of the Si10R0 GFRP-UD. However, the addition of silica-nanoparticles did not significantly affect the crack growth behaviour of the GFRP-PW+T. Hence, only a slight increase in the fracture energy was measured for the Si10R0 GFRP-PW+T. On the other hand, the addition of rubber-microparticles promote the toughening mechanisms in the GFRP-PW+T rather than in the GFRP-UD, as can be seen from the increase in the value of the interlaminar fracture for the GFRP-PW+T, see Table 8.1. Hence, a more significant increase in the measured fracture energy was observed for the Si0R9 GFRP-PW+T. The hybrid modification of the epoxy matrix cancelled out these effects. As can be seen from Figure 8.4, the increasing values of the interlaminar fracture energies with increasing crack length (i.e. a R-curve) were randomly observed for some GFRPs-UD and GFRPs-PW+T as a result of the random fibre/fibre bundle bridging.

A fracture energy of 534 J/m^2 was measured for the Si0R0 GFRP-UD, compared to a value of 541 J/m^2 for the Si0R0 GFRP-PW+T. Comparable values of the interlaminar fracture energies were recorded for both the GFRPs-UD and GFRPs-PW+T composites with Si10R9 matrix formulations; values of 1257 J/m^2 and 1372 J/m^2 were measured respectively. The addition of silica-nanoparticles had a significant effect on the measured fracture energy of the GFRP-UD; an increase of the fracture energy from 534 J/m^2 to 842 J/m^2 was recorded. However, only a small effect on the fracture energy was observed when adding the silica-nanoparticles to the Si0R0 GFRP-PW+T; the fracture energy was improved to only 621 J/m^2. The addition of rubber-microparticles to the Si0R0 GFRPs-PW+T gave a more significant improvement to the fracture energy than to the Si0R0 GFRPs-UD; fracture energies of 1287 J/m^2 and 996 J/m^2 were recorded respectively.

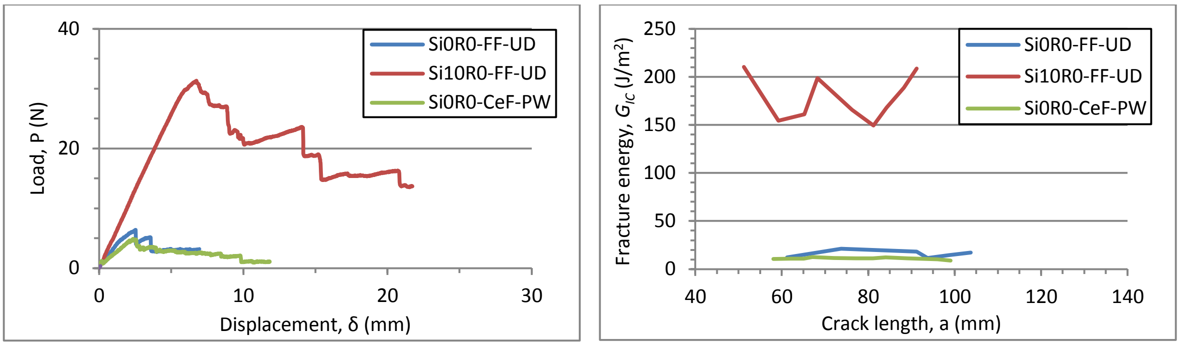

Figure 8.5: Load-displacement curves and R-curves for initial RIFT-processed NFRPs

As can be seen from Figure 8.5, unstable crack behaviour was observed for the initial RIFT-processed FFRPs. As discussed above, this was because of the poor contact between the fibres and matrix and the presence of voids. The same brittle fracture behaviour was also observed for the initial RIFT-processed CeFRPs, see Figure 8.5. For the GFRPs, unstable crack growth (stick-slip behaviour) was observed for the GFRPs-UD, see Figure 8.3. This stick-slip behaviour was associated with the weft stitches across the warp direction used to hold the warp yarns in place, where the crack was likely to slip at the locations of the stitches. For the GFRP-PW+T, due to the architecture of the woven fibre reinforcement, fibres bridging in the warp direction led to fibre bridging in the weft direction and vice versa. This resulted in fibre bundle bridging and partial delamination of the composites. However, stable crack growth was observed, see Figure 8.3, due to the smooth transition of the alternating warp/weft yarns along the length of the specimens, although fibre/fibre bundle bridging existed.

Davidson and Waas [162] have suggested that the interlaminar fracture energy would continue to increase with increasing crack propagation due to the energy contributed from fibre bridging. For all the NFRPs manufactured via the initial RIFT process, the fracture energies were relatively independent of the increasing crack propagation, see Figure 8.5. This was because of the insignificant fibre/fibre bundle bridging observed in the NFRPs. However, more significant fibre/fibre bundle bridging was observed in the GFRPs, see Figure 8.4. The Si0R9 GFRP-PW+T composite reveals a good example of R-curve with fibre/fibre bundle bridging. However, it can also be seen that the R-curve has reached the steady state, i.e. the crack growth has reached the constant bridging zone length.

8.2.2 Mode I Interlaminar Fracture Properties of RIFT-processed NFRPs vs GFRPs – Optimization Study

Efforts to improve the fracture energies of the RIFT-processed NFRPs were made, see section '5.3.3'. However, for simplicity, only the unidirectional flax fibre (FF-UD) reinforced Si0R0 epoxy polymer composite was employed in the optimization study. Three different RIFT process optimization options were evaluated. Table 8.2 summarizes the mode I interlaminar fracture energies of the RIFT-processed NFRPs from the optimization study and compares them with values for the GFRPs manufactured via the RIFT process.

Table 8.2: Summary of mode I interlaminar fracture energies of RIFT-processed FFRPs vs RIFT-processed Si0R0 GFRP – Optimization study

Fibre type and architecture	Modification	Fibre volume fraction, v_f	Void content, v_v (vol%)	Fracture energy, G_{IC} (J/m^2)
Unidirectional Flax (FF-UD)	Initial study	0.31	15	19±5
	Vacuum dry (VD)*	0.32	13	20±2
	Plasma treatment (OP)*	0.34	12	24±3
	Fan-oven dry (OD)*	0.44	1	1112±66
Unidirectional Glass (GF-UD)	Initial study	0.61	2	534±109

*VD = vacuum-dry under vacuum in the RIFT vacuum bagging for 6 hours at 50°C prior to processing; OP = plasma treatment with low pressure O_2 plasma at 50% power for 5 minutes; OD = fan-oven dry in the fan-oven for 12 hours at 75°C prior to processing. For further details, see section '5.3.3'.

Table 8.2 shows that neither: Option 1) VD: the attempt to dry the fibres in the RIFT vacuum bagging under vacuum, nor Option 2) OP: the attempt to plasma treat, using oxygen gas, the fibre surface to enhance the fibre-matrix compatibility, improved the fracture energy of the RIFT-processed FFRP. For example, the moisture content of the vacuum-dried (VD) FFs remained unchanged, which restricted the wetting of the fibres by the epoxy polymer and weakened the fibre-matrix interfacial adhesion. The plasma surface treatment (OP) also gave the same poor outcome without promoting changes on the fibre surface. As a result, relatively low fibre volume fractions, high void contents and low glass transition temperatures were observed in the VD- and OP-modified FFRPs, see Table 5.7. The SEM study also revealed the same brittle fracture surfaces of the VD- and OP-modified FFRPs, compared to that of the initial RIFT-processed FFRP. This confirmed the poor outcome of the VD- and OP-modified FFRPs.

However, a third option, namely the simple technique of drying the FFs in a fan-oven pre-manufacture by the RIFT process, did significantly improve the fracture energy. An improved fibre volume fraction and a reduced void content were also achieved via this OD-modification. The fracture energy of the OD-modified FFRP was improved due to the significantly improved fibre volume fraction and the reduction of the void content as a result of the improved fibre packing density and the improved wettability. The fibre volume fraction was found to increase by 42% to $v_f = 0.44$ and the void content was reduced by 93% to below 1%. On the other hand, these two parameters were generally unchanged for the VD- and OP-modified FFRPs with fibre volume fractions of 0.32-0.34 and void contents of 12-13%. The significant reduction in the void content due to the OD-modification of the RIFT process suggested the elimination of nearly all the water from the NFs, prior to the RIFT manufacturing process. For example, the moisture content in the FFs was reduced from approximately 8.6 wt% to below 1 wt% by drying in the fan-oven. As a result, the water which evaporated into steam at the high temperatures reached during curing was greatly reduced. Also, the elimination of nearly all the water from the NFs led to a minimal dissolution of water in the epoxy matrix. This was confirmed by the value of the glass transition temperature observed for the OD-modified FFRP, compared to the value of the epoxy polymers [147], see Table 5.7: a glass transition temperature of 126°C was measured for the OD-modified FFRP, compared to a value of 131°C for the Si0R0 epoxy polymer. The SEM study confirmed a good fibre-matrix interfacial adhesion in the OD-modified FFRP.

Although the fibre volume fraction achieved in the OD-modified FFRP was found to be approximately 25% lower than the GFRP due to the cellular structure and porous nature of NFs [4], which restricted the compaction of the pre-laid-up reinforcement under vacuum pressure during infusion, the fracture energy of the OD-modified FFRP was found to be double that of the GFRP, see Table 8.2. The fracture surfaces of the OD-modified FFRPs, which was termed the final RIFT-processed FFRP, revealed the extra toughening mechanisms, e.g. fibre/fibre bundle bridging and fibre defibrillation, as will be discussed in detail later. Due to the improved fibre-matrix interfacial adhesion, stable crack growth was observed for the OD-modified FFRP, see Figure 8.6. The observed unstable crack growth (i.e. stick-slip behaviour) in the GFRP was associated with the stitches in the weft direction. As discussed earlier, the fracture energy increased as the crack propagated as a result of the fibre/fibre bundle bridging [162]. A more extensive increase in the fracture energy was observed in the OD-modified FFRP as a result of the combined effect of fibre bridging and fibre bundle bridging, see Figure 8.6.

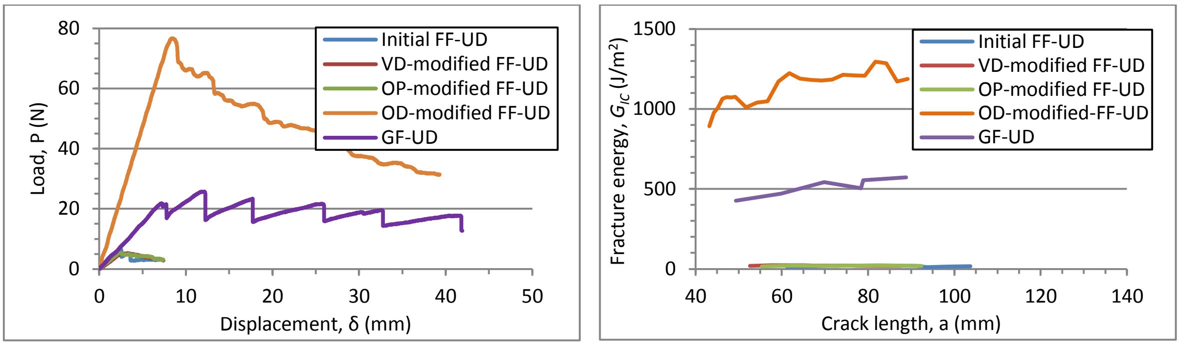

Figure 8.6: Load-displacement curves and R-curves for RIFT-processed NFRPs from the optimization study vs RIFT-processed GFRPs

A fracture energy of 1112 J/m^2 was measured for the OD-modified FFRP, compared to a fracture energy of 534 J/m^2 for the GFRP. Now, no results for the mode I interlaminar fracture energy of FF-UD-reinforced epoxy polymer composites have been previously reported. However, the fracture energy of this FFRP exceeded the value of 600 J/m^2 for the natural fibre-reinforced epoxy composite previously reported by Pinto et al. [52], i.e. a jute-UD-reinforced epoxy polymer composite. Moreover, the value was also found to exceed the previously reported values of 330 J/m^2 and 280 J/m^2 for GFRP-UD [56] and CFRP-UD [22].

8.2.3 **Mode I Interlaminar Fracture Properties of RIFT-processed NFRPs vs GFRPs – Final Study**

As the fan-oven drying of the FFs (OD-modification) revealed a significant improvement of the fracture energy of the RIFT-processed FFRP, the OD-modified FFRPs and CeFRPs with different matrix modifications were further examined in this final RIFT study.

8.2.3.1 ***Mode I Interlaminar Fracture Properties of RIFT-processed FFRPs vs GFRPs – Final Study***

Table 8.3 summarizes the mode I interlaminar fracture energies of the RIFT-processed FFRPs from the initial and final RIFT processes, and compares them with the RIFT-processed GFRPs.

Table 8.3: Summary of mode I interlaminar fracture energies of initial and final RIFT-processed FFRPs vs RIFT-processed GFRPs

Fibre type and architecture	**Matrix formulation**	**Initial RIFT**			**Final RIFT***		
		Fibre volume fraction, v_f	Void content, v_v (vol%)	Fracture energy, G_{IC} (J/m^2)	Fibre volume fraction, v_f	Void content, v_v (vol%)	Fracture energy, G_{IC} (J/m^2)
Unidirectional Flax (FF-UD)	Si0R0	0.31	15	19±5	0.44	1	1112±66
	Si10R0	0.23	13	252±49	0.40	1	1302±78
	Si0R9	0.38	17	139±29	0.36	1	1918±89
	Si10R9	0.33	16	233±41	0.44	1	1936±150
		RIFT					
Unidirectional Glass (GF-UD)	Si0R0	0.61	2	534±109	-	-	-
	Si10R0	0.55	2	842±44	-	-	-
	Si0R9	0.65	2	996±68	-	-	-
	Si10R9	0.65	2	1257±56	-	-	-

*See '5.3.4 RIFT Process – Final Study' for details

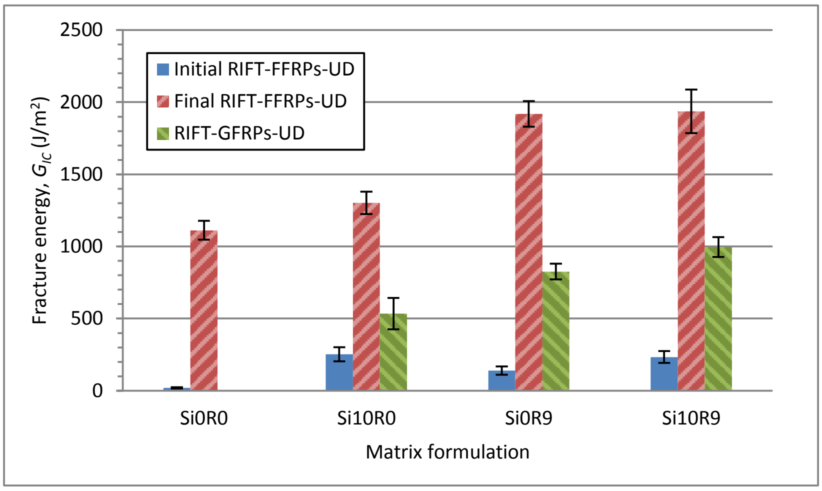

Figure 8.7: Summary of mode I interlaminar fracture energies for initial and final RIFT-processed FFRPs vs RIFT-processed GFRPs

As may be seen from Table 8.3 and Figure 8.7, a significant improvement of the mode I fracture energies was achieved in the final RIFT-processed FFRPs, which is accompanied by a significant void content reduction and an improved fibre volume fraction, compared to those of the initial RIFT-processed FFRPs. As discussed earlier in section '8.2.2', this was because of the removal of nearly all the moisture content in the FFs during the final RIFT manufacturing process. Indeed, as a result, their interlaminar fracture energies exceeded those of the GFRPs.

As discussed earlier in section '5.4.6', an identical morphology for the silica-nanoparticles and rubber-microparticles was observed in both the final RIFT-processed FFRPs and GFRPs. Also, the AFM study revealed a uniform dispersion of silica-nanoparticles and rubber-microparticles in the Si10R0 FRPs and the Si0R9 FRPs, respectively. However, for the Si10R9 FRPs, although the rubber-microparticles were well dispersed, there was some degree of agglomeration of the silica-nanoparticles. The toughening mechanisms induced by the addition of these particles will be discussed later in section '8.3.2'.

The addition of silica-nanoparticles had a relatively little effect on the fracture energy. However, the rubber-microparticle modified FRPs showed a large increase in the fracture energy. Despite the identical morphology and fracture mechanisms of the silica-nanoparticles and rubber-microparticles in the two different FRPs, the measured fracture energies for the final RIFT-processed FFRPs were found to be significantly higher than those of the RIFT-processed GFRPs. Fracture energies of 1112 to 1936 J/m^2 were measured for the FFRPs with the different matrix modifications, compared to values of 534 to 1257 J/m^2 for the GFRPs. Adding either the silica-nanoparticles or rubber-microparticles to the RIFT-processed Si0R0 FFRPs and GFRPs improved their fracture energies. However, adding silica-nanoparticles to the Si0R9 FRPs only gave a small increase in the fracture energy in the GFRPs. This was due to 1) differences in the failure region, i.e. whether the crack propagated through the polymer matrix region at the fibre-matrix interface or through the fibre/fibre bundle, and 2) the amount of fibre/fibre bundle bridging that occurred [56]. These observations are in agreement with Hsieh et al. [56]. In the FFRPs, the crack tended to propagate through the fibre/fibre bundle and the majority of the fracture surfaces revealed by the SEM study were covered with defibrillated and broken fibres/fibre bundles. The main features on the fracture surface involved fibre defibrillation, fibre breakage and fibre/fibre bundle bridging. Only a small number of failures involved plastic deformation of the epoxy matrices, e.g. where shear yielding and plastic void deformation. On the other hand, in the GFRPs, the main fracture feature involved debonding of the fibres with shear yielding and plastic deformation of the epoxy matrices and some fibre bridging. This was confirmed by the examination of the side-view images of the DCB specimens of FFRPs and GFRPs during the fracture test. Further details on the fibre induced toughening mechanisms for the final RIFT-processed FFRPs and the RIFT-processed GFRPs will be discussed in sections '8.3.3.1.2' and '8.3.3.2' respectively.

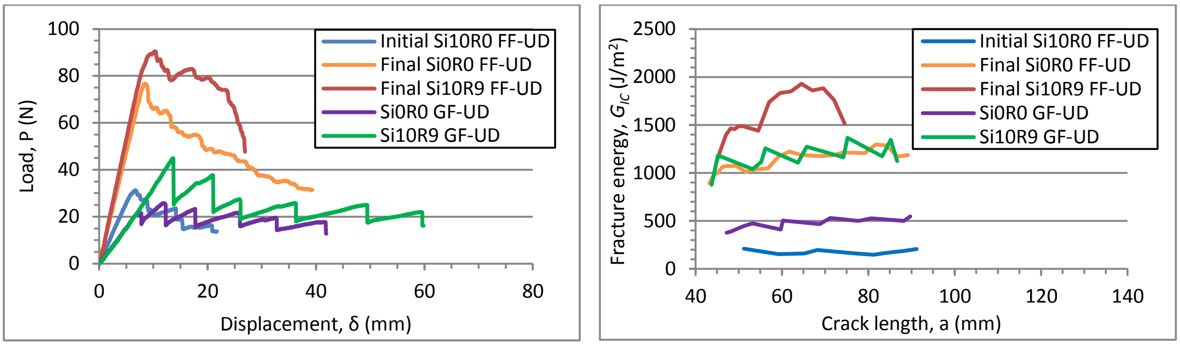

Figure 8.8: Load-displacement curves and R-curves for initial and final RIFT-processed FFRPs vs RIFT-processed GFRPs

From Figure 8.8, stable crack growth was observed for the final RIFT-processed FFRPs. However, as discussed earlier, unstable crack growth (i.e. stick-slip behaviour) was observed for the GFRPs due to the presence of the stitches. The fracture energies of the final RIFT-processed FFRPs were found to jump or increase as the crack propagated, as a result of both fibre bridging and fibre bundle bridging occurring. These fibre bridging and fibre bundle bridging events were found to occur randomly, regardless of the crack length and of the matrix formulation used. The addition of silica-nanoparticles and/or rubber-microparticles to the final RIFT-processed Si0R0 FFRPs increased the fracture energies to 1302 to 1936 J/m^2.

The interlaminar fracture energies of the particle modified GFRPs were found to generally exceed the values of the particle modified GF-UD-reinforced epoxy composite previously reported by Hsieh et al. [56], except for the Si10R0 GFRP. For example, Hsieh et al. measured a fracture energy of 330 J/m^2 for the Si0R0 GFRP [56], compared to a value of 534 J/m^2 measured in the present study. It was reported by Hsieh et al. [56] that the addition of silica-nanoparticles increased the fracture energy to 1015 J/m^2, while only a value of 842 J/m^2 was recorded in the present study. Fracture energies of 996 J/m^2 and 1257 J/m^2 were measured for the Si0R9 and Si10R9 GFRPs in the present study. However, fracture energies of 885 J/m^2 and 860 J/m^2 were reported by Hsieh et al. [56] for the same composites.

8.2.3.2 *Mode I Interlaminar Fracture Properties of RIFT-processed CeFRPs vs GFRPs – Final Study*

Table 8.4 summarizes the values of the mode I interlaminar fracture energy of the RIFT-processed CeFRPs from the <u>initial</u> and <u>final</u> RIFT processes, and compares them with those of the RIFT-processed GFRPs.

Table 8.4: Summary of mode I interlaminar fracture energies of initial and final RIFT-processed CeFRPs vs RIFT-processed GFRPs

Fibre type and architecture	**Matrix formulation**	**Initial RIFT**			**Final RIFT***		
		Fibre volume fraction, v_f	Void content, v_v (vol%)	Fracture energy, G_{IC} (J/m^2)	Fibre volume fraction, v_f	Void content, v_v (vol%)	Fracture energy, G_{IC} (J/m^2)
Plain-woven Cellulose (CeF-PW)	Si0R0	-^	14	20±1	0.64	1	1427±76
	Si10R0	-^	16	23±2	0.67	1	1555±173
	Si0R9	-^	-^	-^	0.65	1	1811±28
	Si10R9	-^	-^	-^	0.67	1	1847±573
		RIFT					
Plain-woven and Twill 2x2 Glass (GF-PW+T)†	Si0R0	0.41	2	541±36	-	-	-
	Si10R0	0.38	2	621±59	-	-	-
	Si0R9	0.42	2	1287±127	-	-	-
	Si10R9	0.44	2	1372±73	-	-	-

*See section '5.3.4' for details

^Values could not be obtained due to the poor quality of the composites.

†These GFRP DCB specimens were backed with twill 2x2 GF fabric to increase the stiffness of the arms. The fracture plane was through the PW fabric layers..

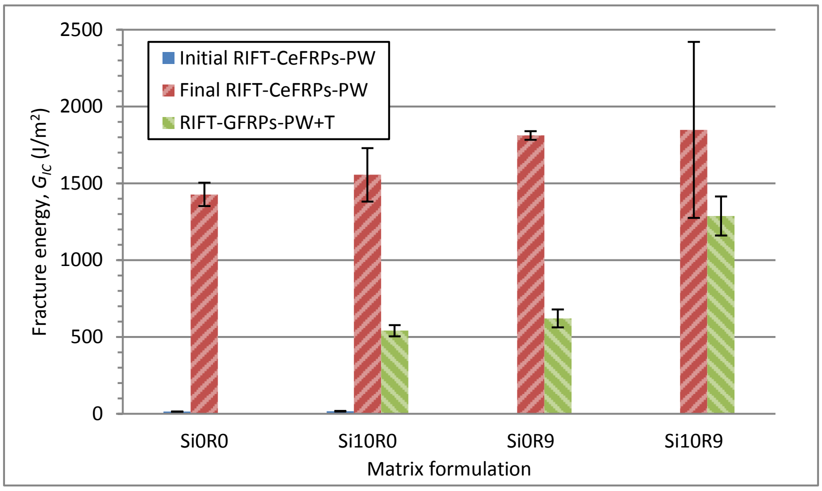

Figure 8.9: Summary of mode I interlaminar fracture energies of initial and final RIFT-processed CeFRPs vs RIFT-processed GFRPs

Due to the complex plain-woven architecture and incompatibility of the CeFs, penetration of the epoxy resins was restricted in the <u>initial</u> RIFT process. Hence, a very poor fibre-matrix interfacial adhesion and an extensive amount of voids were observed, see Table 8.4. As a result, the <u>initial</u> RIFT-processed CeFRPs exhibited brittle fracture and had extremely poor fracture energies. Thus, as might be expected, matrix modification had only little effect.

As may be seen from Table 8.4 and Figure 8.9, significant improvements of the mode I interlaminar fracture energies were found in the <u>final</u> RIFT-processed CeFRPs, accompanied by significant void content reductions and improved fibre volume fractions, compared to those of the <u>initial</u> RIFT-processed CeFRPs. As discussed earlier in section '8.2.2', again, this was because of the removal of nearly all the moisture content in the CeFs during the OD-modification used in the final RIFT process. As a result, their interlaminar fracture energies exceeded those of the GFRPs.

Despite the different fibre reinforcements used in the CeFRPs and GFRPs, the morphology and fracture mechanisms of the silica-nanoparticles and rubber-microparticles were identical, as discussed earlier in section '5.4.6', A good dispersion of silica-nanoparticles and rubber-microparticles was observed in the Si10R0 CeFRPs and Si0R9 CeFRPs, respectively. However, well dispersed rubber-microparticles were observed but with some degree of agglomeration of the silica-nanoparticles for the Si10R9 CeFRPs, see Figure 5.2. The toughening mechanisms induced by the addition of these particles will be discussed later in section '8.3.2'.

The addition of silica-nanoparticles had little effect on the values of the fracture energies. On the other hand, the rubber-microparticle modified FRPs revealed a large increase in the fracture energies. However, adding the silica-nanoparticles to the Si0R9 FRPs did not further significantly increase the fracture energies in both the CeFRPs and GFRPs. The fracture surfaces of the CeFRPs and GFRPs were very similar, where debonding of the fibres resulted in plastic deformation and shear yielding of the epoxy polymer matrix. However, the degrees of fibre and fibre bundle bridging were found to be more extensive in the CeFRPs than in the GFRPs. In addition, fibre defibrillation was only observed in the CeFRPs. Further details on the fibre induced toughening mechanisms for the final RIFT-processed FFRPs and the RIFT-processed GFRPs will be discussed in sections '8.3.3.1.2' and '8.3.3.2', respectively.

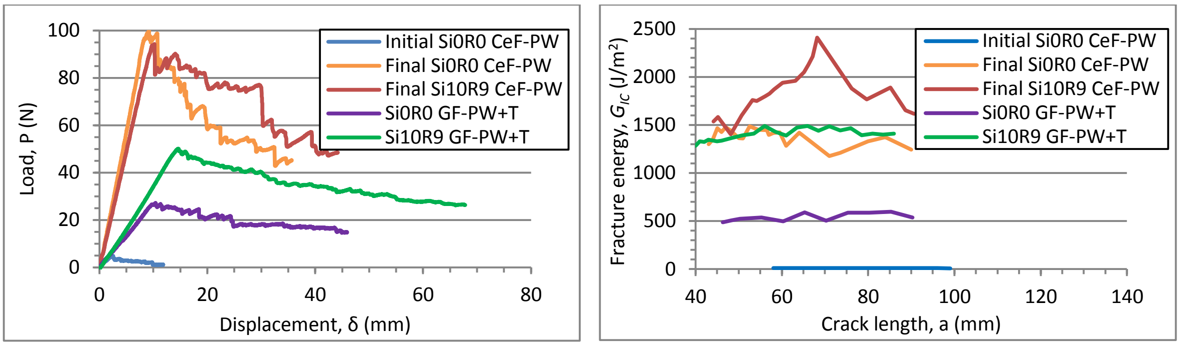

Figure 8.10: Load-displacement curves and R-curves for initial and final RIFT-processed CeFRPs vs RIFT-processed GFRPs

From Figure 8.10, stable crack growth with random unstable jumps was observed for the final RIFT-processed CeFRPs. These unstable crack growths were associated with the extensive fibre/fibre bundle bridging where the bridging led to a jump in the fracture energy [162]. Little fibre/fibre bundle bridging was observed in the GFRPs, and more stable crack growth was obtained.

Although the fracture energies of the final RIFT-processed CeFRPs were found to improve significantly, compared to those from the initial RIFT process, no results for the mode I interlaminar fracture energy of the CeF-PW-reinforced epoxy polymer composites have been previously reported. However, the fracture energy of 1427 J/m^2 for the Si0R0 CeFRP-PW was found to agree well with the values of 747 to 1775 J/m^2 for a silk-PW-reinforced epoxy composite reported by Zulkifli et al. [55]. The fracture energies of the particle modified CeFRPs were also found to generally exceed the values of the particle modified CFRPs epoxy composites with a plain-woven fibre architecture previously reported by Hsieh et al. [56]. For example, a fracture energy of 439 J/m^2 was recorded for the Si0R0 CFRP-PW by Hsieh et al. [56]. The addition of silica-nanoparticles increased the fracture energy of the Si0R0 CFRPs to 489 J/m^2, whilst the addition of rubber-microparticles increased the fracture energy further to 1044 J/m^2. Adding silica-nanoparticles to give a Si10R9 CFRP further increased the fracture energy to 1316 J/m^2. For comparison, fracture energies of 1427 to 1847 J/m^2 were measured for the CeFRPs with the different matrix modifications in the present study.

8.2.4 Mode I Interlaminar Fracture Properties of final RIFT- and RTM-processed NFRPs vs GFRPs

8.2.4.1 *Mode I Interlaminar Fracture Properties of Final RIFT- and RTM-processed FFRPs vs GFRPs*

Table 8.5 summarizes the mode I interlaminar fracture energies of the final RIFT- and RTM-processed FFRPs, and compares them with the GFRPs from the RIFT and RTM processes.

Table 8.5: Summary of mode I interlaminar fracture energies of RIFT- processed vs RTM-processed FFRPs & GFRPs

Matrix formulation	**Final RIFT – FF-UD**			**RTM – FF-UD**			**Significance value of G_{IC} (RIFT vs RTM), P-value***
	Fibre volume fraction, v_f	Void content, v_v (vol%)	Fracture energy, G_{IC} (J/m^2)	Fibre volume fraction, v_f	Void content, v_v (vol%)	Fracture energy, G_{IC} (J/m^2)	
Si0R0	0.44	1	1112±66	0.42	2	963±35	0.003
Si10R0	0.40	1	1302±78	0.41	2	1168±51	0.015
Si0R9	0.36	1	1918±89	0.42	5	1168±46	<0.001
Si10R9	0.44	1	1936±150	0.42	6	1264±53	<0.001
	RIFT – GF-UD			**RTM – GF-UD**			
Si0R0	0.61	2	534±109	0.63	1	564±39	0.579
Si10R0	0.55	2	842±44	0.62	1	935±76	0.074
Si0R9	0.65	2	996±68	-†	-†	-†	-†
Si10R9	0.65	2	1257±56	-†	-†	-†	-†
Significance value of G_{IC} (FF vs GF), P-value^							
Si0R0			<0.001			<0.001	
Si10R0			<0.001			<0.001	
Si0R9			<0.001			-†	
Si10R9			<0.001			-†	

*Comparison of fracture energies of the RIFT- and the RTM-processed FRPs using two-tailed independent t-test with a confidence interval value, α, of 0.05 (unequal variances assumed).

^Comparison of fracture energies of the FFRPs and GFRPs using two-tailed independent t-test with a confidence interval value, α, of 0.05 (unequal variances assumed).

*^P-value ≤ 0.05 = the two groups are significantly different and P-value > 0.05 = the two groups are insignificantly different.

†Values were not be obtained.

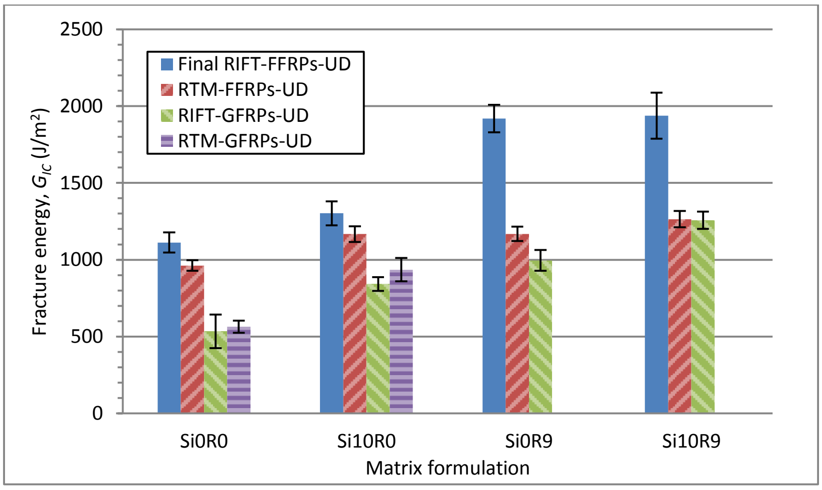

Figure 8.11: Summary of mode I interlaminar fracture energies for RIFT- and RTM-processed FFRPs vs GFRPs

From Table 8.5 and Figure 8.11, a comparison of the values of the interlaminar fracture energies from the RIFT and RTM processes was not conclusive. For the GFRPs, the fracture energies of the same materials from the two processes were comparable. However, for the FFRPs, significantly higher fracture energies were observed for the RIFT-processed Si0R9 and Si10R9 FFRPs, compared to the results from the RTM process. On the other hand, the RIFT-processed Si0R0 and Si10R0 FFRPs gave less significantly higher fracture energies, compared to those from the RTM process. Although the FFRPs generally showed higher fracture energies compared to the GFRPs, for the same matrix formulations, the increases were found to decrease in the Si0R9 and Si10R9 matrix formulations when comparing the RTM-processed GFRPs to the RTM-processed FFRPs.

From sections ‘5.4.6’ and ‘6.4.6’, an identical morphology for the silica-nanoparticles and rubber-microparticles was observed in all the FRPs, from both the RIFT and RTM processes. The AFM study revealed a uniform dispersion of silica-nanoparticles and rubber-microparticles in the Si10R0 FRPs and the Si0R9 FRPs, respectively. However, for the Si10R9 FRPs, the rubber-microparticles were well dispersed but some degree of agglomeration of the silica-nanoparticles was present. Again, the SEM study of the fracture mechanisms of the epoxy matrices in the different FRPs revealed identical fracture mechanisms due to the particles present in the FRPs with the same matrix formulations, regardless of the type of the fibre/fabric reinforcement used, see section ‘8.3.2’ for further details.

However, the fracture mechanisms induced by the fibre/fabric reinforcements were found to be different between the FFRPs and GFRPs. In the FFRPs, the crack tended to propagate through the fibres/fibre bundles and the majority of the fracture surfaces were covered with defibrillated and broken fibres/fibre bundles. The main failures involved fibre defibrillation, fibre breakage and fibre/fibre bundle bridging, as discussed in sections ‘8.3.3.1.2’ and ‘8.3.3.1.3’. Only a minimal degree of plastic deformation of the epoxy matrices was observed to occur. On the other hand, for the GFRPs, the main fracture features involved debonding of the fibres with shear yielding and plastic deformation of the epoxy matrix, and some fibre bridging. This was confirmed by the examination of the side-view images of the DCB specimens of FFRPs and GFRPs during the fracture test, as discussed in section ‘8.3.3.2’.

Although the fibre volume fractions achieved and fracture mechanisms involved in the fracture of the FFRPs from the two manufacturing processes were found to be identical, the measured fracture energies were found to be different, see Table 8.5. As mentioned earlier, significantly higher fracture energies were observed for the RIFT-processed Si0R9 and Si10R9 FFRPs, compared to the results from the RTM process (P-value $<< 0.05$), while only slightly higher fracture energies were observed for the Si0R0 and Si10R0 matrix formulations from the RIFT process (P-value < 0.05), see Table 8.5. This was probably due to the comparably higher void contents observed for the RTM-processed Si0R9 and Si10R9 FFRPs, compared to the other FFRPs (i.e. void contents of 5-6%, compared to 1-2%). These voids reduced the effective fracture-resisting areas in the crack path of the composites, initiated cracks by acting as pre-cracks and reduced the transverse load transfer between the fibre and matrix. As discussed in section ‘6.5’, in the RTM process, the flow speed of the epoxy resins was fully controlled by the pre-programmed injection speed. The pre-programmed constant flow speed in the RTM method might have created a higher level of voids in the FRPs with the higher viscosity matrix formulations (i.e. the Si0R9 and Si10R9 matrix formulations), especially when employing fibre reinforcements with complex microstructures, i.e. the porous bonded/interlocked microfibrils of the NFs, see section ‘6.2.2.1’. This was because the entrapped air required a longer duration to escape from the higher viscosity resins. Due to the relatively high void contents, the respective fracture energies of 1168 J/m^2 and 1264 J/m^2 for the RTM-processed Si0R9 FFRP and Si10R9 FFRP were found to improve slightly, compared to a fracture energy of 963 J/m^2

for the Si0R0 FFRP. These fracture energies of the RTM-processed Si0R9 FFRP and Si10R9 FFRP were found to be comparable to the fracture energy of 1168 J/m^2 for the RTM-processed Si10R0 GFRP. On the other hand, in the final RIFT process, a significant increase in the fracture energies of the FFRPs was recorded when either adding the rubber-microparticles or forming a hybrid epoxy matrix, namely fracture energies of 1918 J/m^2 and 1936 J/m^2 were measured respectively. However, adding silica-nanoparticles to the Si0R0 FFRPs only increased the fracture energy from 1112 J/m^2 to 1302 J/m^2.

The fracture energies for the GFRPs from the two manufacturing processes were found to be comparable (P-value > 0.05). This was due to the equivalent fibre volume fractions and void contents of the GFRPs from the two processes. A fracture energy of 534 J/m^2 was measured for the RIFT-processed Si0R0 GFRP, while a fracture energy of 564 J/m^2 was measured for the same material from the RTM process. Adding silica-nanoparticles to the RIFT- and RTM-processed Si0R0 GFRPs improved the fracture energies to 842 J/m^2 and 935 J/m^2 respectively. Although the values of the fracture energies for the RTM-processed Si0R9 and Si10R9 GFRPs were not measured, the values of their fracture energies were predicted to be comparable to those from the RIFT process. Fracture energies of 996 J/m^2 and 1257 J/m^2 were measured for the RIFT-processed Si0R9 and Si10R9 GFRPs, respectively. These values of fracture energies were also found to be comparable to the RTM-processed FFRPs with the same matrix formulations as a result of the high void contents in the RTM-processed FFRPs. However, the measured fracture energies of the Si0R0 and Si10R0 GFRPs were still found to be far inferior to those of the RTM-processed FFRPs with the same matrix formulations (P-value << 0.05). In addition, all the RIFT-processed FFRPs possessed significantly superior fracture energies, compared to the GFRPs (P-value << 0.05).

The same conclusion can be drawn for the RTM-processed FFRPs and GFRPs when comparing their load-displacement curves to those obtained from the RIFT process. From Figure 8.12, stable crack growth was observed for all of the FFRPs. Crack growth for the GFRPs was found to be unstable with stick-slip behaviour, regardless of the manufacturing process used. The crack was likely to slip across the weft stitches, where these stitches were sewn every 10 mm along the entire length of the GFRPs. As discussed earlier, the fracture energy jumped as fibre/fibre bundle bridging occurred [162]. A significant increase in the fracture energies was randomly observed in the FFRPs as a result of both the fibre bridging and fibre bundle bridging. The final RIFT-processed Si10R9 FFRP-UD sample is a good example of the jump in the fracture energy, see Figure 8.13. However, a slight increase in the fracture energy as the crack propagated was also observed in the GFRPs due to fibre bridging.

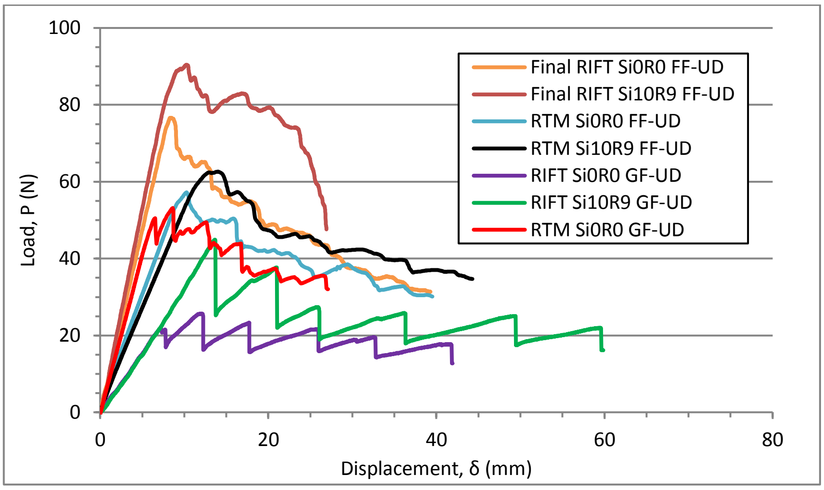

Figure 8.12: Load-displacement curves for RIFT- and RTM-processed FFRPs vs GFRPs

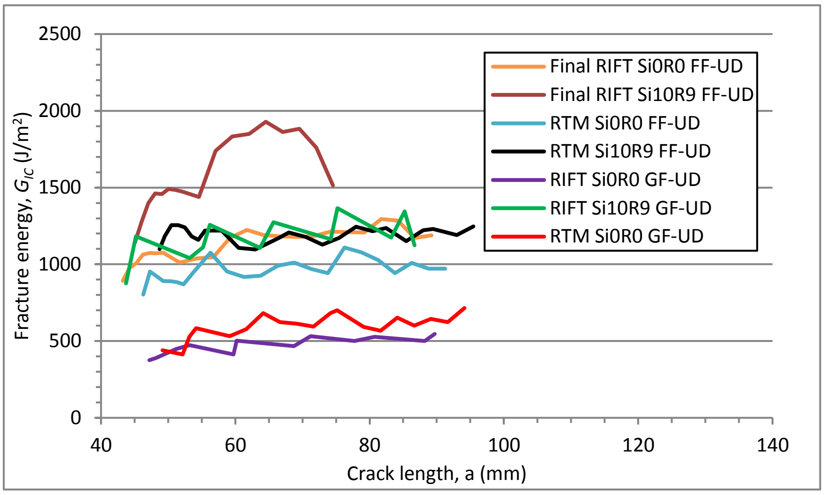

Figure 8.13: R-curves for RIFT- and RTM-processed FFRPs vs GFRPs

8.2.4.2 *Mode I Interlaminar Fracture Properties of Final RIFT- and RTM-processed CeFRPs vs GFRPs*

Table 8.6 summarizes the mode I interlaminar fracture energies of the final RIFT- and RTM-processed CeFRPs, and compares them with the GFRPs from the RIFT and RTM processes.

Table 8.6: Summary of mode I interlaminar fracture energies of RIFT- processed vs RTM-processed CeFRPs & GFRPs

Matrix formulation	**Final RIFT – CeF-PW**			**RTM – CeF-PW**			**Significance value of G_{IC} (RIFT vs RTM), P-value***
	Fibre volume fraction, v_f	Void content, v_v (vol%)	Fracture energy, G_{IC} (J/m^2)	Fibre volume fraction, v_f	Void content, v_v (vol%)	Fracture energy, G_{IC} (J/m^2)	
Si0R0	0.64	1	1427±76	0.57	2	1125±108	0.044
Si10R0	0.67	2	1555±173	0.60	1	1175±357	0.270
Si0R9	0.65	1	1811±28	0.60	2	1372±176	0.044
Si10R9	0.67	1	1847±573	0.59	3	1617±213	0.481
	RIFT – GF-PW+T†			**RTM – GF-PW+T†**			
Si0R0	0.41	2	541±36	0.45	1	556±53	0.595
Si10R0	0.38	2	621±59	0.44	1	629±67	0.850
Si0R9	0.42	2	1287±127	0.44	1	1465±133	0.080
Si10R9	0.44	2	1372±73	0.45	1	1527±101	0.062
Significance value of G_{IC} (CeF vs GF), P-value^							
Si0R0			<0.001			<0.001	
Si10R0			<0.001			0.027	
Si0R9			0.005			0.425	
Si10R9			0.220			0.423	

*Comparison of fracture energies of the RIFT- and the RTM-processed FRPs using two-tailed independent t-test with a confidence interval value, α, of 0.05 (unequal variances assumed).

^Comparison of fracture energies of the CeFRPs and GFRPs using two-tailed independent t-test with a confidence interval value, α, of 0.05 (unequal variances assumed).

*^P-value ≤ 0.05 = the two groups are significantly different and P-value > 0.05 = the two groups are insignificantly different.

†These GFRP DCB specimens were backed with twill 2x2 GF fabric to increase the stiffness of the arms. The fracture plane was through the PW fabric layers..

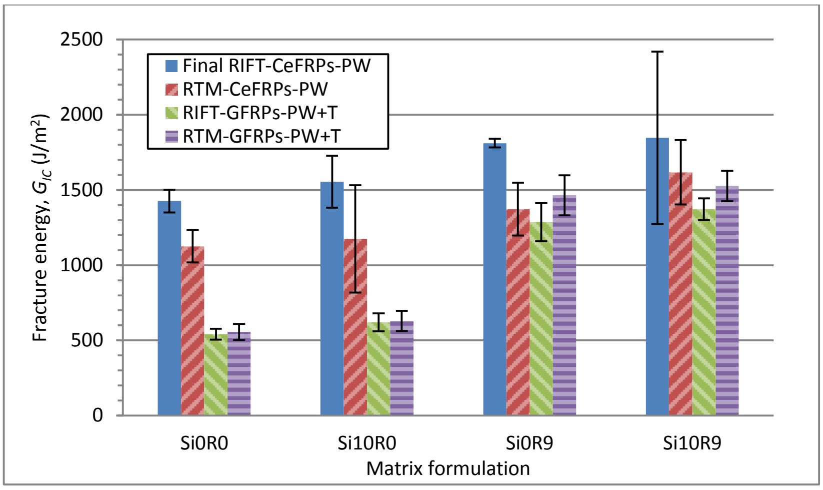

Figure 8.14: Summary of mode I interlaminar fracture energies for RIFT- and RTM-processed CeFRPs vs GFRPs

From Table 8.6 and Figure 8.14, the comparison between the fracture energies from the RIFT and RTM processes was not conclusive. For the GFRPs, the fracture energies from the two processes were comparable. However, the fracture energies of the RIFT-processed CeFRPs were generally higher than those obtained from the RTM process. It can be noticed that due to the random fibre/fibre bundle bridging in the CeFRPs, the fracture energies of some CeFRPs varied considerably. For example, fracture energies of 1442 to 2252 J/m^2 were measured for the final RIFT-processed Si10R9 CeFRPs. Also, fracture energies of 922 to 1584 J/m^2 were measured for the RTM-processed Si10R0 CeFRPs. The fracture energies of the CeFRPs were generally higher than those of the GFRPs, especially when employing the Si0R0 and Si10R0 matrix formulations. Due to the significant increase in the fracture energies of the GFRPs with added rubber-microparticles (i.e. the Si0R9 and Si10R9 matrix formulations), the fracture energies of the GFRPs with these two matrix formulations became more comparable to those of the CeFRPs with the same matrix formulations.

As discussed earlier in sections '5.4.6' and '6.4.6', the morphology of the silica-nanoparticles and rubber-microparticles was identical in all the FRPs from both the RIFT and RTM processes. A good dispersion of silica-nanoparticles and rubber-microparticles was observed in the Si10R0 FRPs and the Si0R9 FRPs, respectively. However, for the Si10R9 FRPs, the rubber-microparticles were well dispersed but there was some degree of agglomeration of the silica-nanoparticles. Again, the fracture mechanisms of the epoxy matrices in the different FRPs revealed identical fracture mechanisms, due to the particles present in the FRPs, with the same matrix formulations, see section '8.3.2' for further details.

Although the fracture surfaces of the CeFRPs and GFRPs were very similar where the debonding of the fibres resulted in plastic deformation and shear yielding of the epoxy polymer, the fibre/fibre bundle bridging was found to be more extensive in the CeFRPs than in the GFRPs. This was probably due to the improved fibre-matrix adhesion of the CeFRPs. Due to the difference in fibre reinforcement architecture, the bridging in the CeFRPs was found to be more extensive than in the FFRPs. However, due to the difference in fibre microstructure, the fibre defibrillation found on the fracture surfaces of the CeFRPs was less extensive than for the FFRPs. Further details on the fibre induced toughening mechanisms for the final RIFT-processed CeFRPs and the RIFT-processed GFRPs will be discussed below.

Although the mechanisms involved in fracture of the CeFRPs from the RIFT and RTM processes were found to be identical, the fracture energies measured were found to be different, see Table 8.6. As discussed in section '8.2.4.1', the pre-programmed constant flow speed in the RTM method might have created a higher level of voids in the FFRPs when working the higher viscosity matrix formulations (Si0R0 and Si10R0 matrix formulations). However, this phenomenon is less likely in the CeFRPs due to the less complex microstructure of the CeFs, compared to the FFs [4][36][38]. A maximum void content of 3% was measured for the RTM-processed Si10R9 CeFRPs, which would not contribute significantly to the decrease in the fracture energy. Instead, the inferior fracture energies of the RTM-processed CeFRPs, compared to those from the RIFT process, were probably due to the approximately 10% lower fibre volume fraction achieved in the RTM process, which contributed to the reduction of the fracture mechanisms contributed from the fibres, e.g. fibre/fibre bundle bridging, fibre breakage and fibre defibrillation, see Table 8.6.

A fracture energy of 1847 J/m^2 was measured for the RIFT-processed Si10R9 CeFRP, compared to a slightly lower value of 1617 J/m^2 for the same material processed by the RTM process. An impressive increase in fracture energy from 1427 J/m^2 to 1811 J/m^2 was measured when adding the rubber-microparticles to the RIFT-processed Si0R0 CeFRPs. The identical procedure only increased the fracture energy from 1125 J/m^2 to 1372 J/m^2 in the RTM process. However, a slight increase in the values of the fracture energies was recorded when adding silica-nanoparticles to the CeFRPs for both of the processing methods; values of 1555 J/m^2 and 1175 J/m^2 were measured for the RIFT- and RTM-processed Si10R0 CeFRPs respectively.

However, the fracture energies for the GFRPs from the two processes were found to be comparable (P-value > 0.05). This was due to the equivalent fibre volume fractions and void contents of the GFRPs from the two processes. A fracture energy of 541 J/m^2 was measured for the RIFT-processed GFRP, while a value of 556 J/m^2 was measured for the RTM-processed GFRP. Adding silica-nanoparticles to the RIFT- and RTM-processed GFRPs improved the fracture energies to 621 J/m^2 and 629 J/m^2 respectively. Fracture energies of 1287 J/m^2 and 1465 J/m^2 were measured for the RIFT- and RTM-processed Si0R9 GFRP respectively. Fracture energies of 1372 J/m^2 and 1527 J/m^2 were measured for the RIFT- and RTM-processed Si10R9 GFRP respectively. It was also observed that the fracture energies of the Si0R9 and Si10R9 GFRPs from the two processes were comparable to the RTM-processed CeFRPs with the same matrix formulations (P-value > 0.05), although the fracture energies of the Si0R0 and Si10R0 GFRPs from the two processes were significantly inferior to the RTM-processed CeFRPs. These observations suggested that the addition of rubber-microparticles had a greater effect on the fracture energies of the GFRPs. This indicated that the fracture mechanisms arising from the epoxy matrices were less dominant in the CeFRPs, while the main fracture mechanisms contributing to their measured fracture energies were from the fibre/fabric reinforcement.

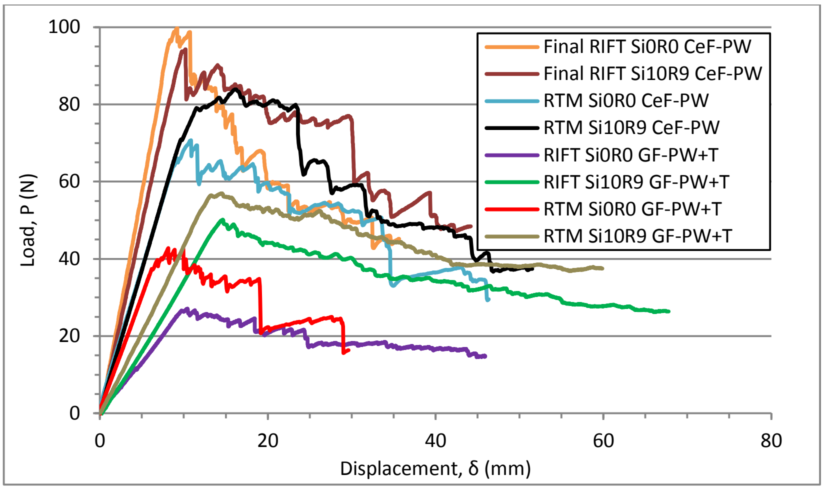

Figure 8.15: Load-displacement curves for RIFT- and RTM-processed CeFRPs vs GFRPs

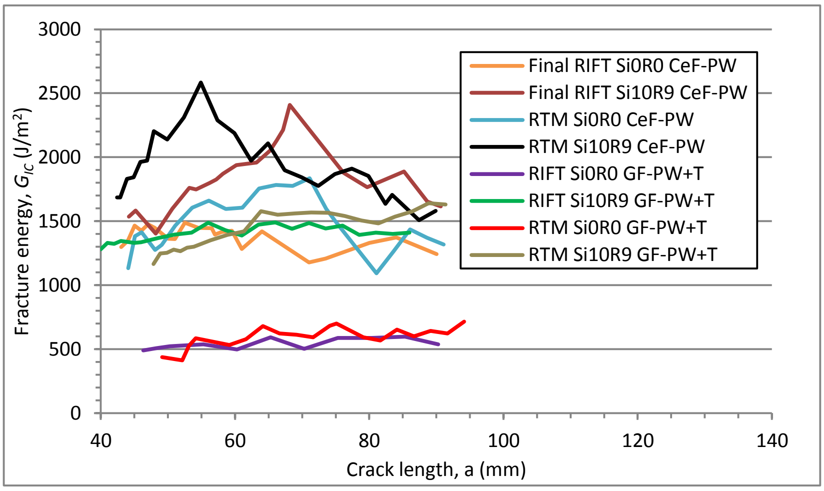

Figure 8.16: R-curves for RIFT- and RTM-processed CeFRPs vs GFRPs

The same conclusion can be drawn for all the CeFRPs and GFRPs when comparing the load-displacement curves. It may be seen that stable crack growth, with random unstable jumps, was observed for both the final RIFT- and RTM-processed CeFRPs, see Figure 8.15. These jumps were associated with the extensive fibre/fibre bundle bridging, where the bridging led to a jump in the fracture energy [162], see Figure 8.16. The same type of crack growth was observed for the GFRPs, but with somewhat more stable behaviour due to the less extensive fibre bridging, compared to the CeFRPs.

8.3 Fracture-toughening Mechanisms

8.3.1 Introduction

The present section illustrates the fracture mechanisms involved in the various FRPs. These include the particle induced toughening mechanisms, the fibre induced toughening mechanisms and the effects of the fibre architecture on the toughening mechanisms. SEM images and side-view images of the DCB specimens are presented.

8.3.2 Particle Induced Toughening Mechanisms

Results for the four different matrix formulations, namely unmodified (Si0R0), silica-nanoparticle modified (Si10R0), rubber-microparticle modified (Si0R9) and hybrid modified (Si10R9) FRPs are presented. It should be noted that the fracture mechanisms involved with the toughening particles on the fracture surfaces of the different FRPs were identical. Hence, the fracture surfaces are shown based on the matrix formulations.

8.3.2.1 *Unmodified Toughening Mechanisms (Si0R0)*

A micrograph of the fracture surfaces of the Si0R0 FRPs is shown in Figure 8.17. A relatively smooth and glassy brittle fracture was observed with some plastic deformation of the epoxy matrix.

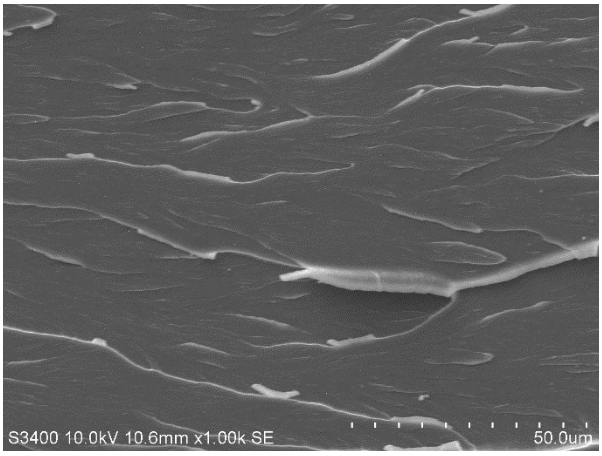

Figure 8.17: SEM image of Si0R0 FRP (crack from left to right)

8.3.2.2 *Silica-nanoparticle Toughening Mechanisms (Si10R0)*

Figure 8.18 shows the fracture surfaces of the Si10R0 FRPs at two different magnifications. This shows particle debonding and plastic void growth due to the debonding of the silica-nanoparticles (Figure 8.18b) in addition to the plastic deformation (Figure 8.18a) observed on the fracture surface of the Si0R0 FRPs. A good dispersion of the silica-nanoparticles was observed (Figure 8.18b). This confirmed the findings discussed earlier in sections ‘5.4.6’ and ‘6.4.6’. It is noted that a less glassy surface was observed for the Si10R0 FRPs, compared to the fracture surface of the Si0R0 FRPs, see Figure 8.17, which correlates with the higher toughness that was recorded for the former composites.

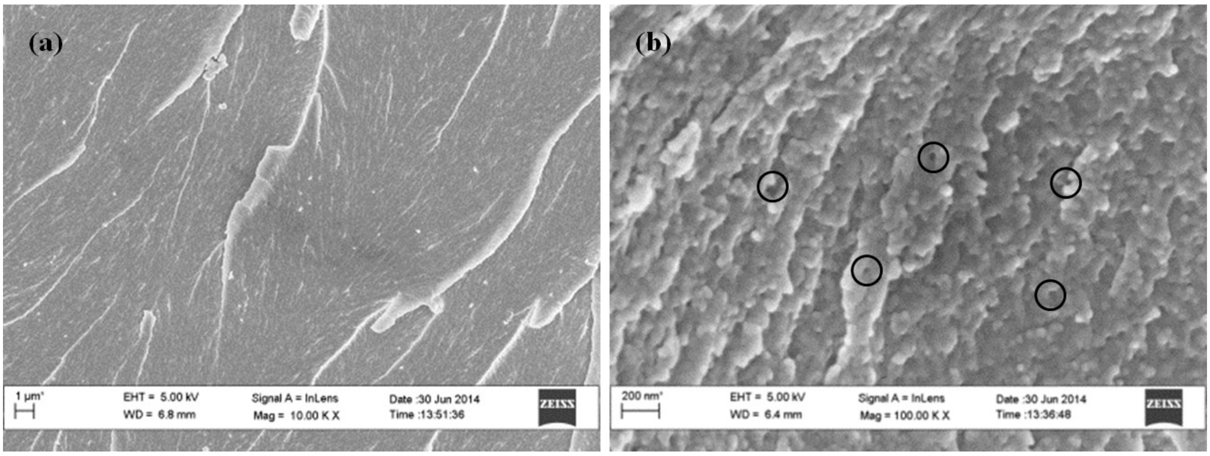

Figure 8.18: SEM images of Si10R0 FRP: some voids around particles are circled (crack from left to right)

8.3.2.3 *Rubber-microparticle Toughening Mechanisms (Si0R9)*

Figure 8.19 shows the fracture surfaces of the Si0R9 FRPs at two different magnifications, showing particle cavitation of the rubber-microparticles and plastic void growth of epoxy matrix (Figure 8.19b), in addition to the plastic deformation (Figure 8.19a) observed on the fracture surface of the Si0R0 FRPs. An average diameter of 2.37±0.80 μm for the cavitated rubber particles was measured from the SEM images, which may be compared to an average diameter of 1.15±0.25 μm for the rubber particles prior to fracture testing, as measured from the AFM images. A good dispersion of the rubber-microparticles was observed (Figure 8.19a). This again confirmed the findings discussed earlier in sections '5.4.6' and '6.4.6'.

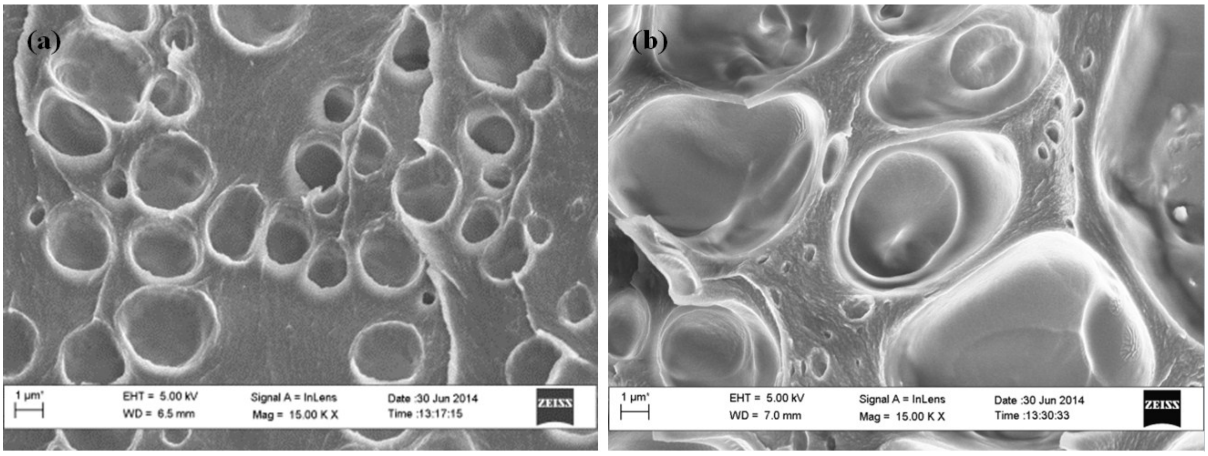

Figure 8.19: SEM images of Si0R9 FRP (crack from left to right)

8.3.2.4 *Hybrid Toughening Mechanisms (Si10R9)*

Figure 8.20 shows the fracture surfaces of the Si10R9 FRPs at three different magnifications. A good dispersion of the rubber-microparticles was observed (Figure 8.20a), while there was some degree of agglomeration of the silica-nanoparticles (Figure 8.20c). This again confirmed the findings discussed earlier in findings discussed earlier in sections '5.4.6' and '6.4.6'. Plastic deformation of the epoxy matrix was observed (Figure 8.20b). It was noted that all the toughening mechanisms found on the fracture surfaces of both Si10R0 and Si0R9 FRPs were observed on the fracture surfaces of the Si10R9 FRPs, e.g. particle debonding and plastic void growth mechanisms for the silica-nanoparticles (Figure 8.20c) and particle cavitation and plastic void growth mechanisms associated with the presence of the rubber-microparticles (Figure 8.20b), see Figure 8.18 and Figure 8.19. An average diameter of 2.65±0.75 μm was measured for the cavitated rubber particles from the SEM images, compared to an average diameter of 1.12±0.20 µm for the rubber particles prior to fracture testing, as measured from the AFM images.

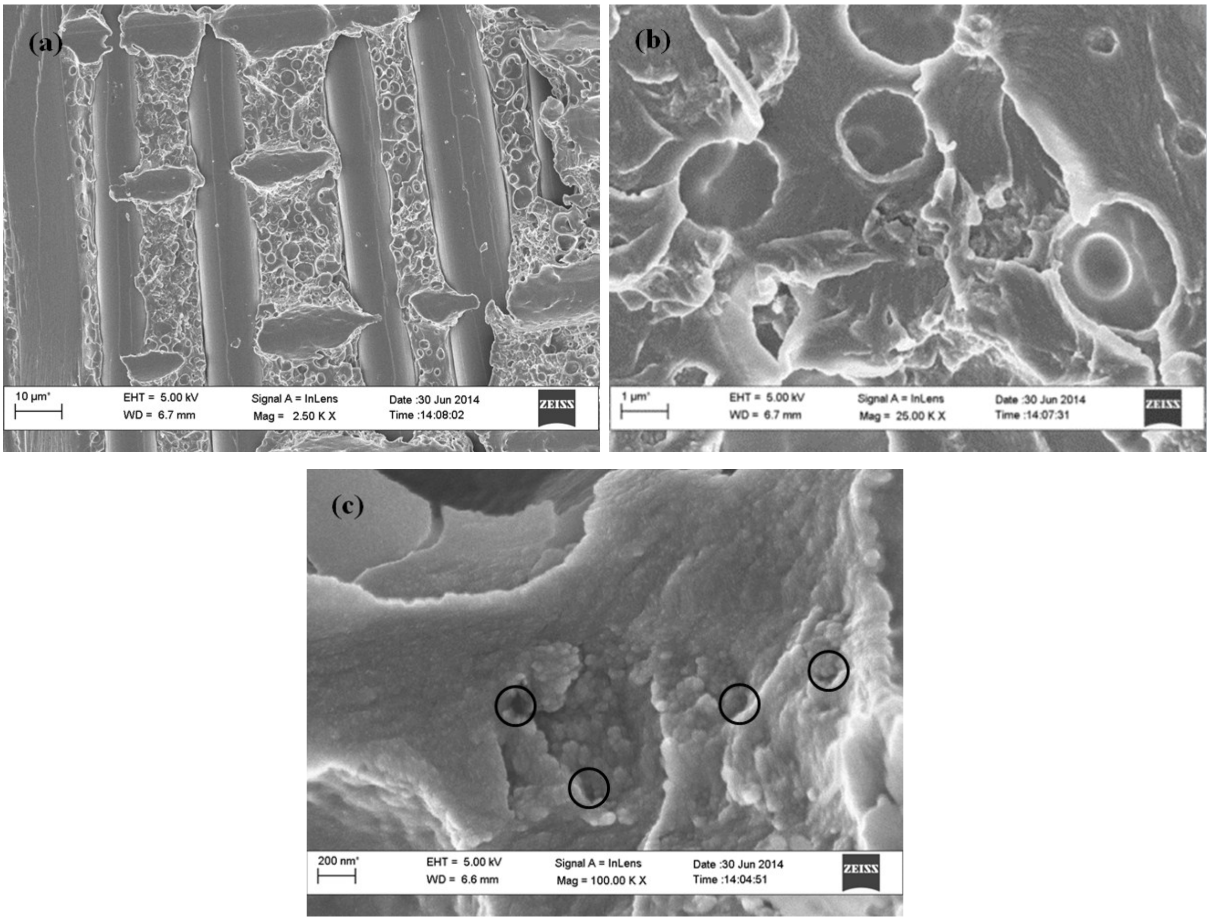

Figure 8.20: SEM images of Si10R9 FRP: some voids around particles are circled (crack from left to right)

8.3.3 Fibre Induced Toughening Mechanisms

8.3.3.1 *Natural Fibre Induced Toughening Mechanisms*

8.3.3.1.1 Initial RIFT-processed NFRPs - Fibre Induced Toughening Mechanisms

Figure 8.21 shows SEM images of the fracture surface of the initial RIFT-processed FFRP-UD at three different magnifications. Due to the relatively poor fibre-matrix adhesion, a clean fibre-matrix debonding surface was observed (Figure 8.21c). This was due to the high moisture content of up to 10 wt% in the NFs pre-manufacturing and the adverse effect the moisture had upon the degree of fibre-matrix adhesion. The transformation of the moisture in the NFs into steam at the high temperatures reached during curing of the epoxy matrix not only decreased the fibre-matrix adhesion but also led to a relatively high void content of up to 17%. This aspect was confirmed from the large number of macro-voids that were observed across the surface (Figure 8.21b). As a result of these various effects, a very low value of the interlaminar fracture energy was recorded (Figure 8.21a). Similar fracture surfaces were observed for the initial RIFT-processed CeFRP-PW, see Figure 8.22. (Note: The VD- and OP-modified FFRPs possessed very similar fracture surfaces to the initial RIFT-processed FFRP, and hence their fracture surfaces are not shown.)

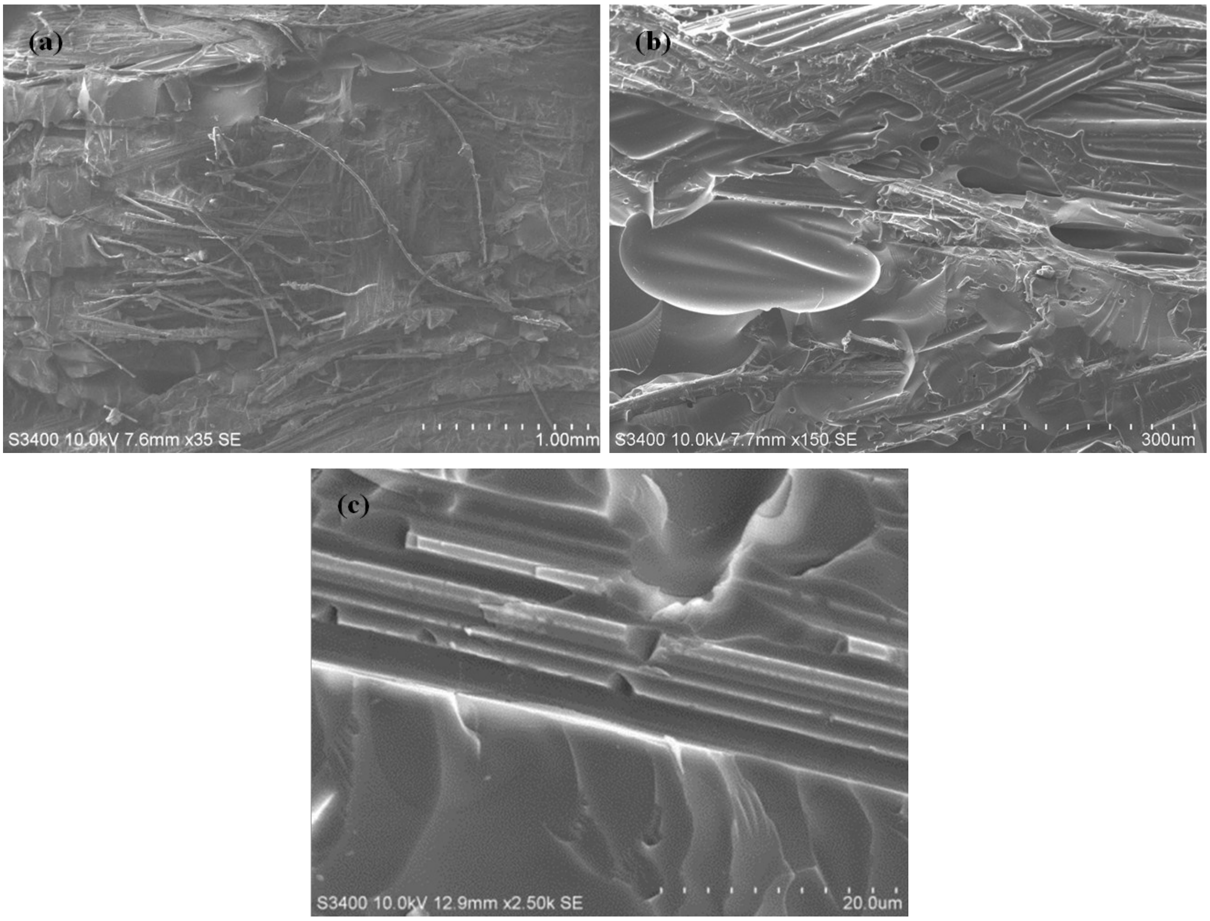

Figure 8.21: SEM images of initial RIFT-processed FFRP-UD (crack from left to right)

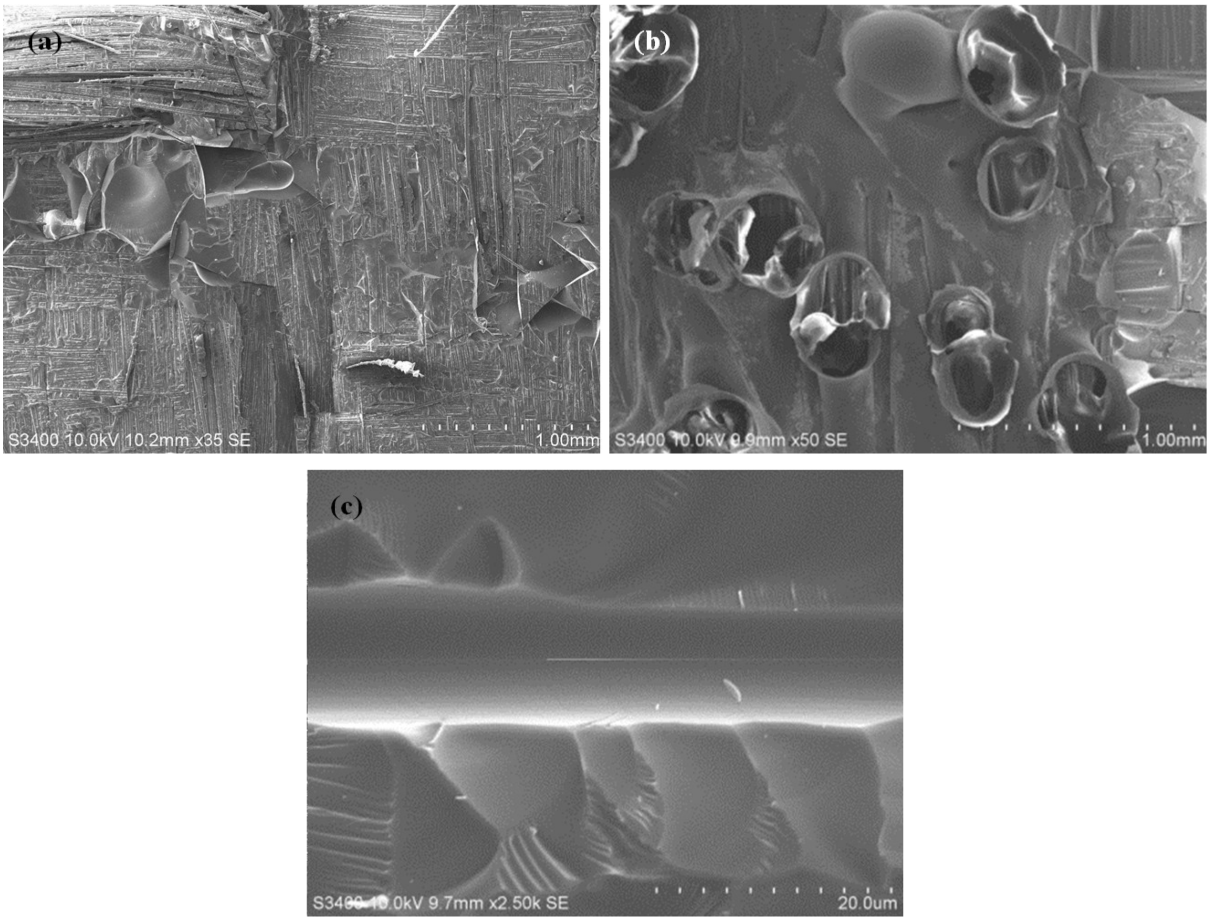

Figure 8.22: SEM images of initial RIFT-processed CeFRP-PW (crack from left to right)

8.3.3.1.2 Final RIFT-processed NFRPs - Fibre Induced Toughening Mechanisms

Figure 8.23 shows the SEM images of the <u>final</u> RIFT-processed FFRP-UD. In the FFRPs, the crack tended to propagate through the fibres/fibre bundles and the majority of the fracture surfaces were covered with defibrillated, bridged and broken fibres/fibre bundles. The main failure mechanisms therefore involved fibre/fibre bundle bridging (Figure 8.23a), fibre breakage (Figure 8.23b) and fibre defibrillation (Figure 8.23c). Due to the dominance of these toughening mechanisms, only a relatively small extent of failure involving the epoxy matrices, e.g. plastic deformation (Figure 8.23d), was observed. This was probably because the short interlocked FFs formed by the elementary fibres/microfibrils [4], bonded together with pectin [36], were susceptible to defibrillation and bridging, which promoted crack propagation through the defibrillated fibres or led to fibre bridging. The side-view image of the specimen during the interlaminar fracture test clearly shows the bridging fibres and fibre bundles, see Figure 8.24. Hence, the interlaminar fracture energy increases with increasing crack length, i.e. there is a pronounced R-curve.

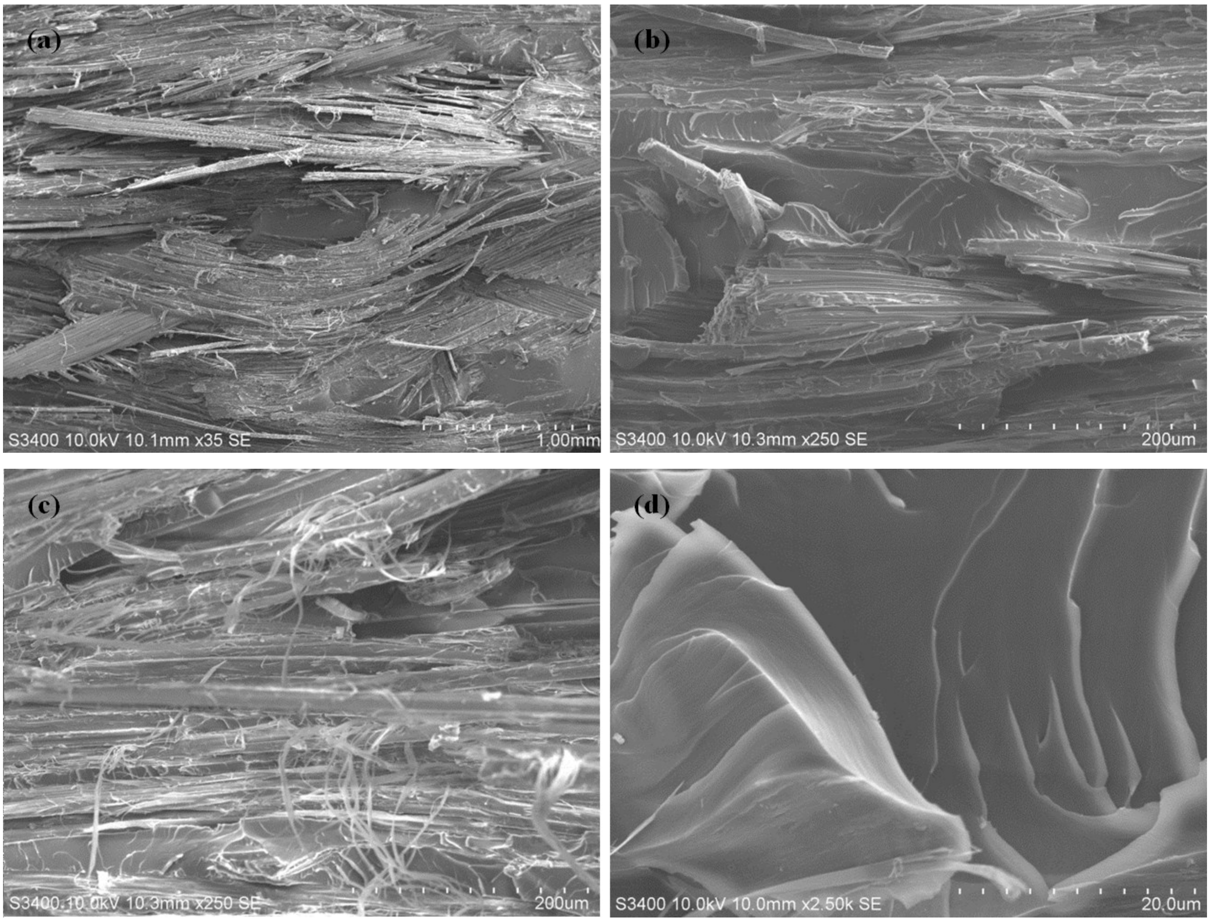

Figure 8.23: SEM images of final RIFT-processed FFRP-UD (crack from left to right)

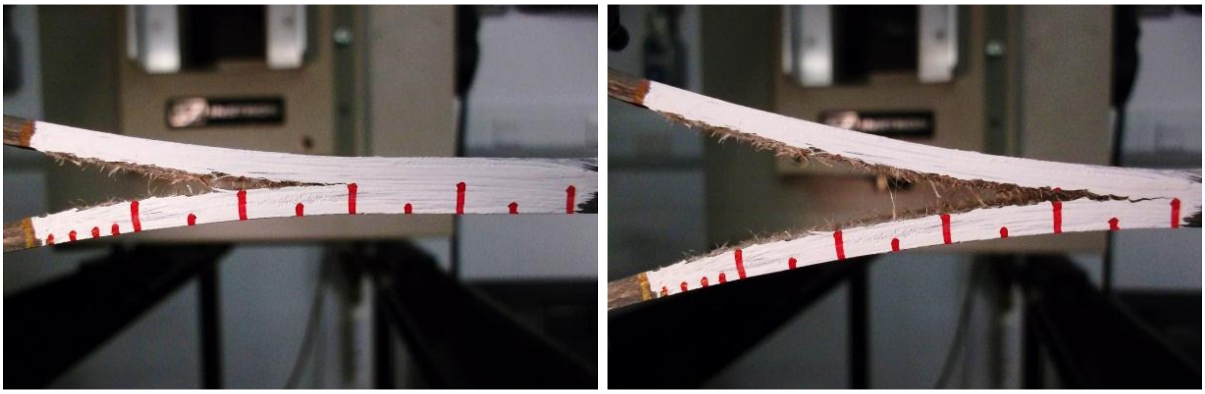

Figure 8.24: Side-view images at two different time-step of final RIFT-processed FFRP-UD DCB specimen during mode I interlaminar fracture test

The fracture surfaces of the final RIFT-processed CeFRP-PW are shown in Figure 8.25. It was noted that the fibre defibrillation found on the fracture surfaces of the FFRPs was more extensive than for the CeFRPs (Figure 8.25b). This was because the CeFs were uniform continuous fibres [38] with less intrinsic defects, compared to the FFs which were made from interlocked spun yarns from naturally occurring fibres bonded together with pectin [4][36]. It is noteworthy that in the FRPs with the plain-woven fibre architecture, the fibres in the weft and warp directions were mechanically interlocked. Hence, fibre/fibre bundle bridging in one direction generally led to bridging in the other direction and delamination (Figure 8.25a). As a result, the fibre/fibre bundle bridging in the CeFRPs was found to be more extensive and more random throughout the fracture surfaces than in the FFRPs. This statement was confirmed by the side-view images of the two specimens during the interlaminar fracture tests where there is more extensive bridging in Figure 8.26 compaed to Figure 8.24. Due to the dominance of these toughening mechanisms, only a small extent of failure in the epoxy matrices, e.g. plastic deformation, was observed (Figure 8.25c).

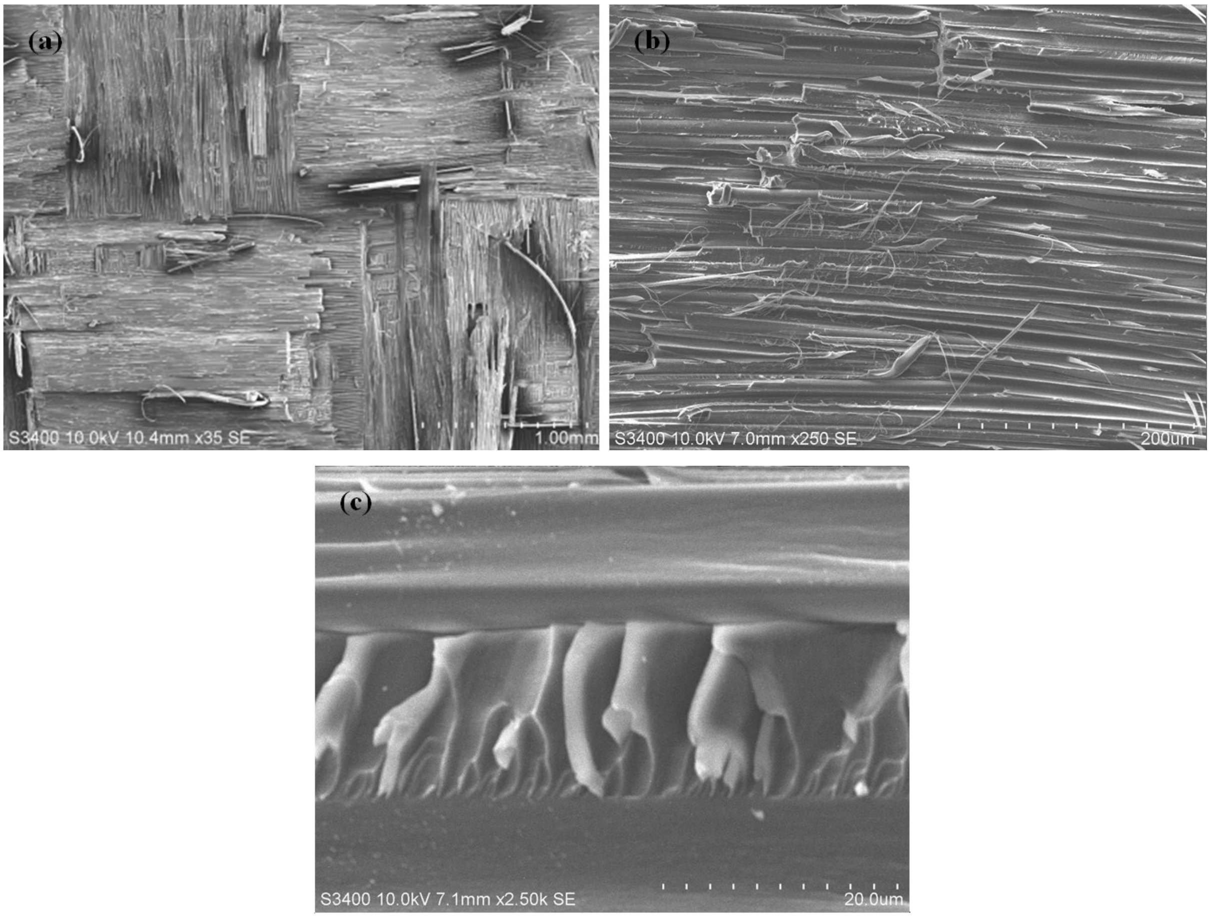

Figure 8.25: SEM images of final RIFT-processed CeFRP-PW (crack from left to right)

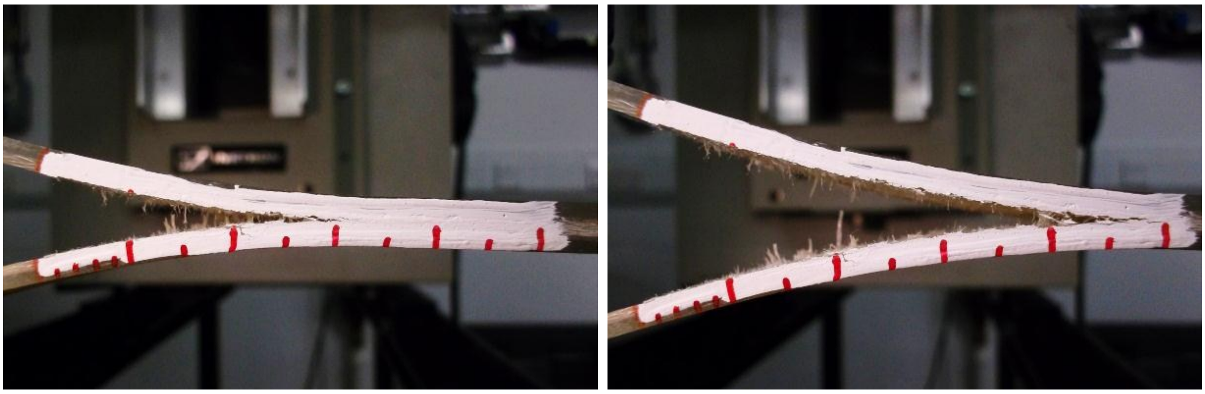

Figure 8.26: Side-view images at two different time-step of RIFT-processed CeFRP-PW DCB specimen during mode I interlaminar fracture test

8.3.3.1.3 RTM-processed NFRPs - Fibre Induced Toughening Mechanisms

Figure 8.27 shows the SEM images of the RTM-processed FFRP-UD composites. The fracture mechanisms involved in the fracture of the FFRPs from the final RIFT process and RTM process were found to be identical. These mechanisms were fibre breakage due to fibre/bundle bridging (Figure 8.27a), fibre defibrillation (Figure 8.27b) and plastic deformation of the epoxy polymer (Figure 8.27c), also see Figure 8.23. However, due to the higher void contents observed for the RTM-processed FFRPs, compared to those from the RIFT process (i.e. void contents of 2-6%, compared to 1%), the measured fracture energies were found to be different. This was especially the case for the Si0R9 and Si10R9 matrix formulations. The presence of voids appeared to compromise the fibre-matrix adhesion. Indeed, as can be seen from the side-view images, a more extensive amount of fibre/fibre bundle bridging was observed for the final RIFT-processed FFRPs (Figure 8.24) than for the RTM-processed FFRPs (Figure 8.28).

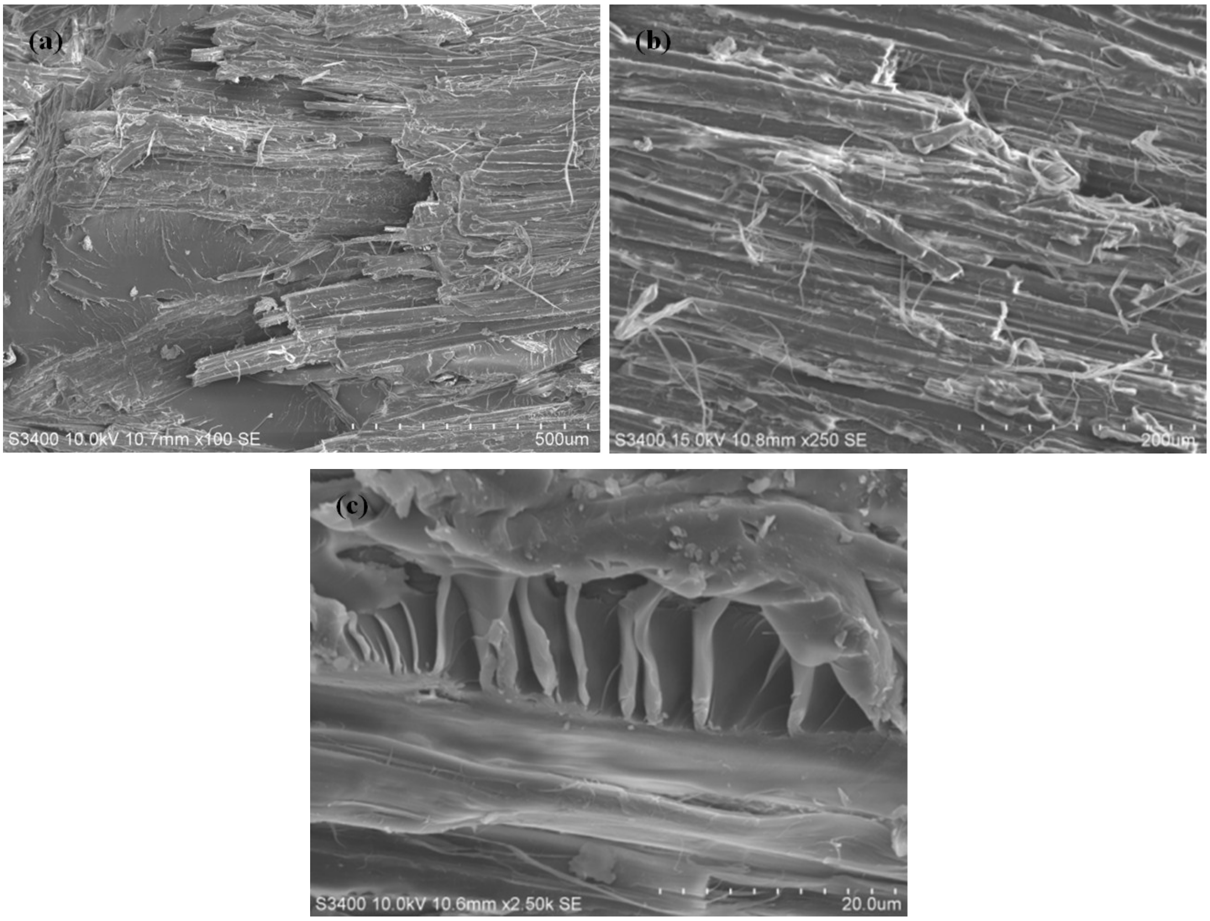

Figure 8.27: SEM images of RTM-processed FFRP-UD (crack from left to right)

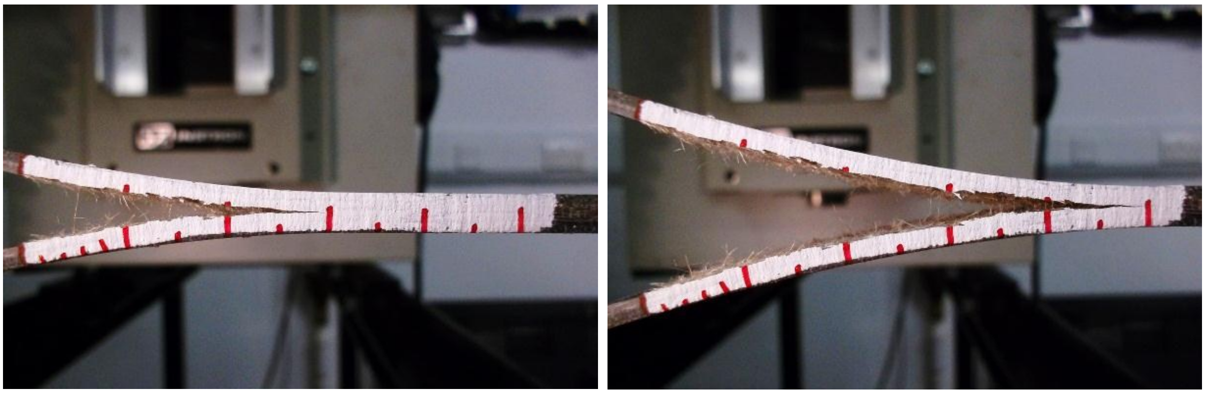

Figure 8.28: Side-view images at two different time-step of RTM-processed FFRP-UD DCB specimen during mode I interlaminar fracture test

Figure 8.29 shows the SEM images of the RTM-processed CeFRP-PW composite. Although the fracture mechanisms involved in the fracture of the CeFRPs from the RIFT and RTM processes were found to be identical (i.e. fibre breakage due to fibre/bundle bridging (Figure 8.29a), fibre defibrillation (Figure 8.29b) and plastic deformation of the epoxy polymer (Figure 8.29c)), the fracture energies measured for the RTM-processed CeFRPs were found to be inferior. This was probably due to the approximately 10% lower fibre volume fractions achieved in the RTM process, compared to the higher fibre volume fractions present in the RIFT-processed CeFRPs. This was confirmed by the side-view images of the two specimens during the interlaminar fracture tests, which show a more extensive fibre/fibre bundle bridging for the final RIFT-processed CeFRPs (Figure 8.26) than in the RTM-processed CeFRPs (Figure 8.30).

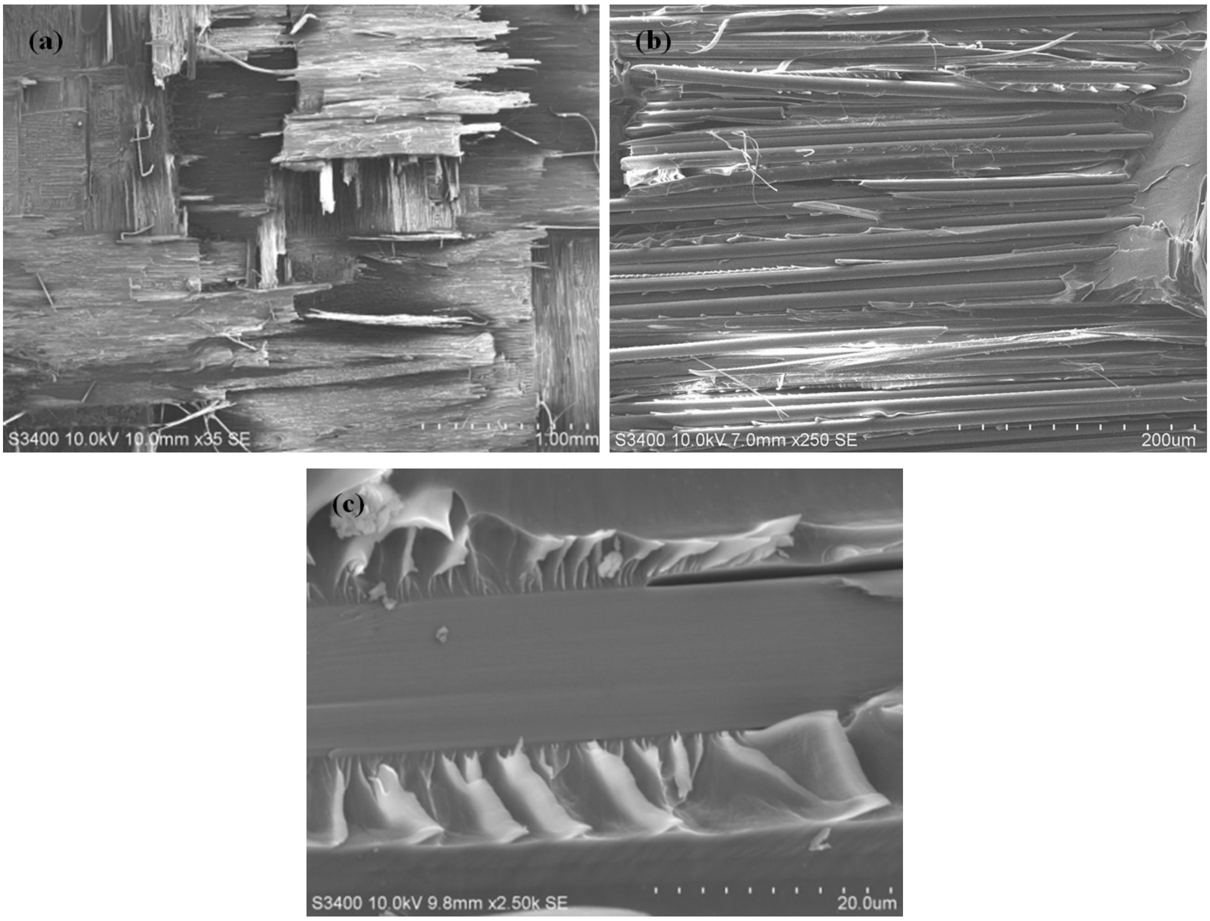

Figure 8.29: SEM images of RTM-processed CeFRP-PW (crack from left to right)

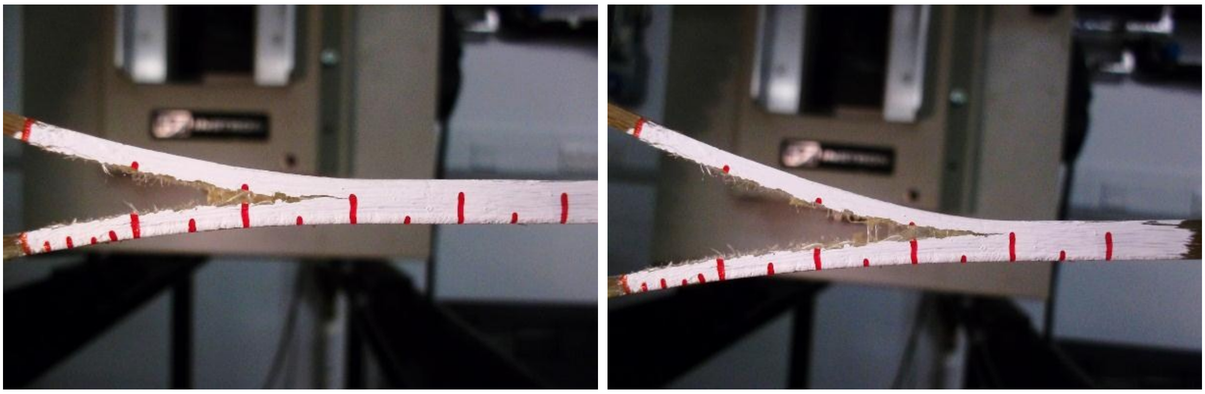

Figure 8.30: Side-view images at two different time-step of RTM-processed CeFRP-PW DCB specimen during mode I interlaminar fracture test

8.3.3.2 *Glass Fibre Induced Toughening Mechanisms*

It was found that the fracture surfaces of the RIFT-processed GFRPs and RTM-processed GFRPs with the same fibre reinforcement architecture were identical. This was confirmed by the identical measured fracture energies from the two processes, as discussed in section '8.2.4'. Figure 8.31 and Figure 8.32 show the fracture surfaces of the GFRPs from the two manufacturing processes, which indicate fibre breakage due to fibre bridging (Figure 8.31a and Figure 8.32a) and plastic deformation of the epoxy polymer (Figure 8.31b and Figure 8.32b). However, due to the difference in the fibre reinforcement architecture, the GFRPs-UD and GFRPs-PW+T composites exhibited different fractures, see Figure 8.33 and Figure 8.34. As mentioned earlier, in the FRPs-PW the fibres in the weft and warp directions were mechanically interlocked. Hence, the fibre/fibre bundle bridging in one direction generally led to the bridging in the other direction and delamination. As a result, the bridging for the GFRPs-PW+T shown in Figure 8.34 was found to be more extensive than for the GFRPs-UD shown in Figure 8.33.

It is noted that due to the improved fibre-matrix adhesion of the CeFRPs in the final RIFT process compared with the initial RIFT process, the fibre/fibre bundle bridging in the GFRPs-PW+T was less extensive than that observed for the CeFRPs-PW, even though they both used a plain-woven fibre architecture. Also, although the fibre bridging mechanism was observed in both the GFRPs-UD and FFRPs-UD, fibre bundle bridging was only observed in the FFRPs-UD. This was probably because of the unique microstructure of the FFs [4][36], as discussed previously.

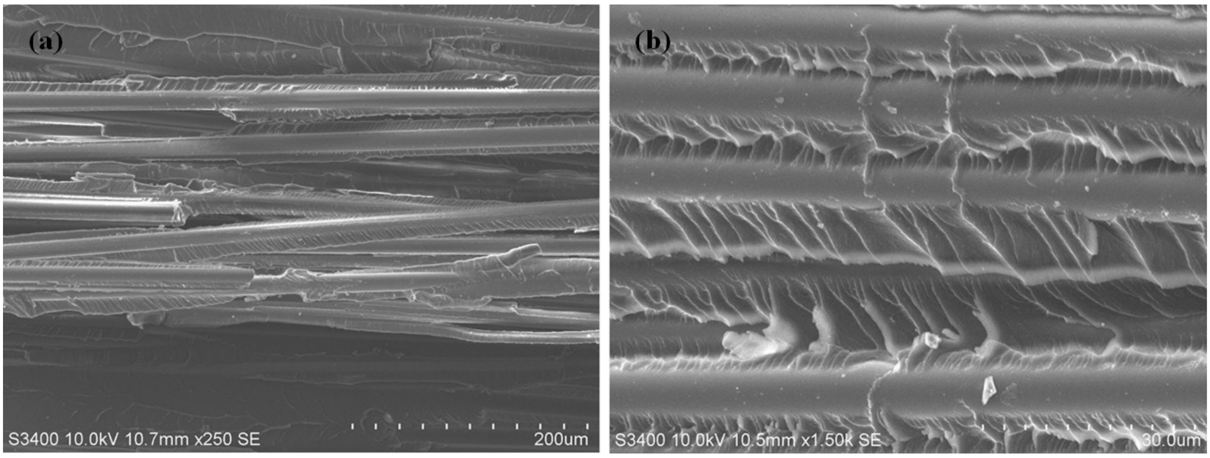

Figure 8.31: SEM images of RIFT-processed GFRPs (crack from left to right)

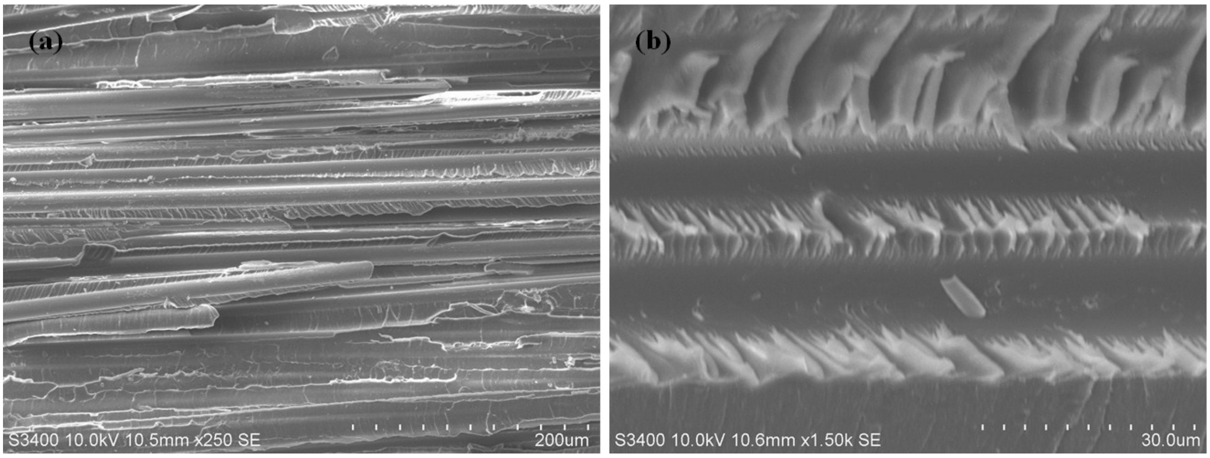

Figure 8.32: SEM images of RTM-processed GFRPs (crack from left to right)

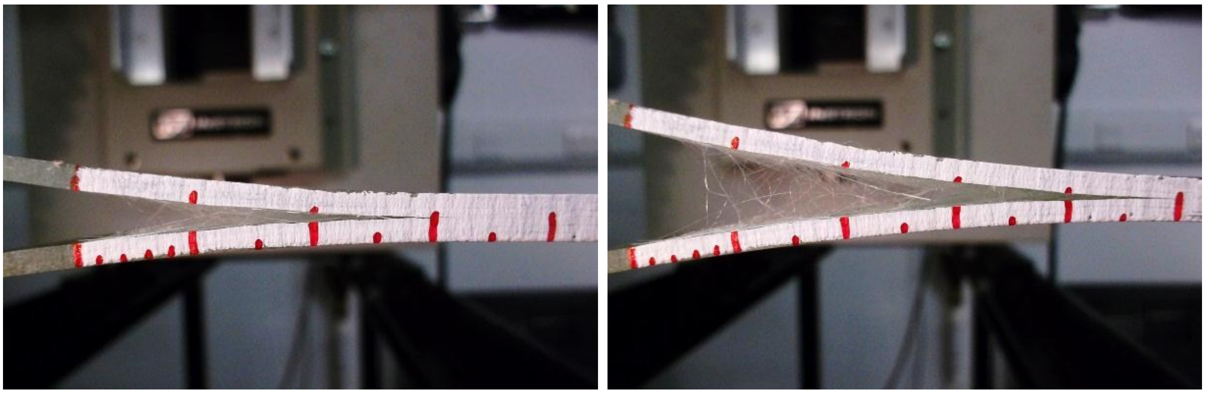

Figure 8.33: Side-view images of GFRP-UD DCB specimen during mode I interlaminar fracture test

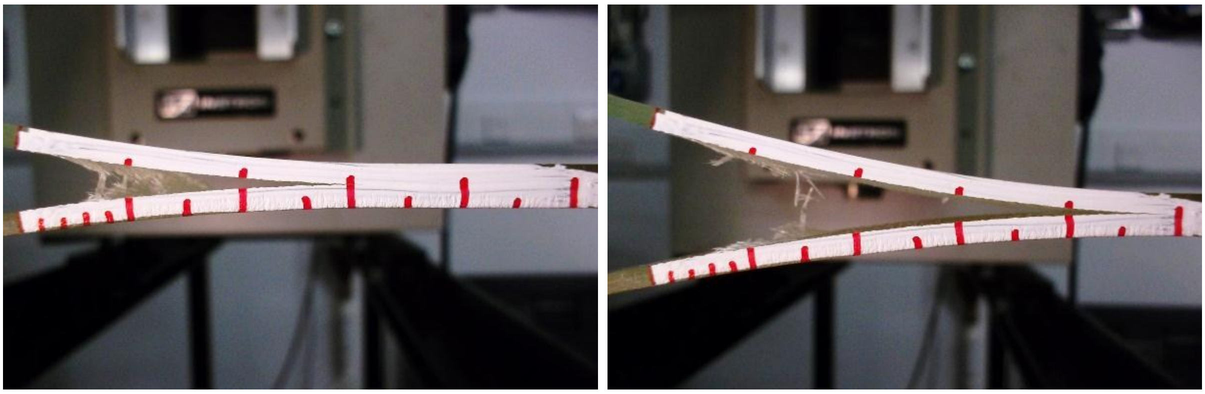

Figure 8.34: Side-view images of GFRP-PW DCB specimen during mode I interlaminar fracture test

8.3.4 Summary of Fracture Mechanisms in FRPs

Table 8.7 summarizes the toughening mechanisms involved in the FRPs with different fibre/fabric reinforcements and different matrix formulations. It should be noted that shear yielding cannot be definitely identified on the fracture surfaces, since this is only really possible using transmission cross-polarised light microscopy [56]. However, shear yielding is known to occur in the plastically deformed epoxy polymer [164] and is initiated by the shear localization around the periphery of the particles [14].

Table 8.7: Summary of toughening mechanisms in FRPs with different fibre/fabric reinforcements

Formulation	FFRPs-UD	CeFRPs-PW	GFRPs-UD	GFRPs-PW+T
Si0R0	- Fibre bridging - Fibre bundle bridging - Fibre defibrillation - Shear yielding - Plastic deformation	- Fibre bridging - Fibre bundle bridging - Fibre defibrillation - Delamination - Shear yielding - Plastic deformation	- Fibre bridging - Shear yielding - Plastic deformation	- Fibre bridging - Fibre bundle bridging - Fibre defibrillation - Delamination - Shear yielding - Plastic deformation
Si10R0	- Fibre bridging - Fibre bundle bridging - Fibre defibrillation - Shear yielding - Plastic deformation - Silica debonding - Plastic void growth	- Fibre bridging - Fibre bundle bridging - Fibre defibrillation - Delamination - Shear yielding - Plastic deformation - Silica debonding - Plastic void growth	- Fibre bridging - Shear yielding - Plastic deformation - Silica debonding - Plastic void growth	- Fibre bridging - Fibre bundle bridging - Fibre defibrillation - Delamination - Shear yielding - Plastic deformation - Silica debonding - Plastic void growth
Si0R9	- Fibre bridging - Fibre bundle bridging - Fibre defibrillation - Shear yielding - Plastic deformation - Rubber cavitation - Plastic void growth	- Fibre bridging - Fibre bundle bridging - Fibre defibrillation - Delamination - Shear yielding - Plastic deformation - Rubber cavitation - Plastic void growth	- Fibre bridging - Shear yielding - Plastic deformation - Rubber cavitation - Plastic void growth	- Fibre bridging - Fibre bundle bridging - Fibre defibrillation - Delamination - Shear yielding - Plastic deformation - Rubber cavitation - Plastic void growth
Si10R9	- Fibre bridging - Fibre bundle bridging - Fibre defibrillation - Shear yielding - Plastic deformation - Silica debonding - Rubber cavitation - Plastic void growth	- Fibre bridging - Fibre bundle bridging - Fibre defibrillation - Delamination - Shear yielding - Plastic deformation - Silica debonding - Rubber cavitation - Plastic void growth	- Fibre bridging - Shear yielding - Plastic deformation - Silica debonding - Rubber cavitation - Plastic void growth	- Fibre bridging - Fibre bundle bridging - Fibre defibrillation - Delamination - Shear yielding - Plastic deformation - Silica debonding - Rubber cavitation - Plastic void growth

From Table 8.7, it may be observed that the main difference in the toughening mechanisms between the FRPs with different fibre/fabric reinforcements was the fibre induced toughening mechanisms. Identical matrix induced mechanisms were observed for the FRPs with the same matrix formulations. Now, the fracture energy can be predicted by identifying the types of toughening mechanisms and estimating their magnitudes and the prediction of the fracture energy of the FRPs, as will be discussed below.

8.4 Analytical Model of Mode I Interlaminar Fracture Energy of Fibre-reinforced Modified Matrix Composites

8.4.1 Introduction

The mode I interlaminar fracture energy of fibre-reinforced modified matrix composites can be expressed [56][57][119][163] by:

$$G_{IC} = G_{ICU} + \psi_{si} + \psi_r + \psi_f \tag{8.1}$$

where G_{ICU} is the fracture energy of the unmodified matrix (which was measured to be 133 J/m^2 [14]), ψ_{si} is the increase in fracture energy caused by the toughening mechanisms contributed from the silica-nanoparticles, the toughening increment ψ_r arises from the CTBN rubber-microparticles and the increment ψ_f arises from the presence of the reinforcing fibres. These contributions will be discussed in turn below.

8.4.2 Silica-nanoparticle Toughening Mechanisms

The increase in fracture energy contributed from the silica-nanoparticles can be categorised into three main toughening mechanisms and can be expressed by [56]:

$$\psi_{si} = \Delta G_{si}^{sb} + \Delta G_{si}^{vp} + \Delta G_{si}^{db} \tag{8.2}$$

where ΔG_{si}^{sb}, ΔG_{si}^{vp} and ΔG_{si}^{db} are the fracture energy contributed from the shear band yielding, plastic void growth and particle-matrix interfacial debonding mechanisms.

8.4.2.1 *Shear Band Yielding – Silica-nanoparticles*

The fracture energy from localized plastic shear band yielding initiated by the presence of the silica-nanoparticles and the corresponding size of the plastic zone can be calculated based on the following equation [119]:

$$\Delta G_{si}^{sb} = 2\int_0^{r_y} U_{si}^{sb}(r)dr \tag{8.3}$$

where r_y is the radius of the plastic zone under plane strain condition and $U_{si}^{sb}(r)$ is the energy contributed from shear band yielding due to the addition of the silica-nanoparticles.

Evans et al. [164] proposed that the lower limit of integration should not be zero but should be the minimum distance from the crack plane at which the matrix between the particles experiences plastic shear band yielding. This distance was suggested to be of the order of the particle radius, since a crack typically passes around one pole of the particle, leaving the plastically deformed polymer at the opposite pole. Thus, the fracture energy from localized plastic shear band yielding initiated by the presence of silica-nanoparticles now becomes:

$$\Delta G_{si}^{sb} = 2\int_{r_p}^{r_y} U_{si}^{sb}(r)dr \tag{8.4}$$

where r_p is the radius of the particles.

According to the work of Dekkers & Heikens [165][166], shear-bands will initiate from all of the particles. With the lower integration limit of r_p instead of zero, the fracture energy contributed from shear band yielding for a silica-nanoparticle modified polymer, ΔG_{si}^{sb}, has been derived [56][105]. Modification has been made to account for the presence of reinforcing fibres and voids and ΔG_{si}^{sb} is expressed as:

$$\Delta G_{si}^{sb} = 0.5 v_p (1 - v_f - v_v) \sigma_{yc} \gamma_{fu} F\left(r_y^{sb}\right) \tag{8.5}$$

where v_p is the volume fraction of the silica-nanoparticles, $\left(1 - v_f - v_v\right)$ is the volume fraction of the modified matrix where v_f is the fibre volume fraction of the fibres and v_v is the fibre volume fraction of the voids, σ_{yc} is the plane-strain compressive yield stress of the unmodified matrix, γ_{fu} is the shear strain to fracture of the unmodified matrix, r_y^{sb} is the radius of plastic zone induced by shear band yielding and $F\left(r_y^{sb}\right)$ is given as [57]:

$$F\left(r_y^{sb}\right) = r_y^{sb}\left[\left(\frac{4\pi}{3v_p}\right)^{\frac{1}{3}} - \frac{54}{35}\right] \tag{8.6}$$

and

$$r_y^{sb} = \left(K_p^{sb}\right)^2 \left(1 + \frac{\mu_m}{\sqrt{3}}\right)^2 r_{yu} \tag{8.7}$$

where K_p^{sb} is the maximum stress concentration around the particles [167][168], μ_m is a material constant allowing for the pressure-dependency of the yield stress and was given in Sultan & McGarry [169], a value of 0.2 was used in the present study [14][105], and r_{yu} is the Irwin prediction of the plane strain plastic zone radius for the unmodified matrix at fracture [170]. The terms, K_p^{sb} and r_{yu} can be calculated using the equations as follow:

$$K_p^{sb} = 0.59 v_p + 1.65 \tag{8.8}$$

and

$$r_{yu} = \frac{1}{6\pi} \frac{E_m G_{ICU}}{\left(1 - \upsilon_m^2\right)\sigma_{yt}^2} \tag{8.9}$$

where E_m, G_{ICU}, υ_m and σ_{yt} are the modulus, fracture energy, Poisson's ratio and uniaxial tensile yield stress of the unmodified matrix respectively.

8.4.2.2 ***Plastic Void Growth – Silica-nanoparticles***

The fracture energy contributed from the plastic void growth in the presence of silica-nanoparticles is related to the increase in volumetric strain of the voids and the size of the plastic zone [119][171]. It may be expressed as:

$$\Delta G_{si}^{vp} = 2\int_0^{r_y} U_{si}^{vp}\left(r\right) dr \tag{8.10}$$

where $U_{si}^{vp}\left(r\right)$ is the dissipated strain-energy density for toughening mechanism contributed from the silica-nanoparticles.

The strain-energy density for voids growing from an initial volume, V_{v0}, to an end volume, V_{v1}, is given by:

$$U_{si}^{vp}\left(r\right)=\int_{V_{v0}}^{V_{v1}} pd\theta \tag{8.11}$$

where p is the local hydrostatic stress or the local mean stress.

The expressions above have been combined and derived by Huang & Kinloch [57] and $U_{si}^{vp}\left(r\right)$ now becomes:

$$U_{si}^{vp}\left(r\right)=0.5\sigma_{yt}\left(v_{vv}-v_{pv}\right) \tag{8.12}$$

where v_{vv} and v_{pv} are the volume fractions of the enlarged voids and the initial particles which show plastic void growth, and these may be directly measured from the appropriate SEM images. Thus, the fracture energy contributed from the plastic void growth in the presence of silica-nanoparticles is modified to account for the presence of reinforcing fibres and voids is then given by:

$$\Delta G_{si}^{vp}=r_y^{vp}(1-v_f-v_v)\left(v_{vv}-v_{pv}\right)\sigma_{yt} \tag{8.13}$$

where the radius of the plastic zone induced by plastic void growth, r_y^{vp}, can be calculated using the equation as follows [14]:

$$r_y^{vp}=\left(K_p^{vp}\right)^2\left(1+\frac{\mu_m}{\sqrt{3}}\right)^2 r_{yu} \tag{8.14}$$

where r_{yu} can be calculated using Equation (8.9) in section '8.4.2.1' and the maximum stress concentration factor around the voids for the particle modified matrix, K_p^{vp}, is given by:

$$K_p^{vp}=0.918v_p+2.11 \tag{8.15}$$

It is noted that the voids around the particles are typically larger than the particles. Hence, the value of the maximum stress concentration factor around the voids for the particle modified matrix, K_p^{vp}, calculated using Equation (8.15) is typically higher than the maximum stress concentration around the particles, K_p^{sb}, calculated using Equation (8.8). This was due to the smaller spaces between voids compared to the spaces between particles.

8.4.2.3 ***Debonding – Silica-nanoparticles***

The debonding mechanism typically promotes the initiation of plastic void growth by allowing the matrix to deform plastically [105][173]. Hence, debonding is typically followed by plastic void growth [14]. Kinloch and Taylor have demonstrated that the voids around particles closed-up when the epoxy polymer was heated above its glass transition temperature and allowed to relax. [160], which shows that the epoxy matrix has plastically deformed. The increase in the fracture energy from interfacial debonding is generally considered to absorb little energy compared to the plastic deformation of the matrix [172].

8.4.3 Rubber-microparticle Toughening Mechanisms

The increase in fracture energy contributed from the rubber-microparticles can be categorised into four main toughening mechanisms and can be expressed by [57][176]:

$$\psi_r = \Delta G_r^{sb} + \Delta G_r^{rb} + \Delta G_r^{vp} + \Delta G_r^{db} \tag{8.16}$$

where ΔG_r^{sb}, ΔG_r^{rb}, ΔG_r^{vp} and ΔG_r^{db} are the fracture energy contributed from the shear band yielding, rubber particle bridging, plastic void growth and particle-matrix interfacial debonding mechanisms.

8.4.3.1 ***Shear Band Yielding – Rubber-microparticles***

The fracture energy contributed from the shear band yielding in the presence of the rubber-microparticles is expressed as [56][57][105][119][165][166]:

$$\Delta G_r^{sb} = 0.5 v_p (1 - v_f - v_v) \sigma_{yc} \gamma_{fu} F\left(r_y^{sb}\right) \tag{8.17}$$

where v_p is the volume fraction of the rubber-microparticles, $F\left(r_y^{sb}\right)$ can be calculated using Equation (8.6).

8.4.3.2 ***Plastic Void Growth – Rubber-microparticles***

The fracture energy contributed from the plastic void growth in the presence of the rubber-microparticles is expressed as [119][171]:

$$\Delta G_r^{vp} = r_y^{vp} (1 - v_f - v_v) \left(v_{vv} - v_{pv}\right) \sigma_{yt} \tag{8.18}$$

where r_y^{vp} can be calculated using Equation (8.14).

8.4.3.3 ***Rubber Bridging - Rubber-microparticles***

The energy due to the rubber bridging is determined by the surface energy of the cavity. The surface energy of the cavity is introduced by the tearing of the rubber particles and is expressed by [119]:

$$\Delta G_r^{rb} = 4\left(1 - \frac{6}{\lambda_r^2 + \lambda_r + 4}\right) \Gamma_r^t v_p \tag{8.19}$$

where λ_r is the extension ratio at which the rubber particle starts to tear and its value generally increases with the decreasing particle size [119]. A value of above 10 for λ_r is estimated for an average particle size below 2 μm measured from the fracture surfaces for the rubber-microparticles [119]. Thus, the total increase in fracture energy per unit area can be approximated by [119][176]:

$$\Delta G_r^{rb} = 4 \Gamma_r^t v_p \tag{8.20}$$

where Γ_r^t is the tearing energy as a function of temperature; a tearing energy at room temperature of the CTBN rubber of 460 J/m^2 was used in the present study [176].

8.4.3.4 ***Rubber Cavitation - Rubber-microparticles***

The energy due to the rubber bridging is determined by the residual volumetric strain energy introduced by the formation of a cavity and the shear strain energy required to stretch the rubber around the cavitated voids and allow the cavity to expand [177][178]. Although the cavitation of the rubber particles promotes plastic void growth of the epoxy matrix [112][118], the increase in the value of the fracture energy directly contributed from the cavitation mechanism is relatively low. Hence, it can be considered to be negligible.

8.4.3.5 *Debonding - Rubber-microparticles*

Rubber particles generally bridge and cavitate, and hence debonding of the rubber-microparticles is considered to be negligible [179].

8.4.4 **Fibre Reinforcement Toughening Mechanisms**

The increase in fracture energy contributed from the reinforcing fibres can be categorised into three main toughening mechanisms and can be expressed by [56][163]:

$$\psi_f = \Delta G_f^{fb} + \Delta G_f^{vp} + \Delta G_f^{fd} + \Delta G_f^{db} \tag{8.21}$$

where ΔG_f^{fb}, ΔG_f^{vp}, ΔG_f^{fd} and ΔG_f^{db} are the fracture energy contributed from the fibre bridging, plastic void growth, fibre defibrillation and fibre-matrix interfacial debonding mechanisms.

8.4.4.1 *Fibre/Fibre Bundle Bridging – Fibre Reinforcement*

Fibre/fibre bundle bridging involves an increase in the fracture energy with an increasing crack length (R-curve), see Figure 8.35. The crack starts with no fibre/fibre bundle bridging and the measured fracture energy is expected to equal the fracture energy of the unmodified epoxy polymer. As the crack propagates, fibre/fibre bundle bridging develops causing the fracture energy to increase. Once a critical bridging peeling length is reached, the bridging fibres/fibre bundles break, so the fracture energy levels off at a constant value which is higher than the initiation value [163].

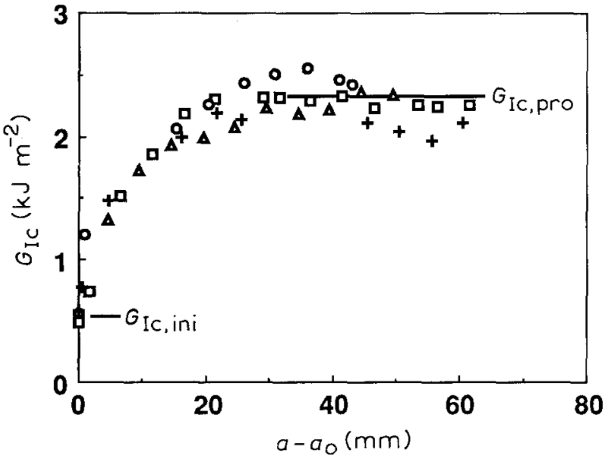

Figure 8.35: Mode I interlaminar fracture R-curves for laminate: (Δ) a_0 = 20.5 mm, (□,+) a_0 = 24.6 mm and (O) a_0 = 25 mm showing initiation fracture energy, $G_{IC,\mathrm{ini}}$, and propagation fracture energy, $G_{IC,\mathrm{pro}}$ [163]

The contribution to the fracture energy caused by the fibre bridging, ΔG_f^{fb}, was proposed by Ye & Friedrich [163][180]. It is expressed by:

$$\Delta G_f^{fb} = G_{ICU}\left(1 + \pi r_f l_f^p n_f^p\right) + \frac{1}{2}\sigma_{tf}\varepsilon_{ff}\pi r_f^2 l_f^b n_f^b \tag{8.22}$$

where G_{ICU} is the fracture energy of the unmodified epoxy polymer, r_f is the radius of the fibres, l_f^p is the average peeling length of the fibres, n_f^p is the number of peeling fibres per unit area, σ_{tf} is the tensile strength of the fibres, ε_{ff} is the failure strain of the fibres, l_f^b is the average length of the fibres at breakage and n_f^b is the number of fibres that break per unit area.

(Note: In order to account for the fibre bundle bridging, the number of fibres in the fibre bundles that peeled and broke was counted from the fracture surfaces. However, the 2nd term in Equation (8.22) is insignificant compared to the 1st term, and hence it can be considered to be negligible.)

8.4.4.2 ***Plastic Void Growth – Fibre Reinforcement***

The fracture energy contributed from plastic void growth in the presence of reinforcing fibres after debonding is expressed as [119][171]:

$$\Delta G_f^{vp} = r_y^{vp}\left(v_{vv} - v_{fv}\right)\sigma_{yt} \tag{8.23}$$

where v_{vv} and v_{fv} are the volume fractions of the enlarged voids and the reinforcing fibres which show plastic void growth. They may be directly measured from the appropriate SEM images of the fracture surfaces. The radius of the plastic zone induced by plastic void growth, r_y^{vp}, can be calculated using Equation (8.14) [14].

8.4.4.3 ***Fibre Defibrillation – Fibre Reinforcement***

The fracture energy of the FRCs incorporating NFs commonly includes a contribution from an additional toughening mechanism, i.e. fibre defibrillation. This is because the NFs are constructed with short interlocked fibres formed by elementary fibres/microfibrils [4] bonded together with pectin [36], which are susceptible to separation. It is noted that NFs can be sourced and processed differently. Therefore, they may have different properties. For example, the FF used in the present study was in the form of continuous yarns spun from short interlocked fibres in unidirectional fabrics [4]. In contrast, the CeF used in the present study was a continuous and non-twisted pure regenerated cellulose fibre in a plain-woven architecture [38]. These two NFs can therefore possess different properties and, for example, the FFs were more prone to fibre defibrillation.

An analytical model to predict the fracture energy contributed from this toughening mechanism has not been established. The prediction in the present study was therefore based on the fibre bridging model developed by Ye & Friedrich [163]. Assuming the bonding among the microfibrils was homogeneous and had the same properties as the fibres, the fracture energy contributed from the fibre defibrillation was then equivalent to the energy due to the fibre-microfibril detachment and the microfibril breakage. However, due to the low fracture energy contribution from the fibre defibrillation mechanism, it can be considered to be negligible.

8.4.4.4 ***Debonding – Fibre Reinforcements***

Natural fibres generally defibrillate and debond which leads to bridging and breakage of the microfibrils and the fibres. Although the debonding mechanism promotes the initiation of plastic void growth [105][173], the fracture energy contribution from fibre-matrix interfacial debonding is relatively small (due to the low specific surface areas involved [173][174][175]) compared to other mechanisms, e.g. fibre bridging and plastic deformation of the epoxy due to fibre debonding. Hence, the contribution from the fibre debonding mechanism can be considered to be negligible.

8.4.5 **Analytical Modelling Results**

All the parameters used in the analytical modelling to predict the fracture energy of the particle modified FRCs from the presence of silica-nanoparticles, rubber-microparticles and the fibre reinforcements are summarized in Table 8.8 to Table 8.11. Table 8.8 presents the parameters used in modelling the increase in the fracture energy due to silica-nanoparticles, Table 8.9 presents the parameters used in modelling the increase in the fracture energy due to rubber-microparticles, Table 8.10 presents the parameters used in modelling the increase in the fracture energy due to flax fibre reinforcements, and Table 8.11 presents the parameters used in modelling the increase in fracture energy due to cellulose fibre reinforcements.

Table 8.8: Parameters used in modelling the increase in fracture energy due to silica-nanoparticles

Parameter	Symbol	Unit	Value	Source
Fracture energy of unmodified epoxy polymer	G_{ICU}	J/m^2	133	[14]
Plane-strain compressive yield stress of unmodified epoxy polymer	σ_{yc}	MPa	123	[14]
Young’s modulus of unmodified epoxy polymer	E_m	GPa	2.90	[14]
Uniaxial tensile yield stress of unmodified epoxy polymer	σ_{yt}	MPa	88	[14]
Failure stain of unmodified epoxy polymer	γ_{fu}	-	0.75	[105]
Poisson’s ratio of unmodified epoxy polymer	υ_m	-	0.35	[56]
Pressure-dependent yield stress parameter	μ_m	-	0.2	[169]
Volume fraction of silica-nanoparticles in epoxy matrix	v_p	-	0.071±0.004	Present study
Volume fraction of reinforcing fibres in composites	v_f	-	0.41±0.04FF 0.66±0.02CeF*	Present study
Volume fraction of voids in composites	v_v	-	0.01-0.02	Present study
Volume fraction of silica-nanoparticles which show plastic void growth in epoxy matrix	v_{pv}	-	0.071	[14]
Volume fraction of enlarged voids due to the plastic void growth in epoxy matrix	v_{vv}	-	0.103	[14]

*FF = Value for FFRPs and CeF = Value for CeFRPs

Table 8.9: Parameters used in modelling the increase in fracture energy due to rubber-microparticles

Parameter	Symbol	Unit	Value	Source
Fracture energy of unmodified epoxy polymer	G_{ICU}	J/m^2	133	[14]
Plane-strain compressive yield stress of unmodified epoxy polymer	σ_{yc}	MPa	123	[14]
Young’s modulus of unmodified epoxy polymer	E_m	GPa	2.90	[14]
Uniaxial tensile yield stress of unmodified epoxy polymer	σ_{yt}	MPa	88	[14]
Failure stain of unmodified epoxy polymer	γ_{fu}	-	0.75	[105]
Poisson’s ratio of unmodified epoxy polymer	υ_m	-	0.35	[56]
Pressure-dependent yield stress parameter	μ_m	-	0.2	[169]
Volume fraction of rubber-microparticles in epoxy matrix	v_p	-	0.106±0.01	Present study
Volume fraction of reinforcing fibres in composites	v_f	-	0.41±0.04FF 0.66±0.02CeF*	Present study
Volume fraction of voids in composites	v_v	-	0.01-0.02	Present study
Volume fraction of rubber-microparticles which show plastic void growth in epoxy matrix	v_{pv}	-	0.106±0.01	Present study
Volume fraction of enlarged voids due to the plastic Void growth in epoxy matrix	v_{vv}	-	0.52±0.10	Present study
Tearing energy of rubber	Γ_r^t	J/m^2	460	[176]

*FF = Value for FFRPs and CeF = Value for CeFRPs

Table 8.10: Parameters used in modelling the increase in fracture energy due to flax fibre reinforcements

Parameter	Symbol	Unit	Value	Source
Fracture energy of unmodified epoxy polymer	G_{ICU}	J/m^2	133	[14]
Plane-strain compressive yield stress of unmodified epoxy polymer	σ_{yc}	MPa	123	[14]
Young's modulus of unmodified epoxy polymer	E_m	GPa	2.9	[14]
Uniaxial tensile yield stress of unmodified epoxy polymer	σ_{yt}	MPa	88	[14]
Poisson's ratio of unmodified epoxy polymer	υ_m	-	0.35	[56]
Pressure-dependent yield stress parameter	μ_m	-	0.2	[169]
Volume fraction of reinforcing fibres in composites	v_f	-	0.41±0.04	Present study
Volume fraction of reinforcing fibres which show plastic void growth	v_{fv}	-	0-0.02	Present study
Volume fraction of enlarged voids due to the plastic void growth	v_{vv}	-	0-0.03	Present study
Tensile strength of reinforcing fibres	σ_{tf}	MPa	500	[41]
Failure strain of reinforcing fibres	ε_{ff}	-	0.02	[41]
Radius of reinforcing fibres*	r_f	µm	17±7	Present study
Average peeling length of reinforcing fibres*	l_f^p	mm	1.1±0.4	Present study
Number of peeling fibres per unit area*	n_f^p	mm^{-2}	60±15	Present study
Average length of reinforcing fibres at breakage*	l_f^b	mm	1.1±0.4	Present study
Number of reinforcing fibres that break per unit area*	n_f^b	mm^{-2}	60±15	Present study

*Values obtained from SEM imaging

Table 8.11: Parameters used in modelling the increase in fracture energy due to cellulose fibre reinforcements

Parameter	Symbol	Unit	Value	Source
Fracture energy of unmodified epoxy polymer	G_{ICU}	J/m^2	133	[14]
Plane-strain compressive yield stress of unmodified epoxy polymer	σ_{yc}	MPa	123	[14]
Young's modulus of unmodified epoxy polymer	E_m	GPa	2.9	[14]
Uniaxial tensile yield stress of unmodified epoxy polymer	σ_{yt}	MPa	88	[14]
Poisson's ratio of unmodified epoxy polymer	υ_m	-	0.35	[56]
Pressure-dependent yield stress parameter	μ_m	-	0.2	[169]
Volume fraction of reinforcing fibres in composites	v_f	-	0.66±0.02	Present study
Volume fraction of reinforcing fibres which show plastic void growth	v_{fv}	-	0-0.03	Present study
Volume fraction of enlarged voids due to the plastic void growth	v_{vv}	-	0-0.05	Present study
Tensile strength of reinforcing fibres	σ_{tf}	MPa	675	[38]
failure strain of reinforcing fibres	ε_{ff}	-	0.06	[38]
Radius of reinforcing fibres*	r_f	μm	10±1	Present study
Average peeling length of reinforcing fibres*	l_f^p	mm	1.3±0.3	Present study
Number of peeling fibres per unit area*	n_f^p	mm^{-2}	113±38	Present study
Average length of reinforcing fibres at breakage*	l_f^b	mm	1.3±0.3	Present study
Number of reinforcing fibres that break per unit area*	n_f^b	mm^{-2}	113±38	Present study

*Values obtained from SEM imaging

The predicted values of the fracture energy for the final RIFT-processed FFRPs and CeFRPs are summarized in Table 8.12 and Table 8.13, respectively.

Table 8.12: Comparison of predicted and measured values of fracture energy from different toughening for the final RIFT-processed FFRPs

Toughening mechanism		**Matrix formulation**			
		Si0R0	Si10R0	Si0R9	Si10R9
Fracture energy of unmodified epoxy polymer, G_{ICU} (J/m^2)		133	133	133	133
Silica-nanoparticle induced fracture energy, Ψ_{si} (J/m^2)	ΔG_{si}^{sb}	N/A	43-52	N/A	43-52
	ΔG_{si}^{vp}	N/A	26-31	N/A	26-31
	ΔG_{si}^{db}	N/A	nil	N/A	nil
Rubber-microparticle induced fracture energy, Ψ_r (J/m^2)	ΔG_{r}^{sb}	N/A	N/A	52-63	52-63
	ΔG_{r}^{rb}	N/A	N/A	99-127	99-127
	ΔG_{r}^{vp}	N/A	N/A	289-489	289-489
	ΔG_{r}^{db}	N/A	N/A	nil	nil
Fibre reinforcement induced fracture energy, Ψ_f (J/m^2)	ΔG_{f}^{fb}	274-1263	274-1263	274-1263	274-1263
	ΔG_{f}^{vp}	0-22	0-22	0-22	0-22
	ΔG_{f}^{fd}	nil	nil	nil	nil
	ΔG_{f}^{db}	nil	nil	nil	nil
$\Psi_{si} + \Psi_r$		0	69-83	440-679	509+762
Ψ_f		274-1284	274-1284	274-1284	274-1284
Predicted G_{IC} (J/m^2)*		912±505	988±512	1471±625	1548±632
Measured G_{IC} (J/m^2)		1112±66	1302±78	1918±89	1936±150
t-test P-value^		0.76	0.65	0.60	0.65

*Predicted $G_{IC} = G_{ICU} + \Psi_{si} + \Psi_r + \Psi_f$ where the range of predictions equals an average±(high bound - low bounds)/2

^Comparison of the predicted and measured fracture energies of the FFRPs with the same matrix formulations using two-tailed independent t-test with a confidence interval value, α, of 0.05 (unequal variances assumed). $P\text{-value} \leq 0.05$ = the two groups are significantly different and $P\text{-value} > 0.05$ = the two groups are insignificantly different.

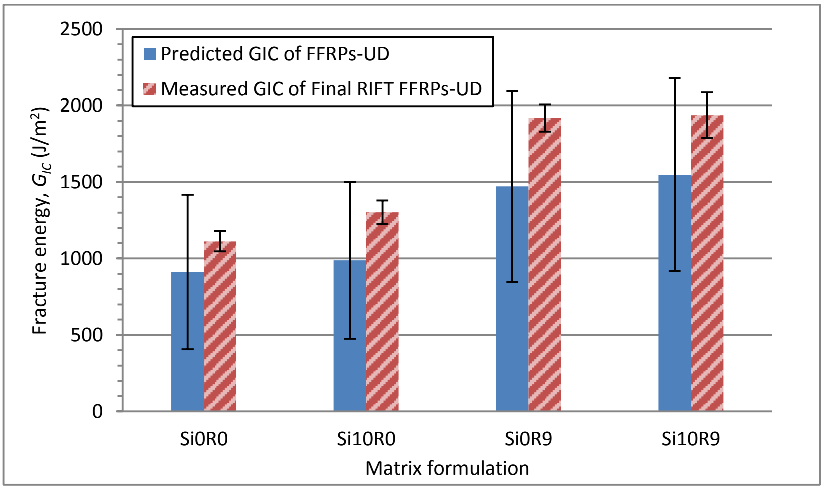

Figure 8.36: Summary of predicted and measured mode I interlaminar fracture energies of final RIFT-processed FFRPs

Table 8.13: Comparison of predicted and measured values of fracture energy from different toughening for the final RIFT-processed CeFRPs

Toughening mechanism		Matrix formulation			
		Si0R0	Si10R0	Si0R9	Si10R9
Fracture energy of unmodified epoxy polymer, G_{ICU} (J/m^2)		133	133	133	133
Silica-nanoparticle induced fracture energy, Ψ_{si} (J/m^2)	ΔG_{si}^{sb}	N/A	24-29	N/A	24-29
	ΔG_{si}^{vp}	N/A	15-17	N/A	15-17
	ΔG_{si}^{db}	N/A	nil	N/A	nil
Rubber-microparticle induced fracture energy, Ψ_r (J/m^2)	ΔG_r^{sb}	N/A	N/A	30-36	30-36
	ΔG_r^{rb}	N/A	N/A	57-71	57-71
	ΔG_r^{vp}	N/A	N/A	167-275	167-275
	ΔG_r^{db}	N/A	N/A	nil	nil
Fibre reinforcement induced fracture energy, Ψ_f (J/m^2)	ΔG_f^{fb}	416-1264	416-1264	416-1264	416-1264
	ΔG_f^{vp}	0-40	0-40	0-40	0-40
	ΔG_f^{fd}	nil	nil	nil	nil
	ΔG_f^{db}	nil	nil	nil	nil
$\Psi_{si} + \Psi_r$		0	40-47	254-381	294-428
Ψ_f		416-1305	416-1305	416-1305	416-1305
Predicted G_{IC} (J/m^2)*		993±445	1037±448	1311±508	1353±511
Measured G_{IC} (J/m^2)		1427±76	1555±173	1811±28	1847±573
t-test P-value^		0.51	0.44	0.50	0.59

*Predicted $G_{IC} = G_{ICU} + \Psi_{si} + \Psi_r + \Psi_f$ where the range of predictions equals an average±(high bound - low bounds)/2

^Comparison of the predicted and measured fracture energies of the FFRPs with the same matrix formulations using two-tailed independent t-test with a confidence interval value, α, of 0.05 (unequal variances assumed). $P\text{-value} \leq 0.05$ = the two groups are significantly different and $P\text{-value} > 0.05$ = the two groups are insignificantly different.

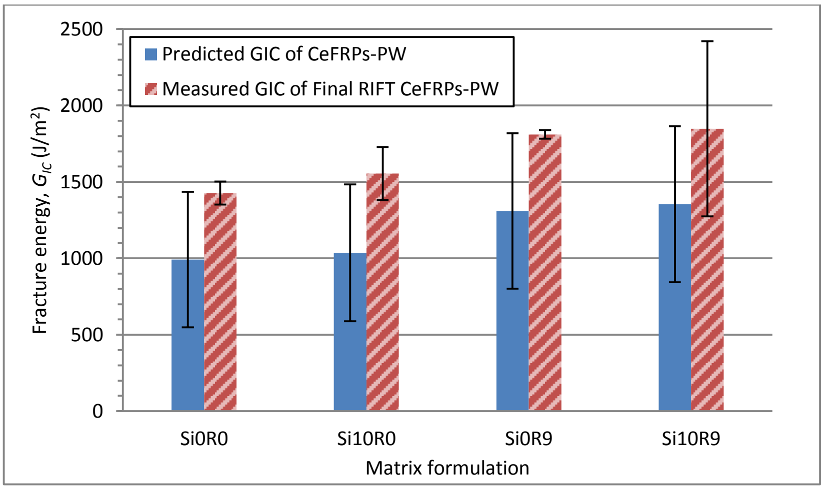

Figure 8.37: Summary of predicted and measured mode I interlaminar fracture energies of final RIFT-processed CeFRPs

As may be seen from Table 8.12 and Table 8.13, and Figure 8.36 and Figure 8.37, although the predicted fracture energies of both the final RIFT-processed NFRPs were slightly low compared to the measured results, the comparison of the fracture energies using a t-test showed a good correlation. Although the prediction of the fracture energy contributed from the addition of silica-nanoparticles and rubber-microparticles has proved to be in good agreement with experimental results [57], the difficulty in quantifying the fibre induced toughening mechanisms has resulted in a wide variability in the prediction of the fracture energy contribution from the fibre reinforcements. Hence, the predicted values covered a wide range as the fibre volume fraction has increased. This is evident by a slightly better correlation for the FFRPs (P-value of 0.60-0.76), compared to the prediction for the CeFRPs (P-value of 0.44-0.59).

The predicted fracture energies of the Si10R0 NFRPs were estimated to be slightly higher than those of the Si0R0 NFRPs. On the other hand, a significant increase in fracture energies was predicted for the Si0R9 NFRPs, compared to the Si0R0 NFRPs. Addition of silica-nanoparticles to the Si0R9 NFRPs, to give the hybrid (Si10R9) matrix, only slightly increased the predicted fracture energies.

Thus, the results reveal that the modelling studies do predict the general trends very well. For example, the steady increase in the value of the interlaminar fracture energy, G_{IC}, as one goes from the unmodified matrix to the hybrid modified (i.e. Si10R9) matrix is captured. Also, the trends in the values of G_{IC} with respect to a comparison of the two types of NFs studied, i.e. the FF-UD versus the CeF-PW, are also predicted. However, although a comparison of the predicted and measured fracture energies show a good statistical correlation, the predicted results are invariably slightly low when compared to the measured results. This undoubtedly arises from the complex toughening mechanisms and fracture processes which were observed in the NFRPs, as well as the inconsistent properties of the NFs. It may be seen that the predicted values of the fracture energy, Ψ_f, contributed by the presence of the fibre reinforcement varied considerably. This resulted in a significant variability in the prediction of the interlaminar fracture energy, G_{IC}. In fact, the standard deviation of the predicted results varied by up to ±55%. Now, analytical models for predicting the fracture energy of the silica-nanoparticle and rubber-microparticle modified epoxy polymers have been well established [57]. Therefore, in order to predict more accurately the interlaminar fracture energies of the NFRPs, a detailed study into the fracture processes of the composites with NF reinforcements and their toughening mechanisms needs to be undertaken.

8.5 Concluding Remarks

The present chapter has summarized the fracture properties of the FRPs manufactured by the two manufacturing methods used in the present study and proposed an analytical model for predicting the value of the interlaminar fracture energy, G_{IC}, for the NFRPs.

It has been observed that the initial RIFT-processed NFRPs possessed very low values of the interlaminar fracture energy due to the high moisture content in the as-received NFs causing 1) poor fibre-matrix interfacial adhesion, 2) a low fibre volume fraction, and 3) a high void content. However, a truly significant improvement of the interlaminar fracture energies was achieved in the final RIFT-processed NFRPs, compared to those recorded for the initial RIFT-processed NFRPs. This is considered to be a major achievement from the present research. This observation of dramatically increased values of G_{IC} in the final RIFT-processed NFRPs, compared to the initial RIFT-processed NFRPs, was due to the reduction of the moisture content in the NFs in the final RIFT manufacturing process, which led to the very significant improvements in the physical properties of such composites, as discussed previously.

The fracture properties of the final RIFT- and RTM-processed NFRPs and GFRPs showed several noteworthy features. Firstly, for the GFRPs-UD and GFRPs-PW, the RIFT and RTM manufacturing processes tends to produce GFRPs with comparable values of the interlaminar fracture energy, G_{IC}. However, for the FFRPs-UD and CeFRPs-PW, the final RIFT process leads to composites with significantly higher values of G_{IC}, compared to the RTM process. Indeed, for the FFRPs-UD, very significantly higher fracture energies were measured for the RIFT-processed Si0R9 and Si10R9 FFRPs, compared to the results from the RTM process; with values of G_{IC} as high as about 1900 J/m^2 being attained. In contrast, the RIFT-processed Si0R0 and Si10R0 FFRPs only gave slightly higher values of G_{IC}, compared to those composites with the same matrix formulations manufactured using the RTM process. These observations are suggested to arise from several interacting effects. One is the corresponding higher void contents observed for the RTM-processed Si0R9 and Si10R9 FFRPs, compared to the other FFRPs. These voids 1) reduce the effective fracture-resisting area in the crack path of the composites, 2) initiate further micro-cracks by acting as pre-cracks, and 3) reduce the transverse load transfer between the fibre and matrix. Thus, leading to relatively lower values of G_{IC}. For the CeFRPs, the fracture energies of the RIFT-processed CeFRPs were again generally higher than those manufactured using the RTM process. It is suggested this is due to the extensive fibre/fibre bundle bridging that took place randomly throughout the fracture surfaces of the CeFRPs, and indeed the observed values of the interlaminar fracture energies of the CeFRPs varied considerably. A maximum void content of 3% was measured for the RTM-processed CeFRPs with the Si10R9 matrix formulation but this feature did not appear to greatly contribute to the decrease in the fracture energy. Instead, the inferior fracture energies of the RTM-processed CeFRPs, compared to those from the RIFT process, are considered to be due to the lower fibre volume fractions achieved in the RTM process. This feature would lead to a reduction of the fibre induced fracture mechanisms, e.g. fibre/fibre bundle bridging, fibre breakage and fibre defibrillation.

Secondly, a major outcome of the present work is that the highest values of G_{IC} are seen for the NFRPs. For example, for the RIFT-processed FFRPs-UD, values of up to 1936 J/m^2 were measured, compared to a maximum value of 1257 J/m^2 for the GFRPs-UD. Thus, although the mechanical properties of the GFs used in the present study were significantly superior to the NFs, the interlaminar fracture energies of the NFRPs from the two manufacturing processes were generally higher than those of the GFRPs. This observation arises from the complex structure of the NFs (i.e. porous bonded/interlocked microfibrils of the FFs [4]) which resulted in new and extra toughening mechanisms being induced by the natural fibre/fabric reinforcements. For example, more extensive fibre/fibre bundle bridging was observed on the fracture surfaces of the NFRPs, compared to those of the GFRPs. In the FFRPs, the crack tended to propagate through the fibres/fibre bundles and the majority of the fracture surfaces were covered with defibrillated and broken fibres/fibre bundles. Thus, the main failure mechanisms involved fibre/fibre bundle bridging, fibre breakage and fibre defibrillation; and the contributions to the toughness from toughening mechanisms in the epoxy matrices, e.g. via shear yielding and plastic deformation, were of less importance.

Thirdly, the addition of only silica-nanoparticles to the epoxy matrix gave a consistent increase in the values of the interlaminar fracture energies of the both the FFRP and GFRP composites, of the order of 20% and 50% respectively. On the other hand, modifying the FRPs with rubber-microparticles (i.e. the Si0R9 FRPs) very significantly increased the values of the interlaminar fracture energies, up to by about 80%. The hybrid matrices containing both silica-nanoparticles and the rubber-microparticles (i.e. the Si10R9 FRPs) resulted in composites which all showed a small further increase in the value of G_{IC} compared to those containing only the rubber-microparticles.

Fourthly, comparing the present results to those reported previously in the literature, then there are no results previously reported for the mode I interlaminar fracture energy of a FF-UD-reinforced epoxy polymer composite. However, the interlaminar fracture energy of 1112 J/m^2 for the Si0R0 FFRP-UD was found to significantly exceed the value of 600 J/m^2 for the jute-UD-reinforced unmodified epoxy composite previously reported by Pinto et al. [52]. Again, no results for the mode I interlaminar fracture energy of the CeFRP-PW have been previously reported. However, the fracture energy of 1427 J/m^2 for the Si0R0 CeFRP-PW agrees well with the values of 747 to 1775 J/m^2 for the silk-PW-reinforced epoxy composite reported by Zulkifli et al. [55]. For the GFRPs, the interlaminar fracture energies of the particle modified GFRPs-UD were also found to generally somewhat exceed the values of the particle modified GF-UD-reinforced epoxy composite previously reported by Hsieh et al. [56], except for the Si10R0 GFRP. For these composites, values of G_{IC} of 330-1015 J/m^2 were measured by Hsieh et al. [56], compared to the values of 534-1257 J/m^2 measured in the present study.

Considering the analytical modelling studies, the model that was proposed slightly under predicted the interlaminar fracture energies of the final RIFT-processed NFRPs. However, the results from the model showed a good correlation with the measured values. Also, the modelling results did predict accurately the trend in the values of G_{IC} for the final RIFT-processed NFRPs when they were formulated using different matrix modifications. However, due to the complex fracture behaviour and inconsistency of the fracture surfaces of the NFRPs, and varying properties of the NFs, relatively wide variations in the predicted fracture energies were obtained.

Finally, the outstanding values of the interlaminar fracture energies achieved in the present work using the final RIFT manufacturing process for the FFRPs-UD and CeFRPs-PW, especially those formulated based on employing the rubber rubber-microparticles (i.e. Si0R9) and hybrid (i.e. Si10R9) matrices, are considered to represent a major advance in increasing the toughness in such composites.

A summary of the main conclusions and recommendations for future work will be presented in the following chapter.

CHAPTER 9 SUMMARY OF MAIN CONCLUSIONS AND RECOMMENDATIONS FOR FUTURE WORK

9.1 Conclusions

Due to an increasing awareness of the need to source sustainable materials, manufacturers have been seeking materials made from natural resources as an alternative to synthetic materials. For example, natural fibre composites (NFCs) offer weight- and cost-savings compared to glass fibre composites (GFCs). In this respect, NFCs have gained momentum in the automotive industry. However, although NFCs possess relatively good specific strength and stiffness properties, they typically possess inconsistent mechanical properties, especially poor interlaminar fracture toughness. This is because natural fibres (NFs) 1) often show relatively poor interfacial adhesion with respect to polymeric matrices, 2) may contain relatively high levels of moisture, and 3) have variable mechanical properties due to the route by which they have been harvested and manufactured.

In the present study, a standard diglycidyl ether of bisphenol A (DGEBA) epoxy resin cured with an accelerated methylhexahydrophthalic acid anhydride was chosen for the matrix. The types of modifiers used for the matrix were silica-nanoparticles and rubber-microparticles. Four different modified epoxy matrix formulations were used in the present study and the terminologies employed in the present study are shown in Table 9.1. Four types of fibres, namely unidirectional flax fibres (FF-UD), plain-woven cellulose fibres (CeF-PW), unidirectional glass fibres (GF-UD) and plain-woven glass fibres (GF-PW), were used in the present study as the reinforcement for the matrices, see Table 9.2. The glass fibres (GFs) were included so as to be able to compare directly the properties of conventional glass fibre reinforced plastics (GFRPs) to the novel natural fibre reinforced plastics (NFRPs).

Table 9.1: Percentage weight of the silica-nanoparticles and rubber-microparticles in the different epoxy formulations

Formulation name	Silica-nanoparticle wt%	Rubber-microparticle wt%
Si0R0	0	0
Si10R0	10	0
Si0R9	0	9
Si10R9	10	9

Table 9.2: Different types and architectures of reinforcements used in the present study

Fibre type*	Fibre architecture*	Planar density (GSM)	Supplier
Flax fibre	Unidirectional	275	Composites Evolution, UK
Cellulose fibre	Plain-woven	210	Porcher Industries, France
Glass fibre	Unidirectional	500	SP Systems, UK
Glass fibre	Plain-woven	86	SP Systems, UK

*Detailed descriptions of different fibre types and architectures can be found in ‘Appendix I’.

The main aims of the present study were to investigate and improve the mechanical properties, especially the mode I interlaminar fracture energy, of the natural fibre-reinforced epoxy polymer composites under quasi-static loading conditions and to study the effects of the types of matrix and fibre reinforcement used. The following sections summarize the three aspects of the present study: manufacturing aspects, mechanical properties and the analytical modelling work.

9.1.1 **Manufacturing Aspects**

9.1.1.1 ***Introduction***

Two manufacturing methods were involved in the present study, namely resin infusion under flexible tooling (RIFT) and resin transfer moulding (RTM). These two techniques share similar principles whereby resin is drawn/pushed into the pre-laid reinforcement within the mould cavity/vacuum bagging containment. Once the composite is cured and post-cured inside the mould, the composite part is then removed. Table 9.3 summarizes the key differences of the two manufacturing methods used in the present study and lists their different advantages and disadvantages. A key finding of the present research was that the RIFT process initially produced very poor quality NFRPs. This was unexpected and the reasons for this were established and a final RIFT process was developed which produced high-quality NFRPs. In contrast, the RTM process did not suffer from such problems.

Table 9.3: Summary of the main difference between the RIFT and RTM processes

RIFT process	RTM process
Advantages - Low-cost tooling [121][123] - Real-time monitoring of the flow (transparent flexible vacuum bagging) [121][123] - The flow speed adapts according to the matrix viscosity **Disadvantages** - High amount of micro- and macro-voids (processed under vacuum and entrapped moisture by flexible vacuum bagging) [121][123] - Relatively low fibre volume fraction for NFs (low packing pressure) [121][123] - Inconsistency of properties, e.g. fibre volume fraction and void content (due to local pressure and flow behaviour) [125][126] - Low glass transition temperature (shorter post-curing duration) - One-sided smooth surface [121][123]	**Advantages** - In-process paint/coating [121][123] - One-sided smooth surface [121][123] - Low amount of micro- and macro-voids (high consolidation under high pressure and escapable moisture through mould cavity) [121][123][146] - High fibre volume fraction (high processing pressure) [121][123] **Disadvantages** - Flow cannot be monitored (closed mould) [121][123] - Expensive tooling [121][123]

9.1.1.2 ***The RIFT Process***

The initial studies of the RIFT process were aimed at studying the feasibility of the RIFT manufacturing process employing the settings which had been used by Hsieh [14] for manufacturing hybrid modified epoxy polymers (i.e. formulation Si10R9, see Table 9.1) with carbon and glass fibres as the reinforcements. This initial RIFT process involved infusing the resin at 50°C into the as-received fibres then curing at 100°C for 2 hours, followed by a post-cure at 150°C for 10 hours. Finally, the cured composite panel was cooled down to room temperature.

These initial settings were employed to manufacture silica-nanoparticle and rubber-microparticle modified fibre-reinforced plastics (FRPs), with NFs (e.g. FF and CeF) and GFs as the reinforcements. However, it was found that due to the relatively high moisture levels retained in the NFs that poor interfacial adhesion between the fibres and the matrix and a relatively high moisture content in the epoxy matrix were observed. Indeed, the RIFT-processed NFRPs from the initial study had a relatively low glass transition temperature, T_g, a low fibre volume fraction, v_f, and a high void content, v_v. As a result, the initial RIFT-processed NFRPs possessed poor mechanical properties, and especially had relatively very low values of the interlaminar fracture toughness.

To overcome the above problems, several different basic changes to the RIFT manufacturing process were explored. Surface plasma treatment of the NFs and drying the fibres under vacuum in the RIFT-vacuum bagging operation were studied. However, these changes did not enhance the compatibility between the NFs and the epoxy polymers. Hence, they did not improve the mechanical properties of the NFRPs manufactured by the RIFT process. However, significantly improved values of the glass transition temperature of the epoxy matrix, the fibre volume fraction and the void content were obtained by fan-oven drying the NFs (termed the 'OD-modification') prior to the RIFT process. This was mainly due to the reduction of the moisture content in the NFs, i.e. from about 9 to 10 wt% to <1 wt%. Further, for example, the matrices in the initial RIFT studies possessed T_g of about 80 to 90°C compared to values of over 100°C which were attained via the final RIFT manufacturing process; and the void content was reduced from about 15% to 1%. Also, unwetted fibres and dry spots were observed on the surfaces of the initial RIFT-processed FRPs as a result of the relatively high void contents. However, unwetted fibres and dry spots were not observed on the surfaces of the final RIFT-processed FRPs where the void contents were much reduced, indicating a better surface quality had indeed now been achieved.

Thus, as a result of the major improvements in the physical properties of the NFRPs manufactured via the final RIFT process, greatly improved mechanical properties of the NFRPs were achieved, as discussed in detail later. The OD-modification was therefore selected to give the final RIFT process and the key parameters for this manufacturing process are summarized in Table 9.4.

Table 9.4: Summary of the key difference of the parameters employed in the final RIFT and RTM processes

Parameter	Final RIFT	RTM
Resin & fibre preparation		
- Mixing	50°C for 15 mins stir	50°C for 20 mins stir under vacuum
- Degassing	50°C for 20 mins under vacuum	
- Fibre pre-processing	75°C for 12 hrs fan-oven dry (OD)	-
- Fibre conditioning	50°C for 30 mins under vacuum	50°C for 4 hrs under vacuum
Resin injection		
- Resin temperature	50°C	50°C
- Mould temperature	50°C	50°C
- Flow rate	5-15 cc/min	25cc/min
- Injection duration	30-100 mins	25 mins
- Packing pressure	Vacuum (-0.1 MPa)*	Under high pressure (0.4 MPa)
- Injection duration	Approx. 30-100 mins	Approx. 25 mins
Cure		
- Heating rate	5°C/min	2°C/min
- Cure conditions	100°C for 2 hours under vacuum	100°C for 2 hrs under vacuum
Post-cure		
- Heating rate	1°C/min	1°C/min
- Post cure conditions	150°C for 10 hrs under atmospheric pressure	150°C for 15 hrs under atmospheric pressure

*Relative pressure to atmospheric pressure

9.1.1.3 *The RTM Process*

Since the temperature of the RTM mould was manually controlled, the resin was injected at 50°C and it was then cured at 100°C for 2 hours, followed by a post-cure at 150°C for 15 hours instead of a post-cure for 10 hours used in the RIFT process. Finally, the composite panel was cooled down to room temperature. This procedure allowed the operators to start the cure at the end of the day and end it the next day, which was necessary due to limited access to the equipment outside of normal working hours. The key parameters for the RTM process are summarized in Table 9.4. As will be shown below, the heating schedule used for the RTM process led to drying of the natural fibres in-situ. Thus, as commented above, the RTM process did not suffer from the problems encountered from a high moisture content being present in the natural fibres as found when using the initial RIFT process.

9.1.1.4 *Comparison of Final RIFT and RTM Manufacturing Methods*

The two manufacturing methods employed in the present study share similar principles. Nevertheless, they yielded different composite properties and Table 9.5 summarizes the physical properties of the FRPs from the two manufacturing methods.

As may be seen from Table 9.5, the glass transition temperature of both the final RIFT- and RTM-processed NFRPs was found to generally decrease when either silica-nanoparticles or rubber-microparticles were added. The addition of both types of particles together (i.e. the Si10R9 matrix) further somewhat reduced the glass transition temperature. For the RTM manufacturing process, the measured glass transition temperatures of the RTM-processed NFRPs were found to be higher than the estimated glass transition temperatures of the epoxy polymer matrix (i.e. assuming that it contained the level of moisture that was in the fibres at the pre-manufacturing level). In fact, it was found that the glass transition temperatures of all the RTM-processed NFRPs were consistent with the measured glass transition temperatures of the corresponding dry (atmospheric-pressure cured) bulk epoxy polymers. This suggests that the moisture in the NFs, i.e. about 3 wt% for the RTM process, had entirely evaporated and escaped during the RTM manufacturing method. However, the reverse was the case for the NFRPs manufactured via the final RIFT process. Here, the estimated glass transition temperature of the dry bulk epoxy matrix, assuming complete dissolution of all the moisture present in the fibres (i.e. less than 1 wt% at pre-manufacturing for the final RIFT process), was found to be somewhat higher than the measured glass transition temperature of the final RIFT-processed NFRPs. This suggests that the amount of moisture in the NFs increased somewhat during their transportation from the drying oven to the RIFT manufacturing equipment. This would lead to the measured values of the glass transition temperatures of the epoxy matrices being reduced when the NFRPs were manufactured using the final RIFT process. Thus, for these reasons, it was found that the glass transition temperatures of all the RTM-processed NFRPs were consistently higher than those obtained from the final RIFT process.

The void contents observed for the NFRPs are all relatively low in value, especially bearing in mind that no form of autoclave processing was used in the present studies, and the void contents recorded for the final RIFT-processed NFRPs are a little lower than those for the RTM-processed NFRPs. Now, the approximate duration for injection of the epoxy matrix in the RTM process was 25 minutes, compared to 30-100 minutes in the RIFT process, depending on the formulation used. Thus, it is suggested that the longer flow time in the final RIFT process, compared to the RTM process, is an advantage since it allows any entrapped air to more readily escape.

The fibre volume fractions of the flax fibre-reinforced plastics (FFRPs) from the final RIFT process and the RTM process were found to be equivalent in value. However, the fibre volume fractions of the final RIFT-processed cellulose fibre-reinforced plastics (CeFRPs) were consistently somewhat higher than those in the NFRPs manufactured via the RTM process. This arose from the contour changing behaviour of the flexible RIFT vacuum bagging. (By ‘contour changing behaviour’ is meant the fact that the RIFT vacuum bagging is flexible and its contours (i.e. shape) may change accordingly to the pressure acting on it. Hence, the local pressure during the infusion of the epoxy resin across the preform may vary and the thickness of the FRPs may vary. As a result, a variation of the fibre volume fraction was observed amongst the different FRPs and a variation in the local fibre volume fraction may also be observed.) Thus, as may be seen from Table 9.5, the continuous CeF reinforcement was significantly better packed by the final RIFT process, compared to the RTM process. However, in the case of the short interlocked FFs, this effect was not observed and the fibre volume fractions from the two manufacturing processes were comparable. It was also noteworthy that, overall, due to the fixed-cavity geometry of the RTM mould, a more consistent fibre volume fraction was obtained from the RTM-processed FRPs.

Table 9.5: Summary of the physical properties of final RIFT- and RTM-processed NFRPs, together with the bulk epoxy polymers

Manufac-turing method	**Matrix formu-lation***	**Measured glass transition temperature, T_g (°C)**		**Estimated glass transition temperature, T_g (°C)***		**Fibre volume fraction, v_f**		**Pre-manufacturing NF moisture content, v_w (wt%)**		**Void content, v_v (vol%)**	**Surface quality**
		FFs^	CeFs^	FFs^	CeFs^	FFs^	CeFs^	FFs^	CeFs^		
Final RIFT-processed NFRPs	Si0R0	126	110	133	133	0.44	0.64	<1.0	<1.0	1	Poor
	Si10R0	119	99	114	114	0.40	0.67			1	
	Si0R9	107	98	113	113	0.36	0.65			1	
	Si10R9	106	94	104	104	0.44	0.67			1	
RTM-Processed NFRPs	Si0R0	138	143	115	117	0.41	0.54	3.3 ±1.6	3.0 ±1.3	2	Good
	Si10R0	124	123	101	103	0.40	0.57			1-2	
	Si0R9	120	119	99	101	0.41	0.58			2-5	
	Si10R9	108	100	97	99	0.40	0.56			3-6	
		100C-2h/150C-10h †	100C-2h/150C-15h †								
Atmospheric-pressure cured (dry) bulk epoxy polymer	Si0R0	141	141	-	-	-	-	-	-	nil	-
	Si10R0	121	124	-	-	-	-	-	-	nil	-
	Si0R9	120	122	-	-	-	-	-	-	nil	-
	Si10R9	111	112	-	-	-	-	-	-	nil	-

*Estimated for the ‘matrix + absorbed water from the fibres’. Total dissolution of moisture from the fibres (i.e. about 1 to 3 wt%, as indicated) into the atmospheric-pressure cured particle modified(dry) bulk epoxy polymer was assumed. The glass transition temperature was estimated using the Fox equation described in ‘Appendix IV’.
^FFs = values for the NFRPs with FF reinforcement; CeFs = values for the NFRPs with CeF reinforcement.
†100C-2h/150C-10h = curing schedule used for the RIFT process (100°C for 2 hours followed by 150°C for 10 hours); 100C-2h/150C-15h = curing schedule used for the RTM process (100°C for 2 hours followed by 150°C for 15 hour).

9.1.2 Mechanical Properties

The RIFT and RTM manufacturing processes not only yielded different physical composite properties but they also yielded different mechanical properties of the FRPs. The mechanical properties of the initial RIFT-, final RIFT- and RTM-processed NFRPs are summarized below.

9.1.2.1 ***General Mechanical Properties***

9.1.2.1.1 General Mechanical Properties of Initial RIFT- vs. Final RIFT-processed NFRPs

The flexural properties of the initial- and final RIFT-processed NFRPs are summarized in Table 9.6. As may be seen, the final RIFT process nearly always resulted in a major increase in the flexural modulus of both NFRPs, compared to the initial RIFT process. This is especially noteworthy for the CeFRPs-PW. This observation was due to the reduction of the moisture content in the NFs in the final RIFT process, which led to the very significant improvements in the physical properties of such composites, as discussed above.

Table 9.6: Summary of the flexural modulus of the initial- and final RIFT-processed NFRPs

Fibre type and architecture	Matrix formulation	Initial RIFT			Final RIFT		
		v_f	v_v (vol%)	E_{flex} (GPa)	v_f	v_v (vol%)	E_{flex} (GPa)
Unidirectional Flax (FF-UD)	Si0R0	0.31	15	12.5±1.1	0.44	1	18.7±0.6
	Si10R0	0.23	13	12.9±0.6	0.40	1	14.2±0.2
	Si0R9	0.38	17	15.1±0.8	0.36	1	14.1±0.6
	Si10R9	0.33	16	13.2±0.3	0.44	1	16.1±0.6
Plain-woven Cellulose (CeF-PW)	Si0R0	-*	14	5.7±0.2	0.64	1	12.1±0.8
	Si10R0	-*	16	6.4±1.1	0.67	1	13.0±1.0
	Si0R9	-*	-*	-*	0.65	1	11.4±1.0
	Si10R9	-*	-*	-*	0.67	1	12.7±1.1

*Values could not be obtained due to the poor quality of the composites.

9.1.2.1.2 General Mechanical Properties of Final RIFT- and RTM-processed NFRPs vs GFRPs

The flexural and tensile properties of the final RIFT- and RTM-processed NFRPs and GFRPs are summarized in Table 9.7. In FRPs, the majority of the load is carried by the fibre/fabric reinforcement and the general mechanical properties, such as flexural modulus, tensile modulus and tensile strength, are primarily dictated by the mechanical properties of the fibre/fabric reinforcement and the fibre volume fraction.

From the results shown in Table 9.7. several interesting points are noteworthy. Firstly, modifying the FRPs with silica-nanoparticles, rubber-microparticles or a combination of both particles, only slightly changed the flexural modulus, tensile modulus and tensile strength with no clear statistical trends being identified. These findings are in good agreement with the study by Manjunatha and his colleagues [110]. Secondly, the strain to break, ε_{ff}, for the NFRPs was always about 1 to 1.5%, compared to about 2% for the GFRPs. Thirdly, indeed, due to the superior mechanical properties of the GFs compared to the NFs, it was observed that the general mechanical properties of the NFRPs were inferior to those of the GFRPs, regardless of the manufacturing routes. Fourthly, for the FFRPs, the RTM process was found to give significantly better general mechanical properties compared to the values obtained from the final RIFT process. This was due, at least in part, to the somewhat higher fibre volume fractions of the RTM-processed FFRPs. For the CeFRPs, despite the lower fibre volume fraction achieved for the RTM-processed CeFRPs, a slightly higher flexural and tensile moduli were observed for the RTM-processed CeFRP, along with only a slightly lower tensile strength. Fifthly, the same trend was observed for the GFRPs-UD, where again the RTM manufacturing process gave slightly higher values of the flexural modulus, tensile modulus and tensile strength, compared to the RIFT process, due to a slightly higher fibre volume fraction being attained in the RTM-processed GFRPs. Thus, the RTM manufacturing process clearly imparts superior physical properties to the composites, as discussed above, and this is also reflected in such manufactured composites having superior general mechanical properties. This aspect is nicely illustrated by observing from Table 9.7 that the specific modulus of the RTM-processed FFRP-UD is very similar to that of the final RIFT-processed GFRP-UD.

Table 9.7: Summary of the flexural and tensile properties of final RIFT- and RTM-processed NFRPs and GFRPs

Matrix formulation	Final RIFT – FF-UD						RTM – FF-UD*					
	v_f	E_{flex} (GPa)	E_t (GPa)	E_t/ρ ($10^6 m^2 s^{-2}$)	σ_t (MPa)	ε_t (%)	v_f	E_{flex} (GPa)	E_t (GPa)	E_t/ρ ($10^6 m^2 s^{-2}$)	σ_t (MPa)	ε_t (%)
Si0R0	0.44	18.7±0.6	20.1±0.1	14.7±0.1	163±2	1.2±0.1	-	-	-	-	-	-
Si10R0	0.40	14.2±0.2	17.7±0.2	12.8±0.1	161±5	1.1±0.1	0.45	28.8±0.5	27.9±0.2	19.9±0.2	194±8	1.0±0.1
Si0R9	0.36	14.1±0.6	15.5±0.4	11.8±0.3	153±5	1.4±0.1	-	-	-	-	-	-
Si10R9	0.44	16.1±0.6	17.2±0.2	12.5±0.1	151±5	1.4±0.3	-	-	-	-	-	-
	Final RIFT – CeF-PW						RTM – CeF-PW*					
Si0R0	0.64	12.1±0.8	13.4±0.1	9.2±0.1	122±1	1.0±0.1	-	-	-	-	-	-
Si10R0	0.67	13.0±1.0	13.7±0.9	9.2±0.6	130±3	1.1±0.1	0.38^	15.1±0.4	14.1±1.1	10.1±0.8	111±2	1.0±0.3
Si0R9	0.65	11.4±1.0	13.2±0.3	9.1±0.2	142±2	1.3±0.1	-	-	-	-	-	-
Si10R9	0.67	12.7±1.1	14.1±0.5	9.6±0.3	147±2	1.3±0.1	-	-	-	-	-	-
	RIFT – GF-UD						RTM – GF-UD*					
Si0R0	0.61	51.5±3.4	46.5±1.5	22.5±0.7	1144±25	1.9±0.1	-	-	-	-	-	-
Si10R0	0.55	51.7±10.6	41.2±1.4	20.6±0.7	1018±52	2.0±0.1	0.62	53.4±0.3	51.9±0.1	24.6±0.1	1167±6	2.0±0.1
Si0R9	0.65	54.1±8.7	44.7±0.5	21.1±0.2	1243±46	2.1±0.1	-	-	-	-	-	-
Si10R9	0.65	54.7±1.9	45.8±0.4	21.5±0.2	1263±37	2.1±0.2	-	-	-	-	-	-

*Since the flexural and tensile properties were minimally affected by the matrix formulation, these tests were only conducted on Si10R0 modified FRPs made using the RTM process.

^This was the highest fibre volume fraction achieved in the RTM process for the CeFRPs.

9.1.2.2 *Fracture Properties*

9.1.2.2.1 Fracture Properties of Initial RIFT- vs. Final RIFT-processed NFRPs

The fracture properties of the initial and final RIFT-processed NFRPs are summarized in Table 9.8.

Table 9.8: Summary of the mode I interlaminar fracture energies of initial and final RIFT-processed NFRPs

Fibre type and architecture	Matrix formulation	Initial RIFT			Final RIFT		
		v_f	v_v (vol%)	G_{IC} (J/m^2)	v_f	v_v (vol%)	G_{IC} (J/m^2)
Unidirectional Flax (FF-UD)	Si0R0	0.31	15	19±5	0.44	1	1112±66
	Si10R0	0.23	13	252±49	0.40	1	1302±78
	Si0R9	0.38	17	139±29	0.36	1	1918±89
	Si10R9	0.33	16	233±41	0.44	1	1936±150
Plain-woven Cellulose (CeF-PW)	Si0R0	-*	14	20±1	0.64	1	1427±76
	Si10R0	-*	16	23±2	0.67	1	1555±173
	Si0R9	-*	-*	-*	0.65	1	1811±28
	Si10R9	-*	-*	-*	0.67	1	1847±573

*Values could not be obtained due to the poor quality of the composites.

From Table 9.8, a truly significant improvement of the mode I fracture energies is achieved in the final RIFT-processed NFRPs, compared to those recorded for the initial RIFT-processed NFRPs. This is considered to be a major achievement from the present research. This observation of dramatically increased values of G_{IC} in the final RIFT-processed NFRPs, compared to the initial RIFT-processed NFRPs, was due to the reduction of the moisture content in the NFs in the final RIFT process, which led to the very significant improvements in the physical properties of such composites, as discussed above.

9.1.2.2.2 Fracture Properties of Final RIFT- and RTM-processed NFRPs vs GFRPs

The fracture properties of the final RIFT- and RTM-processed NFRPs and GFRPs are summarized in Table 9.9 and there are several noteworthy features.

Table 9.9: Summary of the mode I interlaminar fracture energies of the final RIFT- and RTM-processed NFRPs and GFRPs

Fibre type and architecture	Matrix formulation	Final RIFT			RTM		
		v_f	v_v (vol%)	G_{IC} (J/m^2)	v_f	v_v (vol%)	G_{IC} (J/m^2)
Unidirectional Flax (FF-UD)	Si0R0	0.44	1	1112±66	0.42	2	963±35
	Si10R0	0.40	1	1302±78	0.41	2	1168±51
	Si0R9	0.36	1	1918±89	0.42	5	1168±46
	Si10R9	0.44	1	1936±150	0.42	6	1264±53
Plain-woven Cellulose (CeF-PW)	Si0R0	0.64	1	1427±76	0.57	2	1125±108
	Si10R0	0.67	1	1555±173	0.60	1	1175±357
	Si0R9	0.65	1	1811±28	0.60	2	1372±176
	Si10R9	0.67	1	1847±573	0.59	3	1617±213
		RIFT			**RTM**		
Unidirectional Glass (GF-UD)	Si0R0	0.61	2	534±109	0.63	1	564±39
	Si10R0	0.55	2	842±44	0.62	1	935±76
	Si0R9	0.65	2	996±68	-*	-*	-*
	Si10R9	0.65	2	1257±56	-*	-*	-*
Plain-woven Glass (GF-PW)^	Si0R0	0.41	2	541±36	0.45	1	556±53
	Si10R0	0.38	2	621±59	0.44	1	629±67
	Si0R9	0.42	2	1287±127	0.44	1	1465±133
	Si10R9	0.44	2	1372±73	0.45	1	1527±101

*Values were not be obtained.

^These GFRPs were actually backed with a glass-fibre twill fabric (i.e. GF-PW+T) to increase the stiffness of the arms of the test specimens and so enable the tests to be more readily undertaken. However, the fracture plane was between the GF-PW woven fabric layers of the composite.

Firstly, for the GFRPs-UD and GFRPs-PW, the RIFT and RTM manufacturing processes tends to produce GFRPs with comparable values of the interlaminar fracture energy, G_{IC}. However, for the FFRPs-UD and CeFRPs-PW, the final RIFT process leads to composites with significantly higher values of G_{IC}, compared to the RTM process. Indeed, for the FFRPs-UD, very significantly higher fracture energies were measured for the RIFT-processed Si0R9 and Si10R9 FFRPs, compared to the results from the RTM process, with values of G_{IC} as high as about 1900 J/m^2 being attained. In contrast, the RIFT-processed Si0R0 and Si10R0 FFRPs only gave slightly higher values of G_{IC}, compared to those composites with the same matrix formulations manufactured using the RTM process. These observations are suggested to arise from several interacting effects. One is the corresponding higher void contents observed for the RTM-processed Si0R9 and Si10R9 FFRPs, compared to the other FFRPs. These voids 1) reduce the effective fracture-resisting area in the crack path of the composites, 2) initiate further micro-cracks by acting as pre-cracks, and 3) reduce the transverse load transfer between the fibre and matrix. Thus, leading to relatively lower values of G_{IC}. For the CeFRPs-PW, the fracture energies of the RIFT-processed CeFRPs were again generally higher than those manufactured from the RTM process. It is suggested this is due to the extensive fibre/fibre bundle bridging that took place randomly throughout the fracture surfaces of the CeFRPs, and indeed the observed values of the interlaminar fracture energies of the CeFRPs varied considerably. A maximum void content of 3% was measured for the RTM-processed CeFRPs with the Si10R9 matrix formulation but it did not greatly contribute to the decrease in the fracture energy. Instead, the inferior fracture energies of the RTM-processed CeFRPs, compared to those from the RIFT process, are considered to be due to the lower fibre volume fractions achieved in the RTM process. This feature would lead to a reduction of the fibre induced fracture mechanisms, e.g. fibre/fibre bundle bridging, fibre breakage and fibre defibrillation.

Secondly, a major outcome of the present work is that the highest values of G_{IC} are seen for the NFRPs. For example, for the RIFT-processed FFRPs-UD, values of up to 1936 J/m^2 were measured, compared to a maximum value of 996 J/m^2 for the GFRPs-UD. Thus, although the mechanical properties of the GFs used in the present study were significantly superior to the NFs, the interlaminar fracture energies of the NFRPs from the two manufacturing processes were generally higher than those of the GFRPs. This observation arises from the complex structure of the NFs (i.e. porous bonded/interlocked microfibrils of the FFs [4]) which resulted in different fracture mechanisms being induced by the NF and GF fibre/fabric reinforcements. For example, more extensive fibre/fibre bundle bridging was observed on the fracture surfaces of the NFRPs, compared to those of the GFRPs. In the FFRPs, the crack tended to propagate through the fibres/fibre bundles and the majority of the fracture surfaces were covered with defibrillated and broken fibres/fibre bundles. Thus, the main failure mechanisms involved fibre/fibre bundle bridging, fibre breakage and fibre defibrillation; and the contributions to the toughness from toughening mechanisms in the epoxy matrices, e.g. via shear yielding and plastic deformation, were relatively minimal. Due to the difference in fibre microstructure, the fibre defibrillation found on the fracture surfaces of the CeFRPs was less extensive than for the FFRPs. On the other hand, for the GFRPs, the main toughening mechanism involved debonding and fibre bridging of the fibres accompanied by shear yielding and plastic deformation of the epoxy matrix.

Thirdly, the addition of only silica-nanoparticles to the epoxy matrix gave a consistent increase in the values of the interlaminar fracture energies of the both the FFRP and GFRP composites, of the order of 20% and 50% respectively. On the other hand, modifying the FRPs with rubber-microparticles (i.e. the Si0R9 FRPs) very significantly increased the values of the interlaminar fracture energies, up to by about 80%. The hybrid matrices containing both silica-nanoparticles and the rubber rubber-microparticles (i.e. the Si10R9 FRPs) resulted in composites which all showed a small further increase in the value of G_{IC} compared to those containing only the rubber-microparticles.

Fourthly, comparing the present results to those reported previously in the literature, then there are no results previously reported for the mode I interlaminar fracture energy of a FF-UD-reinforced epoxy polymer composite. However, the interlaminar fracture energy of 1112 J/m^2 for the Si0R0 FFRP-UD was found to significantly exceed the value of 600 J/m^2 for the jute-UD-reinforced unmodified epoxy composite previously reported by Pinto et al. [52]. Again, no results for the mode I interlaminar fracture energy of the CeFRP-PW have been previously reported. However, the fracture energy of 1427 J/m^2 for the Si0R0 CeFRP-PW agrees well with the values of 747 to 1775 J/m^2 for the silk-PW-reinforced epoxy composite reported by Zulkifli et al. [55]. For the GFRPs, the interlaminar fracture energies of the particle modified GFRPs were also found to generally somewhat exceed the values of the particle modified GF-UD-reinforced epoxy composite previously reported by Hsieh et al. [56], except for the Si10R0 GFRP. For these composites, values of G_{IC} of 330-1015 J/m^2 were measured by Hsieh et al. [56], compared to the values of 534-1257 J/m^2 measured in the present study.

Finally, the outstanding values of the interlaminar fracture energies achieved in the present work using the final RIFT manufacturing process for the FFRPs-UD and CeFRPs-PW, especially those formulated based on employing the rubber-microparticles (i.e. Si0R9) and hybrid (i.e. Si10R9) matrices, are considered to represent a major advance in increasing the toughness in such composites.

9.1.3 **Analytical Modelling Studies**

9.1.3.1 ***Tensile Modulus***

The comparison of the measured and predicted tensile moduli of the final RIFT-processed NFRPs are summarized in Table 7.10.

Table 9.10: Summary of the measured and predicted values of the Young's modulus of final RIFT-processed NFRPs

Reinforcement	**Matrix formulation**	**Measured *E* (GPa)**	**Normalized predicted *E* (GPa)***	**t-test P-value^**
Unidirectional Flax (FF-UD)	Si0R0	20.1±0.1	25.3±7.1	0.54
	Si10R0	17.7±0.2	23.9±6.7	0.45
	Si0R9	15.5±0.4	21.1±6.2	0.46
	Si10R9	17.2±0.2	25.1±7.1	0.38
Plain-woven Cellulose (CeF-PW)	Si0R0	13.4±0.1	12.3±2.5	0.96
	Si10R0	13.7±0.9	12.9±2.5	0.92
	Si0R9	13.2±0.3	12.3±2.6	0.97
	Si10R9	14.1±0.5	12.7±2.6	0.88

*The predicted values of *E* were normalized to match the v_f of the measured values of *E* with the same matrix formulation.

^Comparison of measured *E* and normalized predicted *E* using a two-tailed independent t-test with a confidence interval value, α, of 0.05 (unequal variances assumed).

P-value ≤ 0.05 = the two groups are significantly different and P-value > 0.05 = the two groups are insignificantly different.

The longitudinal Young's modulus of the continuous unidirectional fibre-reinforced composites was predicted using the rule of mixtures [1][149][150]. On the other hand, the modified curved-beam model proposed by Xiong et al. [157] was used to predict the Young's modulus of the plain-woven (PW) fibre-reinforced composites. This model uses sinusoidal shape functions to idealize the warp and weft yarns as curved beams and so takes into account the interactions between the two yarns.

From Table 7.10, it may be seen that the rule of mixtures approach slightly over predicted the tensile modulus of the FFRPs-UD. This is suggested to be due to the model assuming that 1) the fibres were perfectly aligned with no fibre crimping or waviness, and 2) there were no fibre or fibre-matrix interfacial defects. However, the modified curved beam model took into account the fibre waviness/crimping and the interactions between the interlacing warp and weft yarns. As a result, this model gave results which were in very good agreement with the experimental results for the tensile modulus of the CeFRPs-PW.

9.1.3.2 ***Mode I Interlaminar Fracture Energy***

The comparison of the measured and predicted values of the fracture energy for the final RIFT-processed NFRPs are summarized in Table 9.11.

Table 9.11: Comparison of the predicted and measured values of fracture energy for the final RIFT-processed NFRPs

Fibre type and architecture	**Matrix formu-lation**	**Fracture energy of unmodified epoxy polymer, G_{ICU} (J/m^2)**	**Silica-nanoparticle induced fracture energy, ψ_{si} (J/m^2)**	**Rubber-microparticle induced fracture energy, ψ_{r} (J/m^2)**	**Fibre reinforcement induced fracture energy, ψ_{f} (J/m^2)**	**Predicted G_{IC} (J/m^2)***	**Measured G_{IC} (J/m^2)**	**t-test P-value^^**
Unidirectional Flax (FF-UD)	Si0R0	133	-	-	274-1284	912±505	1112±66	0.76
	Si10R0		69-83	-	274-1284	988±512	1302±78	0.65
	Si0R9		-	440-679	274-1284	1471±625	1918±89	0.60
	Si10R9		69-83	440-679	274-1284	1548±632	1936±150	0.65
Plain-woven Cellulose (CeF-PW)	Si0R0	133	-	-	416-1305	993±445	1427±76	0.51
	Si10R0		40-47	-	416-1305	1037±448	1555±173	0.44
	Si0R9		-	254-381	416-1305	1311±508	1811±28	0.50
	Si10R9		40-47	254-381	416-1305	1354±511	1847±573	0.59

*Predicted $G_{IC} = G_{ICU} + \Psi_{si} + \Psi_{r} + \Psi_{f}$ where the range of predictions equals an average±(high bound - low bounds)/2

^ For the three mechanisms the range of calculated values is given.

^^Comparison of the predicted and measured fracture energies of the FFRPs with the same matrix formulations using two-tailed independent t-test with a confidence interval value, α, of 0.05 (unequal variances assumed). P-value ≤ 0.05 = the two groups are significantly different and P-value > 0.05 = the two groups are insignificantly different.

The mode I interlaminar fracture energy, G_{IC}, of the FRPs unmodified, or modified with silica-nanoparticles and/or rubber microparticles, was theoretically modelled from considering the three main toughening mechanisms that may be operative in the composites. The mechanisms that may be induced are due to the presence of 1) the silica-nanoparticles, Ψ_{si}, 2) the rubber-microparticles, Ψ_{r}, and 3) the fibre reinforcement, Ψ_{f}. These mechanisms act to increase the basic fracture energy of unmodified epoxy polymer, G_{ICU}.

The results shown in Table 9.11 reveal that the modelling studies do predict the general trends very well. For example, the steady increase in the value of the interlaminar fracture energy, G_{IC}, as one goes from the unmodified matrix to the hybrid modified (i.e. Si10R9) matrix is captured. Also, the trends in the values of G_{IC} with respect to a comparison of the two types of NFs studied, i.e. the FF-UD versus the CeF-PW, are also predicted. However, although a comparison of the predicted and measured fracture energies show a good statistical correlation, the predicted results are invariably slightly low when compared to the measured results. This undoubtedly arises from the complex toughening mechanisms and fracture processes which were observed in the NFRPs, as well as the inconsistent properties of the NFs. It may be seen that the predicted values of the fracture energy, Ψ_{f}, contributed by the presence of the fibre reinforcement varied considerably. This resulted in a significant variability in the prediction of the interlaminar fracture energy, G_{IC}. In fact, the standard deviation of the predicted results varied by up to ±55%. Now, analytical models for predicting the fracture energy of the silica-nanoparticle and rubber-microparticle modified epoxy polymers have been well established [57]. Therefore, in order to predict more accurately the interlaminar fracture energies of the NFRPs, a detailed study into the fracture processes of the composites with NF reinforcements and their toughening mechanisms needs to be undertaken, as discussed below.

9.1.4 Final Comments

Comparing the final RIFT and the RTM processing routes for manufacturing components from the NFRPs, several major aspects must be taken into account. Firstly, the cost of the equipment for the RTM process far exceeds that needed for the RIFT process. Secondly, although the final

RIFT process possibly could be further developed to give an improved surface finish to the NFRPs, invariably the RTM manufacturing process will yield composite parts with a better surface finish. Thirdly, considering the mechanical properties, then a major achievement of the present research has been to be identify whereby the RIFT-processed NFRPs may possess excellent fracture properties, even somewhat exceeding those NFRPs manufactured using the RTM process. All these factors need to be taken into account when considering which manufacturing route and which NFRP best suits a given application.

9.2 Recommendations for Future Work

A number of potential areas for further investigation have been identified in the course of the present study. These are briefly discussed below.

9.2.1 Manufacturing Aspects

It has been observed that the values of the fibre volume fractions and void contents of the NFRPs obtained from the final RIFT process varied considerably due to the nature and microstructure of the NFs, as well as due to the local pressure gradient and flow behaviour during the resin infusion process. As a result, the thickness of composite panels manufactured from the final RIFT process varied somewhat. To be able to make these final RIFT-processed NFRP products commercially available, then consistency and tolerance of these properties must be maintained. Hence, further investigation into the relationship between these parameters should be conducted.

Additionally, the surface finish of the FRPs obtained from the final RIFT process was observed to be of rather a poor quality. This was due to the contour changing behaviour of the flexible RIFT vacuum bagging. Hence, these NFRPs are not suitable for applications that require a high quality surface finish. To improve the surface finish, further investigations into the process modification should be conducted.

A study by Messeteau et al. [72] observed that dry NFs can quickly absorb moisture in a laboratory atmosphere (i.e. 2.0 wt% in 90 s). The rapid moisture absorption of the NFs during their transportation from the oven to the RIFT equipment increased the moisture content in the NFs, and so increased the amount of water dissolution into the epoxy matrix. A study of manufacturing the NFRPs in one step, in order to avoid this moisture absorption problem, should be undertaken.

It has been observed that the void contents of the RTM-processed NFRPs with higher viscosity matrix formulations (i.e. Si0R9 and Si10R9 formulations) were higher than those from the final RIFT process. This suggests that the pre-programmed constant flow speed in the RTM method might have created a higher level of voids. A simulation of the flow of the resin during the RTM process should be conducted in order to determine the flow behaviour, optimize the flow settings, and hence reduce the manufacturing defects, e.g. voids or dry regions, in the RTM manufacturing process.

9.2.2 Physical and Mechanical Properties

The significant improvement in fracture toughness of the particle modified NFRPs has proved their potential in many applications, e.g. automotive, construction, sports, etc. However, other mechanical and physical properties, e.g. stiffness, strength, resistance to moisture degradation/absorption and resistance to thermal degradation should also be investigated and improved in order to further expand their suitability in other applications.

It has been observed that a good dispersion of the silica-nanoparticles and rubber-microparticles was present in the silica-nanoparticle modified FRPs and the rubber-microparticle modified FRPs respectively, whilst there was an agglomeration of the silica-nanoparticles in the hybrid toughened FRPs. However, the relationship of the dispersion of these particles and the mechanical properties of the FRPs has not yet been fully investigated. Further investigations may help the manufacturer optimize the mechanical properties in the hybrid toughened FRPs.

9.2.3 **Testing**

It is known that the typical degradation temperatures of the NFs and polymers are comparable. In the present study, degradation temperatures of over 290°C and 330°C were measured for the NFs and epoxy polymers respectively. It is also known that the NFs are susceptible to chemical degradation [181] and so the typical fibre volume fraction determination methods, e.g. the matrix burn-off and the chemical dissolution techniques, are therefore unsuitable for the NFRPs. In the present study, the fibre volume fraction was calculated from the measured densities of the composite, the reinforcement and the matrix. However, the accuracy of this method is not good due the poor quality of the FRPs, e.g. voids on their surfaces. Development of an improved test method to ascertain the fibre volume fraction of the NFRPs would benefit the quality control and consistency of NFRP materials.

9.2.4 **Analytical Modelling**

It has been seen that the additional toughening mechanisms induced by the fibres in the NFRPs, such as fibre bridging and fibre bundle bridging, resulted in a significant increase in their fracture energy. However, these mechanisms are not well understood. Further investigations into these mechanisms should be undertaken in order to accurately account for these toughening mechanisms, and their interactions with other toughening mechanisms, so that the interlaminar fracture energies in FRPs may be accurately predicted.

REFERENCES

[1] Matthews, F. L. & Rawlings, R. D. (1999) *Composite Materials: Engineering and Science.* Woodhead Publishing, Cambridge.

[2] Harris, B. (1999) *Engineering Composite Materials.* The Institution of Materials, London.

[3] Performance Composites (2009) *Mechanical Properties of Carbon Fibre Composite Materials.* [Online] Available from http://www.performance-composites.com/carbonfibre/mechanicalproperties_2.asp [Accessed: 14th December 2011].

[4] Cristaldi, G., Latteri, A., Recca, G. & Cicala, G. (2010) Composites based on natural fibre fabrics. In: Dubrovski, P. D. (eds.) *Woven fabric engineering.* Sciyo, India, 317-342.

[5] Pickering, K. L. (2008) *Properties and Performance of Natural-fibre Composites.* Woodhead Publishing, Cambridge.

[6] Bismarck, A., Aranberri-Askargorta, I., Springer, J., Lampke, T., Wielage, B., Stamboulis, A., Shenderovich, I. & Limbach, H-H. (2002) Surface characterization of flax, hemp and cellulose fibres: Surface properties and the water uptake behaviour. *Polymer Composites,* **23** (5), 872-894.

[7] John, M. J. & Thomas, S. (2008) Biofibres and biocomposites. *Carbohydrate Polymers,* **71** (3), 343-364.

[8] Kalia, S., Kaith, B. & Kaur, I. (2009) Pretreatments of natural fibres and their application as reinforcing material in polymer composites—A review. *Polymer Engineering and Science,* **49** (7), 1253-1272.

[9] McCrum, N. G., Buckley, C. P. & Bucknall, C. B. (1997) *Principles of Polymer Engineering.* Oxford University Press, New York.

[10] Bhatnagar, M. S. (1996) *The Polymeric Materials Encyclopaedia: Epoxy resins (Overview).* CRC Press, New York.

[11] Brydson, J. A. (1999) *Plastics Materials.* Butterworth - Heinemann, Oxford.

[12] Van Krevelen, D.W. (2012) *Properties of Polymers.* 3rd edn, Elsevier Science, Burlington.

[13] Williams, J. G. (1984) *Fracture Mechanics of Polymers.* Ellis Horwood, Chichester.

[14] Hsieh, T. H. (2011) *Properties and Toughening of Silica nanoparticle- and Carbon Nanotube-Modified Epoxy Polymers.* PhD Thesis. Imperial College London.

[15] Owen, M. J. & Rose, R. G. (1973) The fracture toughness and crack propagation properties of polyester resin casts and laminates. *Physics D,* **6** (1), 42-55.

[16] Christiansen, A. & Shortall, J B. (1976) The fracture toughness and fracture morphology of polyester resins. *Materials Science,* **11** (6), 1113-1124.

[17] Charalambides, M. N. & Williams, J. G. (1995) Fracture toughness characterization of phenolic resin and its composite. *Polymer Composites,* **16** (1), 17-28.

[18] Hinkley, J. A. & Mings, M. L. (1990) Fracture toughness of polyimide films. *Polymer,* **31** (1), 75-77.

[19] Ruan, S., Lannutti, J. J., Prybyla, S. & Seghi, R. R. (2001) Increased fracture toughness in nanoporous silica–polyimide matrix composites. *Materials Research,* **16** (7), 1975-1981.

[20] Zhang, H., Zhang, Z., Yang, J-L. & Friedrich, K. (2006) Temperature dependence of crack initiation fracture toughness of various nanoparticles filled polyamide 66. *Polymer,* **47** (2), 679-689.

[21] Gurit (2014) *Guide to Composites.* [Online] Available from http://www.gurit.com/guide-to-composites.aspx [Accessed: 20th July 2014].

[22] Hodgkinson, J. M. (2000) *Mechanical Testing of Advanced Fibre Composites.* Woodhead Publishing, Cambridge.

[23] Baley, C. (2002) Analysis of the flax fibres tensile behaviour and analysis of the tensile stiffness increase. *Composites Part A,* **33** (7), 939–948.

[24] Bledzki, A. K., Reihmane, S. & Gassen, J. (1996) Properties and modification methods for vegetable Fibres for natural fibre composites. *Applied Polymer Science,* **59**, 1329-1336.

[25] Dicker, M. P. M., Duckworth, P. F., Baker, A. B., Francois, G. & Hazzard, M. K. (2014) Green composites: A review of material attributes and complementary. *Composites Part A,* **56**, 280-289.

[26] John, M. J., Varughese, K. T. & Thomas, S. (2008) Green composites from natural fibres and natural rubber: Effect of fibre ratio on mechanical and swelling characteristics. *Natural Fibres,* **5** (1), 47-60.

[27] Ali, M. (2012) Natural fibres as construction materials. *Civil Engineering and Construction Technology,* **3** (3), 80-89.

[28] Sjostrom, E. (1993) *Wood Chemistry: Fundamentals and Applications*. 2nd edn, Gulf Professional Publishing, Houston.

[29] Wiedenhoeft, A. (2010) Structure and function of wood. In: Forest Product Laboratory (FPL) *Wood Handbook: Wood as an Engineering Material,* Wisconsin.

[30] Kontturi, E. (2013) *Cellulose: Structure, Morphology, and Crystalline Forms*. [Lecture] Aalto University, 29th October.

[31] Liu, Y. P. & Hu, H. (2008) X-ray diffraction study of bamboo fibres treated with NaOH. *Fibre and Polymers,* **9**, 735-739.

[32] Sauperl, O., Stana-Kleinschek, K. & Ribitsch, V. (2009) Cotton Cellulose 1, 2, 3, 4 Buthanetetracarboxylic Acid (BTCA) crosslinking monitored by some physical-chemical methods. *Textile Research,* **79**, 780-791.

[33] Yue, Y. (2011) *A Comparative Study of Cellulose I and II Fibres and Nanocrystrals*. MSc Thesis. Graduate Faculty of the Louisiana State University and Agricultural and Mechanical College.

[34] Odian, G. (2004) *Principles of Polymerization.* 4th edn, John Wiley & Sons, New Jersey.

[35] Kontturi, E. (2012) *Cellulose: Structure, Morphology, and Crystalline Forms*. [Presentation] Aalto University, 14th September.

[36] Charlet, K., Baley, C., Morvan, C., Jernot, J. P., Gomina, M., Breard, J. (2007) Characteristics of Hermès flax fibres as a function of their location in the stem and properties of the derived unidirectional composites. *Composites Part A,* **38** (8), 1912-1921.

[37] Savage, L. & Evans, K. (2014) The importance of the mesostructure in toughening cellulosic short fibre composites. *Composites Science and Technology,* **93**, 97-105.

[38] Porcher Industries (2011) *Porcher Greenlite.* [Online] Available from http://www.porcher-ind.com/uploads/files/PorcherGreenlite%202013_web.pdf [Accessed: 14th December 2013].

[39] Kretschmann, D. E. (2010) Mechanical properties of wood. In: Forest Product Laboratory (FPL) *Wood Handbook: Wood as an Engineering Material,* Wisconsin.

[40] Wallenberger, F. T. & Bingham, P. A. (2010) (eds.) *Fibreglass and Glass Technology: Energy-friendly Compositions and Applications*. Springer, London.

[41] Composites Evolution (2012) *Biotex Flax Unidirectional Fabric: Technical Data Sheet.* [Online] Available from http://compositesevolution.com/Portals/0/Biotex%20Flax%20Unidirectional%20TDS%20March%202012.pdf [Accessed: 14th June 2012].

[42] Composites Evolution (2012) *Biotex Flax +/-45 Biaxial Fabric: Technical Data Sheet.* [Online] Available from http://compositesevolution.com/Portals/0/Biotex%20Flax%2045%20Biaxial%20TDS%20March%202012.pdf [Accessed: 14th June 2012].

[43] Lineo (2013) *Flaxtape: Full Technical Guide.* [Online] Available from http://www.flaxtape.com/wp-content/uploads/2013/07/2013-FlaxTape-Technical-Guide.pdf [Accessed: 20th December 2013].

[44] Bhowmick, M, Mukhopadhyay, S. & Alagirusamy, R. (2012) Mechanical properties of natural fibre-reinforced composites. *Textile Progress,* **44** (2), 85-140.

[45] Jose, S., Kumar, R. R., Jana, M. K. & Rao, G. V. (2001) Intralaminar fracture toughness of a cross-ply laminate and its constituent sub-laminates. *Composites Science and Technology,* **61**, 1115–1122.

[46] American Society for Testing and Materials (2007) ASTM D5045-99(2007)e1 Standard test method for plane strain fracture and strain energy release rate of plastic materials, in *Annual Book of ASTM Standards,* Vol. 08.02, ASTM, Pennsylvania.

[47] Sham Prasad, M. S., Venkatesha, C. S. & Jayaraju, T. (2011) Experimental methods of determining fracture toughness of fibre reinforced polymer composites under various loading conditions. *Minerals and Materials Characterization and Engineering,* **10** (13), 1263-1275.

[48] Czabaj, M. W. & Ratcliffe, J. G. (2012) Comparison of intralaminar and interlaminar mode-I fracture toughness of unidirectional IM7/8552 graphite/epoxy composite. *Proceedings of the American Society for Composites 27th Technical Conference, 1-3 Oct 2012, Texus.*

[49] Leach, D. C. & Moore, D. R. (1985) Toughness of aromatic polymer composites reinforced with carbon fibres. *Composites Science and Technology,* **23** (2), 131-161.

[50] Mouritz, A. P. (2007) Review of z-pinned composite laminates. *Composites Part A,* **38**, 2383-2397.

[51] Partridge, I. K. & Cartié, D. D. R. (2005) Delamination resistant laminates by Z-Fibre® pinning: Part I manufacture and fracture performance. *Composites Part A,* **36** (1), 55–64.

[52] Pinto, M. A., Chalivendra, V. B., Kim, Y. K. & Lewis, A. F. (2013) Effect of surface treatment and Z-axis reinforcement on the interlaminar fracture of jute/epoxy laminated composites. *Engineering Fracture Mechanics,* **114**, 104–114.

[53] Li, Y., Mai, Y-M. & Ye, L. (2012) Effects of fibre surface treatment on fracture-mechanical properties of sisal-fibre composites. *Composite Interfaces,* **12** (1-2), 141-163.

[54] Zulkifli, R. (2009) Surface fracture analysis of glass fibre reinforced epoxy composites treated with different type of coupling agent. *European Journal of Scientific Research,* **29** (1), 55-65.

[55] Zulkifli, R., Azhari, C. H., Ghazali, M. J., Ismail, A. R. & Sulong, A. B. (2009) Interlaminar fracture toughness of multi-layer woven silk/epoxy composites treated with coupling agent. *European Journal of Scientific Research,* **27** (3), 454-462.

[56] Hsieh, T. H., Kinloch, A. J., Masania, K., Sohn Lee, J., Taylor, A. C. & Sprenger, S. (2010) The toughness of epoxy polymers and fibre composites modified with rubber microparticles and silica nanoparticles. *Materials Science,* **45**, 1193-1210.

[57] Huang, Y. & Kinloch, A. J. (1992) Modelling of the toughening mechanisms in rubber-modified epoxy polymers Part II: A quantitative description of the microstructure-fracture property relationships. *Materials Science,* **27**, 2763-2769.

[58] Zeng, Y., Liu, H. Y., Mai, Y. W. & Du, X. S. (2012) Improving interlaminar fracture toughness of carbon fibre/epoxy laminates by incorporation of nano-particles. *Composites Part B,* **43** (1), 90-94.

[59] Silva, R. V., Spinelli, D., Bose Filho, W. W., Claro Neto, S., Chierice, G. O. & Tarpani, J. R. (2006) Fracture toughness of natural fibres/castor oil polyurethane composites. *Composites Science and Technology,* **66** (10), 1328-1335.

[60] Hughes, M., Hill, C. A. S. & Hague, J. R. B. (2002) The fracture toughness of bast fibre reinforced polyester composites: Part 1 Evaluation and analysis. *Materials Science,* **37**, 4669-4676.

[61] Wong, K. J., Zahi, S., Low, K. O. & Lim, C. C. (2010) Fracture characterisation of short bamboo fibre reinforced polyester composites. *Materials and Design,* **31**, 4147-4154.

[62] Liu, Q. & Hughes, M. (2008) The fracture behaviour and toughness of woven flax fibre reinforced epoxy composites. *Composites Part A,* **39** (10), 1644-1652.

[63] Benzeggagh, M. L. & Kenane, M. (1996) Measurement of mixed-mode delamination fracture toughness of unidirectional glass/epoxy composites with mixed-mode bending apparatus. *Composites Science and Technology,* **56**, 439-449.

[64] Le Duigou, A., Davies, P. & Baley, C. (2010) Macroscopic analysis of interfacial properties of flax/PLLA biocomposites. *Composites Science and Technology,* **70**, 1612–1620.

[65] Wong, S., Shanks, R. A. & Hodzic, A. (2004) Mechanical behaviour and fracture toughness of poly(L-lactic acid)-natural fibre composites modified with hyperbranched polymers. *Macromolecular Materials and Engineering,* **289** (5), 447-456.

[66] Kafi, A. A., Magniez, K. & Fox, B. L. (2011) Effect of manufacturing process on the flexural, fracture toughness, and thermo-mechanical properties of bio-composites. *Composites Part A,* **42** (8), 993-999.

[67] Alveraz, V. A., Ruseckaite, R. A. & Vazquez, A. (2003) A mechanical properties and water absorption of MaterBi-Y/sisal fibre composites: Effect of alkaline treatment. *Composite Materials,* **37** (17), 1575-1588.

[68] Jiang, Z. X., Huang, Y. D., Liu, L. & Liu, L. (2011) Effects of functional group polarity on interfacial behaviour of non-polar polyarylacetylene resin-silica glass composites. *High Performance Polymers,* **21** (1), 79–89.

[69] Azwa, Z. N. & Yousif, B. F. (2013) Thermal degradation study of kenaf fibre/epoxy composites using thermo gravimetric analysis. In: Noor, M. M., Rahman, M. M. & Ismail, J. (eds.) *3rd Malaysian Postgraduate Conference, MPC 2013, 4-5 July 2013, Sydney, New South Wales, Australia.*

[70] Masoodi, R. & Pillai, K. M. (2012) A study on moisture absorption and swelling in bio-based jute-epoxy composites. *Reinforced Plastics and Composites,* **31**, 285-294.

[71] Rowell, R. M. (1997) Chemical modification of agro-resources for property enhancement. *Paper and Composites from Agro-based Resources,* CRC Press, 351-375.

[72] Masseteau, B., Michaud, F., Irle, M., Roy, A. & Alise, G. (2014) An evaluation of the effects of moisture content on the modulus of elasticity of a unidirectional flax fibre composite. *Composites Part A,* **60**, 32-37.

[73] Athijayamani, A., Thiruchitrambalam, M., Natarajan, U. & Pazhanivel, B. (2009) Effect of moisture absorption on the mechanical properties of randomly oriented natural fibres/polyester hybrid composite. *Materials Science and Engineering A,* **517**, 344-353.

[74] Espert, A., Vilaplana, F. & Karlsson, S. (2002) Comparison of water absorption in natural cellulosic fibres from wood and one-year crops in polypropylene composites and its influence on their mechanical properties. *Composites Part A,* **35**, 1267–1276.

[75] Marcovich, N. E., Reboredo, M. M. & Aranguren, M. I. (1998) Dependence of the mechanical properties of woodflour–polymer composites on the moisture content. *Applied Sciences,* **68**, 2069–76.

[76] Rangaraj, S.V. & Smith, L. (2000) Effects of moisture on the durability of a wood/thermoplastic composite. *Thermoplastic Composite Materials,* **13**, 140–61.

[77] Stark, N. (2001) Influence of moisture absorption on mechanical properties of wood flour–polypropylene composites. *Thermoplastic Composite Materials,* **14**, 421–32.

[78] Zabihzadeh, S. M. (2010) Water uptake and flexural properties of natural filler/hdpe composites. *BioResources,* **5** (10), 316-323.

[79] Hu, R-H., Sun, M-Y. & Lim, J-K. (2010) Moisture absorption, tensile strength and microstructure evolution of short jute fibre/polylactide composite in hygrothermal environment. *Materials and Design,* **31**, 3167-3173.

[80] George, J., Bhagawan, S. S. & Thomas, S. (1998) Effects of environment on the properties of low-density polyethylene composites reinforced with pineapple-leaf fiber. *Composites Science and Technology,* **58**, 1471–85.

[81] Joseph, P. V., Rabello, M. S., Mattoso, L. H. C., Joseph, K. & Thomas, S. (2002) Environmental effects on the degradation behaviour of sisal reinforced polypropylene composites. *Composites Science and Technology,* **62** (10-11), 1357-1372.

[82] Araujo, J. R., Waldman, W. R. & De Paoli, M. A. (2008) Thermal properties of high density polyethylene composites with natural fibres: Coupling agent effect. *Polymer Degradation and Stability,* **93**, 1770-1775. .

[83] Dittenber, D. B. & Gangrao, H. V. S. (2012) Critical review of recent publications on use of natural composites in infrastructure. *Composites Part A,* **43**, 1419-1429.

[84] Manfredi, L. B., Rodriguez, E. S., Wladika-Przybylak, M. & Vazquez, A. (2006) Thermal degradation and fire resistance of unsaturated polyester, modified acrylic resins and their composites with natural fibres. *Polymer Degradation and Stability,* **91**, 255-261.

[85] Suardana, N. P. G., Ku, M. S. & Lim, J. K. (2011) Effects of diammonium phosphate on the flammability and mechanical properties of bio-composites. *Materials and Design,* **32**, 1990-1999.

[86] Yao, F., Wu, Q., Lei, Y., Guo, W. & Xu, Y. (2008) Thermal decomposition kinetics of natural fibres: Activation energy with dynamic thermogravimetric analysis. *Polymer Degradation and Stability,* **93**, 90-98. .

[87] Beg, M. D. H. & Pickering, K. L. (2008) Accelerated weathering of unbleached and bleached Kraft wood fibre reinforced polypropylene composites. *Polymer Degradation and Stability,* **93**, 1939-1946.

[88] Ahmed, A. (2007) *A Review of Plasma Treatment for Application on Textile Substrate.* BSc Thesis. The Textile Institute of Pakistan.

[89] Reichel, K. (2001) *Plasma Treatment, Process Diversity and Sustainability*. German Federal Ministry of Education and Research.

[90] Morales, J., Olayo, M. G., Cruz, P., Herrera-Franco, P. & Olayo, R. (2005) Plasma modification of cellulose fibres for composite. *Applied Polymer Science,* **101**, 3821–3828.

[91] Kafi, A. A., Magniez, K. & Fox, B. L. (2011) A surface-property relationship of atmospheric plasma treated jute composites. *Composites Science and Technology,* **71**, 1692-1698.

[92] Paglicawan, M. A., Basilia, B. A. & Kim, B. S. (2013) Water uptake and tensile properties of plasma treated abaca fibre reinforced epoxy composite. *Composites Research,* **26** (3), 165-169.

[93] Sinha, E. & Panigrahi, S. (2009) Effect of plasma treatment on structure, wettability of jute fibre and flexural strength of its composite. *Composite Materials,* **43** (17), 1791-1802.

[94] Felix, J. M. & Gatenholm, P. (1991) The nature of adhesion in composites of modified cellulose fibres and polypropylene. *Applied Polymer Science,* **42**, 609-620.

[95] Taylor, A. C. (2011) *Fracture of Composites*. [Lecture] Imperial College London.

[96] AFGROW (2011) *Handbook for Damage Tolerance Design.* [Online] Available from http://www.afgrow.net/applications/DTDHandbook/default.aspx [Accessed: 14th June 2013].

[97] Irwin, G. R. (1957) Analysis of stresses and strains near the end of a crack traversing a plate. *Applied Mechanics,* **24** (3), 361-364.

[98] La Saponara, V. (2010) *Introduction to Fracture Mechanics and Fatigue*. [Lecture] University of Califonia, 4th March.

[99] Callister, W. (1994) *Materials Science and Engineering.* John Wiley & Sons, New York.

[100] Griffith, A. A. (2004) The phenomena of rupture and flow in solids. *Philosophical Transactions of the Royal Society of London,* **221** (1921), 163-198.

[101] Hutchinson, J. W. & Jensen, H. M. (1990) Models of fibre debonding and pull-out in brittle composites with friction. *Mechanics of Materials,* **9** (2), 139-163.

[102] Remmers, J. J. C. & de Borst, R. (2001) Delamination buckling of fibre–metal laminates. *Composites Science and Technology,* **61** (15), 2207–2213.

[103] Krasnikovs, A. & Varna, J. (1997) Transverse cracks in cross-ply laminates: 1 Stress analysis. *Mechanics of Composite Materials,* **33** (6), 565-582.

[104] Committee on Evaluation of Long-term Aging of Materials and Structures Using Accelerated Test Methods (1996) *Accelerated Aging of Materials and Structures: The Effects of Long-Term Elevated-Temperature Exposure*. National Materials Advisory Board, Commission on Engineering and Technical Systems, National Research Council, National Academy Press, Washington, D.C.

[105] Masania, K. (2010) *Toughening Mechanisms of Silica Nanoparticle Modified Epoxy Polymers*. PhD Thesis. Imperial College London.

[106] Sprenger, S., Kinloch, A. J. & Taylor, A. C. (2008) *Silica Nanoparticles & Rubber Toughening – A Aynergy in Adhesives & Composites Applications.* [Presentation] Thermoset Resin Formulators Association, Chicago, Illinois, 15-16 September.

[107] Deng, S., Ye, L. & Friedrich, K. (2007) Fracture behaviours of epoxy nanocomposites with nano-silica at low and elevated temperatures. *Materials Science,* **42** (8), 2766-2774.

[108] Johnsen, B. B., Kinloch, A. J., Mohammed, R. D., Taylor, A. C. & Sprenger, S. (2007) Toughening mechanisms of nanoparticle modified epoxy polymers. *Polymer,* **48** (2), 530-541.

[109] Blackman, B. R. K., Kinloch, A. J., Sohn Lee, J., Taylor, A. C., Agarwal, R., Schueneman, G. & Sprenger, S. (2007) The fracture and fatigue behaviour of nano-modified epoxy polymers. *Materials Science,* **42** (16), 7049-7051.

[110] Manjunatha, C. M., Taylor, A. C., Kinloch, A. J. & Sprenger, S. (2009) The effect of rubber micro-particles and silica nano-particles on the tensile fatigue behaviour of a glass-fibre epoxy composite. *Materials Science,* **44** (1), 342-345.

[111] Kinloch, A.J. (2003) Theme article - Toughening epoxy adhesives to meet today's challenges. *Materials Research Society Bulletin,* **28** (6), 445-448.

[112] Sue, H-J. (1991) Study of rubber-modified brittle epoxy systems. Part II: Toughening mechanisms under model fracture. *Polymer Engineering and Science,* **31** (4), 275-288.

[113] Hsieh, T. H., Kinloch, A. J., Masania, K., Taylor, A. C. & Sprenger, S. (2010) The mechanisms and mechanics of the toughening of epoxy polymers modified with silica nanoparticles. *Polymer,* **51**, 6284-6294.

[114] Kinloch, A. J., Maxwell, J. M. & Young, R. J. (1985) Micromechanisms of crack propagation in hybrid-particulate composites. *Materials Science Letters,* **4**, 1276-1279.

[115] Amdouni, N., Sautereau, H., Gerard, J. F., Fernagut, F., Coulon, G. & Lefebvre, J. M. (1990) Coated glass beads epoxy composites - Influence of the interlayer thickness on pre-yielding and fracture properties. *Materials Science,* **25**, 1435-1443.

[116] Spanoudakis, J. & Young, R. J. (1984) Crack propagation in a glass particle-filled epoxy resin: Part 1 Effect of particle volume fraction and size. *Materials Science,* **19**, 473-486.

[117] Kawaguchi, T. & Pearson, R. A. The effect of particle-matrix adhesion on the mechanical behaviour of glass filled epoxies: Part 1 A study on yield behaviour and cohesive strength. *Polymer,* **44**, 4229-4238.

[118] Yee, A. F., Li, D. & Li, X. (1993) The importance of constrain relief caused by rubber cavitation in the toughening of epoxy. *Materials Science,* **28**, 6392-6398.

[119] Kunz-Douglass, S. C., Beaumont, P. W. R. & Ashby, M. F. (1980) A model for the toughness of epoxy-rubber particulate composites. *Materials Science,* **15**, 1109-1123.

[120] Guven, G. (1997) *Shear Band Propagation in Cross Linked Epoxies*. MSc Thesis. Lehigh University.

[121] Gurit (n.d.) *Guide to Composites*. [Online] Gurit. Available from http://www.gurit.com/files/documents/Gurit_Guide_to_Composites(1).pdf [Accessed: 11th March 2013].

[122] Quinn, J. A. (1989) Pultrusion - An economic manufacturing technique. *Metals and Materials,* **5**, 270-273.

[123] Clifford, M. (2011) *Liquid Moulding Technologies.* [Lecture] Imperial College London, 28th March.

[124] Wells, G. M. (2011) *Manufacturing Science: Filament Winding & Pultrusion.* [Lecture] Imperial College London, 14th March.

[125] ETH Zürich, IMES-ST (2007) *Liquid Composite Moulding.* [Online] Available from: http://www.structures.ethz.ch/education/master/intro/compulsory/composites/Skript/151-0307-V4.0-K08_LCM-Verfahren.pdf [Accessed: 10th June 2013].

[126] Summerscales, J. (2012) *Composites Design and Manufacture: Resin Infusion Under Flexible Tooling (RIFT*). [Presentation] Plymouth University, 29th November.

[127] Nanoresins (2005) *Modifying Epoxy Resins with Nanocomposites.* [Online] Available from: http://www.nanoresins.ag/content/view/52/55/lang,en/ [Accessed: 14th June 2013].

[128] Gurit (2014) *UT-E500 Glass Fabric.* [Online] Available from http://www.gurit.com/files/documents/ute500pdf.pdf [Accessed: 20th July 2014].

[129] Gurit (2014) *RE86P Glass Fabric.* [Online] Available from http://www.gurit.com/files/documents/re86ppdf.pdf [Accessed: 20th July 2014].

[130] Gurit (2014) *RE165T Glass Fabric.* [Online] Available from http://www.gurit.com/files/documents/re165tpdf.pdf [Accessed: 20th July 2014].

[131] Engineering Archives (2012) *Tensile Test.* [Online] Available from: http://www.engineeringarchives.com/les_mom_tensiletest.html [Accessed: 14th June 2013].

[132] Instron (2013) *Rheology Testing.* [Online] Available from http://www.instron.us/wa/applications/test_types/rheology/default.aspx?ref=https://www.google.com/ [Accessed: 14th December 2013].

[133] American Society for Testing and Materials (2008) ASTM D4440-08 Standard Test Method for Plastics: Dynamic Mechanical Properties: Melt Rheology, in *Annual Book of ASTM Standards,* Vol. 08.02, ASTM, Pennsylvania.

[134] American Society for Testing and Materials (2008) ASTM D4473-08 Standard Test Method for Plastics: Dynamic Mechanical Properties: Cure Behaviour, in *Annual Book of ASTM Standards,* Vol. 08.02, ASTM, Pennsylvania.

[135] American Society for Testing and Materials (2008) ASTM E1356-08 Standard Test Method for Assignment of the Glass Transition Temperatures by Differential Scanning Calorimetry, in *Annual Book of ASTM Standards,* Vol. 14.02, ASTM, Pennsylvania.

[136] Coats, A. W. & Redfern, J. P. (1963) Thermogravimetric analysis: A review. *Analyst,* **88**, 906–924.

[137] American Society for Testing and Materials (2008) ASTM E2550-11 Standard Test Method for Thermal Stability by Thermogravimetry, in *Annual Book of ASTM Standards,* Vol. 14.02, ASTM, Pennsylvania.

[138] Furuse, A. (1989) *Volume Measuring Apparatus and Method*. U.S. Patent 4,888,718 (Patent).

[139] Quantachrome (2013) *Pycnometers: True Density Analysis of Powders, Forms and Bulk Solids Rev B*. Quantachrome Corporation, Florida.

[140] American Society for Testing and Materials (2012) ASTM D2320-98(2012) Standard Test Method for Density (Relative Density) of Solid Pitch (Pycnometer Method), in *Annual Book of ASTM Standards,* Vol. 02.05, ASTM, Pennsylvania.

[141] Terlingen, J. G. A. (2004) *Chapter 2: Functionalization of Polymer Surfaces, Introduction of Functional Groups at Polymer Surfaces by Glow Discharge Techniques.* [Online] Available from: http://www.uzaktanegitimplatformu.com/UEP/uep_lisans/tek303/tek303_downloads/EP%20TP%20Functionalization%20of%20polymer%20surfaces.doc.pdf [Accessed: 14th June 2013].

[142] Blackman, B. R. K. (2011) Personal Communication with Mana Techapaitoon.

[143] American Society for Testing and Materials (2013) ASTM D5528-13 Standard Test Method for Mode I Interlaminar Fracture Toughness of Unidirectional Fibre-Reinforced Polymer Matrix Composites, in *Annual Book of ASTM Standards,* Vol. 15.03, ASTM, Pennsylvania.

[144] American Society for Testing and Materials (2010) ASTM D790-10 Standard Test Methods for Flexural Properties of Unreinforced and Reinforced Plastics and Electrical Insulating Materials, in *Annual Book of ASTM Standards,* Vol. 08.01, ASTM, Pennsylvania.

[145] American Society for Testing and Materials (2008) ASTM D3039/D3039M-08 Standard Test Method for Tensile Properties of Polymer Matrix Composite Materials, in *Annual Book of ASTM Standards,* Vol. 15.03, ASTM, Pennsylvania.

[146] Ohara, T., Ueno, I., Ogihara, S. & Watanabe, K. (2009) Wetting behaviour between fibre & resin in vacuum assisted resin transfer moulding (VaRTM). *Proceedings of the International Conference on Composite Materials, ICCM 17, 27-31 July 2009, Edinburg.*

[147] Fox, T. G. (1956) Influence of diluent and of copolymer composition on the glass temperature of a polymer system. *Bulletin of the American Physical Society,* **1**, 123.

[148] Radius Engineering Inc. (n.d.) *Radius 5000cc RTM Injector User Manual*. Radius Engineering Inc., Utah.

[149] Chawla, K. K. (1998) *Composite Materials, Science and Engineering*. 2nd edn, Springer, New York.

[150] Jones, R. M. (1999) *Mechanics of Composite Materials*. 2nd edn, Taylor & Francis, London.

[151] Messiry, M. E. (2013) Theoretical analysis of natural fibre volume fraction of reinforced composites. *Alexandria Engineering Journal,* **52** (3), 301–306.

[152] Mortensen, A. (ed.) (2007) *Concise Encyclopedia of Composite Materials*. 2nd edn, Elsevier Science, Oxford.

[153] Ishikawa, T. & Chou, T-W. (1982) Stiffness and strength behaviour of woven fabric composites. *Materials Science,* **17**, 3211-3220.

[154] Naik, N. K. & Shembekar, P. S. (1992) Elastic behaviour of woven fabric composites: II Laminate analysis. *Composite Materials,* **26** (15), 2226-2246.

[155] Redman, C. J. & Douglas, C. D. (1993) Theoretical prediction of the tensile elastic properties of braided composites. *38th International SAMPE Symposium,* 719–727.

[156] Carey, J., Munro, M. & Fahim, A. (2003) Longitudinal elastic modulus prediction of a 2-D braided fibre composite. *Reinforced Plastics and Composites,* **22**, 813-831.

[157] Xiong, J. J., Shenoi, R. A. & Cheng, X. (2009) A modified micromechanical curved beam analytical model to predict the tension modulus of 2D plain weave fabric composites. *Composites Part B,* **40**, 776-783.

[158] Naik, N. K., Tiwari, S. I. & Kumar, R. S. (2003) An analytical model for compressive strength of plain woven fabric composites. *Composites Science and Technology,* **63** (5), 609-625.

[159] Ameli, A., Papini, & Spelt, J. K. (2011) Hygrothermal degradation of two rubber-toughened epoxy adhesives: Application of open-faced fracture tests. *International Journal of Adhesion & Adhesives,* **31**, 9–19.

[160] Kinloch A. J. & Taylor A. C. (2002) The toughening of cyanate-ester polymers. Part I: Physical modification using particles, fibres and woven-mats, *Materials Science,* **37** (3), 433.460.

[161] Fernlund, G. & Spelt, J. K. (1994) Mixed-mode fracture characterization of adhesive joints. *Composites Science and Technology,* **50** (4), 441–449.

[162] Davidson, P. & Waas, A. M. (2012) Non-smooth mode I fracture of fibre-reinforced composites: an experimental, numerical and analytical study. *Philosophical Transaction of The Royal Society A,* **370**, 1942-1965.

[163] Ye, L. & Friedrich, K. (1992) Fibre bridging in double cantilever beam specimens and its effect on mode I interlaminar fracture toughness. *Materials Science Letters,* **11**, 1537-1539.

[164] Evans, A. G., Williams, S. & Beaumont, P. W. R. (1985) On the toughness of particulate filled polymers. *Materials Science,* **20** (10), 3668-3674.

[165] Dekkers, M. E. J. & Heikens, D. (1984) Shear band formation in polycarbonate-glass bead composites. *Materials Science,* **19** (10), 3271-3275.

[166] Dekkers, M. E. J. & Heikens, D. (1985) Crazing and shear deformation in glass bead-filled glassy polymers. *Materials Science,* **20** (11), 3873-3880.

[167] Guild, F. J. & Young, R. J. (1989) A predictive model for particulate filled composite materials. Part 1 Hard particles. *Materials Science,* **24**, 298-306.

[168] Guild, F. J. & Young, R. J. (1989) A predictive model for particulate filled composite materials. Part 2 Soft particles. *Materials Science,* **24**, 2454-2460. .

[169] Sultan, J. N. & McGarry, F. J. (1973) Effect of rubber particle size on deformation mechanisms in glassy epoxy. *Polymer Engineering and Science,* **13** (1), 29-34.

[170] Caddell, R. M. (1989) *Deformation and Fracture of Solids*. Prentice-Hall, New Jersey.

[171] Evans, A. G., Williams, S. & Beaumont, P. W. R. (1986) Mechanisms of toughening in rubber toughened polymers. *Acta Metallurgica,* **34**, 79-87.

[172] Kinloch, A. J., Johnsen, B. B., Mohammed, R. D., Taylor, A. C. & Sprenger, S. (2007) Toughening mechanisms in novel nano-silica epoxy polymers. *5th Australasian Congress on Applied Mechanics (ACAM 2007), 10-12 December 2007, Brisbane*.

[173] Chen, J., Huang Z. & Zhu, J. (2007) Size effect of particles on the damage dissipation in nanocomposites. *Composites Science and Technology,* **67**, 2990-2996.

[174] Baller, J., Becker, N., Ziehmer, M., Thomassey, M., Zielinski, B., Muller, U. & Sanctuary, R. (2009) Interactions between silica nanoparticles and an epoxy resin before and during network formation. *Polymer,* **50**, 3211-3219.

[175] Vallo, C. I., Hu, L., Frontini, P. M. & Williams, R. J. J. (1994) Toughened-hybrid epoxies - Influence of the rubber-phase morphology on Mechanical-properties. *Materials Science,* **29**, 2481-2486.

[176] Kunz, S. C. & Beaumont, P. W. R. (1981) Low-temperature behaviour of epoxy rubber particulate composites. *Materials Science,* **16** (11), 3141-3152.

[177] Ayre, D. S. & Bucknall, C. B. (1998) Particle cavitation in rubber-toughened PMMA: experimental testing of the energy-balance criterion. *Polymer,* **39** (20), 4785-4791.

[178] Bucknall, C. B., Karpodinis, A. & Zhang, X. C. (1994) A model for particle cavitation in rubber-toughened plastics. *Materials Science,* **29**, 3377-3383.

[179] Huang, Y. & Kinloch, A. J. (1992) The role of plastic void growth in the fracture of rubber-toughened epoxy polymers. *Materials Science Letters,* **11**, 484-487.

[180] Ye, L. & Friedrich, K. (1993) Mode I interlaminar fracture of co-mingled yarn based glass/polypropylene composites. *Composites Science and Technology,* **46** (2), 187-198.

[181] Area M. C. & Cheradame, H. (2011) Paper aging: recent findings and research methods. *BioResources,* **6** (4), 5307-5337.

[182] Fibermax Composites (2007) *Weaving Styles.* [Online] Available from http://www.fibermax.eu/index_files/weavingstylesandpatterns.htm [Accessed: 20th July 2014].

[183] Phillips, L. N. (1989) *Design with Advanced Composite Materials.* The Design Council, London.

APPENDICES

Appendix I: Reinforcements Used in the Present Study

Table A.1 show the different types and architectures of fibre/fabric reinforcements used in the present study.

Table A.1: Different types and architectures of reinforcements used in the present study

Fibre type	Fibre architecture	Theoretical Planar density in warp/weft (GSM)	Fibre in warp/weft (tex)	Count in warp/weft (end/cm)	Planar density (GSM)	Supplier
Flax fibre[41]	Unidirectional with cotton weft stitch	252/23	N/A	11/1	275	Composites Evolution, UK
Cellulose fibre[38]	Plain-woven	105/105	N/A	7.14/7.14	210	Porcher Industries, France
Glass fibre[128]	Unidirectional with polyester weft stitch	500/2	1200/10	4.16/0.56	500	SP Systems, UK
Glass fibre[129]	Plain-woven	41.5/43.3	34/34	12/12.5	86	SP Systems, UK
Glass fibre[130]	Twill 2x2	83.1/83.1	68/68	12/12	165	SP Systems, UK

Unidirectional fibre/fabric reinforcement

A unidirectional (UD) fabric has the majority of fibres running in one direction only. A small amount of fibre or other material may run in other directions to hold the primary fibres in position, see Figure A.1. The other fibres may also offer some structural properties. These UD fabrics can vary their fibres in their primary direction from 75 wt% to 100 wt% of the fabric. These true UD fabrics are straight and uncrimped; they yield the highest possible fibre properties.

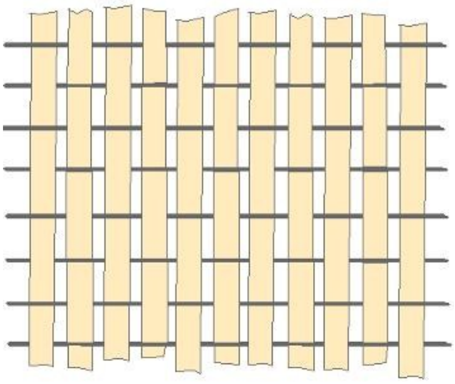

Figure A.1: Unidirectional fibre/fabric reinforcement [182]

Plain-woven fibre/fabric reinforcements

A plain-woven (PW) fabric has its fibres in the warp and weft directions, where each warp fibre passes alternately under and over each weft fibre, see Figure A.2. Typically, the PW fabrics are symmetrical, with good stability and reasonable porosity. However, they are hard to drape and due to the high level of fibre crimping relatively poor mechanical properties are expected, compared with other fibre architectures.

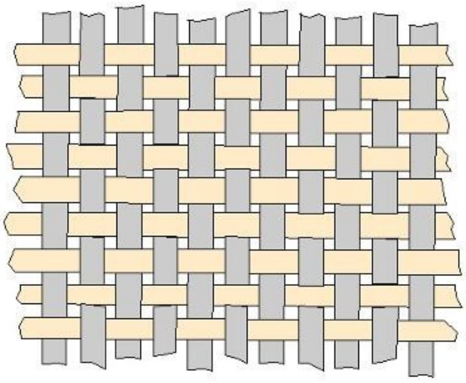

Figure A.2: Plain-woven fibre/fabric reinforcement [182]

Twill 2x2 fibre/fabric reinforcements

A twill 2x2 fabric has its warp fibres weaving over/under two weft fibres in a repeated manner, see Figure A.3. Relatively higher mechanical properties than the PW fabrics are expected due to the reduction of the fibre crimping. Also, the fabrics are relatively easy to drape than those in PW architecture.

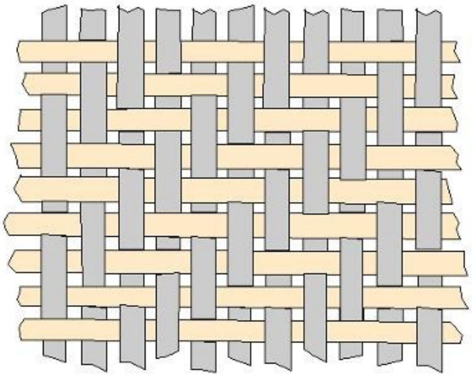

Figure A.3: Twill 2x2 fibre/fabric reinforcement [182]

Appendix II: ESIS Proposal for a Multi-span 3-point Bend Test Method with Multi-span Calibration

The multi-span 3-point bend test basically uses the procedure as in ASTM D790-02 [144] but the test is conducted at a number of different span widths (6-8 span widths are recommended), recommended span-to-depth ratios are 30:1 / 35:1 / 40:1 / 45:1 / 50:1 / 55:1 / 60:1 / 65:1. However, due to variation of thickness of the specimens with different reinforcements, fixed spans of 60, 90, 120, 150 and 180 mm were used regardless of sample thickness which yielded the span-to-depth ratios of approximately 11-24 to 33-72. The estimation of the flexural modulus from the European Standard Integrity Society (ESIS) proposal for multi-span 3-point bend test method [142] is as follows.

The flexural modulus can be calculated by:

$$\frac{1}{E_B^{'}} = \frac{1}{E_B} + \frac{1}{kG_{12}}\left(\frac{h}{S}\right)^2 + \frac{4b}{k_{sys}}\left(\frac{h}{S}\right)^2 \tag{A.1}$$

which can be simplified as

$$\frac{1}{E_B^{'}} = \frac{1}{E_B} + \frac{1}{kG_{12}}\left(\frac{h}{S}\right)^2 \tag{A.2}$$

where E_B' is modulus from $E_B' = S^3 m / 4bh^3$; *m* is the slope of load-displacement curve , E_B is the real modulus, *k* is the constant, G_{12} is the in-plane shear modulus, *h* is the depth, *S* is the span, *b* is the width and k_{sys} is the machine compliance.

E_B is determined by using the intercept point of the plot of $\frac{1}{E_B'}$ vs $\left(\frac{h}{S}\right)^2$ where standard deviation of $\frac{1}{E_B'}$ can be calculated using the following equation

$$\sigma = \left[\frac{1}{n-2}\Sigma\left(y_i - mx_i - c\right)^2\right]^{0.5} \tag{A.3}$$

where *n* is number of samples. However, this plot gives standard deviation of $\frac{1}{E_B'}$ not the standard deviation of E_B' . The plot of E_B' vs $\left(\frac{h}{S}\right)^2$ is then plotted where the accuracy of E_B still lies within 1-5% with the plot of $\frac{1}{E_B'}$ vs $\left(\frac{h}{S}\right)^2$ and the standard deviation of E_B' can be calculated.

Figure A.4 and Figure A.5 show examples of the $\frac{1}{E_B'}$ vs $\left(\frac{h}{S}\right)^2$ and E_B' vs $\left(\frac{h}{S}\right)^2$ curves from a set of multi-span 3-point bend test experiment on the same material. The pure flexural modulus can be determined at $\left(\frac{h}{S}\right)^2 = 0$ where the effect from shear modulus becomes zero.

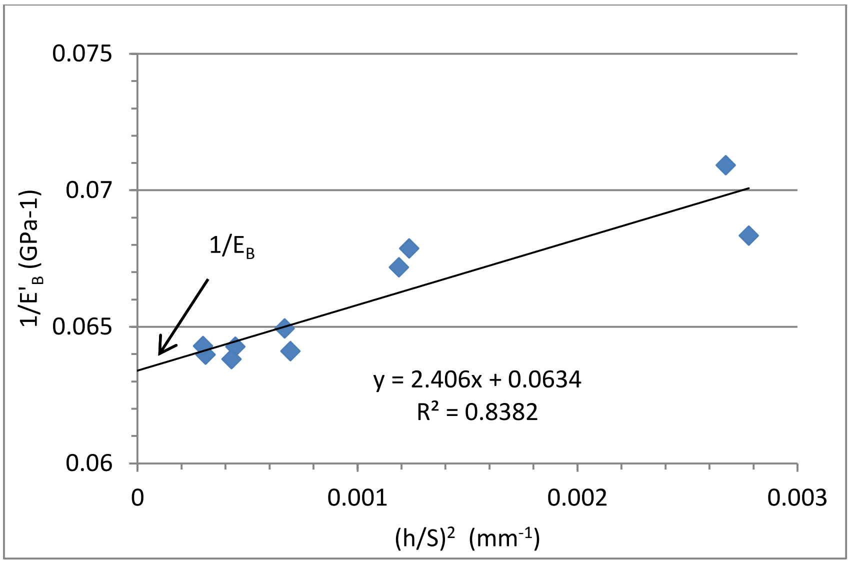

Figure A.4: An example of a 1/E'$_B$ vs (h/S)^2 curve from a multi-span 3-point bend test

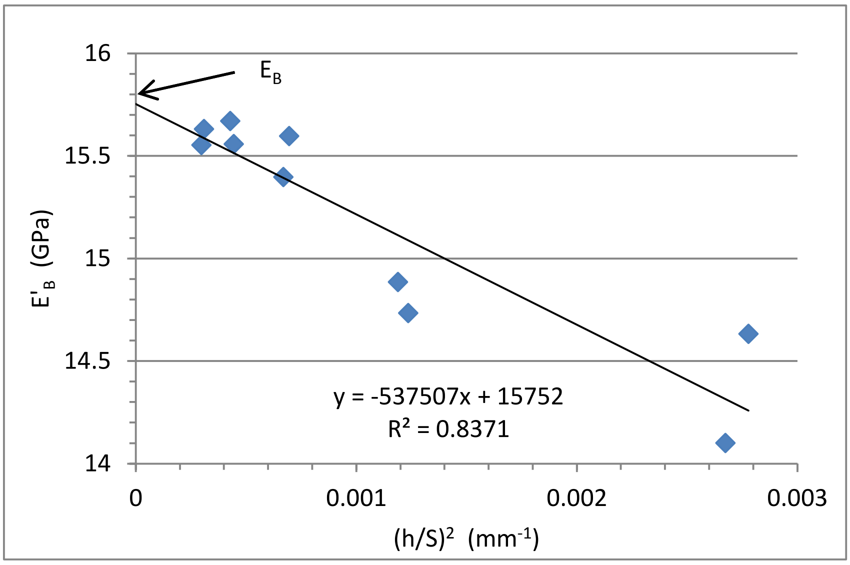

Figure A.5: An example of a E'$_B$ vs (h/S)^2 curve from a multi-span 3-point bend test

Appendix III: Void Content Determination

Void content is widely accepted to be a useful quality-control measurement of cured composites [183]. Instead of the resin-burn off technique commonly used for composites reinforced with synthetic fibres, optical microscopy was used due to the low degradation temperature of around 200°C for the NFs [4][7]. The same method was also used for the GFRPs, to keep the results consistent.

Figure A.6 shows examples of pre- and post-processed optical images for macro- and micro-void volume fraction determination. The analysis involved merging several optical images due to the limited field of view of the microscope.

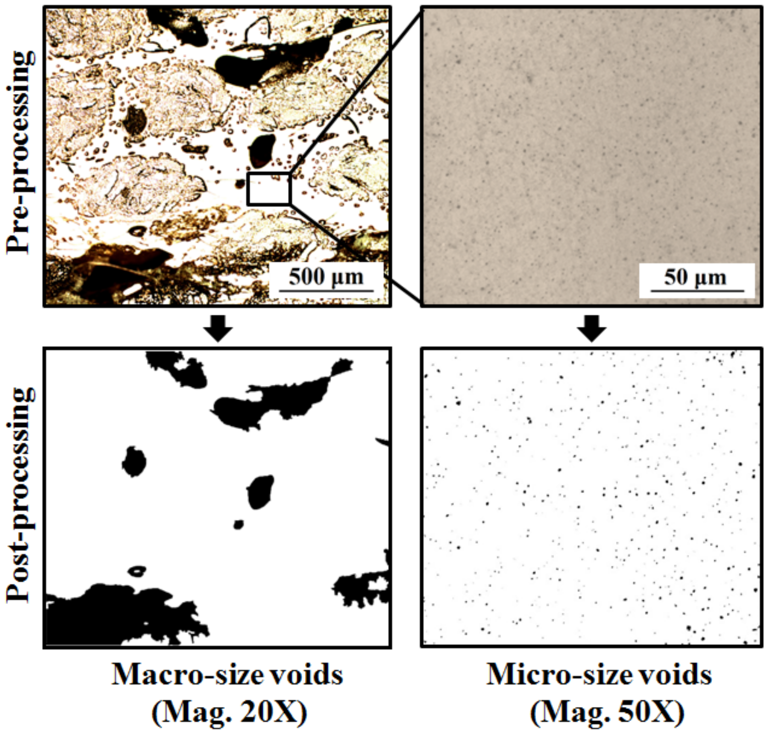

Figure A.6: Pre- and post-processed OM images for void determination showing macro-voids and micro-voids (Images of cross-sectional sample of the initial RIFT-processed Si0R0 FFRPs)

The cured transparent epoxy polymer block, with sample's cross-section embedded, was polished. For macro-void determination, a cross-sectional area of 4.5mm x 0.6mm was captured at a magnification of 20X; due to the limited field of view of the microscope a total of twelve images were necessary for each sample. For micro-void determination, the cross-section was captured at a magnification of 50X in several resin-rich regions throughout the cross-section.

The images were then assembled using the 'Adobe Photoshop CS6' software. Due to the low contrast between the voids and the composites, the voids were then highlighted manually with black pixels. The images were then converted to monochrome images using a threshold function to isolate the filled in regions whose area was then measured by the software.

Calculations

The void volume fraction could be then calculated from the counted number of pixels for void and fibre.

Macro-voids (diameter of 50-1000 µm)

$$v_v^M = \frac{n_v^M}{n_t^M} \tag{A.4}$$

where n_v^M is the number of pixels counted for macro-voids and n_t^M is the total number of pixel counted.

Micro-voids (diameter of 1-50 µm)

$$v_v^m = \frac{\left(1 - v_f\right) n_v^m}{n_t^m} \tag{A.5}$$

where n_v^m is the number of pixels counted for micro-voids respectively, n_t^m is the total number of pixel counted in the resin-rich region and v_f is the fibre volume fraction.

Total void volume fraction

$$v_v = v_v^M + v_v^m \tag{A.6}$$

Appendix IV: The Fox Equation

The Fox equation is used to estimate the glass transition temperature, T_g of a blend of polymer and a low molecular weight diluent (e.g. plasticizer) based on its composition in a bulk state. This diluent increases the free volume of the system and subsequently lowers the T_g. This relationship is expressed by the following equation [147]:

$$\frac{1}{T_g} = \frac{w_1}{T_{g,1}} + \frac{w_2}{T_{g,2}} \tag{A.7}$$

where w_1 and w_2 are the weight fractions of constituent 1 and 2 respectively and $T_{g,1}$ and $T_{g,2}$ are the glass transition temperatures (in degree Kelvin) of constituent 1 and 2 respectively.

This relationship can be used to explain the effect of the polymer-water blend on T_g, i.e. the effect of using reinforcements which contain moisture to fabricate the composites on T_g of the NFRPs.

Example

Table A.2: Summary of glass transition temperature of DGEBA epoxy polymer and water

Constituent	T_g	
	(°C)	(K)
DGEBA epoxy polymer	140.9	414.1
Water	-137.2	136

Table A.3: Summary of glass transition temperature of DGEBA epoxy polymer -water blend at different moisture content

Moisture content, v_w	T_g	
	(°C)	(K)
0 wt% water	140.9	414.1
1 wt% water	132.6	405.8
5 wt% water	102.5	375.6
10 wt% water	70.6	343.8

Appendix V: Fibre Compaction Test

The number of layers of fibre/fabric reinforcements required to be pre-laid within the RTM mould cavity to obtain the required fibre volume fraction was determined using the method discussed in ‘4.2.1’.

Figure A.7 to Figure A.10 show the load-thickness curves for the different types of fibre/fabric reinforcements used in the present study to determine the number of layers of fibre/fabric reinforcement and the mould clamp load.

Unidirectional Flax Fibre (FF-UD)

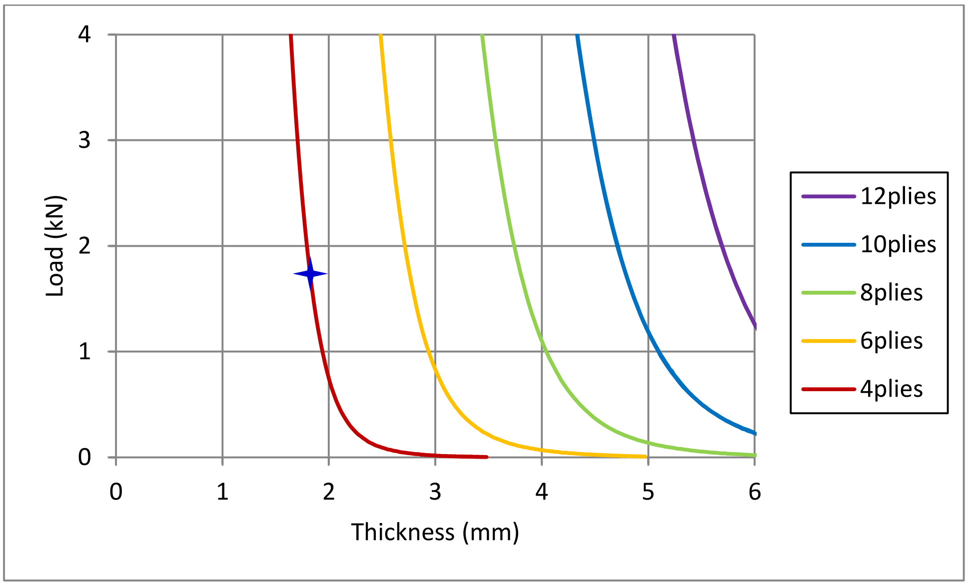

Figure A.7: Fibre compaction test of FF-UD (the blue star represents the number of layers of FF required when GF backing of the FFRPs is undertaken)

Plain-woven Cellulose Fibre (CeF-PW)

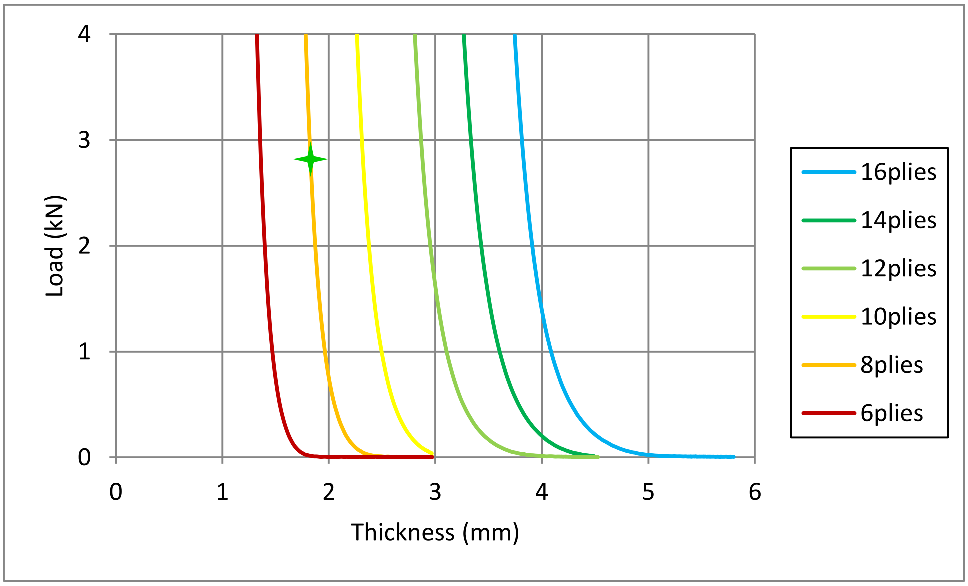

Figure A.8: Fibre compaction test of CeF-PW (the green star represents the number of layers of CeF required when GF backing of the CeFRPs is undertaken)

Unidirectional Glass Fibre (GF-UD)

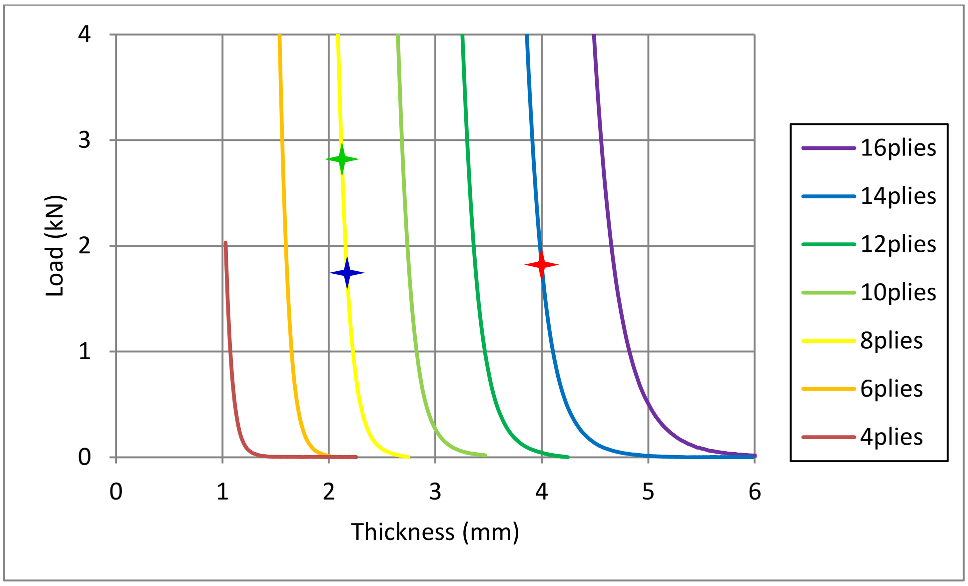

Figure A.9: Fibre compaction test of GF-UD (the red star represents the number of layers of GF required for the GFRPs and the blue and the green stars represent the numbers of layers of GF required when GF backing is undertaken for the FFRPs and CeFRPs respectively)

Plain-woven and Twill 2x2 Glass Fibre (GF-PW+T)

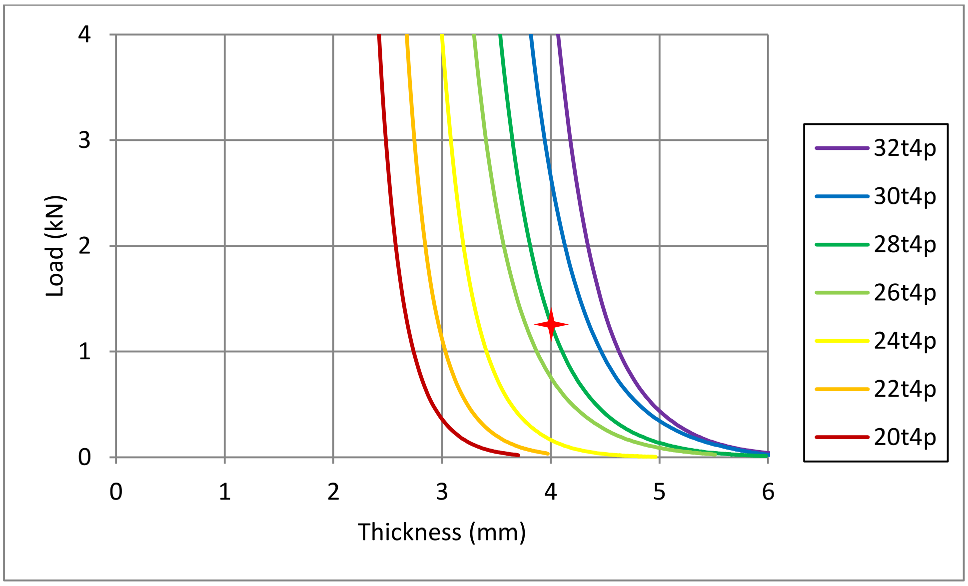

Figure A.10: Fibre compaction test of GF-PW+T (the red star represents the number of layers of GF required for the GFRPs)

As can be seen from Figure A.7 to Figure A.10, a lower number of layers of fibre/fabric reinforcements requires a lower mould clamp load to maintain the thickness and fibre volume fraction that is required. The total combined thickness of both the NFs and the GFs under the equivalent load in the glass-fibre backed NFRPs must be 4 mm, which can be seen as 'blue stars' for the glass-fibre backed FFRPs in Figure A.7 and Figure A.9 or as 'green stars' for the glass-fibre backed CeFRPs in Figure A.8 and Figure A.9; whilst the 'red stars' seen in Figure A.9 and Figure A.10 represent the numbers of layers of reinforcements required for unidirectional and plain-woven & twill 2x2 GFRPs respectively.

Under the fix cavity thickness of the RTM mould of 4 mm, the fibre volume fraction can be estimated by:

$$v_f = \frac{\sum \rho_f^A}{\rho_f t_{mould}} \tag{A.8}$$

where $\sum \rho_f^A$ is the total density per unit area of the stack of fibres, ρ_f is the density of the fibre (the value of the density of fibre after being fan-oven dried at 50°C for 4 hours was used) and t_{mould} is the RTM mould cavity thickness. Table A.4 summarizes the number of layers of fibre/fabric reinforcements and total clamp load required to obtain the required fibre volume fraction.

Table A.4: Summary of fibre compaction test of the reinforcements used in RTM process

Fibre type and architecture*	Stacking Sequence	$F_{f,CT}$ (kN)^	$F_{f,RTM}$ (kN)^	$F_{m,RTM}$ (kN)^	F_{RTM} (kN)^	Estimated fibre volume fraction, v_f †
Unidirectional flax fibre (FF-UD)	$[(0_{GF})_4(0_{FF})_2]_s$^^	1.8	6.6	124	131	0.37††
Plain-woven cellulose fibre (CeF-PW)	$[(0_{GF})_4(0_{CeF})_4]_s$^^	2.4	8.8	124	133	0.55††
Unidirectional glass fibre (GF-UD)	$(0)_{14}$	1.8	6.6	124	131	0.67
Plain-woven and twill 2x2 glass fibre (GF-PW+T)**	$[(0_T)_{14}(0_{PW})_2]_s$	1.6	4.8	124	129	0.47

*For further details, see 'Appendix I'.

^$F_{f,CT}$ = load required to obtain the fibre thickness from the compaction test, $F_{f,RTM}$ = RTM mould clamp load required to obtain the fibre thickness, $F_{m,RTM}$ = RTM mould clamp load required to counteract the resin hydrostatic pressure and F_{RTM} = total RTM mould clamp load.

†The estimated fibre volume fraction was calculated based on the fibre density after being fan-oven dried at 50°C for 4 hours using the total volume per unit area of certain stacking sequences (fibre volume fraction = total density per unit area/fibre density/thickness).

**As the only balanced plain-woven glass fibre (balanced ratio of warp to weft yarns) was available in a very low density per unit area (GSM), in order to match the balanced plain-woven cellulose fibre, the balanced twill 2x2 glass fibre backing was added to the stacking sequence of plain-woven glass fibre. This minimally affected the mechanical properties of the GFRPs while having fewer numbers of layers for ease of manufacturing. Hence, the direct comparison between the CeFRPs-PW and GFRPs-PW+T could be made.

^^Glass fibre backing was required in order to eliminate the plastic deformation and promote linear-elastic behaviour for LEFM assumption.

††The estimated fibre volume fraction of the NFRP regions in the glass-fibre backed NFRPs, see 'Appendix VI'.

As can be seen from Table A.4, the RTM mould clamp load required to maintain the fibre thickness, and so to counteract the resin hydrostatic pressure, was calculated for each composite system. An estimate of the resulting fibre volume fraction and the corresponding stacking sequence of the RTM-processed FRPs are also shown. (However, the actual fibre volume fraction of the RTM-processed FRPs varied somewhat and this aspect was discussed earlier in Table 6.7 in '6.4'.)

Appendix VI: Calculation of Fibre Volume Fraction of the Glass-fibre Backed NFRPs

Due to a significant amount of plastic deformation in the substrate arms of the NFRP DCB specimens (which cannot be tolerated when measuring the mode I interlaminar fracture energy using the LEFM assumption [98]), see Figure A.11, the value of the mode I interlaminar fracture energy could not be measured accurately. Therefore, the NFRPs were manufactured with glass fibre backing using a co-cure method in order to stiffen/strengthen the substrate arms of the DCB specimens to eliminate the plastic deformation.

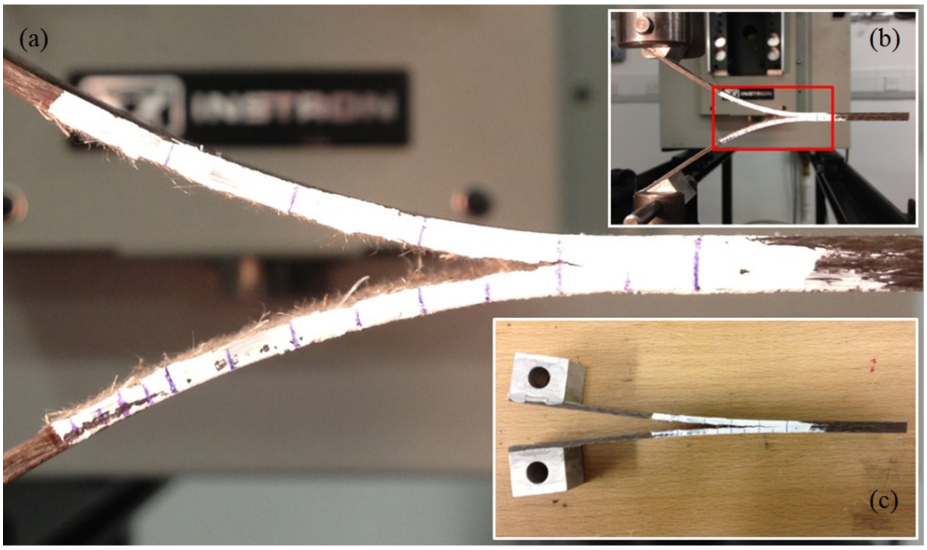

Figure A.11: An example of RTM-processed NFRP DCB specimen under mode I interlaminar fracture toughness test: (a) large bending of the substrate arms, (b) close-up of the specimen and (c) post-test plastic deformation of the substrate arms

Instead of resin-burn off technique commonly used for composites reinforced with synthetic fibres, the fibre volume fraction was calculated using the measured density and geometry due to the low degradation temperature of the NFs [4][7]. The calculation of density and fibre volume fraction of the glass-fibre backed NFRPs is then as follows.

Fibre volume fraction of GF in the GFRP region

$$v_{gf}^{local} = v_{gf}^{entire}\left(t_{nf} + t_{gf}\right) / t_{gf} \tag{A.9}$$

Fibre volume fraction of NF in the NFRP region

$$v_{nf}^{local} = v_{nf}^{entire}\left(t_{nf} + t_{gf}\right) / t_{nf} \tag{A.10}$$

Density of the GFRP region

$$\rho_{gfrp} = \rho_{gf} v_{gf}^{local} + \rho_m\left(1 - v_{gf}^{local} - v_v\right) \tag{A.11}$$

Density of the FFRP region

$$\rho_{nfrp} = \rho_{nf} v_{nf}^{local} + \rho_m\left(1 - v_{nf}^{local} - v_v\right) \tag{A.12}$$

where the ratio between the fibre volume fraction of NF and the fibre volume fraction of GF is given by:

$$R_{nfgf} = \left(W_{nf} / W_{gf}\right)\left(\rho_{gf} t_{gf} / \rho_{nf} t_{nf}\right) \tag{A.13}$$

and the fibre volume fraction of GF in the entire region is given by:

$$v_{gf}^{entire} = \left(\rho_c - \rho_m\right) / \left(\rho_{gf} + \rho_{nf} R_{nfgf} - \rho_m - \rho_m R_{nfgf}\right) \tag{A.14}$$

and the fibre volume fraction of NF in the entire region is given by:

$$v_{nf}^{entire} = v_{gf}^{entire} R_{nfgf} \tag{A.15}$$

and the fibre volume fraction of matrix in the entire region is given by:

$$v_m^{entire} = 1 - v_v \left(v_{nf}^{entire} + v_{gf}^{entire}\right) \tag{A.16}$$

where t_{nf} and t_{gf} are the thicknesses of the NFRP and GFRP regions respectively, ρ_{nf}, ρ_{gf}, ρ_c and ρ_m are the densities of the NFs, GFs, composite and matrix respectively, W_{nf} and W_{gf} are the weights of the NFs and GFs respectively and v_v is the volume fraction of voids.